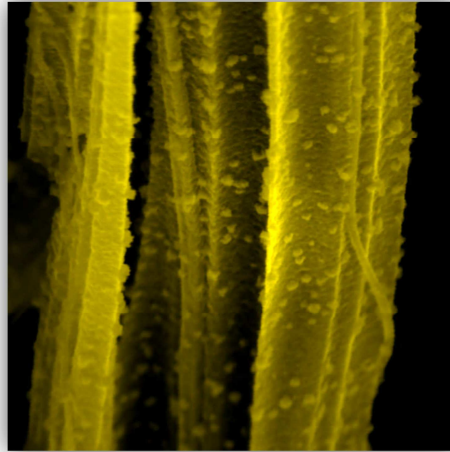


Solar Diodes: Novel Heterostructured Materials for Self-Powered Gas Sensors



Inaugural-Dissertation

zur Erlangung des Doktorgrades
der Mathematisch-Naturwissenschaftlichen Fakultät
der Universität zu Köln

vorgelegt von

Alaaeldin Abdeltawab Mohamed Gad

aus

Fayoum, Egypt



Köln, 2013

Angefertigt mit Genehmigung der Mathematisch-Naturwissenschaftlichen Fakultät der
Universität zu Köln

Gutachter 1: Prof. Dr. Sanjay Mathur

Gutachter 2: Prof. Dr. Gerd Meyer

Vorsitzender: Prof. Dr. Reinhard Strey

Beisitzer: Dr. Ingo Pantenburg

Tag der Promotion: 22.10.2013

This work was carried out under the supervision of Prof. Sanjay Mathur at Institute of Inorganic Chemistry, University of Cologne, Cologne, Germany and was supported by a doctoral fellowship of German Academic Exchange Service (DAAD) and the Egyptian Ministry of Higher Education in the framework of the German-Egyptian Long-Term Scholarship (GERLS, Grant No. A/09/92414).

Gedruckt mit Unterstützung des Deutschen Akademischen Austauschdienstes

Mayada, Jana, Hana,
und
meiner Familie

اهداء

إلى

والذي الطيب

إلى

أهـى الجنونه

إلى

الأبـ الذي ربي (احمد جاد)

إلى

عائـتى الصغـيره (ميادة-جنى-هنا)

إلى

اخـ كـأبـ (ناصر)

إلى

محمد جيهان نهـى ولاء كـريمه صفاء هند

إلى

سعاد الـهى اهدتـنى اجمل هديه

إلى

اصدقائى

إلى

شهداء الثورة المصريه ومن قضى لأجل الحريه

إلى

زياد قطايرجى ورميد الرفاعى

إلى

روح الغاليه كاميلىا

Acknowledgments

I would like to express my sincere gratitude to my supervisor Prof. Dr. Sanjay Mathur for giving me the chance of being a member of his group. I am thankful for his patience, support, and valuable advices from the beginning of writing my proposal to DAAD scholarship and later during this research work. I thank him for the financial support to attend many interesting international conferences and the valuable research visit to Barcelona. Not only his scientific support was helpful in many ways but as well his personal support for me and my family in various issues.

I would like to thank Prof. Dr. Gerd Meyer for evaluation of my work as second assessors. Special thanks to my thesis committee Prof. Dr. Reinhard Strey, Dr. Ingo Pantenburg for being members of my PhD. Defense committee.

I would like to extend my sincerest thanks for Dr. Hao Shen for all discussions, cooperation, useful recommendations and guidance during the first two years of my work.

Thanks Martin Hoffmann for working together and developing what was a kind of crazy idea at first glance but we believed in our ideas and we were able to prove them. Thanks Martin for the introduction to SEM and gas sensing. It was always a pleasure to discuss on scientific and non-scientific topics during our yellow breaks with Tessa.

I would also like to thank Dr. Francisco Ramírez-Hernández and Dr. J. Daniel Prades from the IREC and University of Barcelona. We worked together on the development of the concept of SDS. When it comes to the electrical or physical borders, I was sure that I could count on your expertise. Thanks Francisco for your hospitality during my visit to Barcelona.

I am thankful for Dr. Jiandong Wei and Prof. Dr. Andreas Waag for kelvin probe force microscopy (KPFM) measurements at institute of semiconductor technology, technical university of Braunschweig. Thanks are due to Prof. Klaus Meerholz and Dr. Heike Klesper for support on C-V measurements. I am also thankful to Stefan Röllgen (workgroup of Prof. Klaus Meerholz) for ITO sputtering.

This work has been financially supported by the German Academic Exchange Service (DAAD) and the Egyptian Ministry of Higher Education. I am grateful to them for supporting me during my thesis.

I acknowledge Tessa, Robin, Silke for the thorough reading and fast correcting of my thesis. Thanks Thomas Lehen for the German translation of my abstract and your help at the beginning

Acknowledgments

my work here. Special thanks for Tessa for the introduction to ALD world and for keeping me motivated during the hard times of my work.

I am thankful to Thomas Fischer for his assistance in writing many lab-view programs for the sensing setup and helping me every time to fix the annoying software problems.

Thanks Johannes Schläfer for HR-TEM measurements, Nurgül Tosun, Peter Golus, and Andreas Mettenbörger for plasma etching, Raquel Fiz for the AFM measurements. Thanks Dr. Wieland Tyrre for your advices, Dr. Trilok Singh for the XRD measurements in India. Thanks Dr. Stefan Stucky for your valuable discussions and your time trying to help me. Thanks Lisa Czypiel for your help in crystal structure images.

Thanks Martin, Ania, Karim, Tessa, Mahboubeh, Ashish for being nice friends and for being their whenever help is needed.

Thanks for all the group members of AK-Mathur for all nice things we did together in the last three and half years.

Thanks prof. Dr. Adli Hanna and Prof. Dr. Ashraf F. Ali my supervisors during my master work.

“Et hätt noch emmer joot jejange” This is simply Köln, a city that you don’t feel neither as a foreigner (except the days of your Visa extension) nor as a stranger (except the days of Carnival, only because of your costume).

My deep gratitude is due, to my parents and my family for their devotion, sacrifices and prayers. Last but not least, I owe very special thanks to my ever-supporting wife Mayada for her endless encouragement over the last years. Without you, this would not have been possible. Thanks for your love, understanding, and support. Thanks to my lovely daughters Jana and Hana, you’re the happiness of my life.

Abstract

The integration and correlation of multiple nanomaterial components and junctions in a singular device can open exciting new avenues for more advanced functionalities in nanodevices. One of the key challenges is to achieve controlled and reproducible synthetic protocols of such complex heterostructures with optimal material combinations and geometries. Due to the current global challenges including growing energy demand, limitation of natural resources, as well as environmental issues, research efforts have been devoted to the development of self-powered nanodevices that are capable of harvesting renewable energies such as solar and mechanical energies. Nevertheless, the current concept of self-powered nanodevices is based on coupling an external energy harvesting unit, such as a solar cell or piezo-electric nanogenerator, with the functional nanodevices. In this work, an innovative approach, named solar diode sensor (SDS), has been developed to realize an autonomously operated gas sensor with no additional need of coupling it to a powering devices. The SDS based on a CdS@n-ZnO/p-Si nanosystem unifies gas sensing (CdS@n-ZnO) and solar energy harvesting (n-ZnO/p-Si) functionalities in one single device. A novel sensing mechanism (change of open circuit voltage, ΔV_{oc}), in comparison to the well-known conductometric sensors (ΔR), was demonstrated. It was explained in terms of modulated polarization of the nanoparticles/nanowire interface, gas-material surface interactions and the subsequent changes in the donor density of ZnO (N_D), which is manifested in the variation of V_{oc} in CdS@n-ZnO/p-Si. The fabricated sensors were capable of detecting oxidizing (e.g. oxygen) and reducing gases (such as ethanol and methane) with reproducible response at room temperature and with no need of any other energy source except solar light illumination to deliver a self-sustained gas sensor signal. The generality of the new concept was demonstrated by extending the approach to other nanomaterial geometries including radial heterojunctions of CdS@ZnO/p-Si nanowires and thin-film planar heterojunction.

Additionally, the fabrication of stand-alone single nanowire devices was employed to study the inherent intrinsic electrical and functional properties of single coaxial heterostructures. In this work, the electrical characterization, the photovoltaic and gas sensing performances of a heterojunction device based on a single coaxial n-ZnO/p-Si nanowire were preliminary assessed.

Zusammenfassung

Die Integration und Korrelation verschiedener Nanomaterialien und die damit verbundene Erzeugung von Grenzflächen-bestimmende Eigenschaften innerhalb eines Bauteils, eröffnet interessante Wege für die Herstellung neuartiger Nanobauteile mit kombinierten Funktionen. Eine der zentralen Herausforderungen hierbei liegt in der Entwicklung kontrollierter und reproduzierbarer Syntheseprotokolle solcher komplexer Heterostrukturen mit optimaler Materialkombination und Geometrie. Aufgrund der aktuellen globalen Herausforderungen wie steigender Energienachfrage, Ressourcenknappheit, sowie zunehmender Umweltverschmutzung, wird vermehrt an der Entwicklung von Nanobauteilen mit eigener Energieversorgung geforscht, welche die Möglichkeit besitzen, regenerative Quellen wie Solarenergie und mechanische Energie zu nutzen. Dennoch basieren die aktuellen Konzepte für energetisch autarke Nanobauteile auf der reinen Kopplung zwischen einer externen Energiequelle, wie Solarzellen oder Piezoelementen, und einer funktionalen Einheit. In dieser Arbeit wurde ein innovativer Ansatz namens Solar-Dioden-Sensor (SDS) verfolgt, um einen selbstversorgenden Gassensor zu entwickeln, welcher ohne die Kopplung an eine Energiequelle auskommt. Dieser Ansatz basiert auf CdS@n-ZnO/p-Si Nanosystemen welche einen Gassensor (CdS@n-ZnO) und eine Solarzelle (n-ZnO/p-Si) in einer einzigen Baueinheit vereinen. Ein im Vergleich zu den bekannten konduktometrischen Sensoren (ΔR) neuartiger Sensorik-Mechanismus (Änderung der Leerlaufspannung, ΔV_{oc}) wurde entwickelt und erläutert. Grundlage hierfür sind eine modulierte Polarisation von Nanopartikeln/Nanodrähten, Gas-Material-Wechselwirkung und darauffolgende Änderungen im Dotierungslevel (N_D), welche sich durch eine Variation der V_{oc} in CdS@n-ZnO/p-Si widerspiegelt. Die hergestellten Sensoren waren in der Lage bei Raumtemperatur und ohne externes Bauteil zur Energieversorgung nur mit Hilfe von Sonnenlicht ein reproduzierbares und anhaltendes Sensorsignal auf oxidierende (z.B. Sauerstoff) und reduzierende (z.B. Ethanol und Methan) Gase zu liefern. Die Allgemeingültigkeit und Anwendbarkeit dieses neuen Konzeptes wurde demonstriert durch Erweiterung des Ansatzes auf andere Geometrien wie radiale Heterostrukturen basierend auf CdS@ZnO/p-Si Nanodrähten und Dünnschicht-Heterostrukturen.

Zusätzlich wurden autonome Einzeldraht-Nanobauteile hergestellt, um die inhärenten intrinsischen elektrischen und funktionellen Eigenschaften von koaxialen Heterostrukturen zu studieren. In dieser Arbeit wurde die elektrische Charakterisierung, die Photovoltaikleistung und die sensorische Effizienz einer Heterostruktur basierend auf einzelnen, koaxialen n-ZnO/p-Si Nanodrähten zum ersten Mal adressiert.

Table of Contents

1. Motivation and Research Objectives	1
1.1 Novel approaches for low- and self-powered nanodevices	1
1.2 Research objectives	4
2. State-of-the-Art	9
2.1 Conductometric gas sensors	9
2.1.1 Gas sensing mechanism of conductometric gas sensors.....	10
2.1.2 Surface activation of conductometric gas sensors	12
2.2 Energy production by clean energy harvesting	19
2.2.1 Solar energy harvesting	19
2.2.2 Mechanical energy harvesting	24
2.3 Towards self-powered nanodevices and nanosystems	25
2.4 ZnO general properties and synthesis methods	27
2.4.1 Crystal structure and general properties	27
2.4.2 Synthetic strategies and surface modification of ZnO nanowires	29
3. Experimental and Methods	39
3.1 Chemicals and substrates.....	39
3.2 Synthesis and controlled growth of one-dimensional ZnO nanomaterials.....	40
3.2.1 Hydrothermal growth of aligned ZnO nanowires.....	40
3.2.2 Synthesis of ultra-long ZnO nanowires and nanotubes through anodization	42
3.2.3 Synthesis of ZnO nanorods by simple oxidation of Zn foil:	43
3.3 Fabrication of Si nanowires	43
3.4 Fabrication of p-n heterojunctions and their surface modifications	44
3.4.1 p-NiO film deposition on n-Si substrate.....	44

3.4.2	Synthesis of CdS nanoparticles@ZnO heterostructures	44
3.4.3	Synthesis of ZnS @ZnO heterostructures	45
3.4.4	Synthesis of 3D heterostructures of ZnO nanowire arrays	45
3.5	Material characterization techniques	45
3.5.1	Morphology and composition characterization	46
3.5.2	Optical characterization	48
3.5.3	Surface wettability	48
3.5.4	Electrical measurements	48
3.5.5	Gas sensing measurements	49
4.	Fabrication and Controlled Growth of Functional Nanomaterials.....	51
4.1	Synthesis and controlled growth of one-dimensional ZnO nanomaterials.....	51
4.1.1	Hydrothermal growth of aligned ZnO nanowires.....	51
4.1.2	Synthesis of ultra-long ZnO nanowires and nanotubes through anodization	66
4.1.3	Synthesis of ZnO nanorods by oxidation of Zn foil	72
4.2	Fabrication of Si nanowires	76
4.3	Fabrication of p-n heterojunctions and their heterostructures	79
4.3.1	Planar Heterojunctions.....	80
4.3.2	Radial Heterojunctions	83
5.	Self-Powered Solar Diode Sensors (SP-SDS)	97
5.1	Solar diode sensor (SDS) based on CdS@ZnO nanowires/p-Si heterojunction	98
5.1.1	Structural analysis of the system and the prototype device fabrication	98
5.1.2	The electrical and optical characterization of the SDS system.....	102
5.1.3	Gas sensing properties of SDS	103
5.1.4	The proposed sensing mechanism of self-powered SDS (<i>SP-mode</i>)..	108
5.2	Solar diode sensor based on radial CdS@n-ZnO/ p-Si nanowires heterojunction	117
5.2.1	Structural analysis of the system and the prototype device fabrication	118
5.2.2	The electrical characterization of the radial SDS system	119

5.2.3	The gas sensing and the proposed mechanism of the radial SDS device	120
5.3	Solar diode sensor based on thin-film planar heterojunctions	122
5.3.1	n-ZnO/p-Si film junction	122
5.3.2	p-NiO/n-Si substrate	124
5.4	Current challenges and future prospects of SP-SDS concept	128
5.4.1	Charge separation at CdS/ZnO interface	128
5.4.2	Modification and miniaturization of SDS device architecture	129
6.	Single Nanowire–Based Heterostructures for Energy and Sensing Applications	133
6.1	Coaxial n-Zno/p-Si single nanowire for energy and sensing applications	133
6.1.1	Structural characterization and prototype device fabrication	134
6.1.2	Electrical properties	137
6.1.3	Gas sensing properties	139
6.2	Current challenges and future prospects of single nanowire devices	142
7.	Summary	145
8.	References	149
9.	List of Figures	163
10.	List of Tables	170
11.	Erklärung	171
12.	Teilpublikationen	172
	Curriculum Vitae	173

Abbreviations and List of Symbols

°	degree
°C	degree Celsius
NP, NPs	Nanoparticle, Nanoparticles
QDs	Quantum Dot
NW, NWs	Nanowire, Nanowires
MO _x	Metal oxide
0D	Zero dimensional
1D	One dimensional
2D	Two dimensional
3D	Three dimensional
θ	Bragg diffraction angle
e.g.	exempli gratia
i.e.	id est
SEM	Scanning Electron Microscopy
TEM	Transmission Electron Microscopy
HR-TEM	High Resolution Transmission Electron Microscopy
AFM	Atomic Force Microscopy
EDX	Energy-Dispersive X-ray Spectroscopy
FIB	Focused Ion Beam
UV-vis	Ultraviolet-visible Spectroscopy
ALD	Atomic Layer Deposition
XRD	X-ray Diffraction

Abbreviations and List of Symbols

λ	Wavelength
CA	Contact Angle
CVD	Chemical Vapor Deposition
I-V	Current-Voltage
C-V	Capacitance-Voltage
DC	Direct Current
AC	Alternative Current
I	Current
V	Voltage
I_{sc}	Short circuit current
V_{oc}	Open Circuit voltage
ΔV_{oc}	Change of open Circuit voltage
N_D	Donor density
ΔN_D	Change of donor density
FTO	Fluorine doped tin oxide
ITO	Indium tin oxide
TCO	Transparent conductive oxide
ppm	parts per million
UV	Ultraviolet rays
VB	Valence band
CB	Conduction band

1. Motivation and Research Objectives

Nanotechnology is one of the most challenging and promising scientific research avenue during the last two decades. Recent interest and advances in this field can be related to the invention of nano-characterization techniques, such as scanning tunneling microscope (STM) in 1981, which gives scientists insights into the small wonders of “nano-world” and led to the discovery of fullerenes in 1986 and carbon nanotubes in 1991 [1,2]. However, the conceptual background of this field happened over a longer period of time, starting by introducing the idea of manipulating, and controlling materials by Richard Feynman in his famous talk “There’s Plenty of Room at the Bottom” in 1959 [3]. Additionally the term "nanotechnology" was first coined by Tokyo Science University Professor Norio Taniguchi in 1974, to refer to precision processes in semiconductor engineering [4].

Exploration, synthesis, and characterization of new nanomaterials were the major research objectives during the last years, a huge number of reports have been published reporting new materials with novel nanoarchitectures [5–8]. After such relatively long time of active research, the products based on nanotechnology are still peripheral in market and are far away from the bullish anticipations about their commercialization. “Research is high and the market is far away” [9] this statement, published in a recent report about nanotechnology and market, summarizes the current situation. Such limitations shifted the research orientation towards the challenging issues that impedes the production of mature nanodevices based on nanomaterials building blocks that can replace the dominating microelectronic technologies in real life applications.

One of the key challenges is to achieve controlled and reproducible synthesis of nanomaterials. Furthermore, the ability to tailor their structures and compositions is crucial for tuning their properties according to the application requirements. To meet such goals, a substantial amount of work is required to improve and optimize our current approaches in nanomaterials synthesis. This can open up the possibility of developing new concepts and applications benefit from the outstanding merits of such tailored nanostructures.

1.1 Novel approaches for low- and self-powered nanodevices

The global challenge of population growth, the tremendous energy demands, and natural resources limitation are widely recognized. Unconventional strategies are required to face such daunting challenges; this requires fundamental improvements in all aspects of the energy chain,

from generation to storage and use. In this regard, developing renewable energy technologies is rising nowadays as an alternative to overcome the fossil fuel depletion crisis. In particular, solar energy is one of the potential energy solutions in future, since it is available in abundance in most parts of the world. The amount of solar energy incident on the earth's surface is approximately 1.5×10^{18} kW/year, which is about 10,000 times the current annual energy consumption of the entire world. The sun's total energy is composed of 7% ultraviolet radiation, 47% visible radiation, and 46% infrared (heat) radiation [10], see the spectrum in Figure 1.

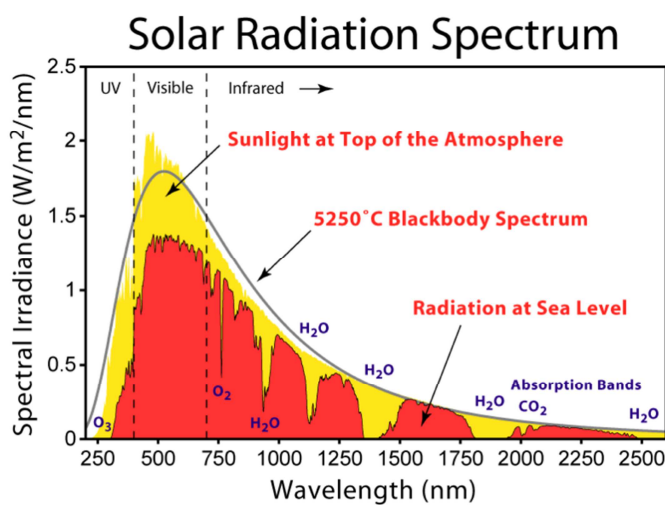


Figure 1 The solar spectrum [11].

Along with energy challenges, air pollution and environmental problems are of critical importance due to their impact and harmful effects on human health besides other safety concerns. Gas sensors have been developed for environmental application including air pollution monitoring, and detection of harmful and explosive gases. Current research effort is mainly directed towards the development of small dimensional, inexpensive, sensitive, and low-power consuming gas sensors.

With the advance in nanotechnology and its diverse applications, which is expected to cover and dominate almost every aspect of our daily life, there is a need to develop low- and self-powered nanodevices with multi-functionalities. With this in mind, the current thesis work was inspired by the concourse of the well-established knowledge and progress in three different research disciplines namely, conductometric gas sensors, solar cells, and self-powered devices,

to postulate and develop a novel concept of self-powered devices that can be used in fields such as gas sensing and photo-detection applications. ZnO nanostructures were the first candidate materials to accomplish such a goal because of their multi-functional characteristics¹ making them suitable for many applications in fields such as electronics, optoelectronics, and energy applications [12].

In the field of gas sensors, one-dimensional ZnO nanostructures such as nanowires, nanorods, and nanotubes, are excellent sensing materials for the detection of oxidizing and reducing gases due to their features such as good charge carrier transport, relatively high conductivity and good crystalline quality. The conductometric gas sensors based on semiconductor metal oxides such as ZnO, are operated by providing applied currents to deliver the sensing signal (change of resistance ΔR) in addition to supplying energy (in the form of heat or UV light) needed to activate the analyte gas/ metal oxide interaction. Despite eliminating the need for thermal heating, the requirement of a UV light source to generate excitons in the wide band gap of common metal oxides hinders the convenience of this approach. Recently visible light assisted gas sensors have been reported as a promising approach to overcome the need of UV activation, by coating narrow band gap sensitizers on the surface of ZnO, which extend the photo-response into the visible-light region. However, such sensors still need applied currents to operate.

On the other hand, ZnO heterojunctions with p-type semiconductors, such as p-doped silicon substrates, are interesting for applications such as solar cells or photodiodes. Due to the difficulty involved in producing stable p-type ZnO, such heterojunctions represent good alternatives to p-n homojunction of ZnO.

In parallel with the above mentioned research areas, an active field of research focusing on developing self-powered nanodevices has been emerged recently, profiting from the advances made in the field of nanogenerators². The current concept of self-powered nanodevices is based on coupling an external energy harvesting unit, such as a solar cell or a nanogenerator with functional nanodevices (e.g. gas sensor or UV sensor) to provide the power needed for their operation. Despite of the novelty of this approach, the powering solution still manifested the integration of different macroscopic functional units and the challenge associated with the assembly of complementary functionalities, such as powering and sensing units at the nanoscale.

¹ For example, ZnO is exhibiting semiconducting and piezoelectric dual properties [12].

² Nanogenerators are based on harvesting mechanical energies to convert them into electricity [12].

Learning from all these different aspects and taking into account their promises and challenges, considerable efforts should be undertaken to fabricate low power consuming gas sensors and to use the available renewable energies such as solar energy to develop self-powered nanodevices for future applications. With these goals in mind, an innovative approach, named solar diode sensor (SDS), has been developed in this work (European Patent number: EP 11179783.3). SDS is a real self-powered gas sensor that is autonomously operated with no additional need of other powering devices. It is based on the integration and correlation of complementary functionalities originating from multiple junctions in a singular nanostructure. In this work, the gas sensing and solar energy harvesting abilities of ZnO nanostructures were utilized to design a self-sustained gas sensor, where a new sensing mechanism was proposed and the proof of concept was demonstrated. Then, the generality of the new concept was expanded to other materials and systems.

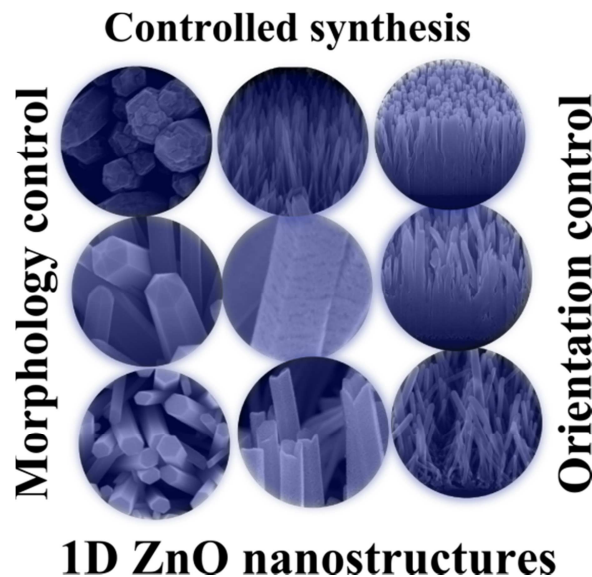
Additionally, the fabrication of stand-alone single nanowire devices was employed to study the inherent intrinsic electrical and functional properties of single coaxial heterostructures. In order to achieve a better understanding and analysis of the quality of interfaces of their analog bulk-type nanowire arrays systems, since the interfering factors of the bulk systems (such as the statistical dispersion and contact effects) are minimized. Such fundamental studies on the single nanowire scale is curial for providing deeper understanding needed for development of more efficient bulk nanodevices based on nanowire arrays.

1.2 Research objectives

Heterostructures of inorganic materials such as metal/metal oxide or oxide/oxide offer a new paradigm for assembling nanoscopic structures into functional devices, which requires fundamental advances in the synthesis of multiscale structures with controlled properties and interfaces. This work deals with the design and controlled synthesis of ZnO nanowires as well as their heterostructures. The synthesized materials will be used to fabricate functional devices (either based on nanowire arrays or single nanowires). The research objectives of this work will be as follows (see figure 2):

- 1. Controlled synthesis of 1D ZnO nanostructures*

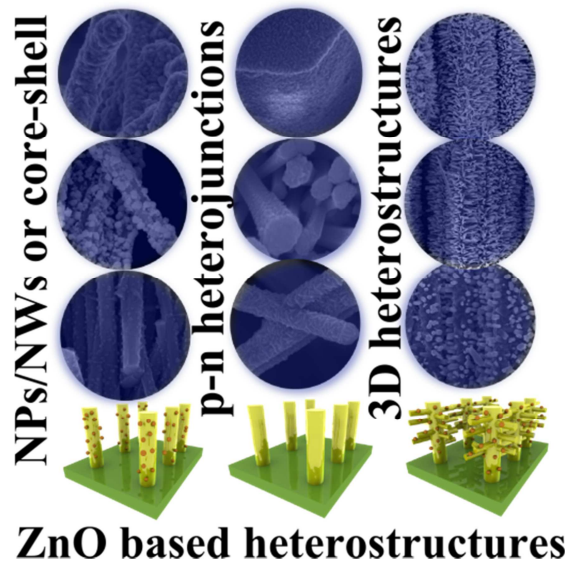
Many synthesis routes have been developed to prepare ZnO nanomaterials, however, for realizing prototype devices based on ZnO nanostructures and heterostructures controlled and reproducible synthesis is crucial to fully realize their unique electrical, chemical or morphological properties. The controlled synthesis of well aligned one-dimensional ZnO nanostructures required for applications that need efficient generation and transport of charge carriers and ions such as optoelectronic, energy conversion and gas sensing applications will form the primary focus of this work (see Goal 1) [Chapter 4 entitled “Fabrication and controlled growth of functional nanomaterials” will address this objective].



Goal 1 Controlled synthesis of 1D ZnO nanostructures.

2. *Fabrication of ZnO based heterostructures with tailored properties*

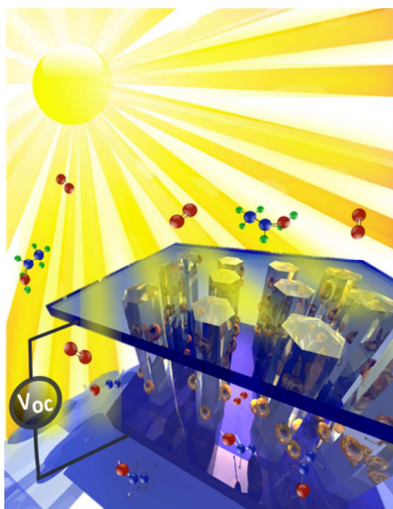
Hybrid materials and heterostructures are promising approaches to build nanosystems with multifunctional and adjustable properties. In this work, different heterostructures based on ZnO were fabricated such as p-n heterojunctions (in combination with different p-materials such as planar p-Si substrates and p-Si nanowires and different p-metal oxides), and morphologies enabling both radial (core-shell) as well as planar diode structures (see Goal 2) [This objective will be introduced in chapter 4 “Fabrication and controlled growth of functional nanomaterials”, (see sections 4.2, and 4.3)].



Goal 2 Fabrication of ZnO based heterostructures with tailored properties.

3. *Exploration, demonstration and validation of self-powered solar diode sensor (SP-SDS) concept*

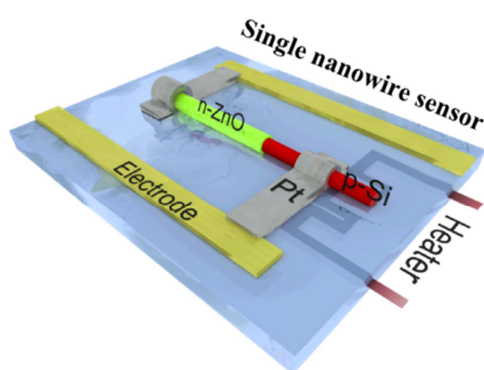
The new concept of self-powered solar diode sensors (SP-SDS) will be introduced and discussed in terms of structural analysis of the system and the prototype device fabrication (see Goal 3), the demonstration of their electrical, optical, and gas sensing properties. The underlying gas sensing mechanisms will be examined to explain their gas sensing behavior toward different gases. Additionally, different heterostructure combinations and systems will be used to prove the generality of the SP-SDS concept. Finally the current challenges and limitations and the future prospects to develop the SDS concept will be discussed [The details will be given in chapter 5 entitled “Self-powered solar diode sensors (SP-SDS)”].



Goal 3 Exploration, demonstration and validation of self-powered solar diode sensor (SP-SDS) concept.

4. Fabrication of stand-alone single nanowire devices for energy and sensing applications

The prototype devices based on single nanowire heterostructures will be investigated in terms of their fabrication, electrical characterization as well as their potential applications as stand-alone nanodevices (see Goal 4) for energy and gas sensing applications [Chapter 6 entitled “Single nanowire heterostructures for energy and sensing applications” will address this objective in detail].



Goal 4 Fabrication of stand-alone single nanowire devices for energy and sensing applications

Final Objective of this thesis is to demonstrate concepts enabling integration of heterostructures in conventional device designs in order to enhance their functional performance.

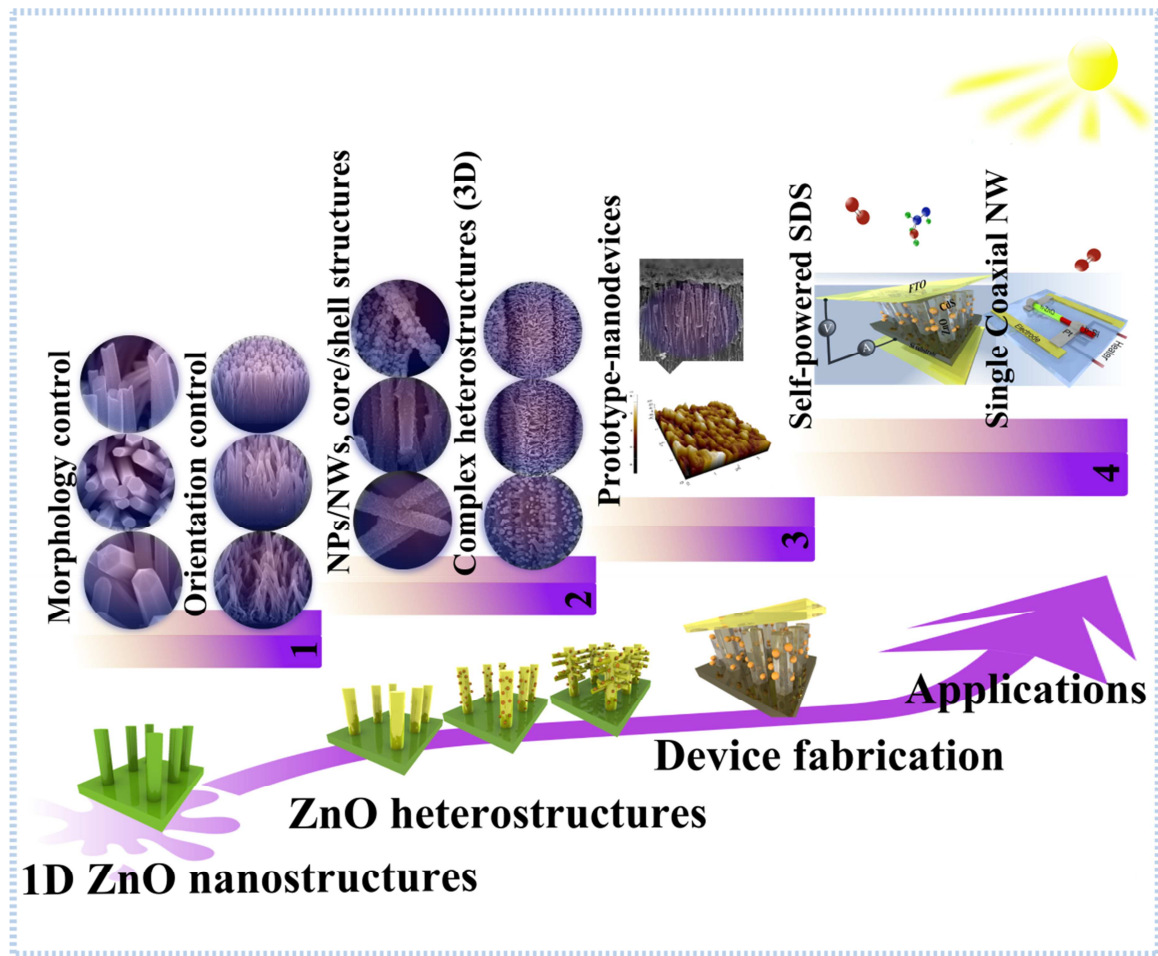


Figure 2 Schematic representation of the research objectives of this thesis: 1) controlled synthesis of 1D ZnO nanostructures, 2) Fabrication of ZnO based heterostructures with tailored properties, 3) Integration and testing their device potential, and 4) Investigation of self-and low powered gas sensing applications.

2. State-of-the-Art

Zinc oxide (ZnO) represents one of the most important materials that are expected to play a key role in future applications based on nanotechnology. This result from their unique merits including their important physical and chemical properties combined with a rich family of nanostructures and different morphologies. ZnO has been effectively used in enormous of applications in fields of electronic, optoelectronic, electrochemical, and electromechanical devices such as ultraviolet (UV) lasers, gas sensors, solar cells, light-emitting diodes, field emission devices, piezoelectric nanogenerators, and nanopiezotronics [13–15]. ZnO represents the best candidate for fabrication of hybrid systems, benefit from their facile synthesis, tunable and modulated chemical composition, size, and morphology, as well as their multifunctional character³.

In this work, the main focus is the development of self-powered, solar light-activated gas sensors based on p-n junction composed of n-ZnO and other p-doped materials (such as p-Si substrate, p-Si nanowires, p-NiO), respectively. Therefore, in this chapter the use of ZnO in gas sensing, and energy-harvesting related domains is highlighted. Later, the basic properties of one-dimensional ZnO nanomaterials are introduced and the fundamental advances in their synthetic strategies and their modification to produce heterostructures are discussed.

2.1 Conductometric gas sensors

Among the different gas sensor technologies, conductometric gas sensors based on metal oxides unify the highest robustness level and minimum costs. Typically the term conductometric sensors refer to sensing materials that change their electrical resistance when exposed to different atmospheres such as oxidizing or reducing gases. The first fabricated conductometric sensor goes back to the 1960s by Seiyama and Taguchi [16,17]. Semiconductor metal oxides (mainly SnO₂ and ZnO) are the most widely used materials for the commercial solid state chemical sensors, as their properties (chemical, physical, and electrical) are often highly dependent on the changes in the chemical environment [18–20] .

³ ZnO has a unique ability to demonstrate semiconducting and piezoelectric, catalytic activity, or surface adsorption characteristics simultaneously [6].

ZnO nanomaterials are favoured for sensing and photovoltaic applications due to their high conduction electrons mobility ($200 \text{ cm}^2 \text{ V}^{-1} \text{ s}^{-1}$), as compared to other metal oxides such as TiO_2 , WO_3 , In_2O_3 , and SnO_2 (0.4, 10, 100, and $160 \text{ cm}^2 \text{ V}^{-1} \text{ s}^{-1}$, respectively), which promotes an efficient carrier collection [21,22].

Since the work done by Yamazoe [23], which showed that the reduction of the size of SnO_2 crystallite resulted in a significant increase in sensor performance, there was an active research on fabricating gas sensors with smaller structures [24]. Among ZnO nanomaterials, one-dimensional structures such as nanowires, nanorods, nanotubes, are recently used more often for the detection of chemicals and gases due to their large surface-to-volume ratios and Debye length comparable to their size. Besides their facile fabrication process and good stability (due to their high crystallinity), low power consumption, and integration capabilities in microsystems [24–26].

Due to the large number of reports as well as the wide variety of research aspects published in this field, only some relevant points will be addressed in the following narrative.

2.1.1 Gas sensing mechanism of conductometric gas sensors

The sensing mechanism of ZnO mainly relies on the change of electrical conductivity (ΔG) contributed by interactions between the metal oxide surface and the surrounding ambient. The sensing response of ZnO to different gases is attributed to the chemisorption of oxygen on the ZnO surface and the subsequent reaction between adsorbed oxygen and different gas (oxidative or reductive), which causes the change of conductivity (ΔG). The sensing response can be described by the following steps: Surface adsorption, surface reaction, and DC conductance change (ΔG) (or resistance change, ΔR) which is the sensing response signal.

(i) *Surface adsorption*

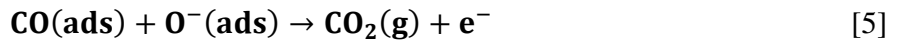
The first interaction between gaseous molecules and the ZnO surface takes place by adsorption processes, where the gas species are physisorbed on the metal oxide surface. Physisorption is a slightly exothermic process that does not need activation [24].

(ii) *Surface reaction*

The ZnO nanowire in the ambient atmosphere is surrounded with oxygen molecules, which upon providing suitable activation energies (either by thermal heating or illumination) are ionosorbed on ZnO surface to oxygen species (O_2^- , O^- , O^{2-}) according to the following simplified reaction steps [27]:



The sensing mechanism in metal oxides gas sensors is basically related to the surface reactions between the gaseous species and ionosorbed surface oxygen. When a reducing gas (such as CO) is introduced to the metal oxide surface, it reacts with the ionosorbed oxygen moieties and oxidizes to CO₂ (see equation 4 [28]), with the consequent release of captured electrons back to the metal oxide surface, as shown in equation 5 [28], which result in a drastic surface resistance drop [24].



The details of the specific surface reactions are not certain till now and still a subject of scientific debate. As an example, another proposed scenario for CO sensing was explained by the reaction with hydroxyl groups that produces atomic hydrogen, which in turn recombines with oxygen of the lattice to release a free electron [29]. In addition to the above mentioned possibilities, a direct adsorption of CO (as CO⁺) can also takes place [24,30]. Direct adsorption of oxidizing gases, like the strongly electronegative NO₂ gas, is also proposed which result in a surface resistance increase (see equations 6 and 7 [28]).



(iii) DC conductance (resistance) change

The sensor response towards analyte gas for metal oxides sensors, such as ZnO, is defined as the (relative) change of conductance or resistance, where the conductance of a ZnO nanowire can be calculated according to equation8 [21]:

$$\mathbf{G} = \mathbf{N}_0 \cdot \mathbf{e} \cdot \boldsymbol{\mu} \cdot \boldsymbol{\pi} \cdot \mathbf{d}^2 / \mathbf{L} \quad [8]$$

where N_0 is the original donor density, e the electronic charge, μ the mobility of the electrons, and d and L are the radius and length of the metal oxide nanowire, respectively.

The change in conductance can be expressed by equation 9 [21]:

$$\Delta G = \Delta N_D \cdot e \cdot \mu \cdot \pi \cdot d^2 / L \quad [9]$$

Equation 9 can be simplified as follows (equation 10) [21]:

$$\Delta G/G = \Delta N_D/n_0 \quad [10]$$

The change in conductance (ΔG) is depending on the change of donor density of ZnO (ΔN_D) which results from the variation of surface carriers [21].

2.1.2 Surface activation of conductometric gas sensors

The sensing signal of metal oxides is derived by applying a constant bias current and monitors the change in resistance upon gas exposure. Since the adsorption and desorption of gas molecules on the surface of metal oxides are an endothermic processes, activation energies are needed for the interaction of gas molecules on the metal oxide surface. The activation energies usually supplied either in form of thermal heating or by a non-equilibrium process such as illumination (UV-, or visible- light illumination) [24,31,32].

2.1.2.1 Thermally activated conductometric gas sensors

Adsorption and desorption of gas molecules on the surface of metal oxides are both activated processes, typically high temperatures in the range of 200-400 °C are needed to enhance the adsorption/desorption process on the sensor surface [33]. The physisorption is a slightly exothermic process that typically occurs at low temperatures, while the chemisorption takes place at higher temperatures due to the energy barrier that has to be overcome for a physisorbed molecule to reach the chemisorption well according to Lennard-Jones adsorption model (as is illustrated in figure 3) [27]. For the thermally activated gas sensing process, the molecular form of ionosorbed oxygen (O_2^-), which has lower activation energy, is dominating up to about 200 °C, while at higher temperatures above 200 °C the atomic form (O^-) dominates [28].

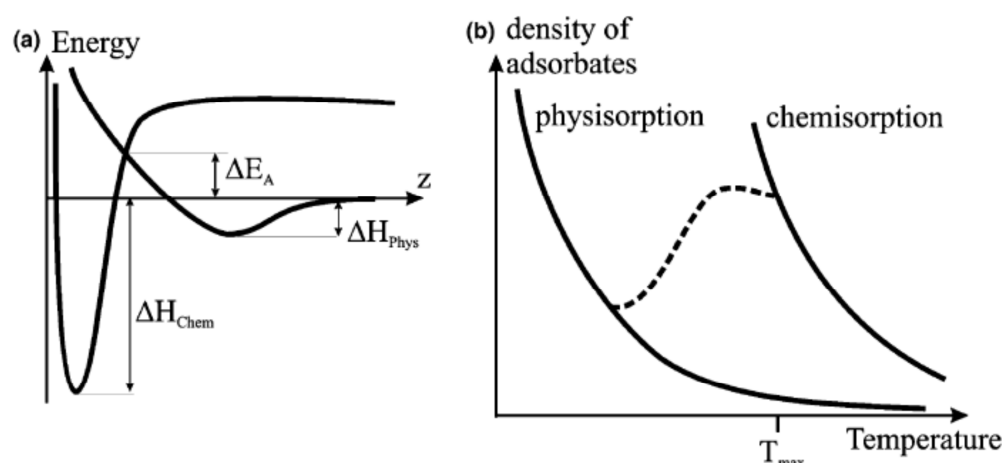


Figure 3 (a) Lennard-Jones model for physisorption and chemisorption of a molecule. An energy barrier ΔE_A has to be overcome for a physisorbed molecule to reach the chemisorption well. Typical adsorption isobars are shown in (b). The solid lines are equilibrium physisorption and a chemisorption isobar, the dashed line represents irreversible chemisorption. A maximum coverage of chemisorbed molecules is obtainable at a temperature T_{\max} . Below T_{\max} the chemisorption is irreversible because the rate of desorption becomes negligible [27].

Identification of optimal working temperature for metal oxides is a key factor determining the gas sensor responses. For optimal conditions, the sensor must be operated in a temperature range where reversible chemisorption takes place [24].

2.1.2.2 UV light activated conductometric gas sensors

Nowadays, exploring viable alternatives to thermal heating for activating gas sensors at room temperature sensors is earning more interest, not only for energy consumption reduction but also for safety requirements. Heated gas sensors are not favourable in some applications like explosive environments. Furthermore, the typically high temperatures used for sensing activation can affect both the devices lifetime and sensitivity, in addition to the complex circuitry required to maintain accurate temperature control during operation [34].

Ultraviolet (UV) light illumination of metal oxides (such as ZnO) is the most studied alternative to replace the traditional thermally activated gas sensors. A wide variety of gases, such as O_2 , H_2O , $HCHO$, C_2H_5OH , and NO_2 , has been detected under UV light irradiation by using different ZnO nanostructures [24,34–39]. The illumination of the ZnO surface with UV light, with energy equal or larger than its band gap (3.4 eV), generates a large numbers of photo induced carriers

that decreases the depletion layer width, which influences the adsorption and desorption of surface molecules [40].

The gas sensing mechanism of UV-activated gas sensors can be explained as following:

Under dark conditions, the chemisorbed oxygen species are thermally stable and cannot be removed from the metal oxide surface at room temperature condition because of the large adsorption energy (figure 4 a) [40].

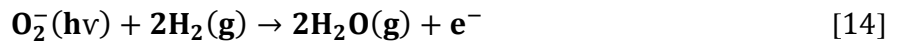
Under UV-light illumination, electron-hole pairs are generated and the photoinduced holes discharge the negatively charged chemisorbed oxygen ions, causing desorption of oxygen ions (O_2^-) from the ZnO surface in the form of oxygen as described by equations 11, 12 (see figure 4 b) [40]:



Additionally, photoinduced oxygen ions are created due to the reaction between the ambient oxygen molecules with the photoelectrons, according to equation 13 [40], which results in a slight increase of ZnO resistance. These two processes continue until a steady state is reached where the rates of oxygen adsorption and desorption becomes equal (figure 4c).



The photoinduced oxygen ions ($O_2^-(h\nu)$) are highly reactive and are responsible for the room temperature gas sensitivity of ZnO. These photoinduced oxygen ions, which are weakly bounded to ZnO surface as compared to the strongly attached chemisorbed oxygen ions, are participating in redox reactions when a reduced gas like H_2 is introduced (figure 4 d, e). The electrons released from this process cause the changes in the measured electrical resistance of ZnO [40].



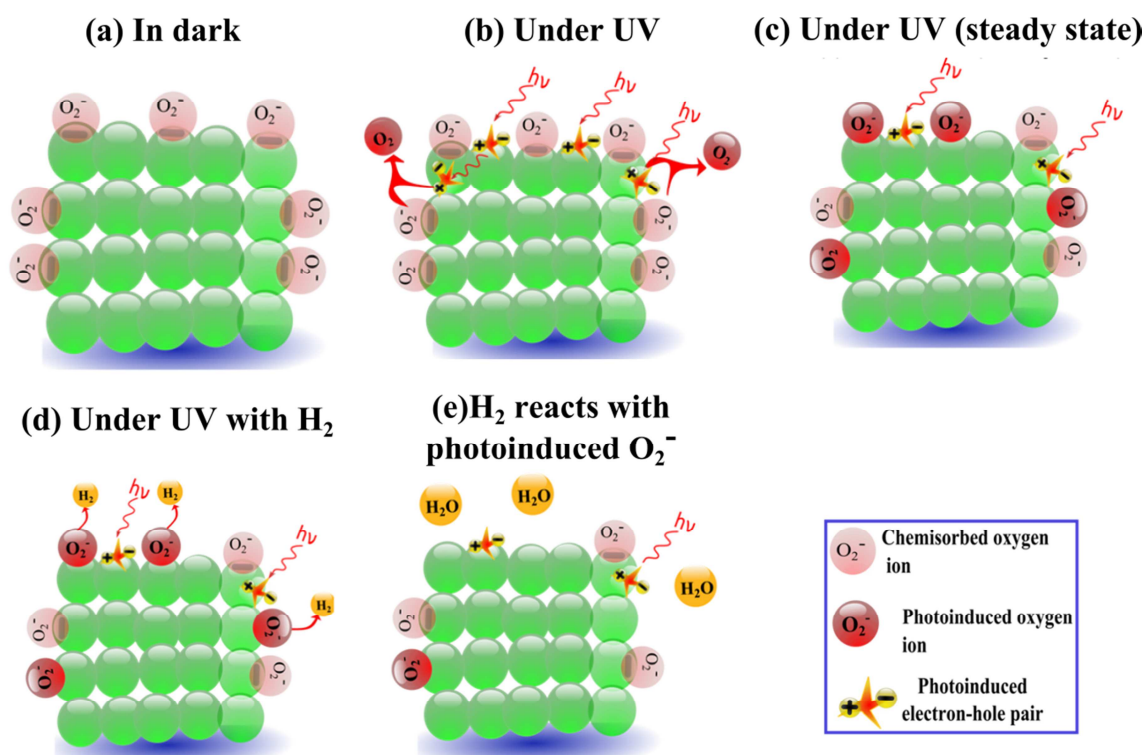


Figure 4 Schematic representation of the UV-activated gas sensing mechanism of metal oxides at room- temperature. The photoinduced oxygen ions are highly reactive and able to interact with H₂ at room temperature [40].

2.1.2.3 Visible light activated conductometric gas sensors

Room temperature operated gas sensors could be achieved by using UV illumination (as alternative to thermal activation), as discussed above. However, the practical application of such sensors is hindered due to the high cost of UV light sources and the harmful nature of UV-exposure on the human body, which may causes acute and chronic health effects on the skin and eyes. Visible-light-activated gas sensors have recently been reported as a promising sensor platform for practical applications [31,32,41–45]. If compared to UV light, there is much more energy produced by the sun in the visible light range of spectrum, also visible light sources have lower costs [42].

Many approaches have been used to extend the absorption of wide band gap metal oxides from the UV light region into the visible light spectral range such as incorporation of transition-

metal ions (like La, Ni, Mn, and Fe) [41,45–49], forming heterostructures with other metal oxides (such as CuO [50], Fe₂O₃ [51], WO₃ [31], In₂O₃ [42]), incorporation of a narrow band gap semiconductor (such as CdS [52], CdSe [53], PbS [54], Bi₂S₃ [55], and LnP [56]), or incorporation of oxyhalides such as bismuth oxyhalides (e.g. BiOI) [57]. Many reports have shown the promises of using such modified heterostructures for visible light-driven applications such as photocatalysis [51,58], solar cells [59], photoelectrochemical (PEC) hydrogen generation [53,60].

Han *et al.* fabricated a visible-light assisted gas sensor based on In₂O₃/ZnO heterostructure for detection of formaldehyde by applying external voltage of 10 V and under 460 nm visible light illumination [31]. The room temperature photoelectric gas sensing of formaldehyde (HCHO) based on the Fe-doped flowerlike ZnO powders was studied (under 532 nm visible light irradiation, and applied bias of 10 V) [41]. Zhai *et al.* used CdS NP/ZnO microcrystal heterostructures to develop visible light induced gas sensors, where applied constant voltage was used to enable measuring the sensing signal, the used sensor is shown schematically in figure 5 [32]. It was shown that the response is enhanced with increasing of surface coverage density of CdS on ZnO to a maximum value and then decreased with further decoration density, where the fully covered sample with CdS shell on ZnO core showed almost no sensitivity to the gases indicating that ZnO is the active sensing element in this system [32]. An unclear point in this regard is that the ON/OFF sensing curves were obtained by tuning ON/OFF the 500 W Xe lamp. Obviously the ON/OFF curves showed the best appearance because the photocurrent is zero under dark, which could better reflect the photocurrent detection rather than the sensing response (i.e. the recovery was not real in such case).

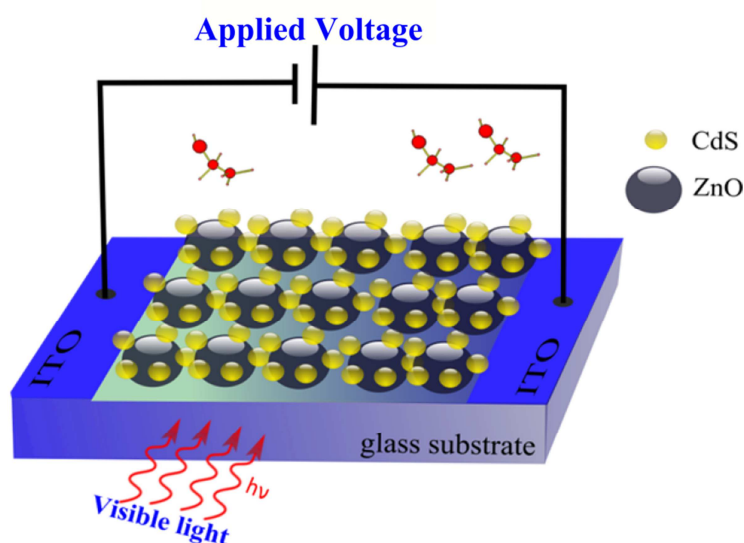


Figure 5 Schematic representation of visible-light assisted gas sensor based on CdS/ZnO heterostructures [32].

The gas sensing mechanism of visible-light activated gas sensors is similar to that described for the UV-light activated sensors, where the photoinduced oxygen species, created due to light interaction with MO_x surface, plays a major role in enabling room temperature sensing. Under dark conditions oxygen is adsorbed on the surface to form chemisorbed oxygen species which results in a high-resistance depletion layer (figure 6 a). Under visible-light illumination electron-hole pairs are generated and holes discharge and release the captured adsorbed oxygen ions such as (O_2^-), in a form of oxygen causing thinning of the depletion layer and an increase in the conductance of the metal oxide (figure 6 b). Additionally, oxygen in the ambient atmosphere reacts with photogenerated electrons and creates photoinduced oxygen species that are weakly bounded to the sensor surface (see figure 6 b). The processes of oxygen adsorption and desorption will continue until a steady state is reached where the rates of the two processes equals (figure 6 c). Thus the thickness of the depletion layer as well as the conductivity of MO_x gradually achieves a stable state. Upon exposure to a reducing gas such as formaldehyde, the highly active photoinduced oxygen ions ($O_2^-(h\nu)$) participate in a redox reaction at room temperature (according to equation 15 and as shown schematically in figure 6 d, e) and electrons released to the surface of the MO_x cause a decrease in the measured resistance of the gas sensor [31].



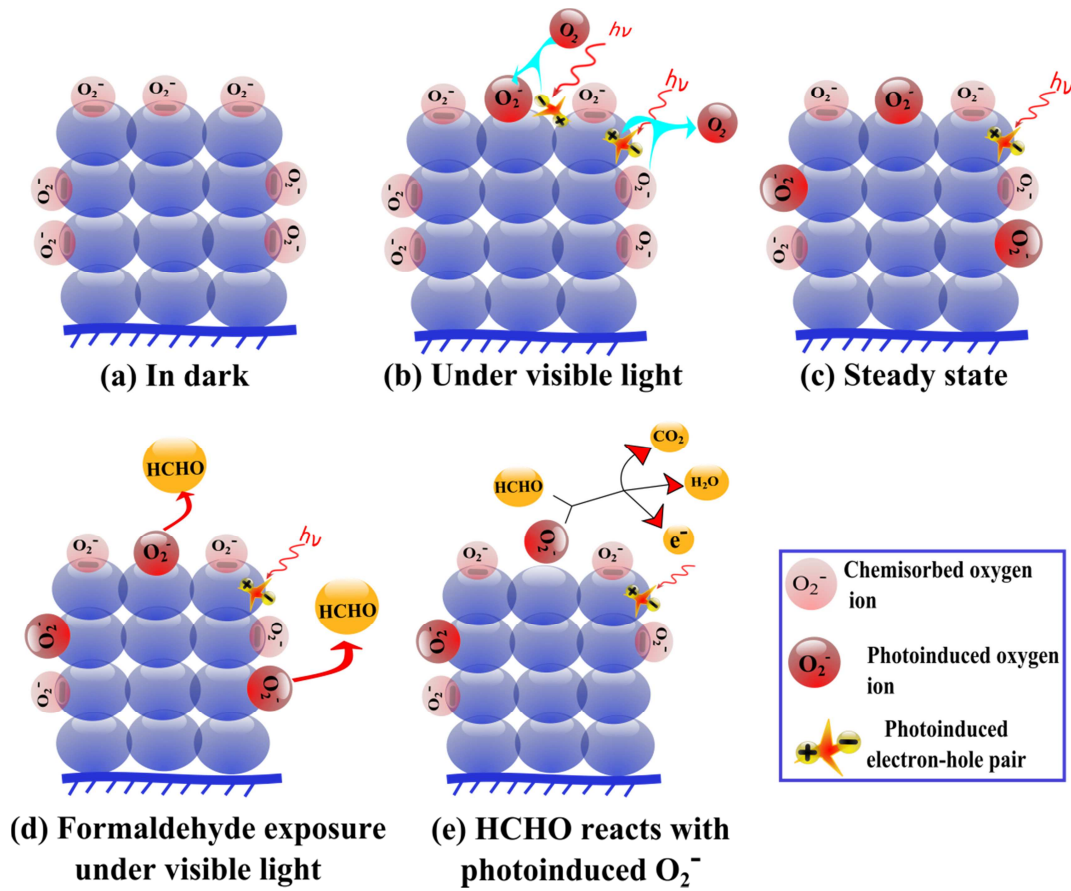


Figure 6 Schematic representation of the visible-light activated gas sensing mechanism of metal oxides at room temperature [31].

2.1.2.4 Self-heating of individual nanowires

Many approaches have been used to activate gas sensors and to enhance their surface chemistry in order to reduce their operational temperature such as the use of UV or visible light for photoactivation as previously mentioned. Alternatively, the self-heating of individual semiconducting nanowire chemiresistors is another promising approach for producing low power consumption gas sensors. The main idea of operation is based on applying well-controlled bias current values through individual nanowires (i.e. conductometric sensor) in the way that the Joule heating⁴ released in the chemiresistor is sufficient to warm up the nanowire to the temperature required for surface redox reactions and thus the requirement of external heating is avoided [61–63].

⁴ Also known as ohmic heating and resistive heating.

2.2 Energy production by clean energy harvesting

A fundamental demand for developing renewable energy sources is rising as an alternative to overcome the fossil fuel depletion crisis. In this regard, many renewable energy technologies have been developed such as solar cells, fuel cells, biofuels, and nanogenerators [64]. In this section the solar light harvesting by solar cells followed mechanical energy harvesting by nanogenerators will be discussed in detail.

2.2.1 Solar energy harvesting

Solar light harvesting is an attractive approach for production of clean and renewable green energy. Nanomaterials have been extensively studied as the building blocks for energy-related applications such as solar fuels, in which solar energy is converted into chemical energy, and solar cells, where solar energy is converted into electrical energy.

Many types of solar cells have been investigated such as dye-sensitized solar cells (DSSC), bulk heterojunction (BHJ) photovoltaic cells, and quantum dot solar cells (QDSC) [65]. The focus will be devoted to quantum dot sensitized solar cells. Albeit different in their modes of operation and working principles, QDSC share common similarities to the model system that will be used in the current thesis work regarding the light absorption, charge separation, and charge collection processes [66].

Heterostructures capable of absorbing solar light are generally composed of a donor semiconductor in contact with an acceptor material through shared interfaces. While the donor material should possess a high absorption coefficient across the solar spectrum (e.g. metal chalcogenide such as CdS, CdSe, PbS, and PbSe), the acceptor materials are generally wide band gap semiconductors (such as TiO₂, ZnO, or SnO₂) that act as conductive pathways for transferring photoexcited carriers between the donor and the current-collecting electrode [67]. In addition to the solar light absorbing nanomaterials, there are other components needed to design the solar cell device such as electrodes and hole-transporting material (usually an electrolyte solution containing a chemically and energetically compatible redox couple such as (S²⁻/S_n²⁻) and its analogues). The combination of nanoparticles with one dimensional metal oxide nanowires is one of the promising approaches to produce efficient solar cells. Depending on the synthesis method NPs can be directly contacted to the MOx surface (e.g. SILAR, successive ionic layer adsorption

and reaction, and chemical bath deposition methods) or through a molecular linkage between the NPs and MOx (such in case of linker-assisted binding method).

Upon light illumination of a semiconductor, photons with energy larger than its band gap are absorbed. This results in excitation of electrons in the valance band to the conduction band and the creation of an exciton (i.e. electron-hole pair). The major charge transfer processes can be summarized in the following steps as shown schematically in figure 7, (1) electron injection from the excited metal chalcogenide (donor) into the metal oxide (acceptor), (2) electron transport to the collecting electrode surface, (3) scavenging of holes with a redox couple, and (4) regeneration of the redox couple at the counter electrode. During these processes there is a possibility that unfavourable processes can occur such as (5 and 6) the charge recombination of electrons at the electrolyte interface [68].

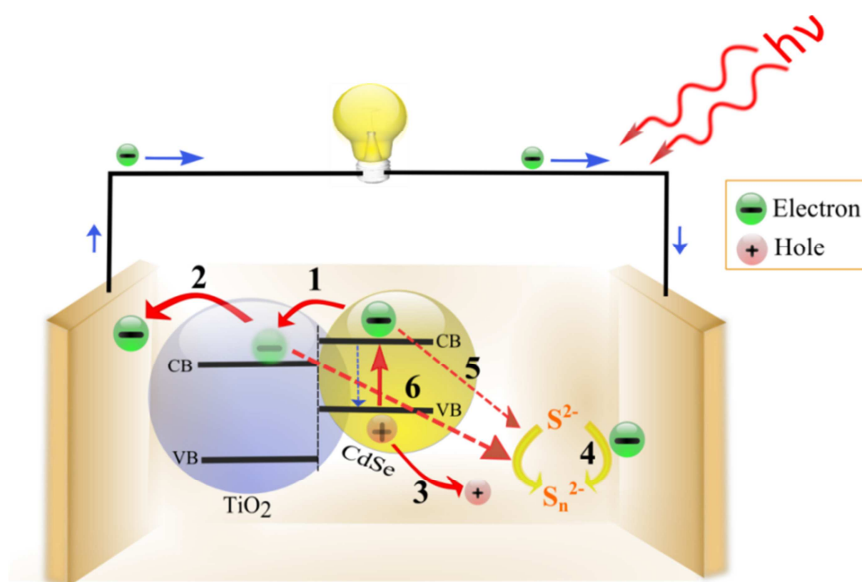


Figure 7 A schematic representation of the charge transfer processes that occur upon illumination in quantum dot sensitized solar cells (QDSCs). The electron transfer steps are described on the text [68].

Since the charge carrier separation occurs at the heterojunction interfaces, it is crucial to fabricate heterostructures with suitable band energy alignment and high-quality interfaces which enable an efficient charge transfer and hence an efficient solar energy conversion [67]. Band gap alignments can be classified into three types (see figure 8): straddling (type I), staggered (type II), and broken (type III). Type I band alignment promotes recombination (i.e. not suitable for solar

energy harvesting) where the band energy levels of one material straddle those of the other, resulting in the transfer of both holes and electrons to the narrower band gap material (i.e. both holes and electrons accumulate in one of the two semiconductors) such in case of CdS@ZnS, CdSe@ZnSe, InAs@CdSe [69]. Conversely in case of type II and type III heterostructures the charge separation occur, where the band energy levels are staggered (type II) (i.e. either if the band edges of the core material are located in the gap of the shell material, such as CdS@ZnO, ZnSe@CdS, CdTe@CdS, CdTe@CdSe, Cu₂S@CuS) [69] or broken (type III) so that charge separation is energetically favorable.

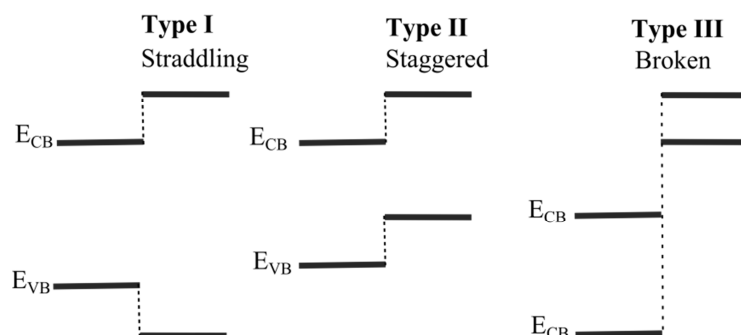


Figure 8 Different types of heterostructure band alignments [67].

2.2.1.1 Charge transfer at interfaces of nanoscale heterostructures

Despite the growing interest on investigation of heterojunctions of metal chalcogenides (e.g., CdS, CdSe, PbS, and PbSe) with wide band-gap metal oxides (MO_x such as TiO₂, ZnO) for wide range of applications, there are only few studies on the charge transfer and recombination kinetics of metal chalcogenides@MO_x heterostructures. Improving the fundamental understanding of charge transfer at interfaces of nanoscale heterostructures is essential for future development of efficient solar conversion devices.

Kamat *et al.* have studied the transient absorption spectra for molecularly linked CdSe QDs on various metal oxide acceptors (SiO₂, SnO₂, TiO₂, and ZnO) following 387 nm excitation at different pump–probe delay times. As shown in figure 9 (A-E), different rates of suppression were observed due to electron injection from the CdSe QDs to the metal oxides. This difference can be more clearly compared in the transient absorption kinetic spectra (figure 9 F). Additionally the electron transfer rates were calculated by fitting the obtained kinetic traces where ultrafast

electron transfer rates were estimated, generally in the picosecond range [70]. Other researchers have demonstrated charge transfer on analogous systems (such as PbS/TiO₂, PbS/SnO₂, CdS/TiO₂) [67,71–73]. It can be concluded that the charge transfer rate and mechanisms are influenced by the driving force from the band energy alignment, the linker length, and the electronic coupling. It was shown that the higher electron transfer rates and yields occur when shorter molecular linkers are used [67].

The epitaxial connection between the donor and acceptor semiconductors is expected to improve the charge-transfer efficiency due to the direct contact as well as the high-quality of shared interfaces [74,75]. Preliminary investigations by Gomez *et al.* showed that charge transfer in CdSe QDs decorated TiO₂ prepared by SILAR is generally faster than in analogous QDs with molecular linkers [76]. When compared to molecularly linked heterostructures, the charge transfer properties of epitaxially sensitized QDs/MOx heterostructures have not been investigated in depth. Tachibana *et al.* have provided a deeper insight into the photoinduced charge transfer processes at an *in situ* chemical bath-deposited CdS/TiO₂ interface by comparing of the transient absorption spectra between CdS/TiO₂ and CdS/Al₂O₃ (Al₂O₃ employed as an insulator) it was concluded that an efficient electron injection occurs from CdS into the TiO₂ conduction band [77].

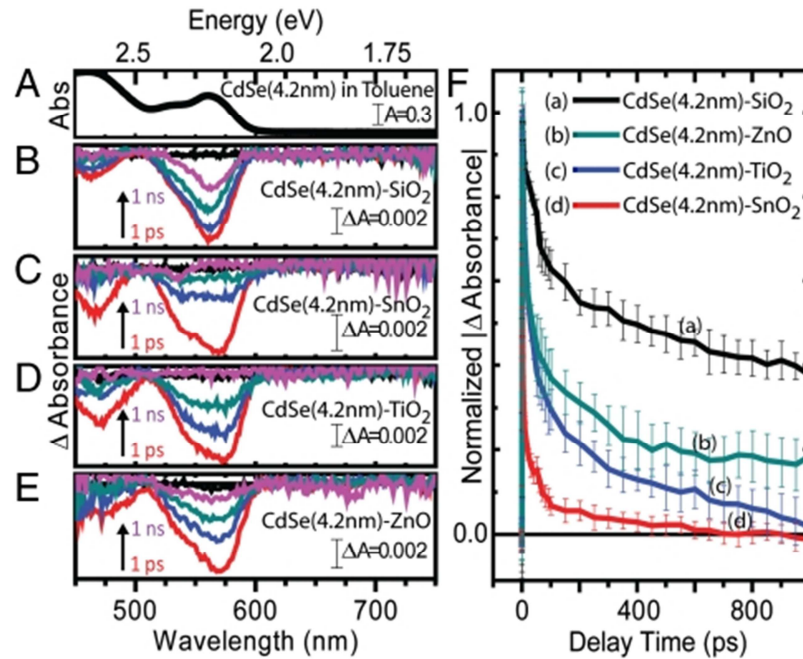


Figure 9 Time resolved spectroscopic investigation of chemically linked CdSe QDs. (A) UV-visible and (B–E) transient absorption spectral traces of 4.2-nm-diameter CdSe quantum dots (A) in toluene and attached to (B) SiO₂, (C) SnO₂, (D) TiO₂, and (E) ZnO. Transient spectra shown at pump-probe delay times of 0 (black), 1 (red), 10 (blue), 100 (cyan), and 1,000 ps (pink). Also, transient absorption kinetic traces (F) of 4.2-nm-diameter CdSe quantum dots attached to each MOx substrate at the $1S_{3/2}-1S_e$ transition [Taken from reference [70]].

Surface photovoltage (SPV) is a contactless technique for characterizing semiconductors by observing changes in surface voltage resulting from illumination at a given wavelength, where the difference between the surface potential barrier in dark and the one under illumination is defined as the SPV signal [78]. SPV measurements can also confirm the occurrence of charge separation and provide information about the charge carriers and their dynamics: the identity of the dominant carrier, lifetime, and diffusion length [79–81]. The dependence of surface photovoltage (SPV) on the CdS shell thickness was systematically studied based on the separation of photogenerated electron-hole pairs at the interface of CdS shell/TiO₂ core heterostructure. It was shown that the diffusion length of an electron in CdS shell is between 30 and 60 nm. The optimal CdS shell thickness for optoelectric application of CdS/TiO₂ heterostructure should be thinner than light penetration depth and the electron diffusion length in CdS [81].

Kelvin probe force microscopy (KPFM), as one of scanning probe microscopy technique, is a very powerful tool for real space exploration of the correlation between structural and electrical/electronic properties of hybrid interfaces [82–86]. Recently, KPFM has been used to observe

photovoltaic effects on nanoscale structures. Particularly, the charge generation at the interface can be easily visualized and correlated with the morphology by KPFM [84]. As an example, KPFM measurement were used to visualize the doping transition across a homojunction of ZnO nanorods (see figure 10), in which the As-doped ZnO nanorod (p-type) was grown onto undoped ZnO nanorods (intrinsic n-type) [87].

Multiresonant coherent multidimensional spectroscopy (CMDS) is one of the emerging surface and interface characterization methodologies to investigate the coupling between the quantum states of nanostructures as well as their dynamics with quantum state resolution. The technique is a mixed frequency- and time-domain method that selectively excites individual, energetically disparate quantum states, with multiple tunable femtosecond or picosecond excitation pulses, and measures their dynamics [67,88]. Picosecond CMDS technique has been successfully used to reveal quantum state resolved dynamics of the surface states in PbSe QDs [88].

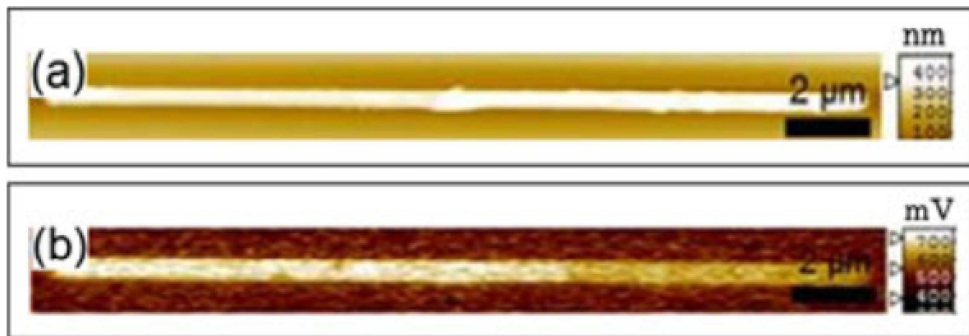


Figure 10 (a) Topography image and (b) KPFM image of a homojunction ZnO nanorods, where brightness contrast appears obviously near the middle region of the nanorod where the brighter region corresponds to the n-ZnO part, whereas the darker region corresponds to the p-doped ZnO part in the homojunction [taken from reference [87]].

2.2.2 Mechanical energy harvesting

Harvesting energy directly from the environment is the end goal for many active ongoing researches, as one of the most effective approaches for powering nanodevices and it is expected to dominate wide range of future applications. Besides solar energy harvesting, mechanical

energy represents another source of green energy. In our daily life we are surrounded by many forms of mechanical energy such as sonic waves, mechanical vibrations and impacts, air flow, friction, hydraulic and ocean waves. The concept of nanogenerators (NG) which is converts different forms of mechanical energy into electric power using piezoelectric nanostructures was introduced by Wang *et al.* (see figure 11) [89]. The mechanism of the nanogenerator relies on the coupling of piezoelectric and semiconducting properties of ZnO, where a piezoelectric potential is created once it is subjected to a strain. This piezopotential is created due to the polarization of the ions in the crystal. This potential can drive a transient flow of the electrons in the external circuit, which is a process of generating electric energy. In addition to ZnO, which has intensive-ly investigated by Wang *et al.*, the piezoelectric properties of many other materials for the use as nanogenerators have been demonstrated recently such as lead zirconate titanate (PZT), cadmium sulfide, barium titanate, and gallium nitride [12,90,91].

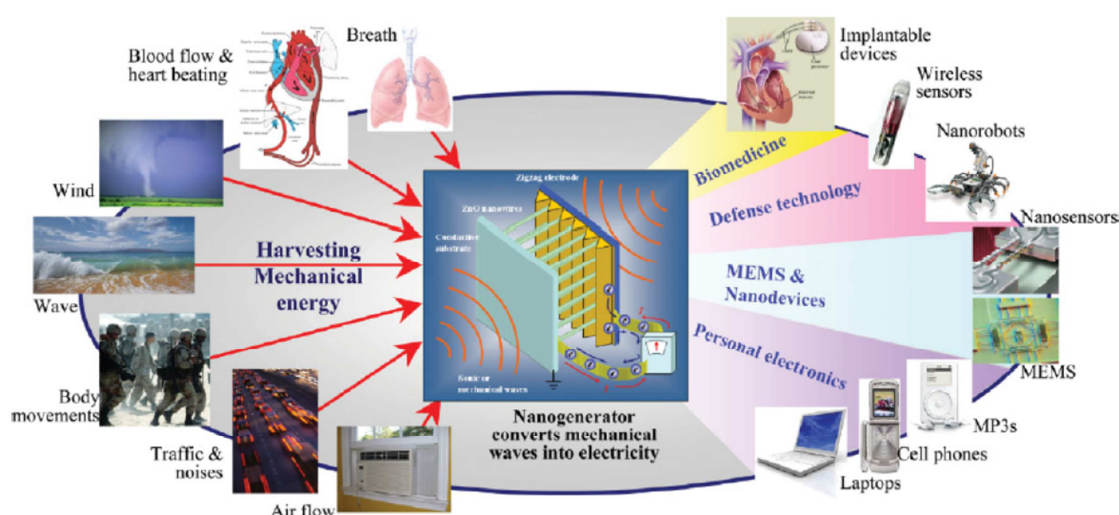


Figure 11 Different forms of mechanical energy that can be harvested by a nanogenerators and the potential future applications of nanogenerators for powering variety of functional devices [92].

2.3 Towards self-powered nanodevices and nanosystems

Self-powered nanosystems (which can operate independently and sustainably by itself without using a battery) are attracting more and more attention due to the growing energy demands in world. These innovative self-powered systems have been fabricated profiting from the

recent advances in environmental energy harvesting technologies, which open an access for developing environmental friendly, independent, remote and mobile, maintenance-free operating nanodevices. The current concept of self-powered nanodevices is based on coupling an external energy harvesting unit (i.e. powering unit), such as a solar cell or a nanogenerator, with the functional nanodevice of concern (e.g. gas sensor or UV sensor) to fulfil the demand for the operation.

Recently, Wang *et al.* have demonstrated that nanogenerators, based on vertical and lateral integration of ZnO nanowires into arrays, can produce sufficient power to operate nanodevices such as UV sensors, pH sensor, environmental sensors (for Hg^{2+} ion detection) and electrochromic (EC) devices (that are capable of reversibly changing optical properties upon charge injection and extraction driven by an externally applied voltage) [12,93–95]. For instance, dye-sensitized solar cells (DSSC) based on ZnO nanotubes, as photoanodes, were used as robust power source to drive a humidity sensor as shown in figure 12 [22].

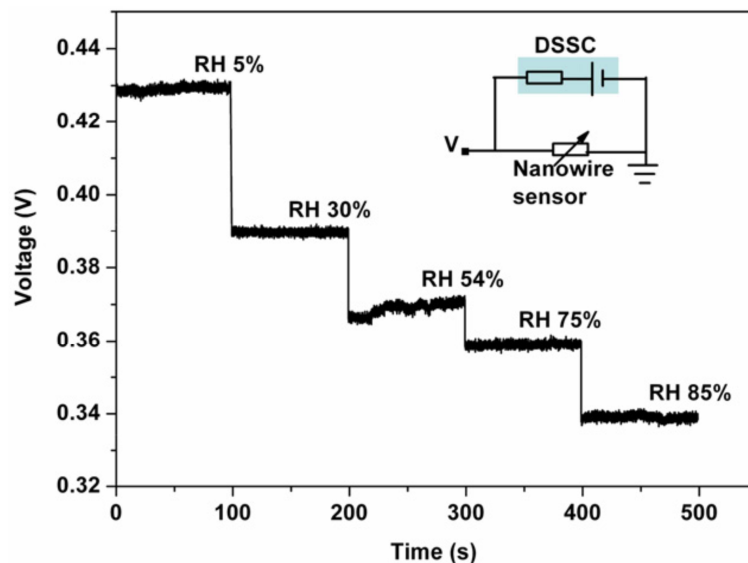


Figure 12 The voltage drop across a humidity sensor as a function of the relative humidity (RH). The sensor was powered by a DSSC shown by the schematic circuit in the inset [Taken from reference [22]].

As previously discussed, ZnO based heterostructures have been demonstrated as materials of potential for gas sensing and energy harvesting applications. However, these applications required a controlled synthesis and assembly of these nanomaterials into devices, which is still

challenging. In the following section the synthesis and post-functionalization of ZnO nanomaterials will be discussed in detail.

2.4 ZnO general properties and synthesis methods

Among wide bandgap semiconductors, ZnO is one of the most popular acceptor oxide materials attract increasing interests for energy conversions and other related applications. Because of the rapidly expanding body of literature on ZnO nanostructures, attention will be to selected structural and fundamental characteristics of ZnO, their solution based synthetic strategies, and their modification with narrow bandgap donors to enable their use in the desired device application.

2.4.1 Crystal structure and general properties

ZnO is a (II–VI) binary compound semiconductor whose ionicity resides at the borderline between the covalent and ionic semiconductors. ZnO has different crystal structures, where the thermodynamically stable phase is the hexagonal wurtzite structure besides two other metastable cubic phases (zinc blende and rocksalt) as schematically shown in Figure 13. The zinc blende phase can be stabilized only by growth on cubic substrates whereas the rocksalt (NaCl) structure may be obtained at relatively high pressures. In the wurtzite structure Zn and O are arranged into a hexagonal form with interpenetrating lattices where each Zn ion is surrounded by four O ions at the corners of a tetrahedron or vice versa [6]. ZnO crystals have a noncentral symmetric wurtzite structure and are composed of close packed O^{2-} and Zn^{2+} layers piled alternatively along the c-axis, producing positively charged Zn-terminated (0001) polar surfaces and negatively charged O-terminated ($000\bar{1}$) polar surfaces [96]. Additionally, ZnO has also non-polar surfaces (1120) and (1010) which have an equal number of Zn and O atoms. Because of the low symmetry of the wurtzite crystal structure combined with a large electromechanical coupling in ZnO, ZnO has strong piezoelectric and pyroelectric properties.

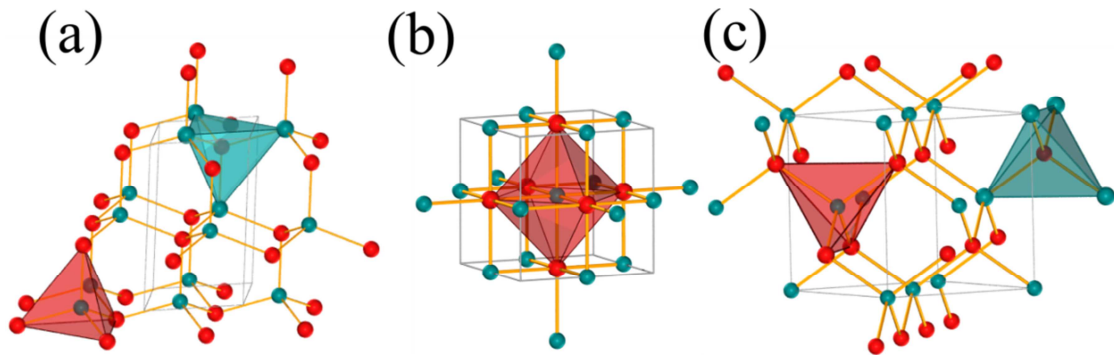


Figure 13 Stick-and-ball representation of ZnO crystal structures: (a) hexagonal wurtzite [97], (b) cubic rocksalt [98], (c) cubic zinc blende [99]. Green and red spheres denote Zn and O atoms, respectively.

ZnO is a direct bandgap semiconductor with an energy gap of 3.37 eV at room temperature [100]. Generally in direct bandgap materials the global extrema of the uppermost valence (VB) and the lowermost conduction bands (CB) occur at the same point in Brillouin zone at $k=0$ (i.e. Γ -point) [100]. In case of ZnO, the lowest CB (LUMO) is formed from the empty 4s states of Zn^{2+} or the antibonding sp^3 hybrid states, while the VB (HOMO) is originating from the occupied 2p orbitals of O^{2-} or from the bonding sp^3 orbitals [100]. ZnO has many advantages associated with its large bandgap such as high-temperature and high-power operation, high breakdown voltages, and ability to sustain large electric field [6]. ZnO also possesses a high exciton binding energy of 60 meV, compared with, e.g. 25 meV in GaN. This large exciton binding energy indicates that efficient excitonic emission in ZnO can persist at room temperature and even higher. Additionally, ZnO exhibits strong luminescence in the green–white region of the spectrum, which enables its application as a phosphor material [101]. ZnO displays a native n-type behavior because of deviation from stoichiometry due to the presence of intrinsic defects such as O vacancies (V_{O}) and Zn interstitials (Zn_i). Despite it is experimentally known that unintentionally doped ZnO is n-type, the origin of these defects and their assignment are still controversial issues. Undoped ZnO shows n-type conductivity with electron densities as high as 10^{21}cm^{-3} [6].

ZnO probably has the richest family of nanostructures among all nanomaterials such as nanowires, nanorods, nanotubes, needles, nanobelts, nanospheres, nanocombs, nanorings, nanocages, and complex structures (some examples are shown in figure 14). A combination of the three types of fast growth directions ($\langle 2110 \rangle$, $\langle 0110 \rangle$, and $\langle 0001 \rangle$) and the three area-adjustable facets

({2110}, {0110}, and {0001}) of ZnO enable the growth of a diverse group of hierarchical nanostructures [15,102].

Among various ZnO nanostructures, one-dimensional (1D) materials such as nanowires (NWs) (which are a set of materials with size < 100 nm in two out of three dimensions) are exhibiting a variety of interesting and fascinating properties such as quantum confinement effects and high surface-to-volume ratios. These novel properties offer a basis for the exploration of new and interesting phenomena in different fields such as physics, chemistry, biology, and materials science [15,64,103].

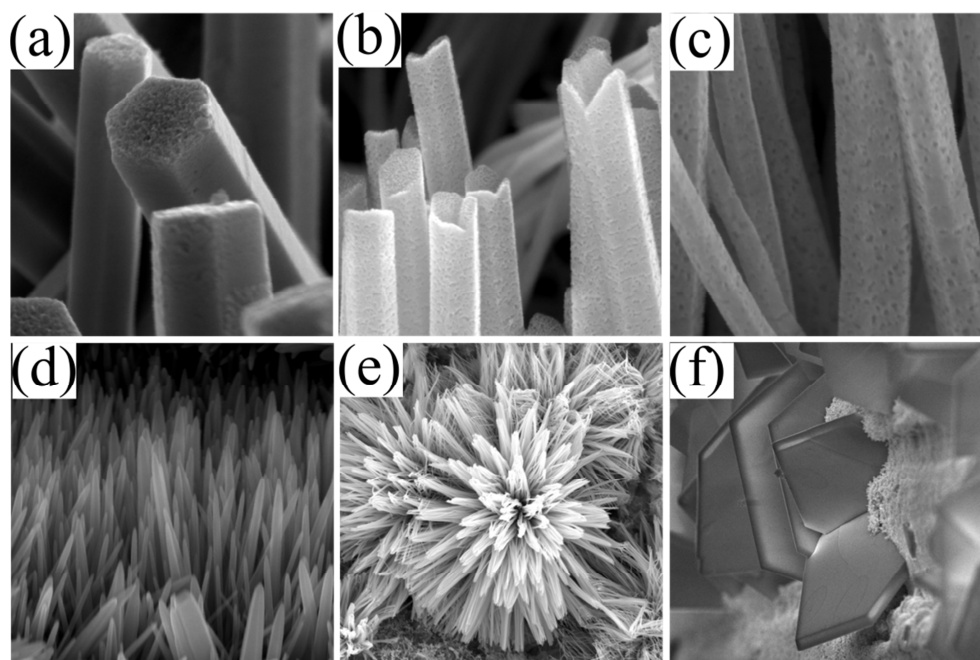


Figure 14 Examples of different ZnO nanostructures synthesized under controlled conditions by solution based synthesis methods; a) nanorods, b) nanotubes, c) nanowires, d) needles, e) flower-like, and f) platelets.

2.4.2 Synthetic strategies and surface modification of ZnO nanowires

ZnO nanostructured arrays can be synthesized by a variety of techniques which can basically be divided into two main categories: Gas-phase synthesis and solution-phase synthesis.

- **Gas- phase synthesis:**

In the initial studies of ZnO NW growth vapor-phase methods has been conventionally used for synthesis, where condensed or powder source materials are vaporized at elevated temperatures and the formed vapor phase condenses under certain conditions on a high-temperature substrate with Au catalyst to form the desired products. Many techniques based on vapor-phase methods have been extensively exploited such as chemical vapor deposition (CVD), thermal evaporation, metal organic chemical vapor deposition (MOCVD), and catalyst-assisted laser ablation. The growth of 1D nanomaterials via vapor phase processes is governed by two main mechanisms, either by vapor-liquid-solid (VLS) mechanism or vapor-solid (VS) mechanism [104,105]. Despite the fact that gas-phase approaches usually produce high-quality ZnO NWs, however the high growth temperatures (above 500 °C), low product yield, limited choices of substrate, and the possibility to incorporate catalyst impurities into the produced nanostructures hinders their integration and assembly into devices as well as their commercial potential [14,106].

- **Solution-phase synthesis**

In contrast to the fabrication complexity and cost of gas-phase synthesis, solution based synthesis provides many advantages such as facile and inexpensive procedures, need of moderate or ambient temperature, compatibility with large scale fabrication, and good reproducibility of physical properties [107]. The solution-phase methods can also be classified under two main categories namely; template-assisted and template-free methods.

Template-assisted methods: these methods include using of a template as a scaffold for guiding the growth, where the precursor can fill or cover the template to produce nanostructures that mimic the shape of the used template. The resulting materials are then separated from the template by a post synthetic treatment. The main drawback of this approach is the difficulty to obtain single-crystalline nanowires [108]. 1D nanostructures can be synthesized by using periodic structured porous templates, such as anodic aluminum oxide (AAO), molecular sieves, and polymer membranes [24].

Template-free methods: template-free methods have attracted the interest of many researchers for the deposition of 1D nanostructures in liquids such as wet chemical synthesis, surfactant-assisted methods, solvothermal and hydrothermal routes, and microwave synthesis.

The low temperature solution based synthesis of ZnO nanowires as well as their modification and decoration to tailor their properties for the desired application requirements will be discussed in more detail.

2.4.2.1 Solution-based synthesis of ZnO nanowires

The main approach for achieving 1D growth is to exploit the difference in surface chemistry between the polar and non-polar facets of ZnO, by selectively promoting or suppressing growth on these facets. Due to the high energy of the polar facets (like \pm (0001) facet), the incoming precursor molecules tend to favorably adsorb on the polar surfaces during the growth of the newly formed ZnO nucleus. After adsorption of one layer of precursor molecules, the polar surface transforms into another polar surface with inverted polarity (i.e. from Zn^{2+} -terminated into O^{2-} -terminated surfaces or vice versa). This process is repeated over time, leading to a fast growth along the \pm [0001] directions and thus results on growth of 1D nanostructure [14].

ZnO is expected to crystallize by hydrolysis of Zn salts in a basic solution, which can be formed using strong (e.g. KOH or NaOH) or weak alkalis (e.g. $\text{NH}_3\cdot\text{H}_2\text{O}$, and amine compounds). The synthesis of ZnO nanowires from zinc salts in solution as well as the growth mechanisms will be highlighted in the following narrative.

Growth mechanisms

i. Growth in alkaline solutions

An alkaline solution is needed for the formation of ZnO nanostructures since divalent metal ions do not hydrolyze in acidic environments [109]. KOH and NaOH are commonly used alkali compounds for synthesis of ZnO. In aqueous solution, Zn^{2+} coordinates in tetrahedral complexes and can exist in a series of intermediates including $\text{Zn}(\text{OH})^+$, $\text{Zn}(\text{OH})_2$, $\text{Zn}(\text{OH})_3^-$, $\text{Zn}(\text{OH})_4^{2-}$. These intermediate forms are in equilibrium, with the major forms being different under different reaction conditions. At a given Zn^{2+} concentration, the stability of these intermediate complexes

is dependent on the pH value and temperature of the solution as shown in figure 15. ZnO forms finally by the condensation of these intermediates [14].

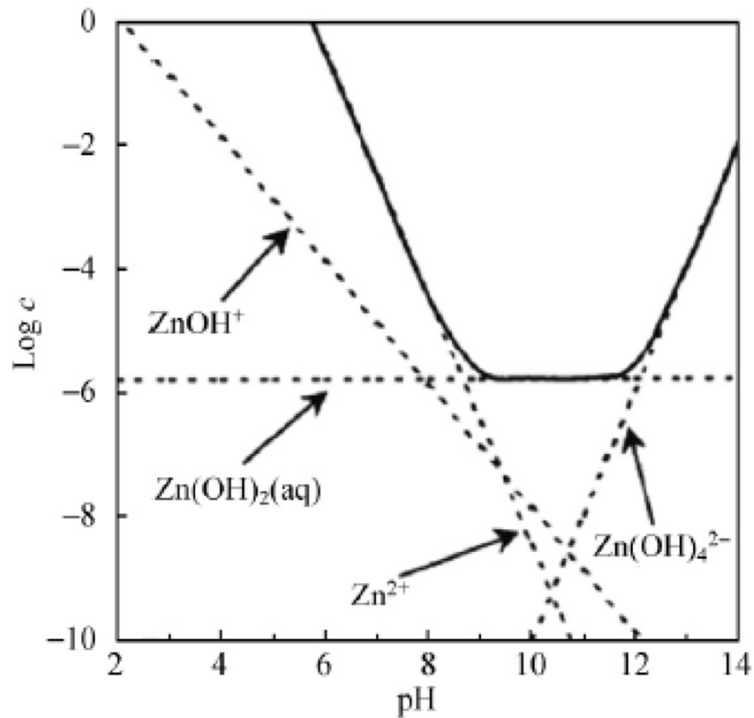
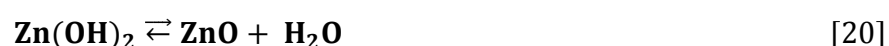


Figure 15 Phase stability diagrams for the ZnO (s)-H₂O system at 25 °C as a function of precursor concentration and pH value, where the dashed lines denote the thermodynamic equilibrium between the Zn²⁺ soluble species and the corresponding solid phases [Taken from reference [110]].

ii. Growth in hexamethylenetetramine (HMTA) aqueous solution

It is known that weak bases such as amines protonates in aqueous Zn environments and slowly release hydroxide ions, which forms various Zn-hydroxide complexes. The most successful and commonly used condensation reaction for ZnO nanowires growth is the hydrolysis of zinc nitrate in water in the presence of HMTA. The exact role of HMTA during the growth of ZnO nanowire is still an area of debate in literature. It has been suggested that HMTA, which is a nonionic cyclic tertiary amine, act as a bidentate Lewis base that is capable of bridging two zinc (II) ions in solution [85]. HMTA is a rigid molecule and it hydrolyzes in water and gradually producing formaldehyde and ammonia as shown in equation 16 (in the pH and temperature range of the growth reaction).



The slow decomposition of HMTA, which act as a pH buffer, provide a gradual supply of ammonia which can form ammonium hydroxide as well as complex with Zn^{2+} to form $[\text{Zn}(\text{NH}_3)_4]^{2+}$ as can be seen in equations 17, and 18 [109]. This ability to coordinate to Zn^{2+} and keeping the free Zn^{2+} concentration low prevents the quick precipitation of Zn^{2+} ions which might result in fast consumption of the nutrient and prohibit the oriented growth of ZnO nanowires. Additionally, the attachment of HMTA to the nonpolar side facets of wurtzite ZnO also facilitates the anisotropic growth along the polar surfaces in the [0001] direction. One or all of these suggested scenarios might explain the controversial role of HMTA in the morphology control of ZnO during the growth [14].

Besides the above mentioned mechanisms, the counter-ions are found to play an additional role on the resulting ZnO morphology. Acetate, formate, and chloride mainly result in the formation of nanorods; while nitrate and perchlorate are found to produce nanowires; and sulfate yields flat hexagonal platelets [111].

Examples of solution based synthetic methodologies

Simple wet-chemical synthesis methods have been used for the synthesis of different ZnO nanostructures at low temperatures such as hydrothermal, low temperature wet chemical growth, anodization, and surfactant-assisted methods.

(i) Hydrothermal synthesis of ZnO nanowires

Hydrothermal method is one of the well-established and commonly used routes for the synthesis of 1D ZnO nanomaterials. In this method, an aqueous solution containing a soluble metal salt (metal or metal organic) of the precursor material is placed in an autoclave held at relatively

low temperatures in the range 100–400 °C and under high pressures (above 1 atm) [101]. ZnO nanostructures have been synthesized hydrothermally by using different Zn salts, capping agents, and bases. Hu *et al.* have synthesized ZnO nanorods hydrothermally by using ZnCl₂, Na₂CO₃, and sodium dodecyl sulfonate (SDSN) in a Teflon-lined stainless steel auto-clave at 140 °C for 12 h [112]. Recently, flower-like ZnO nanorods have been successfully synthesized via a surfactant assisted hydrothermal method [113]. Additionally, thinner ZnO nanorods (with diameters less than 50 nm) have been achieved by hydrothermal treatment (at 180 °C for 20 h) of a mixture of Zn(NO₃)₂ and NaOH (1 : 20 molar ratios) in pure alcohol with an ethylenediamine as a capping agent [114]. Another simple method was reported for direct synthesis of ZnO nanorods by cetyltrimethylammonium bromide (CTAB) favored hydrothermal oxidization of zinc metal at 180 °C [115]. Different morphologies of ZnO can be obtained by using various capping agents in solution; for example ZnO nanobelt (NB) were produced hydrothermally by using a mixture of ZnSO₄, urea, and ethanol in a Teflon autoclave at 160 °C for 12 h, where the selective adsorption of urea on certain planes promotes the growth of nanobelt morphology [116].

(ii) Low temperature wet chemical growth

In comparison to hydrothermal synthesis, which requires relatively high temperatures and pressures in an autoclave, wet chemical methods provide lower temperature pathway, low cost, as well as a wide variety of material compatibility. Andres *et al.* reported the growth of ZnO nanorods from a mixture of HMTA and Zn(NO₃)₂ or ZnCl₂ at temperatures below 100 °C [109]. Different zinc salts including acetates, formates, nitrates, perchlorates, and chlorides as well as many capping agents such as ethylenediamine, sodium dodecyl sulfate, and polyethylenimine, have been successfully used in the synthesis of 1D ZnO nanostructures [117–119].

(iii) Anodization

The anodization technique is a versatile surface treatment, in which an electrochemical etching of metal foil results in very uniform and adhesive oxide films on metals. The synthesis is simple and scalable and can also be used for decorating a metal surface and/or improving corrosion/wear resistance. However, the resulting structures are typically polycrystalline. Inspired by the breakthrough in the anodic formation of self-ordered porous oxide films on aluminum reported by Masuda and Fukuda in 1995, more attention has been paid to anodization of other

metals such as Ti and Ta to produce nanostructure metal oxides [120]. However, there are only few reports on formation of ZnO nanostructured via Zn anodization [121–125]. Kim *et al.* reported formation of self-assembled ZnO stripe arrays by anodization of Zn in ethanolic H₂SO₄ [126]. He *et al.* reported ZnO thin films with diverse nanostructures, including nanodot, nanowire and nanoflower, by anodizing zinc foil in mixed electrolyte of water, HF, and methanol [124]. Long ZnO nanowire arrays were reported by anodizing zinc foil at room temperature in a slightly basic solution [127].

Direct growth of well-oriented nanowire arrays

The controlled growth of well oriented nanostructures is one of the fundamental challenges for many applications that require efficient generation and transport of electrons, ions, and other molecular species such as in photovoltaics, batteries, gas sensors, capacitors, thermoelectronics, and other unconventional methods of energy conversion [128]. Due to the large lattice mismatch between ZnO and the desired substrates (e.g. lattice mismatch with Si ~40%), it is difficult to directly grow well-aligned ZnO nanowires on a pristine Si substrate. One of the possible approaches to overcome this problem is using other materials that have relatively small lattice mismatch with ZnO such as Au [129], Pd [130], and Cu, etc [131]. However, introducing such metal catalysts might be unfavorable for some optoelectronic applications. Alternatively, vertical growth from textured ZnO seeds has been developed, where a ZnO seed layer deposited on a nonepitaxial substrate (such as silicon or glass) can act as a nucleation layer for nanowires growth. This method is substrate-independent and can be applied on a large scale to almost any surface. Also the produced nanostructures have direct contact with the substrate, which is crucial for device applications that require pure interfaces [128]. Growth on existing seeds is more favorable than nucleation in homogeneous solution since in presence of the pre-deposited ZnO seeds heterogeneous nucleation is favored as it has a lower activation energy barrier than homogeneous nucleation. Moreover the interfacial energy between crystal and substrate is usually lower than that between crystal and solution [14,111,128]. Seed layer can be prepared by many methods including deposition of ZnO or deposition of Zn followed by oxidation, sol-gel/spin coating, and atomic layer deposition (ALD) techniques. The nanowire growth can be influenced by the properties of the seed layer such as thickness, grain size and roughness, and post-annealing treatment [104]. Various attempts have been made to synthesize ZnO nanowire arrays with

proper orientation in a controlled manner, but still more research is needed to achieve such a goal.

2.4.2.2 Surface modification of ZnO nanowires

Hybrid materials are good candidates to build nanosystems with multifunctional and adjustable properties. As previously discussed, facile charge transfer as well as efficient solar energy conversion can be obtained via heterostructures with a suitable band energy alignment and high-quality interfaces [67]. While band energy alignment could be controlled by the appropriate choice of materials and by tuning the bandgap of the sensitizer (or donor) such as CdS NPs the later factor still remains a challenge in terms of forming favorable interface in order to facilitate efficient electron transfer. The design strategies that have been used to integrate sensitizer (NPs) on the surface of metal oxide nanowire acceptors can be classified into the following three main categories: proximally contacted NPs, chemically linked NPs, and epitaxial attached NPs (as shown in figure 16).

i. Proximally contacted NPs:

Include deposition of NPs suspensions, which were prepared separately using standard NPs synthesis techniques, on the acceptor material (ZnO NWs) either by drop-casting or spin-coating. Since the donor NPs are very small in dimension they can easily intercalate in-between and into the surface of NWs [67]. The NPs attached by this approach suffer from inhomogeneous and unordered distribution and low coverage of NPs on the oxide acceptor, as well as low charge transfer efficiency.

ii. Chemically linked NPs

The NPs are attached to the acceptor material through a bifunctional molecule, which has preferential binding of the different groups to the acceptor and donor materials. One of the commonly used linkers is 3-mercaptopropionic acid (MPA), which is bifunctional linker bearing carboxylate and thiol functional groups, since the carboxylic acid group ($-\text{COOH}$) is a good ligand to most metal oxides and the thiol ($-\text{SH}$) group is a good ligand to bind to the metal chalcogenide (see figure 16) [67]. Despite the advantages of this method such as the ability to tailor the size and control the coverage of NPs on the acceptor material, the lack of a direct lattice connection can

affects the charge- transfer efficiency, where the transfer rate decreases with the increase of the linker size [65].

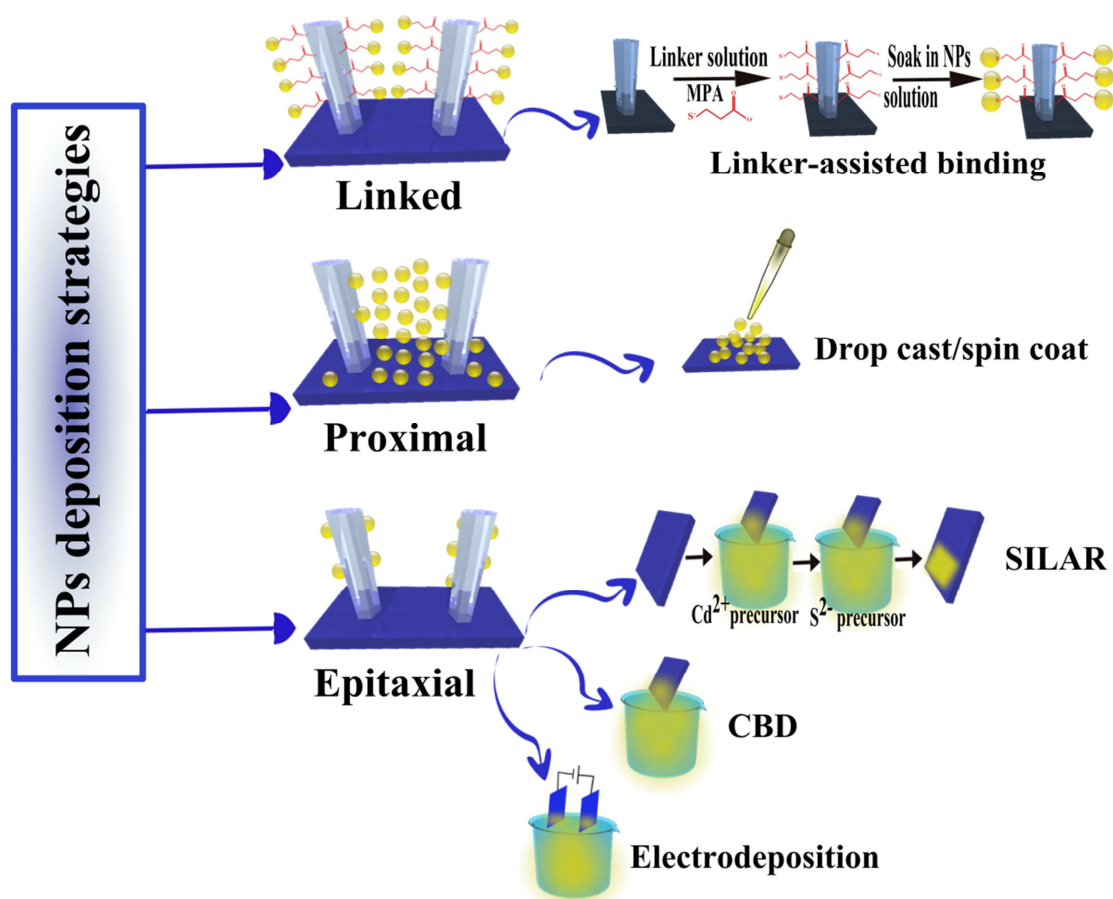


Figure 16 Schematic illustrations of different binding strategies of NPs/MOx heterostructure and their corresponding deposition techniques.

iii. Epitaxial attached NPS

This approach involves a direct growth of a donor NPs on the acceptor material, where an epitaxial interface is more likely to be achieved by benefiting from the nanoscale dimension that can better tolerate interfaces formed between crystal lattices with large lattice mismatches and different crystal structures than their bulk counterparts. There are numerous methods used to obtain the epitaxial contact of NPs such as chemical bath deposition (CBD), successive ion layer adsorption and reaction (SILAR), and electrodeposition (as shown in figure 16). The advantage

of these approaches is the high coverage of the acceptor surface, but it provides less control over the NPs size and morphology than the methods in which pre-synthesized colloidal NPs are used as discussed above [65] [132].

Chemical bath deposition (CBD) is performed by submerging a substrate in a dilute solution of the precursors required for the synthesis of the semiconductor QDs, where various metal salts and molecular chalcogenide sources (e.g. thioacetamide, thiourea, or hydrogen chalcogenides) are allowed to react at ≤ 100 °C under ambient pressure in tightly sealed vessels [69]. At proper concentrations, the donor material is deposited on the acceptor surface and also precipitates from solution, where the growth of crystallites can be controlled by the reaction time.

Successive ion layer adsorption and reaction (SILAR), includes sequential dipping of a substrate, bearing acceptor material (e.g. ZnO NWs), into individual cationic and anionic precursor solutions. The size of the QDs prepared by SILAR can be controlled to some degree by the number of SILAR reaction cycles; however, this method requires a time-consuming rinsing step between the successive adsorption processes for Cd^{2+} cations and S^{2-} anions, to remove the excess ions from the surface [67].

Electrodeposition is carried out by suspending the substrate with acceptor material as electrode in a precursor solution. Then by passing a current through the substrate, a reduction (or oxidation) of the precursors takes place at the electrode surface which is resulting in NPs growth [67]. This method has many merits such as the ability to control the desired amount of QD loading on the electrode surface by manipulating the concentration or time of deposition, although the produced materials often suffer from impurity phases and low morphological quality [67].

3. Experimental and Methods

3.1 Chemicals and substrates

All chemicals were of analytical grade and used as received without further purification (see table 1). The used substrates were typically cleaned in acetone, ethanol and isopropanol successively in an ultrasonic bath (10 min each) before their use, unless otherwise specified.

Table 1 Commercially purchased chemicals and substrates.

Substance	Formula	Company
Zinc nitrate hexahydrate	$H_{12}N_2O_{12}Zn$	Merck
Hexamethylenetetramine	$C_6H_{12}N_4$	Merck
Aluminum isopropylate	$C_9H_{21}AlO_3$	Sigma-Aldrich
Formamide	CH_3NO	Acros Organics
Thioacetamide	C_2H_5NS	Merck
Ammonia	NH_3	Merck
Thiourea	CH_4N_2S	Acros Organics
Cadmium sulfate	$Cd_3O_{12}S_3 \cdot 8H_2O$	Acros Organics
Monoethanolamine	C_2H_7NO	Acros Organics
sodium hydrogen carbonate	$NaHCO_3$	Alfa Aesar
2-Methoxyethanol	$C_3H_8O_2$	Alfa Aesar
Hydrofluoric acid 40%	HF	Merck
Sodium hydroxide pellets	NaOH	Merck
Sodium chloride	NaCl	Merck
Zinc acetate dehydrate	$C_4H_{10}O_6Zn$	Merck
Oxygen	O_2	Air Products
Synthetic air	N_2 / O_2	Air Products
Ethanol (1000 ppm)	C_2H_6O	Air Products
Zinc foil 0.25mm thick	Zn	Alfa Aesar
Silicon wafer	Si	Crys Tec

3.2 Synthesis and controlled growth of one-dimensional ZnO nanomaterials

3.2.1 Hydrothermal growth of aligned ZnO nanowires

– **Seed layer thin films depositions:**

Sol-gel seed layer: Typically, a sol–gel solution was prepared [133] by dissolving zinc acetate (ZA) dehydrate, $\text{Zn}(\text{CH}_3\text{COO})_2 \cdot 2\text{H}_2\text{O}$, (0.75 mol L^{-1}) in 2-methoxyethanol (2MOE) (0.75 mol L^{-1}) with monoethanolamine (MEA) (20 ml) as stabilizer, where the molar ratio of ZA to MEA was kept at 1. The resultant solution was stirred at $60 \text{ }^\circ\text{C}$ for 30 min until clear and homogeneous solutions were formed. Then the obtained solutions were aged for 24 h at room temperature. The prepared sol was stable and transparent with no precipitation observed in more than 2 weeks. The ZnO seed layers were prepared by spin-coating the sol (2000 revolutions per minute (rpm) for 10 s) onto clean silicon substrates. After each spin coating cycle, the films were dried at $350 \text{ }^\circ\text{C}$ for 5 min to evaporate the solvent and to remove organic residuals. The thickness of the obtained films was controlled by repeating the spin coating/drying procedures. Finally ZnO seed layer was obtained by annealing the films at $500 \text{ }^\circ\text{C}$ for 1 h.

DC-sputtering: The Zn film was prepared by sputtering a Zn (99.99 %) metal by applying $50 \text{ }\mu\text{A}$ direct current (DC) for different time periods in presence of high purity Ar (99.999 %) gas. The sputtered metal films were oxidized via annealing in air at $500 \text{ }^\circ\text{C}$ for 1 h to obtain a crystalline ZnO seed layer. The thickness of the seed layer was controlled by adjusting the sputtering time.

ALD seed layer: Atomic layer deposition (ALD), as a vapor-phase technique, is becoming an important tool for deposition of thin films with atomic-scale thickness control. ALD film growth is a self-limited process⁵ that is based on surface reactions [134,135]. ALD has the advantage of depositing conformal coating on high aspect-ratio nanostructures with excellent uniformity [134].

In this work, ALD technique was used for deposition of ZnO seed layers on different substrates as well as for coating high aspect-ratio Si nanowires, by using Beneq TFS 200 ALD system. Two liquid precursors were used namely, diethylzinc (DEZ) as a precursor for zinc and deionized water as the oxidation source. The pulse durations of water and DEZ were 200 ms for each precursor. The purge and pumping periods were 1 s and N_2 was used as the purge gas. The

⁵ ALD involves a sequence of two self-limiting reactions between gas-phase precursor molecules and a solid surface, thus the precursor reacts with the target substrate until all available surface reaction sites are consumed [134].

substrate temperature was maintained at certain temperature during the deposition (see table 2). Each ALD growth cycle contain the following sequence of DEZ/N₂/ H₂O/N₂ with their corresponding durations. The thickness of the deposited films was controlled by the number of ALD growth cycles. After the deposition, the thin films were annealed in ambient air at certain temperature for 1 h to obtain a better crystallinity. The details of the ALD deposition and post annealing conditions are summarized in Table 2.

Table 2 ALD deposition parameters and post annealing conditions used to deposit different ZnO seed layers on substrates.

Precursor 1/ precursor 2	Substrate temperature (°C)	pulse durations (ms)	Purge/pumping time (s)	Number of cycles (n)	Post- annealing temperature (°C)
DEZn/H ₂ O	125-200	200	1/1	100-1000	400-800

– **Growth of ZnO nanowire arrays on p-Si substrate**

ZnO nanowire arrays were grown on ZnO seed layer, deposited by the above mentioned techniques, by using a second step of hydrothermal synthesis reported previously [136]. The growth solution was composed of equimolar aqueous solutions of zinc nitrate hexahydrate (Zn(NO₃)₂.6H₂O) and hexamethyl-enetetramine (C₆H₁₂N₄, HMTA) with (saturated) or without (hydrothermal) addition of aluminum-iso-propylate (see table 3). The temperature of the growth solution was maintained at 75 °C in a water tank and the pH value of the growth solution was monitored at 7.2 during the growth process. The substrate was removed from the growth solution, washed with deionized water, dried at 80 °C for 20 minutes, and then annealed in air at 400 °C for 1 h.

Table 3 Summary of the experimental conditions used in the hydrothermal synthesis of ZnO NWs.

Method	H ₂ O (ml)	Zn(NO ₃) ₂ .6H ₂ O (mol L ⁻¹)	HMTA (mol L ⁻¹)	aluminum- iso-propylate (mol L ⁻¹)	reaction time (h)
Hydrothermal	100	0.025	0.025	0	20
Saturated	100	0.025	0.025	0.005	20

3.2.2 Synthesis of ultra-long ZnO nanowires and nanotubes through anodization method:

The method for preparing ultra-long ZnO nanowires is similar to that of Hu *et al.* [127] a zinc foil (99.99% purity, 0.25 mm thickness, 2cm × 6cm) was first cleaned with acetone, ethanol and deionized water in an ultrasonic bath (5 min each). Subsequently, an electropolishing step was performed by immersing zinc foils in a solution of phosphoric acid and ethanol (3:7 volume ratio) at 20 V DC and 5 °C with strong stirring for 20 min. in a slightly basic electrolyte of 0.05 M NaHCO₃ aqueous solution. The anodization was performed in a two-electrode electrochemical cell, in which the zinc foil is acting as the working electrode and a graphite plate as the counter electrode. The distance between the two electrodes was 10 cm. A direct current power supply was used to drive the anodization at a certain cell potential for a selected time at different operation temperatures. Finally, the as-anodized foils were rinsed using deionized water and dried at 80 °C for 20 min followed by an annealing step at 250 °C in air for 30 min (see table 4).

Table 4 Summary of different anodization parameters used for ultra-long ZnO NWs synthesis.

Applied voltage (V)	Anodization time (min)	Anodization temperature (°C)	Electrolyte concentration (mol L ⁻¹)
5-20	1-60	5-70	0.05

3.2.3 Synthesis of ZnO nanorods by simple oxidation of Zn foil:

– Direct oxidation of zinc foil in an aqueous solution of formamide

Zn foil (99.9% purity, $20 \times 40 \times 0.25 \text{ mm}^3$) was initially mechanically polished with abrasive paper, and then cleaned in deionized water and ethanol in an ultrasonic bath for 10 min each. Then, the Zn foil were immersed in 100 mL of 5% formamide aqueous solution (v/v) in sealed vial placed in a hot bath at a constant temperature of $65 \text{ }^\circ\text{C}$ for 24 h. The samples were then rinsed thoroughly with deionized water and dried in air.

To study the effect of ionic strength and possible etching effects of Cl^- ions on the growth of ZnO nanostructures, 0.45 M NaCl was added to the above aqueous solution (5% formamide) and the reaction was repeated under the same conditions for 24 h and the samples were then rinsed thoroughly with deionized water and dried in air.

– Direct oxidation of zinc foil in an aqueous solution of NaOH

Zn foil (99.99% purity, $60 \times 40 \times 0.25 \text{ mm}^3$) was first polished with abrasive paper and then cleaned ultrasonically in ethanol, and deionized water respectively for 10 minutes each. Then, the zinc foil was placed into a teflon-lined stainless steel autoclave (200 ml) with 160 ml aqueous solution containing 0.63 g NaOH then the solution was heated at $80 \text{ }^\circ\text{C}$ for 24 h. The as-grown products were rinsed with de-ionized water and then dried in air. One of the foils with the as-grown ZnO nanowires were ultrasonicated in deionized water for 20 min to remove the formed nanowires and then the above mentioned growth procedure in autoclave was repeated again at $80 \text{ }^\circ\text{C}$ for 24 h and finally the obtained products were rinsed with de-ionized water and then dried in air.

3.3 Fabrication of Si nanowires

Silicon nanowire (Si NW) arrays have been realized using wet chemical etching of bulk silicon wafers (p-Si and n-Si) according to a method used by Sivakov *et al.* [137], where p-Si(100) ($1\text{-}40 \text{ } \Omega\cdot\text{cm}$), p-Si (111) ($1\text{-}20 \text{ } \Omega\cdot\text{cm}$), and n-Si (100) ($1\text{-}20 \text{ } \Omega\cdot\text{cm}$) wafers were mainly used in this work. Initially silicon wafers were ultrasonically cleaned in ethanol followed by deionized water for 10 min each. Native SiO_2 was removed by dipping the wafers shortly in 40% hydrofluoric acid (HF) solution followed by a 2% HF rinse for 1 min. Finally, the samples were rinsed in

deionized water and dried under nitrogen stream. A hydrogen-terminated silicon surface is produced which promotes the subsequent silver deposition on an oxide free silicon surface. The chemical etching method to produce Si NWs is based on a two-step process. In the first step, Ag nanoparticles were deposited on silicon wafer surfaces by immersing the wafers in aqueous solution of 0.02 M silver nitrate (AgNO_3) and 5 M HF in the volume ratio 1:1 (solution I) for 60s. Subsequently, silicon wafers covered with Ag nanoparticles were immersed in a 50 mL of second etching solution containing 5 M HF and 30% H_2O_2 in the volume ratio 10:1 (solution II) (45.5 ml HF and 4.5 ml H_2O_2) in a Teflon vessel for different etching times at room temperature. Finally the Si wafers were rinsed several times in deionized water and dried at room temperature. The Si NWs arrays were washed in a concentrated (65%) nitric acid (HNO_3) for 15 min to remove residual Ag nanoparticles from the SiNW surfaces.

3.4 Fabrication of p-n heterojunctions and their surface modifications to obtain heterostructures

3.4.1 p-NiO film deposition on n-Si substrate

NiO were deposited on Si substrate (n-doped, (100), resistivity 1-20 $\Omega\cdot\text{cm}$, cut in 1 cm x 1 cm dices) by DC sputtering using Ni target (99.99 % purity metal) and high purity Ar gas (99.999 %) and 50 μA applied current for 16 min. The as-deposited metal film was then annealed in air at 500 $^\circ\text{C}$ for 5 h to obtain a crystalline NiO film. Prior to the deposition of Ni film, a thin isolation layer of SiO_x film was deposited on a small part of the n-Si substrate (2 mmx1cm) for device fabrication requirements. SiO_x film was deposited by plasma enhanced chemical vapor deposition technique (PECVD), where the reactants used were hexamethyldisiloxane (HMDSO) and O_2 with a gas flow of 25 sccm and 50 sccm respectively at 50 W and 15 mTorr. (sccm denotes cubic centimetre per minute at STP).

3.4.2 Synthesis of CdS nanoparticles@ZnO heterostructures

CdS nanoparticles (NPs) were deposited on the surface of different ZnO nanostructures via a chemical bath deposition (CBD) [138]. 2 mM precursor solution was prepared by dissolving cadmium sulfate ($\text{CdSO}_4\cdot 8/3\text{H}_2\text{O}$) and thiourea ($\text{CS}(\text{NH}_2)_2$) (molar ratio urea: $\text{Cd}^{2+} = 5:1$) in 1 mol L^{-1} ammonia solution. Before the decoration reaction the ZnO substrates were cleaned in a

N₂ flow and then immersed into the CdS precursor solution for few minutes to ensure the diffusion of the precursor into ZnO nanostructures. The solution containing the ZnO substrate was heated in an oil bath at 60 °C. During the CBD process, the sample colour was changed from colourless to bright yellow indicating the precipitation of colloidal CdS. The CBD deposition times varied depending on the desired CdS NPs coverage on ZnO surface. After the CBD process, the ZnO samples were immediately washed with deionised water and dried in air.

3.4.3 Synthesis of ZnS @ZnO heterostructures

ZnS shell was synthesized on ZnO nanowires by chemical conversion of ZnO nanowires at low temperatures (< 100 °C) [139]. The substrate of ZnO nanowires was immersed into a sealed vial containing 0.2 M thioacetamide (TAA) (CH₃CSNH₂) aqueous solution and the sulfidation reaction was carried out in a hot bath at a constant temperature of 90 °C for 5 h. Finally, the obtained products were washed with deionized water and then dried in air.

3.4.4 Synthesis of 3D heterostructures of ZnO nanowire arrays

Branched 3D heterostructures of ZnO were fabricated by aqueous solution method [140]. First, the arrays of ZnO nanowires were synthesized on seeded substrates as described in section (3.1.1). Secondly, the ZnO nanowires substrate obtained from the first step were recoated with seed layers of ZnO nanoparticles by ALD or DC-sputtering techniques. Finally, the branched nanowires were grown by using the same wet chemical method used in section (3.1.1) for different synthesis times. The branched ZnO nanowires were finally rinsed with deionized water and annealed in air at 450 °C for 1 h to remove any residual organics.

3.5 Material characterization techniques

After the synthesis of nanomaterials and before their use in different applications a variety of characterization methods are utilized to assess their physical and chemical properties. The details of structure and property characterization methods used to investigate the produced nanomaterials in this dissertation will be discussed in the following subsections.

3.5.1 Morphology and composition characterization

– X-ray diffraction (XRD) analysis

XRD technique is frequently used to study the internal crystalline structure of inorganic materials to reveal information about their chemical composition, crystal structure and grain size. XRD involves monitoring the diffraction of X-rays after they interact with the sample. Only materials that have ordered structure can be characterized with this technique, while, it cannot be used directly to study amorphous materials. Atoms of crystalline materials are ordered in a space lattice forming series of parallel planes separated by a distance d , which is varying depending on the nature of the material. This interplanar spacing (d) of crystal can be calculated by Bragg's Law (as shown in equation 21) [141]:

$$2d\sin\theta = n\lambda \quad (21)$$

Where λ is the wavelength of the incident X-ray beam, θ is the angle of the diffracted wave, and n is an integer known as the order of the diffracted beam.

In this work, the phase composition of nanomaterials was characterised on a STOE-STADI MP X-Ray vertical diffractometer operating in a reflection mode using CuK_α (1.5406 Å) radiation.

Scanning Electron Microscopy (SEM) and Energy-Dispersive X-ray Spectroscopy (EDX) analysis

The SEM is one of the most routinely utilized techniques for the characterization of materials with nanoscale resolution, revealing their topographical and morphological features through scanning an electron probe across a surface and monitoring the secondary electrons emitted. Additionally, the compositional analysis of nanomaterial can be also determined by monitoring X-rays produced by the electron-specimen interaction and thus providing detailed maps of elemental distribution [141]. In this work, the microstructures of the samples were examined using field-emission scanning electron microscopy (FE-SEM, FEI Nova NanoSEM 430) equipped with an EDX analyser.

Transmission Electron Microscopy (TEM) analysis

TEM is a powerful characterization tools in nanotechnology that can to provide a wide range of information from the measured nanostructures, including morphology, diffraction patterns, lattice constants, particle sizes and elemental compositions. In a TEM, a beam of focused high energy electrons is transmitted through a thin sample and only certain parts of it are transmitted. An image is formed from the interaction of the electrons transmitted through the specimen. The obtained image is magnified and focused onto an imaging device, such as a phosphor screen or a charge coupled device (CCD). Crystal structures can also be investigated by high resolution transmission electron microscopy (HRTEM) where the images are formed due to differences in phase of electron waves scattered through a thin specimen [141]. In this work, TEM measurements were performed on a Philips CM300 FEG/UT-STEM (300 kV) transmission electron microscope.

Atomic Force Microscope (AFM)

AFM is used to measure attractive or repulsive forces between the scanning probe tip and the sample surface and to acquire atomic-scale images of surfaces. AFM can provide valuable information about surface roughness, grain size and shape of the tested materials. The AFM can be operated in different modes such as contact mode, constant force mode and tapping mode or dynamic force mode. Contact mode is the most common mode, where the tip is in intimate contact with the surface. As it is raster-scanned across the surface, it is deflected as it encounters surface corrugations [141]. In this work, Atomic force microscopy (XE-100 Park system equipped with 910 ACTA cantilever, operating in contact and noncontact modes) was used to analyze the topography of the films and nanowire arrays.

Focused ion beam tomography (FIB)

FIB is a versatile maskless lithography technique that is used in numerous fields. FIB systems generally employ a beam of Ga ions which can be focused to a spot size as small as 7 nm in diameter and can be accelerated up to 50 keV energies. Recently, FIB etching is used to develop prototype devices, such as integrated circuits, electrical and optical devices, as well as direct milling on the different surfaces. Additionally FIB can used in nanopatterning, where metal

electrodes can be deposited by using a high-energy Ga-FIB [142]. In this work, individual nanowires were electrically contacted by direct Focused-Ion-Beam (FIB) platinum deposition, using dual beam FIB FEI-235 equipment.

3.5.2 Optical characterization

Ultraviolet-visible (UV-vis) spectroscopy is widely used to characterize inorganic nanomaterials. The constituents of a substance, concentrations, and the functional groups in molecules can be identified by this technique. Additionally, size dependent properties, such as peak broadening and shifts in the absorption wavelength, can be observed in a UV-visible spectrum. Besides electronic properties, such as the band gap of a material, that can also be determined by this technique. The absorption spectra was recorded in a UV spectrometer (Lambda 950 UV/vis spectrometer from Perkin Elmer) in transmission mode in the wavelength range from 800-200nm.

3.5.3 Surface wettability

Wettability is a very important characteristic of a solid surface. The surface wettability is depending on the chemical composition and morphology of surface and can be determined by measuring their water contact angle, where surfaces can be hydrophilic (if water contact angle < 90 deg) or hydrophobic (when water contact angle > 90 deg) [143]. In this work, surface wettability of the produced thin-films was studied by measuring the water contact angle (CA) via a DSA100 Krüss instrument at 25 °C using the sessile drop fitting method for the static contact angle and deionized water (5 µL) as test solution. Contact angles were determined using the tangent method.

3.5.4 Electrical measurements

The current-voltage characteristics (I-V curves) of different heterojunctions were acquired by using a Keithley 2400 source meter, in a two probe configuration. The capacitance-voltage (C-V) measurement (1 MHz) was performed in a reverse bias condition and in different atmospheres (Agilent E4980A LCR meter).

3.5.5 Gas sensing measurements

To evaluate gas sensing properties, the device was placed in a test chamber with gas inlet and quartz window (Figure 17). The device was illuminated by a solar simulator (Newport 96000 Oriel 150 W, AM 1.5) with an output intensity of 100 mW/cm^2 , as the light source. The open circuit voltages as well as electrical resistances of the sample under different gases were measured with a Keithley 2400 source meter. Synthetic air, nitrogen, oxygen and reducing gases such as ethanol and methane were used as baseline and test gases, respectively.

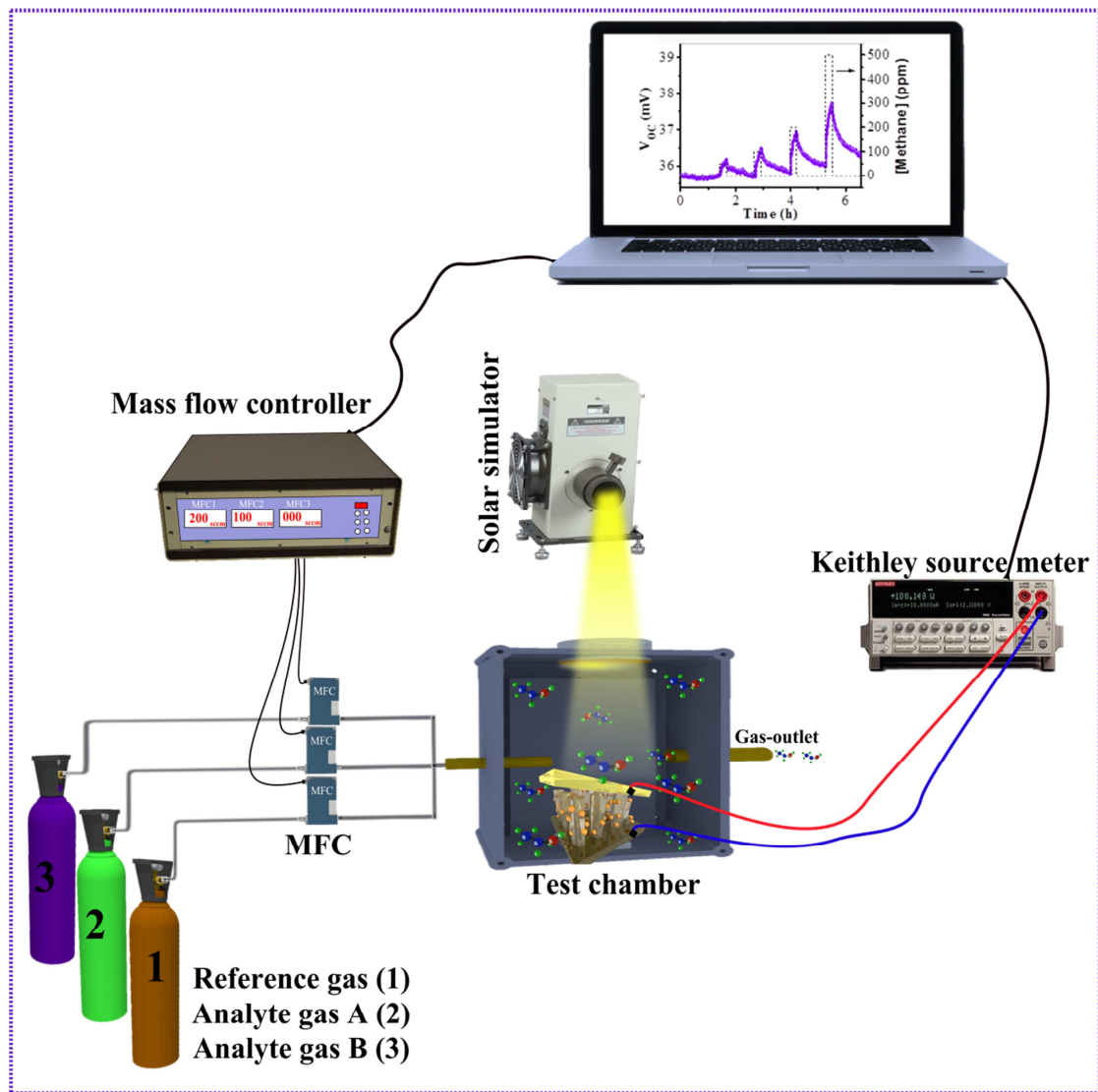


Figure 17 Schematic representation of the PC-automated gas sensing system used in this work.

4. Fabrication and Controlled Growth of Functional Nanomaterials

In this chapter, the controlled growth of ZnO based nanostructures and heterostructures for various nanodevice applications will be studied. Many issues still remain to be investigated, including ability to control their size, shapes and uniformity over large surfaces. Additionally, the growth of well aligned one-dimensional ZnO nanostructures that is needed for gas sensing and energy applications will be given particular focus.

4.1 Synthesis and controlled growth of one-dimensional ZnO nanomaterials

4.1.1 Hydrothermal growth of aligned ZnO nanowires

The hydrothermal synthesis of metal oxide semiconducting materials is one of the commonly used solution-based syntheses as an alternative route to the high temperatures synthesis. It offers potential for large-scale, low-cost production, and it enables the possibility to systematically control and tailor the growth of nanomaterials [101]. A key requirement for many applications is to grow highly oriented and well aligned ZnO nanowires directly on conducting substrates, and thus realize homogeneous material interfaces for suitable electrical transitions. To achieve such a goal a seed layer of ZnO is required before the hydrothermal growth, since the growth on existing ZnO seeds (i.e. heterogeneous nucleation) is more favorable than nucleation in homogeneous solution, since it has a lower activation energy barrier [14,111,128]. Moreover, the use of ZnO seeds for the nanowire growth is beneficial for the purity of the produced nanowires since it excludes the need of using metal catalyst for the VLS growth of nanowires which may introduce impurities into the final products. In this work, the influence of pre-deposited ZnO seed layers, prepared by different deposition techniques, on the growth of aligned ZnO nanowires is investigated.

– The role of ZnO seed layer thin films on the growth of ZnO nanowire

The growth and alignment of ZnO nanowires are influenced by the crystallinity, orientation and thickness of the underlying ZnO seed layer [104]. For this reason substantial efforts were made to optimize the quality and orientation of the ZnO seed layer deposited by different approaches, such as sol-gel/spin-coating, DC-sputtering/annealing, and atomic layer deposition (ALD).

i. ZnO seed layer deposited by sol-gel/ spin-coating and DC-sputtering/annealing techniques

ZnO thin films serving as the seed layer for the growth of ZnO nanowires were deposited by either sol-gel method or DC-sputtering/annealing techniques as described in details in the experimental section. Figure 18a shows the XRD pattern of the DC-sputtered and sol-gel deposited ZnO seed layers on a p-Si substrate indicating the enhanced crystallinity of the DC-sputtered seed layer with a preferred growth orientation in the (002) direction (JCPDS: 80-0075) in comparison to the sol-gel seed layer.

The SEM images of the DC-sputtered ZnO seed layer (figure 18c) illustrated a uniform coating over large surface with high reproducibility of the deposited films for all prepared samples. In contrast, the uniformity and reproducibility of sol-gel/spin-coated ZnO thin films was poor due to from the formation of bubbles during the spin coating process, which affects the homogeneity of the produced film and hence the nanowire growth. For this reason, mainly DC-sputtered/annealing technique due to many advantages such as ability of thickness control, reproducibility, homogeneity, and uniformity over large surface areas up to a wafer scale, were preferentially used in this work. The thickness of the DC-sputtered ZnO seeds can be easily controlled by changing the deposition time as presented in figure 19 (a,b). The deposition rate is approximately 4 ~ 5 nm/minute as shown in figure 19c. Figure 19d shows EDX spectrum of the DC-sputtered ZnO seed layer, in which the feature peaks are corresponding to the elements Zn and O can be observed in this spectrum in addition to the Si peak due to the underlying silicon substrate. This finding is not due to an incomplete coverage of the seed layer, but is caused by the penetration depths of the electron beam that is larger than the ZnO film thickness. The detection of only Zn, O and Si atoms confirms the high purity of the deposited ZnO films.

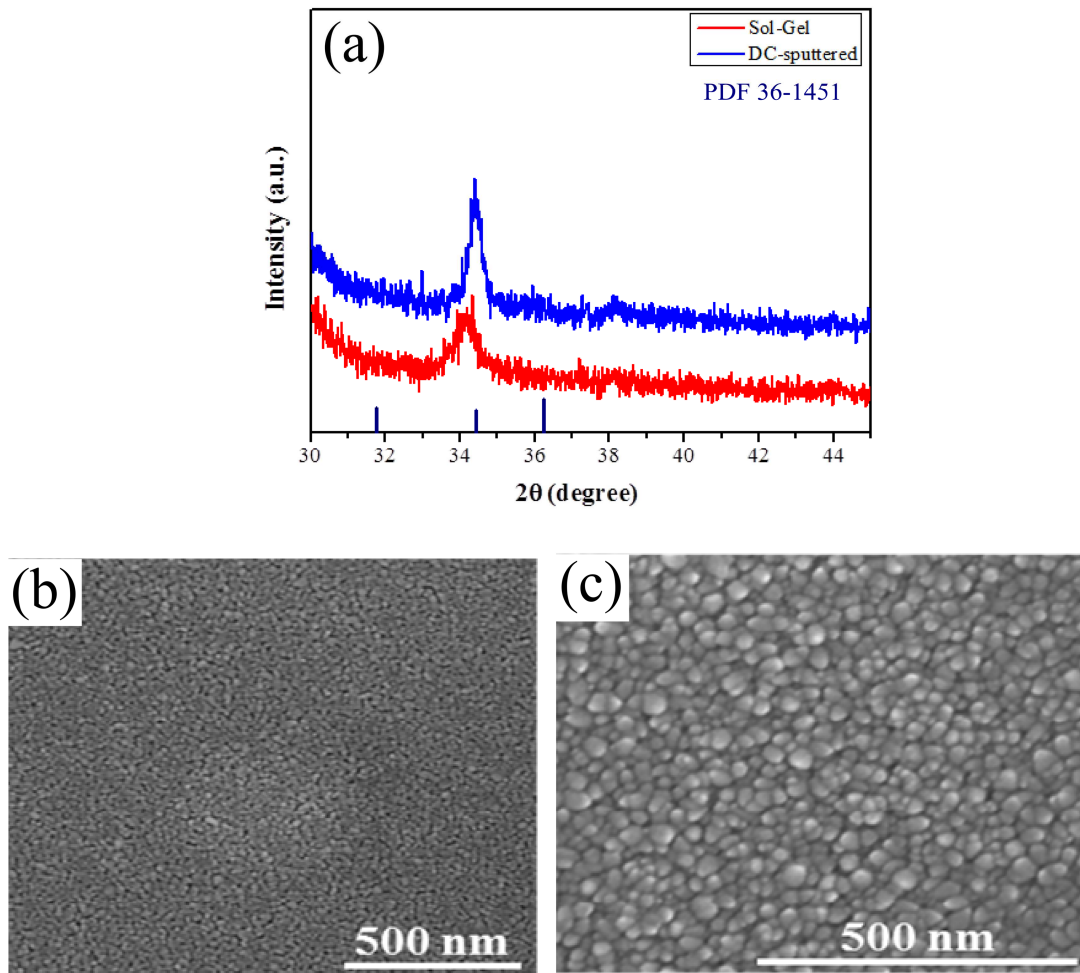


Figure 18 XRD pattern of ZnO seed layer prepared by spin-coating and DC-sputtering and annealing technique (a). SEM of ZnO seed layer prepared by spin-coating (b) and by DC-sputtering technique (c).

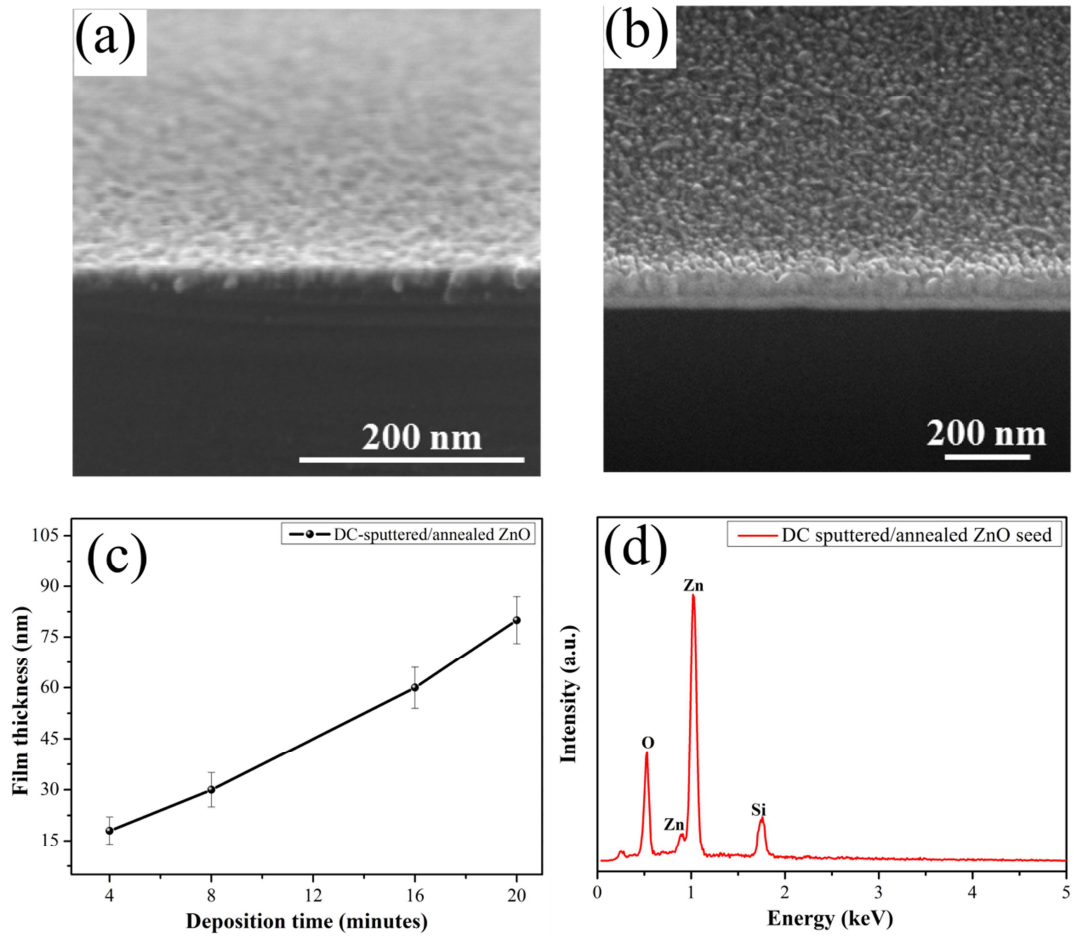


Figure 19 Cross-sectional SEM images of DC-sputtered/annealed seed layer deposited for (a) 4 minutes, (b) 20 minutes. (c) the change of film thickness with deposition time and (d) EDX spectrum of ZnO DC-sputtered/annealed seed layer.

The DC-sputtered seed layer were deposited for 20 minutes and annealed at 400 to 800 °C in air for 1 hour. The XRD patterns in figure 20a show only the characteristic (002) peak of ZnO, which indicates a c-axis orientation of the deposited films. The crystallinity was improved by increasing the annealing temperature up to 700 °C. The intensity of the (002) peak slightly decreased at 800 °C. Similar behavior was observed by Fang *et al.*, which can be attributed to the disturbance of the crystal structure at higher temperatures [144].

The crystallite size of ZnO films (D) can be calculated from the full-width at half-maximum (FWHM) of (0 0 2) diffraction peak by the Scherrer equation (see equation 22) [141].

$$D = \frac{K\lambda}{\beta \cos \theta} \quad [22]$$

where K is the shape factor (if a Gaussian function is used to describe the broadened peak, then the constant K is equal to 0.89), λ is the X-ray wavelength, θ is Bragg diffraction angle and β is the FWHM of the ZnO (0 0 2) diffraction peak.

XRD data in figure 20b show that the FWHM was decreased with increasing annealing temperature due to the slight increase of crystal size with annealing. Further AFM image of figure 20c presents the formation of a uniform ZnO film annealed at 500 °C with a surface roughness of about 1.2 nm.

The contact angle (CA) measurement (figure 20d) demonstrated a contact angle of $\sim 58.90^\circ$, indicating a slight hydrophilicity of the DC-sputtered films.

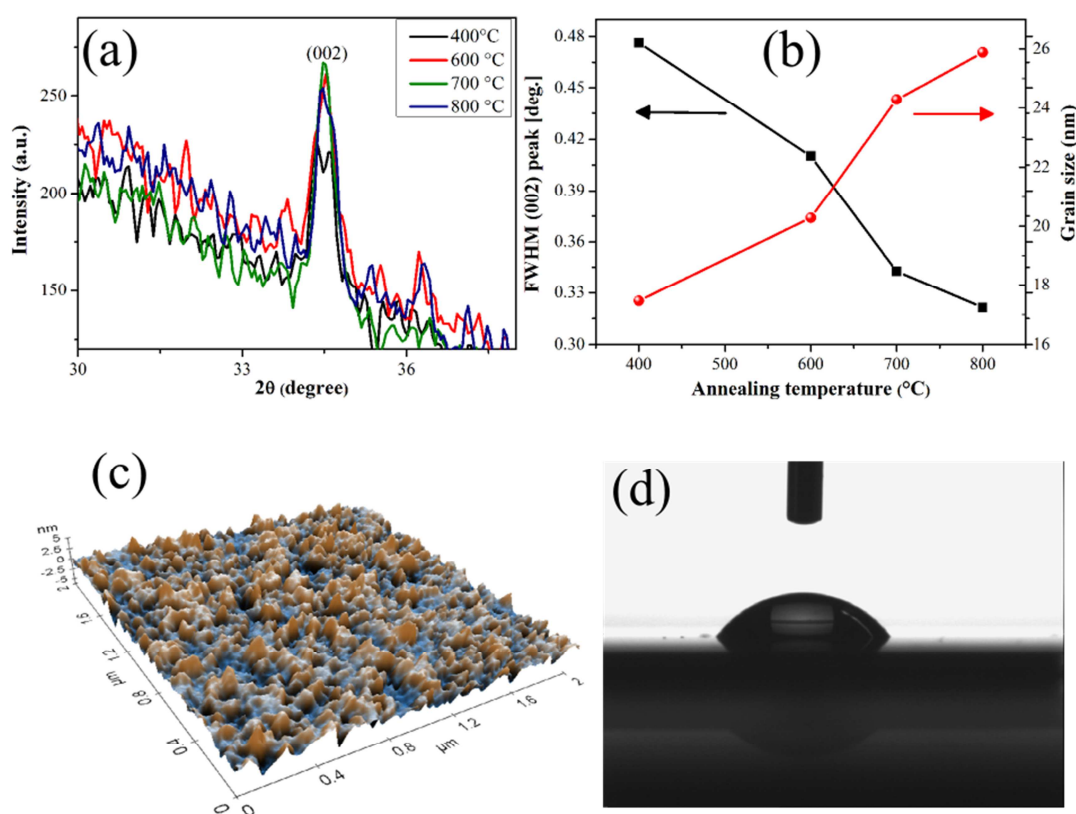


Figure 20 (a) XRD pattern of DC-sputtered ZnO film at different annealing temperatures. (b) the variation of FWHM of the (002) peak and the grain size of the ZnO film with the annealing temperature. (c) AFM image of DC sputtered film and annealed at 500 °C. (d) the contact angle measurement for surfaces of the DC-sputtered ZnO film at 500 °C.

After the successful deposition of ZnO seed layer on the desired substrates (such as p-Si, conductive glass (F:SnO₂, FTO), and Ni-foil), hydrothermal synthesis was used to grow ZnO

nanowires on the deposited seeds. Since the orientation of ZnO nanowires is influenced by the properties of the used ZnO seed layers, it is important to study the effect of ZnO seed layers on the growth of ZnO nanowire arrays.

The top and cross-sectional images of ZnO nanowires in Figure 21 show that the ZnO nanowires grown on seed layer prepared by DC-sputtering/annealing, and sol-gel/spin-coating techniques have c-axis orientation perpendicular to their substrates with average diameter of 140-160 nm. However, the ZnO nanowire on DC-sputtered/ annealed ZnO seed layer show a better alignment as compared to the nanowires grown on sol-gel/spin coated films.

The nanowire alignment of the ZnO nanowires with respect to the surface of the substrate can be studied by XRD. Figure 22 shows that the ZnO nanowires grown on the DC-sputtered/annealed seed layer are uniform and vertically aligned on their substrate and that the other prominent peaks in powder diffraction patterns are not seen. This is in agreement with the fact that the (002) peak of ZnO nanowires originates from ZnO seeds that have their c-axis aligned perpendicular to the substrate surface [14]. For the ZnO nanowires grown on sol-gel/spin-coated seed layer the intensity of the (002) peak is less intensive when compared to the ZnO nanowires on DC-sputtered and annealed films and the other prominent peaks are present in the diffraction spectrum. The extent of the nanowire alignment can be further examined by calculating the ratio of the (002) peak height to the (101) peak height which indicates the relative fraction of nanowires that are growing vertically from the surface of the substrate [145,146]. The (002)/(101) ratio is 197 and 8 for the ZnO nanowires on DC-sputtered and annealed films and sol-gel/spin-coated seed layers respectively. These values indicate better alignment for the ZnO nanowires grown on DC-sputtered and annealed seed layer, which is consistent with the SEM observations (shown in figure 21). The uniform orientation of ZnO nanowires on sputtered/annealed seed layer additionally showed a very uniform height and top flat surfaces. Thus, the high quality of the seed layer also enables a homogeneous growth speed along the entire sample. It will be shown in chapter 5 that the here achieved uniform height of ZnO nanowires on p-Si substrates is a crucial property to enable the direct assembly of these nanostructures in devices for gas sensing applications.

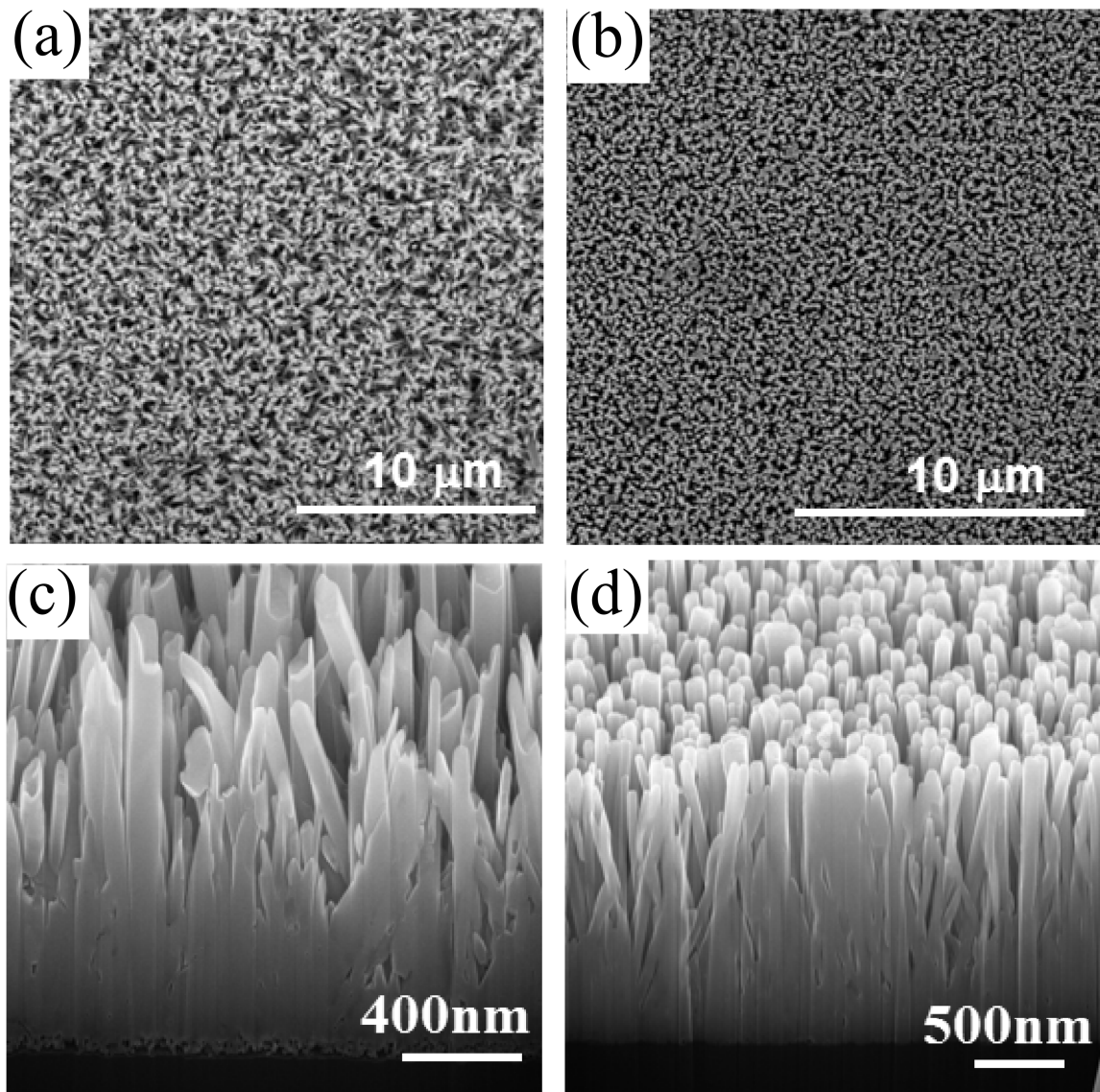


Figure 21 SEM micrographs (top and cross sectional view) of ZnO nanowires on seed layer prepared by (a,c) sol-gel/ spin-coating and (b,d) DC sputtering and annealing depositions.

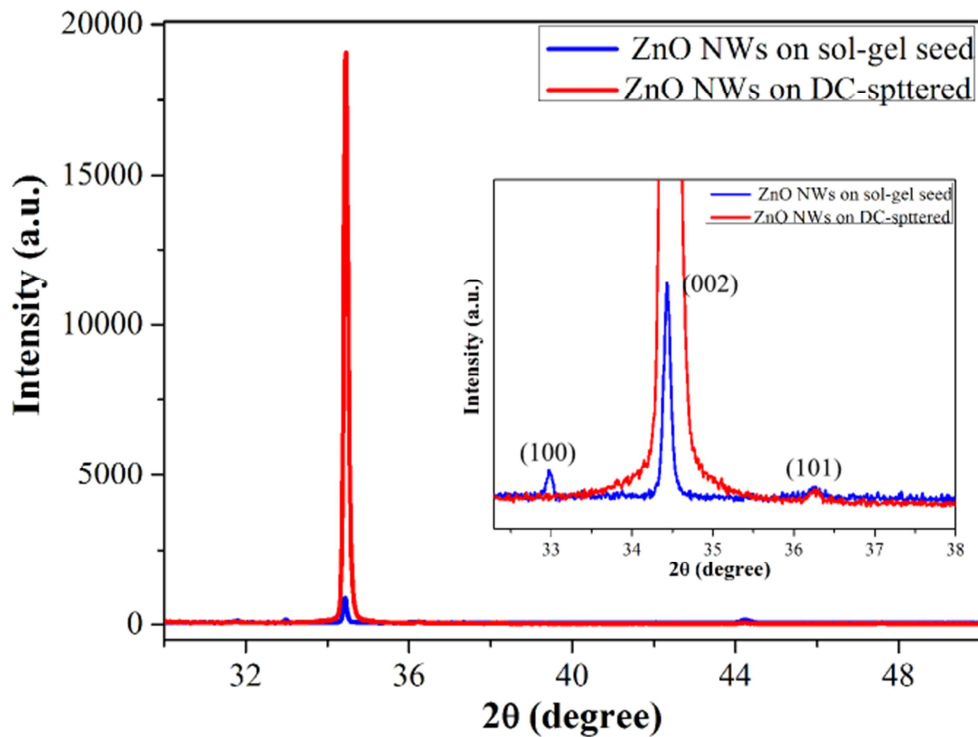


Figure 22 XRD patterns of ZnO nanowires on the top of seed layer prepared by DC-sputtering and annealing, and sol-gel spin-coated techniques. Inset shows a magnified part of these spectra.

ii. ZnO seed layer deposited by Atomic layer deposition (ALD)

To continue identification of optimal growth parameters for the growth of aligned ZnO nanowires, the ALD technique was used to deposit ZnO seed layers for growing aligned ZnO nanowires. The sequential deposition of atomic ZnO layers enables the realization of very homogeneous seeds with a very good control of the seed layer thickness. A series of depositions were performed to study and to optimize the influence of ALD process parameters, such as deposition temperatures, as well as the effect of post-annealing treatment on the as-deposited films.

ZnO films were deposited at different temperatures of 125, 175, and 200 °C, keeping the number of deposition cycles constant. The XRD spectrum in figure 23a shows the characteristics peaks in the range of $2\theta \sim 30^\circ\text{-}40^\circ$ ascribable to a polycrystalline wurzite phase of ZnO. All ALD deposited films showed very low peak intensities compared to previous films prepared by sputtering or spin coating possibly due to low film thicknesses and accordingly lower diffractions

values. The crystallinity of the ZnO seed could be slightly enhanced by increasing the deposition temperatures during the ALD process. Figure 23b shows the effect of post annealing temperatures on the crystallinity of the produced ZnO films. It is clear that the crystallinity is increasing by increasing the annealing temperature and the intensity of the (002) characteristic peak ($2\theta \sim 34.5^\circ$) is increasing, which indicates that the c-axis orientation is also dominating in these samples.

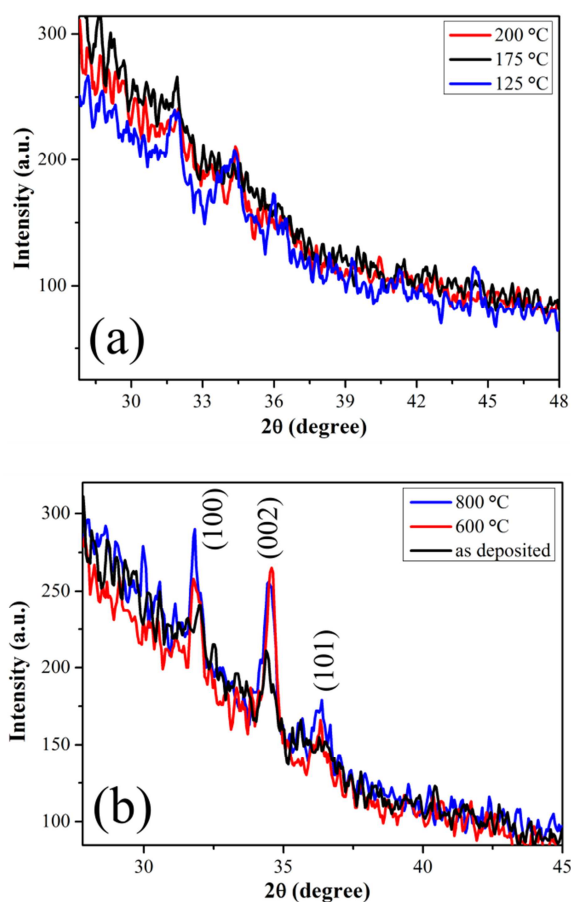


Figure 23 (a) XRD patterns of ALD ZnO films at different ALD deposition temperatures, and (b) for the film deposited at 200 °C with different post annealing temperatures.

The cross sectional SEM images, in figure 24 (a-d), show the dependence of the thickness of the deposited films on the number of ALD deposition cycles.

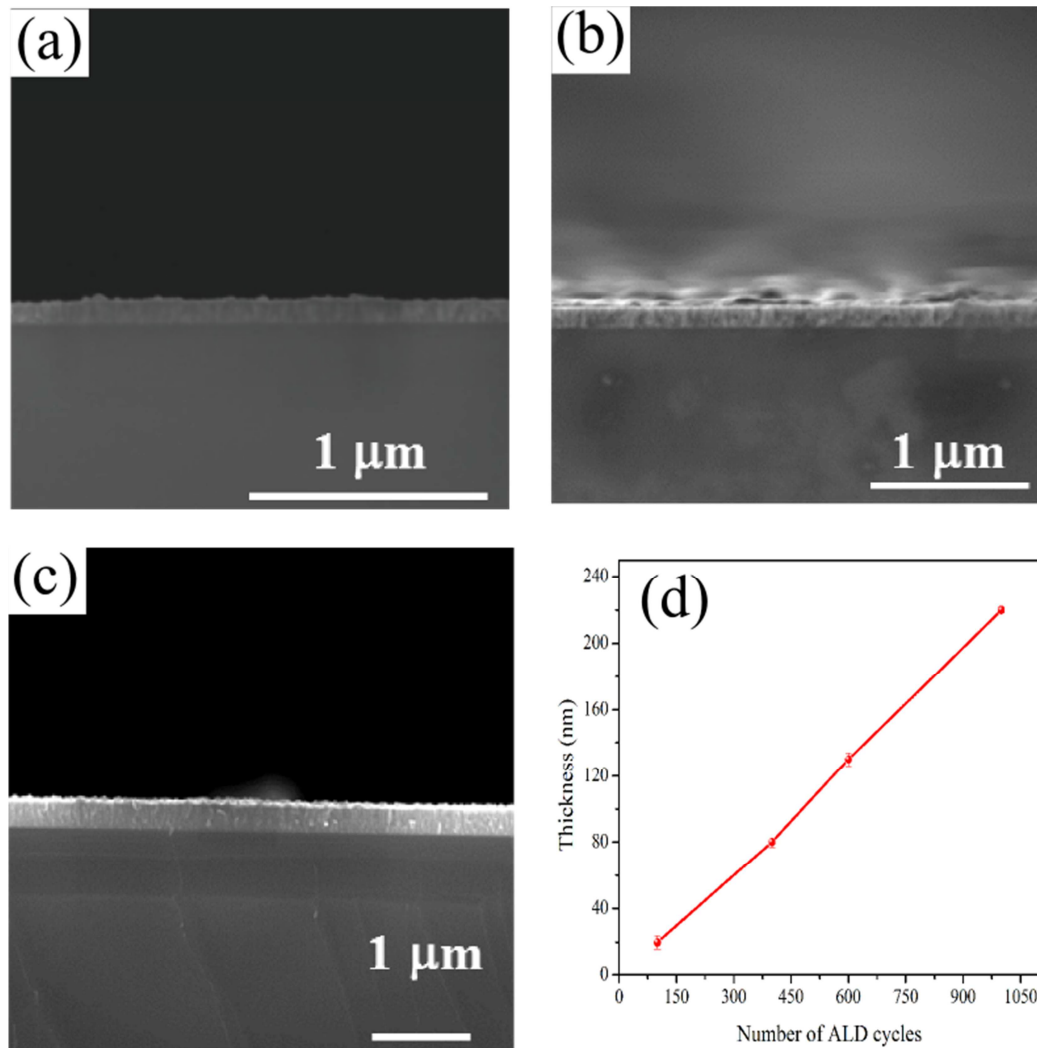


Figure 24 Cross-sectional SEM images of ALD deposited ZnO seed layer for (a) 400 cycles, (b) 600 cycles, and (c) 1000 cycles. (d) the relation between the number of deposition cycles and the film thickness.

The AFM images in figure 25 demonstrate that the ALD deposited films are highly homogeneous and uniform. The root-mean-square (R_q) of surface roughness derived from the AFM studies is depending on the number of ALD cycles (i.e. thickness of the film). The R_q values were 0.6 nm for films deposited in 100 cycles, 0.7 nm for 250 cycles, and 0.8 nm for 300 cycles. These results indicate that the roughness of the film is increasing with the increase of the film thickness. The roughness of ALD deposited films ($R_q = 0.8$ nm) is lower than that of the DC-sputtered films of the same thickness ($R_q = 1.2$ nm).

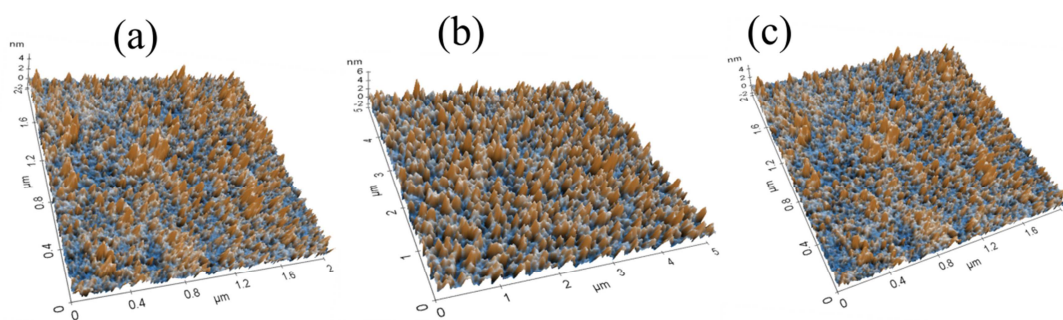


Figure 25 AFM images of ZnO films deposited by ALD after (a) 100 cycles, (b) 250 cycles, and (c) 300 cycles.

Electrical properties of two ZnO films (80 nm thick) deposited at 200 °C and post annealed at 400 and 500 °C were studied by the Hall effect measurements, which was carried out by the direct current (DC) four point probe method at room temperature. The donor concentration of ZnO films annealed at 400 and 500 °C were $5.97 \times 10^{19} \text{ cm}^{-3}$ and $1.08 \times 10^{18} \text{ cm}^{-3}$, respectively. A substantial reduction in the free electron concentration is observed with the increasing of the post annealing temperature which can be related to the better crystallinity and the lower number of defects and oxygen vacancies in the films annealed at higher temperatures [147].

The contact angle measured for ZnO thin films deposited at different ALD deposition temperatures (see figure 26) show hydrophobic character of the deposited films, where the sample was kept for 1 day in dark before the measurements. The slight variation of the measured contact angle of the thin films can be primarily attributed to the difference in their surface roughness and crystallinity [148]. The contact angle decreases for three ZnO films upon UV-light irradiation (for 4 hours) indicating that the hydrophilicity of the films increased through the UV-light irradiation (see figure 26 b,d,f). These decreases in contact angle can be explained in terms of surface activation by UV-light. Upon UV illumination, electron-hole pairs are generated at the surface of ZnO. The created holes can react with lattice oxygen to form surface oxygen vacancies, while the electrons react with lattice metal ions (Zn^{2+}) to form defective sites (i.e. surface trapped electrons). These defective sites are kinetically more favorable for adsorption of hydroxyl group (or water molecules). This results in improvement of surface hydrophilicity and the water contact angle is significantly reduced [148]. It is also worth to mention that this transition from hydrophobicity to hydrophilicity is reversible by exposure to UV light and can be revert back to

its original state by keeping the films in dark for 5 days. This result from the replacement of hydroxyl groups adsorbed on the defective sites by oxygen atoms, since the oxygen adsorption is thermodynamically favored [148].

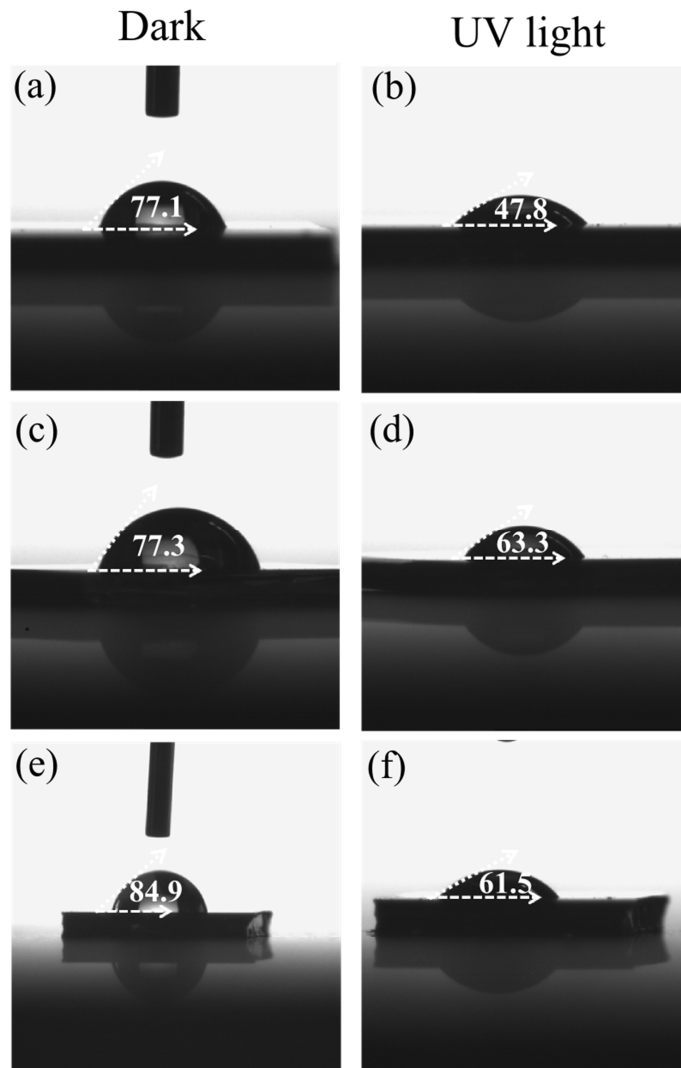


Figure 26 Contact angle measurements for surfaces under UV-light irradiation and in dark condition of the ZnO film deposited at different temperatures of (a, b) 125 °C, (c, d) 175 °C, and (e, f) 200 °C.

The orientation of the nanowires is a key factor that influences the design of prototype devices for gas sensing applications. The XRD diffractogram of the ZnO nanowire arrays on ALD seed layer (see figure 27a) show three characteristic diffraction peaks that can be indexed to the

(100), (002), (101) planes of the wurtzite ZnO, respectively. It confirms that as-prepared nanowire arrays are wurtzite ZnO with a vertical orientation along the c-axis. The SEM image, in figure 27b, shows the grown ZnO nanowires with a diameter of 50-80 nm which is remarkably thinner when compared to ZnO nanowires grown on DC-sputtered and annealed films. The ratio of the (002) peak height to the (101) peak height for different seed layers of the same thickness were 196, 14 and 8 for ZnO nanowires on DC-sputtered and annealed, ALD, and sol gel/spin coated seed layers respectively. These values are in agreement with the SEM observations and indicate that the alignment of ZnO nanowires on the DC-sputtered and annealed is the most suitable candidate for fabrication of prototype gas sensing devices (see chapter 5).

ALD and DC sputtering techniques will be mainly used for most of the depositions depending on the application requirements. DC-sputtered technique will be used for device design which requires better alignment and ALD depositions will be used for applications that need good control in terms of homogeneity, composition, and thickness to produce heterostructures or to be used as a seed layers to produce thinner nanowires and seed layers on 3D structured substrates.

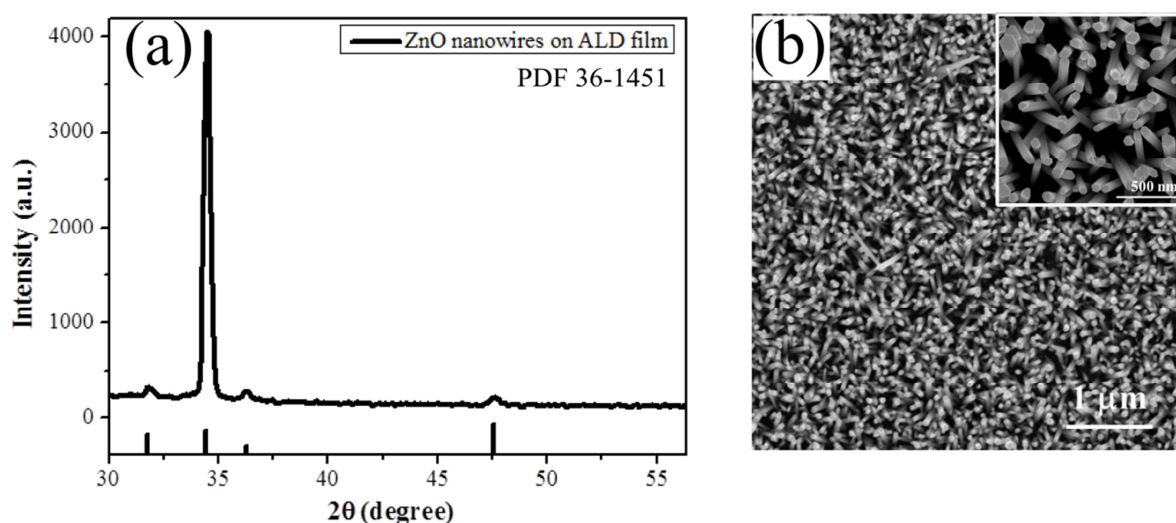
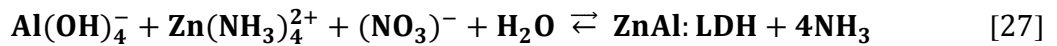
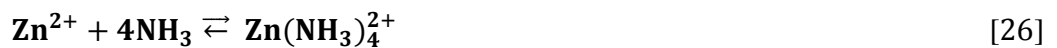
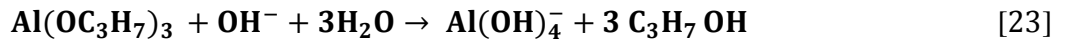


Figure 27 (a) XRD pattern and (b) top-view SEM image of ZnO nanowires on ALD deposited ZnO seed layer.

Besides the effect of ZnO seed layer, the influence of saturation level of hydrothermal solution on the crystal morphology is also studied as follows.

- **The effect of super saturated solution on the alignment of ZnO nanowires:**

In order to control the orientation of nanowires a promising strategy has been used to control the crystal growth during the hydrothermal synthesis through suppression of the homogeneous nucleation of ZnO in the bulk solution, which would otherwise consume the ZnO precursor and negatively affect the growth of ZnO nanowires on the substrate [136,149]. Figure 28 shows the SEM images of the nanowire arrays prepared with and without aluminum-iso-propylate on sol-gel/spin coated and DC-sputtered seed layers under the same conditions and for 20 h growth time. The ZnO nanowires synthesized in presence of aluminum-iso-propylate were more vertically aligned with higher aspect ratio when compared to the nanowires grown without the addition. The presence of aluminum-iso-propylate could provide sustainable support for the preparation of long length and high aspect ratio nanowires because it induces the formation of zinc aluminum layered double hydroxide (ZnAl:LDH) instead of ZnO nanoparticles in the bulk solution and promote the anisotropic growth of long ZnO nanowire arrays on the substrate [136]. The reactions that may be involved in the growth of ZnO nanowires in solution containing aluminum-iso-propylate are described as follows [136]:



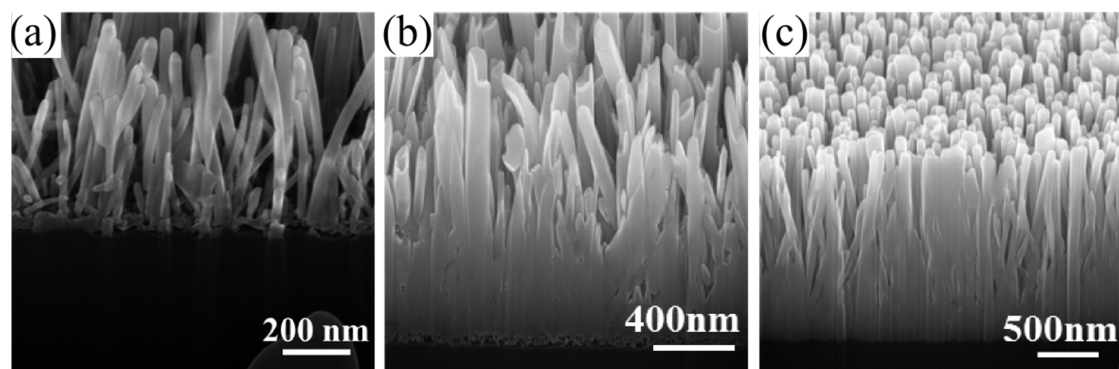


Figure 28: cross-sectional SEM images of ZnO nanowires on sol-gel spin coated seed layer without (a) and with (b) aluminum-iso-propylate, and (c) on DC sputter seed layer with aluminum-iso-propylate.

As can be seen in the SEM images in figure 28c, the combination of the controlled supersaturation growth on a proper seed layer could achieve an optimal alignment of the nanowire arrays. Achieving such well aligned nanoarrays on substrate is a fundamental step towards direct synthesis and integration of nanostructures in the desired nanodevices.

The growth of ZnO nanowire arrays is subjected to the reaction-limited growth, where the rate of nanowire growth is found to be decreasing or even vanishing after a certain time [136]. To overcome such limitation, multicycles of growth of ZnO nanowires in fresh solutions was used to elongate the length of nanowires perpendicular to their substrates and thus increase the surface to volume ratio of the nanowires. Figure 29 shows that ZnO nanowires of about 4 μm were obtained after 3 cycles of growth. Such long nanowires with high aspect ratio are favorable for solar energy harvesting applications [150].

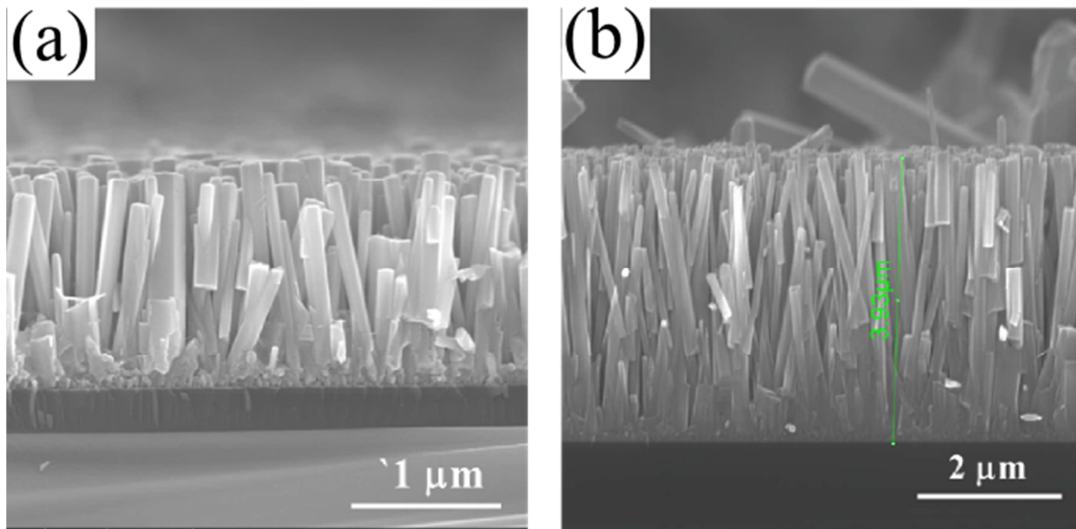


Figure 29: cross-sectional SEM of ZnO nanowires produced after (a) 1 cycle and (b) 3 cycles of growth, where the duration of each cycle was of 8 hours.

4.1.2 Synthesis of ultra-long ZnO nanowires and nanotubes through anodization method

In a further approach [151], ZnO nanowires were synthesized by anodizing Zn foil in slightly basic electrolyte of NaHCO_3 . The XRD diffraction pattern (figure 30a) of Zn foil anodized at 5 and 10 °C under the same anodization conditions (10 V applied voltage, anodization time 1h, electrolyte concentration 0.05 M NaHCO_3 , then annealed at 250 °C for 1 h in air) show the characteristic peaks of the polycrystalline hexagonal phase of ZnO (JCPDS 36-1451) in addition to the zinc peaks originated from the zinc substrate (JCPDS 04-0831). The crystallinity of the nanowires obtained at 10 °C anodization was higher compared to other temperatures used. The nanostructures produced via anodization were mixture of nanowires and nanotubes as shown by SEM images in figure 30 (b,c). The formation of nanotubes from nanowires has already been observed for several materials (such as ZnO and ZnS) and can be attributed to the chemical dissolution of the nanowire core [152,153].

The TEM image (figure 30d) shows the polycrystalline and the porous nature of the produced nanowires with a diameter of 170 nm and length of 25 μm

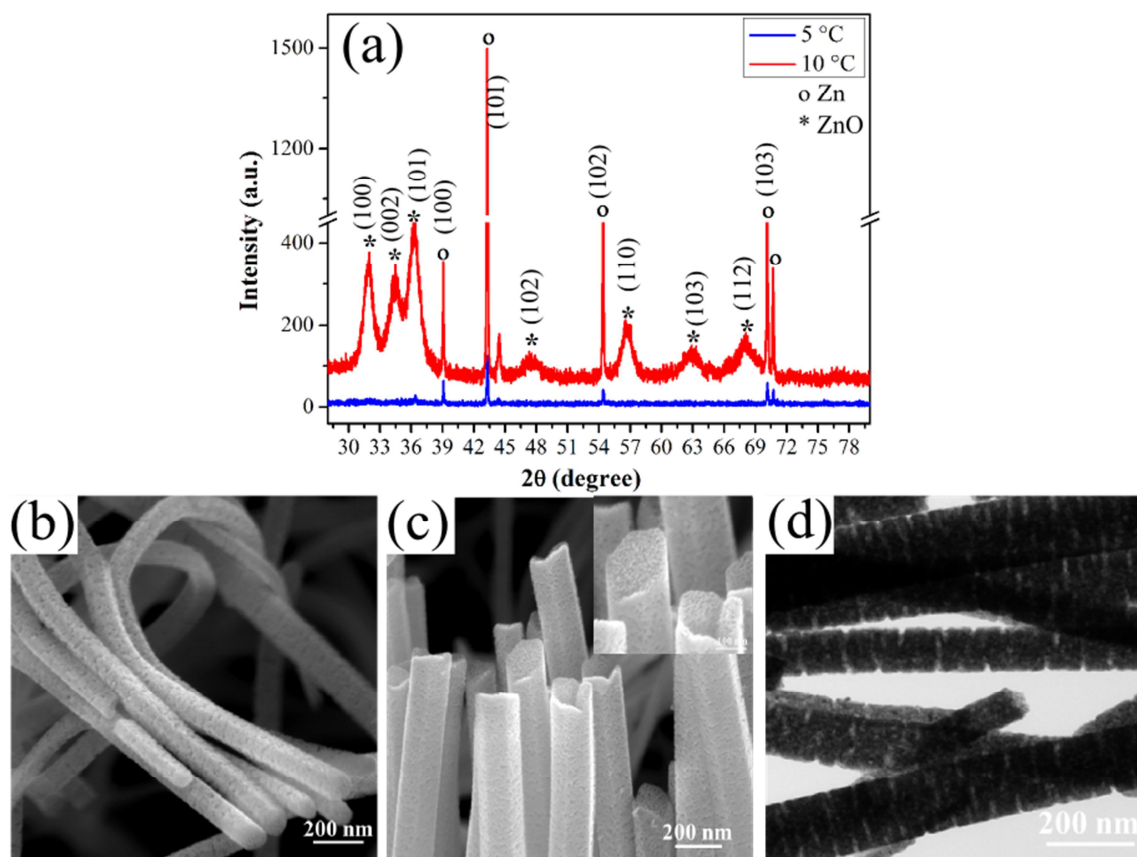


Figure 30: (a) XRD patterns of Zn foil anodized at 5 and 10 °C under the same anodization conditions followed by annealing treatment at 250 °C. (b, c) SEM and (d) TEM images of ZnO nanowires and nanotubes obtained from anodization at 10 °C under 10V applied voltage for 1 h.

The effect of different parameters of the anodization process was studied to understand the growth mechanism and to optimize the growth process.

- **The effect of electropolishing pretreatment of the Zn foil**

The electropolishing of Zn foils before anodization is very important to obtain a more uniform nanowire film on the whole substrate. Electropolishing is reducing the surface roughness and removing the irregular surfaces as can be observed from the SEM images (see figure 31b) of untreated foils and their electropolished counterparts.

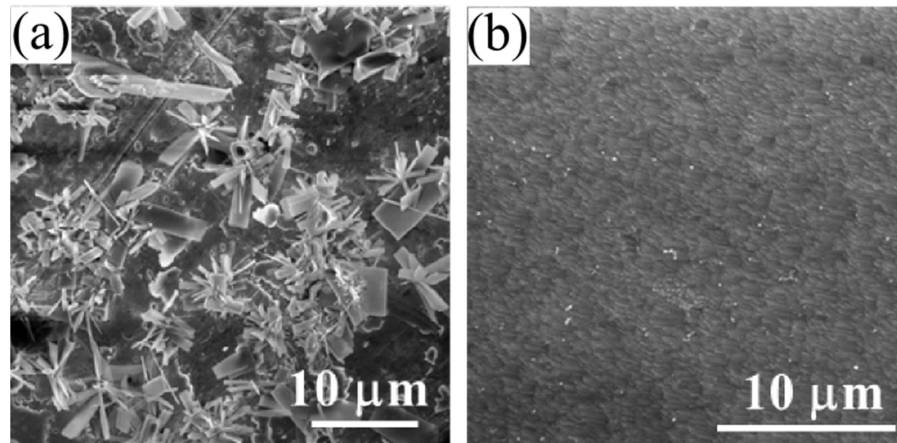


Figure 31 SEM of Zn foil with (a) no pretreatment and (b) electropolishing pretreatment.

- **The effect of growth time**

The early stages of ZnO nanowires growth were observed by successive SEM images taken at different growth times. The SEM image of Zn foil anodized for 1 min (figure 32a) show many surface pits with flower like thin needles inside it. The number of surface pits increased with time with longer flower like needles springing out of the pits (figure 32b). The needles are grow longer with time and form long nanowires that covered most of the foil surface at 20 min anodization period (figure 32c). The increment of anodization growth time results in growth of ultra-long nanowires with length of about 40 μm for 1h anodization (figure 32d).

- **The effect of applied voltage**

The effect of applied voltage was studied and as shown in SEM images a lower applied voltage is favorable for the growth of nanowires with uniform sizes and lengths. Films start to crack when higher voltages are applied (20 V) and the films peel off from the surface of the foil. The obtained ZnO nanowires are mesoporous on the side walls as can be seen in figure 33. The porosity of the nanowires is found to decrease with increasing the applied voltage up to 15 V. The suitable control over the applied voltage can lead to control over the porosity of the produced nanowires which is interesting for applications that require higher surface areas and better diffusion such as gas sensing applications.

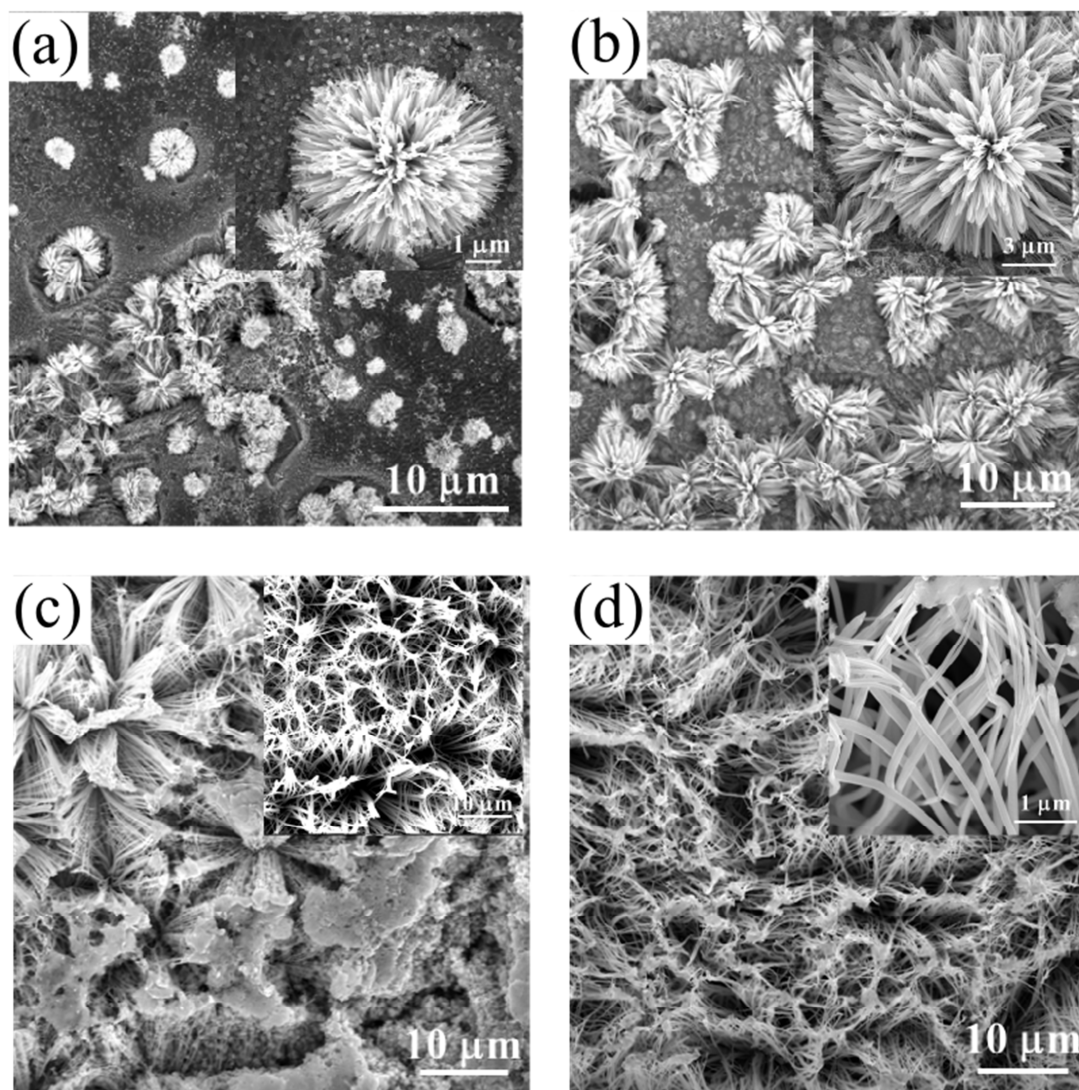


Figure 32 SEM images of ZnO nanowires at different growth times of (a) 1 min., (b) 5 min., (c) 10 min., and (d) 20 min.

- **The effect of reaction temperature**

SEM observations (see figure 34) indicate that the reaction temperature has an influence on the growth of nanowires and that lower temperatures (e.g. 10 °C) are favorable for the nanowire growth up to room temperature. When the temperature increases up to 40°C irregular nanowires are grown and surface cracking was observed. With further increasing of the temperatures up to 70 °C, hair-like microstructures were observed. The best results of homogenous dense and

uniform nanowires arrays were obtained for films anodized below room temperature, possibly due to more controlled etching process.

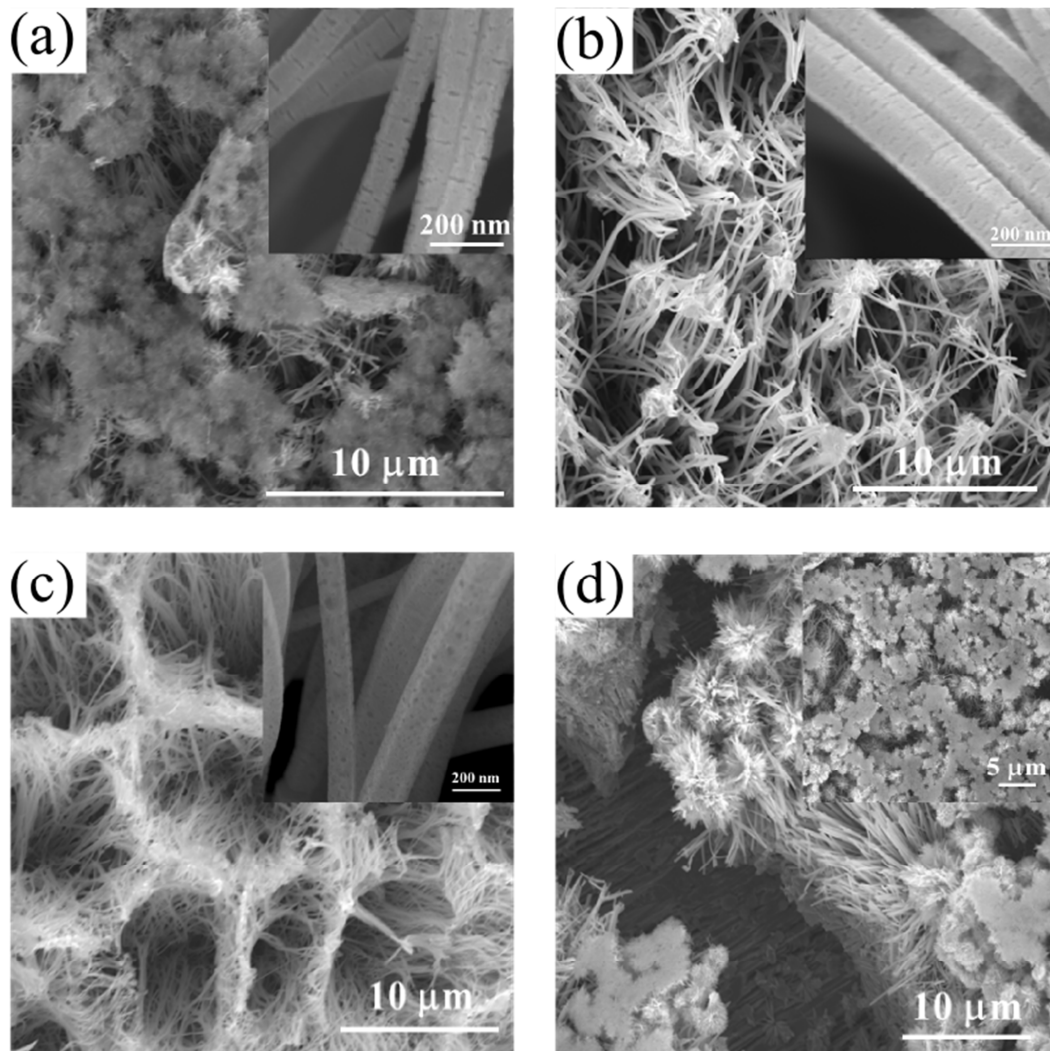


Figure 33 SEM images of ZnO nanowires at different applied voltages of (a) 5 V, (b) 10 V, (c) 15 V, and (d) 20 V.

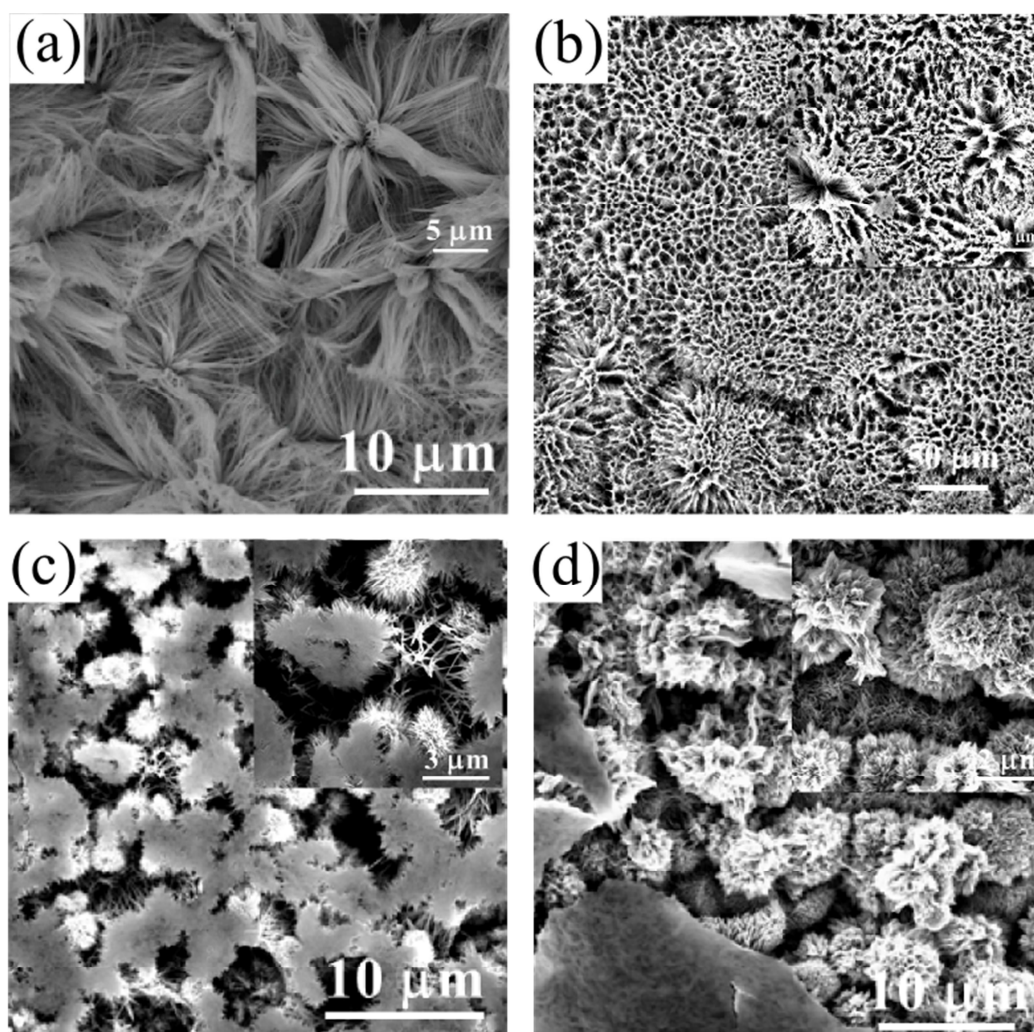


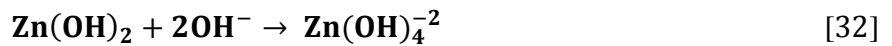
Figure 34 SEM images of ZnO nanowires at different growth temperatures of (a) 10 °C, (b) room temperature, (c) 40 °C, and (d) 70 °C.

The proposed growth mechanism of ZnO nanowires by anodization:

Based on the above observations, the growth mechanism of ZnO nanowires by anodization will be explained. The aqueous solution of NaHCO_3 is slightly basic which in presence of an applied voltage corrodes the Zn foil and thus chemical and electrochemical etching processes are simultaneously active on the zinc surface. In accordance with literature for a similar electrolyte, the electrochemical etching process dominates at lower applied voltages (in the range of 10-20 V) [127]. In the presence of low applied voltages, zinc tends to dissolve and result in the formation

of the local pits observed from the first minute of anodization. The ongoing anodic and cathodic reactions are described in the following equations [127]:

Cathode reaction:



Anode reaction:



When a voltage is applied, Zn(OH)_4^{2-} ions form the needles like nanostructures which become nanowires with increasing reaction time. The obtained products were converted to uniform ZnO nanowires by annealing at 250 °C in air.

The use of Zn foil to produce ZnO nanowires via anodization offers many advantages such as the lattice match between ZnO and Zn, which facilitates the growth of well aligned nanowire arrays. Additionally, no catalyst or a seed layer is needed for the growth, since Zn foil act as both the reactant and the substrate [127]. The main disadvantage of the anodization method is the difficulty to integrate the produced nanowires into Si based electronic and optoelectronic devices. Besides the instability of the produced nanowires films on their substrates, that hinders exploitation of their useful properties as well as their practical applications.

4.1.3 Synthesis of ZnO nanorods by oxidation of Zn foil

The current approach for a simple synthesis of one-dimensional ZnO nanostructures is based on natural oxidation of Zn foil in presence of alkaline solutions such as ammonia or NaOH solution or with the aid of aqueous solutions of formamide. Acceleration of the natural oxidation is needed due to the fact that of oxidation of zinc metal in water by the naturally dissolved oxygen is very slow caused by the formation of a passive ZnO surface layer on its surface [154].

- **Direct oxidation of zinc foil in an aqueous solution of formamide**

Formamide aqueous solutions are used to accelerate the slow zinc oxidation process. Zn reacts with formamide to form zinc-formamide complexes (equation 34) [155,156]. These complexes are continuously supplied from the zinc foil and then dissociate thermally to produce zinc ions that readily oxidize and produce ZnO.



The XRD patterns shown in figure 35a verify the presence of hexagonal wurtzite ZnO with a preferential orientation in the [002] direction in addition to less intensive (001) and (101) reflections. SEM images (see figure 35b) show the formation of ZnO nanorods of about 80 nm diameter.

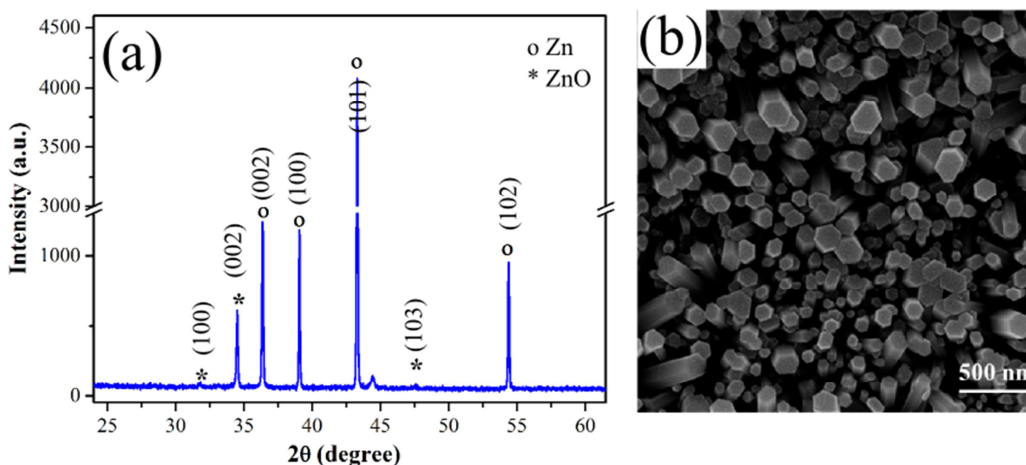


Figure 35 (a) XRD patterns, (b) SEM image of ZnO nanorods grown on a zinc substrate immersed in an aqueous formamide solution for 24 h at 66 °C.

- **Salt assisted oxidation of zinc foil in formamide**

In order to control the shape of the nanostructures produced by oxidation of Zn foil, a certain amount of NaCl salt was added to the formamide aqueous solution (keeping the same reaction conditions) as a shape-control agent. Novel well-defined platelet-like ZnO microstructures were formed as can be seen in SEM image in figure 36a. The formation of the platelet-like ZnO microcrystals can be explained based on the so called “salt effect” where upon introduction of

NaCl into the solution precursor chloride ions would be selectively adsorbed on the positive polar face of the (0001) ZnO and hinder further growth along the $\langle 0001 \rangle$ direction and thus accelerates the radial growth to form platelet-like structures [157]. The chemical composition of the produced platelet-like ZnO was confirmed by EDX measurements (see figure 36b). It shows the presence of only Zn and O elementary components with a little of Cl impurity.

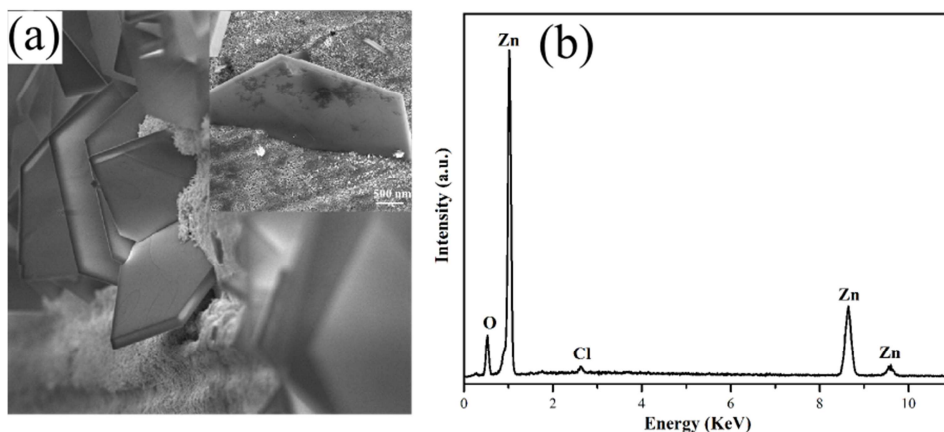


Figure 36 (a) SEM image and (b) EDX spectra of platelet-like ZnO grown on a zinc substrate immersed in 5% formamide aqueous solution containing 0.45 M NaCl salt for 24 h at 65 °C.

- **Direct oxidation of zinc foil in an aqueous solution of NaOH**

The zinc foil turned to grey when it was immersed in the alkaline solution of NaOH at 80 °C for 24h due to the surface oxidation process of the Zn foil. The Zn foil reacts with the alkaline solution to form a complex of $\text{Zn}(\text{OH})_4^{2-}$ which further decomposes to form ZnO. The SEM image (figure 37a) shows the formation of ZnO nanorods with hexagonal pyramid-like sharp tips and well-defined crystallographic faces. The formation of the pyramid-like sharp tips can be attributed to differences of growth rates of different crystal faces which control the final shape of the produced ZnO nanorods [158]. The EDX spectrum shows that the elementary components existing are Zn and O only (see figure 37b).

The as grown ZnO nanorod layer were ultrasonically removed, a pattern was left on the foil surface of the foil (see figure 37c) that act as a seed layer for the growth of thicker ZnO nanorods composed of multi-segments with rougher surface and diameter of about 200-250 nm (see figure 37d). The size of the produced nanorods suggests that the nanorods were directly grown on the

pattern left on the Zn foil surface. This can be a promising approach for developing novel nanostructures by using scaffold nanostructures on the surface of the desired substrates to design a nano-imprint pattern for a second step growth. The EDX spectrum shows that the elementary components existing are Zn and O only.

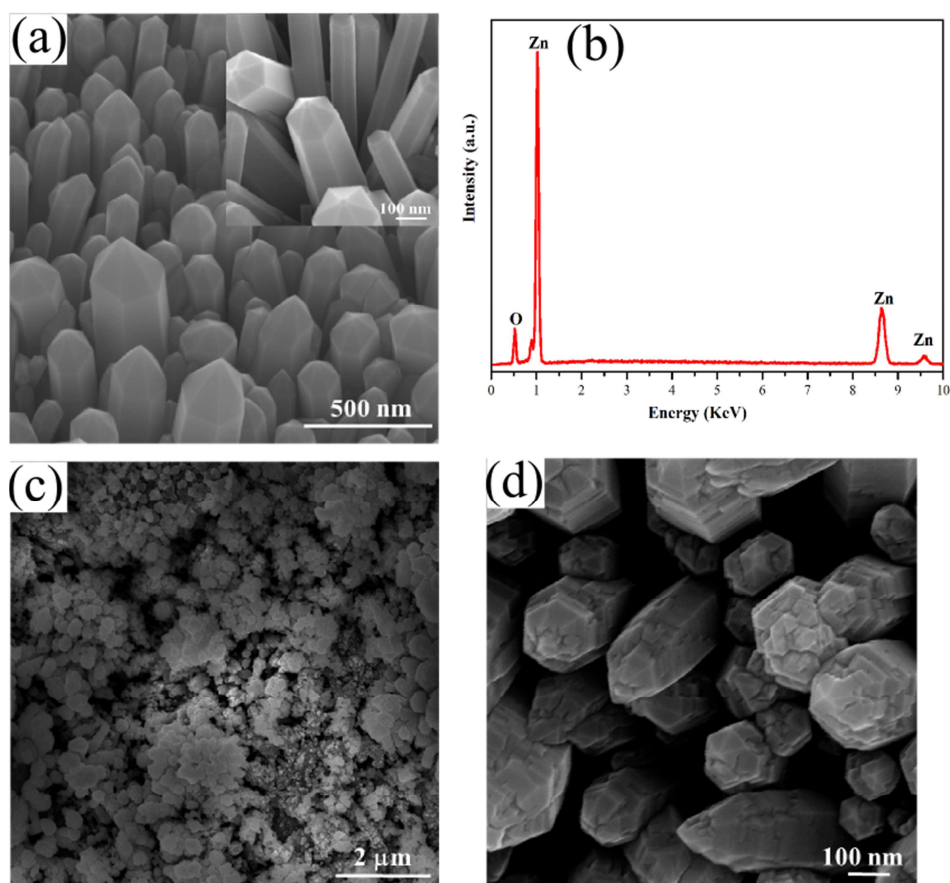


Figure 37 (a) SEM image and (b) EDX spectra of ZnO nanorods with pyramid-like sharp tips grown on a zinc substrate. (c) the pattern left on the ZnO foil after ultrasonic treatment. (d) multi-segments nanorods formed on the pattern in shown in c.

To sum up, the various ZnO nanostructures synthesized on Zn foil by the different methods mentioned in this section are summarized in table 5.

Table 5 Summary of ZnO nanostructures synthesized on Zn foil by different methods.

Method	Morphology	Precursors
Anodization	Ultralong NWs/nanotubes	NaHCO ₃ electrolyte
Formamide assisted oxidation	Highly oriented nanorods	Formamide aqueous solution
Formamide/salt assisted oxidation	Platelet-like	5% Formamide + 0.45 NaCl
NaOH assisted oxidation	Nanorods with pyramid-like tips	NaOH aqueous solution
NaOH assisted oxidation on pre-pattern	Microrods composed of multi-segments	NaOH aqueous solution

4.2 Fabrication of Si nanowires

Silicon nanowires (Si NWs) are promising building blocks for new nanoelectronics and energy harvesting applications as an alternative to planar Si devices due their attractive properties such the excellent light-harvesting capabilities and the enhanced carrier collection and transport efficiencies [159,160].

The metal-assisted chemical etching was chosen here to fabricate Si NWs as a simple and low cost method, besides it can provide nanowires free from contamination usually found in the traditional vapor–liquid–solid approaches [159]. The fabrication of Si NWs can be achieved by etching the Si wafer in two solutions; solution I (consist of AgNO₃/HF) to form an Ag layer on the surface of the Si wafer where the morphology of the deposited Ag nanoparticles is strongly depending on the immersion time, followed by solution II (contain H₂O₂/HF) as schematically represented in figure 38. The mechanism of etching of Si NWs is still not clear so far and is an active subject of debate [161,162]. One of the explanations is considering that Ag particles protect the underneath Si from etching solution and only etching occurs in the surrounding area which results in Ag capped Si NWs, while the other proposed mechanism argues that Ag particles catalytically etching away the underneath silicon that is directly in contact with them [162]. The explanation of the etching mechanism was not investigated in this work; the attention was mainly paid to optimize the fabrication process to produce Si NWs with controllable and repro-

ducible lengths. The produced Si NWs will be further used, as it will be described later, for the fabrication of p-n heterojunctions with metal oxides such as ZnO and NiO.

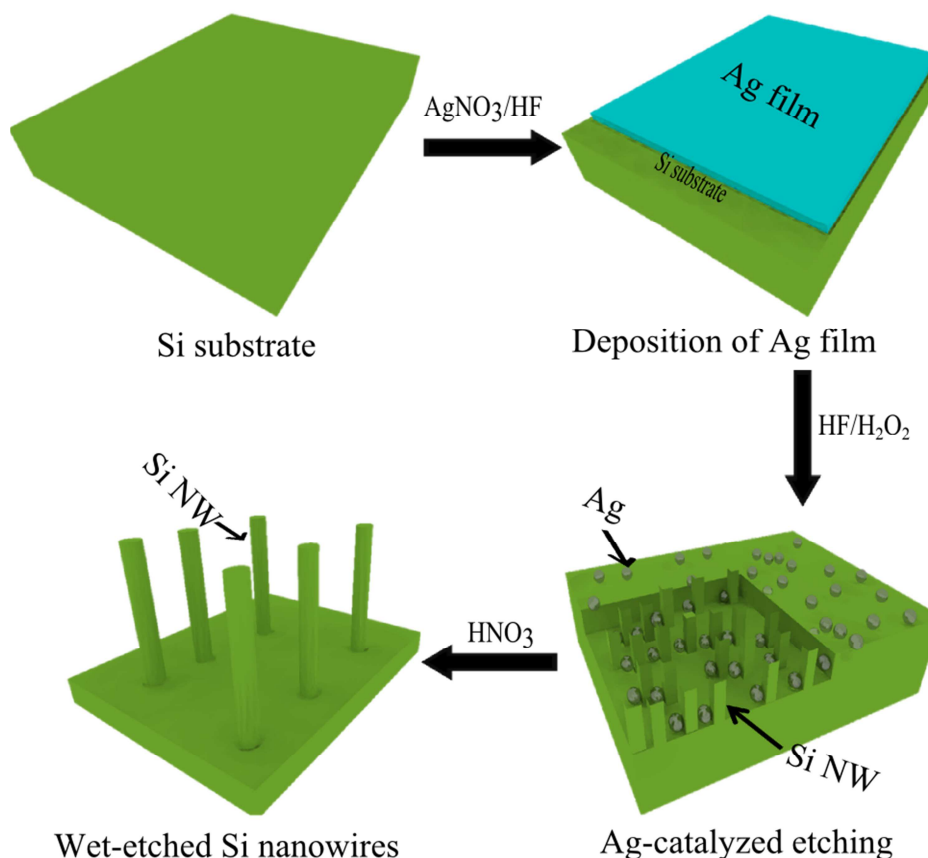


Figure 38: A schematic illustration of wet chemical etching process of silicon substrate by using two solutions; solution I (consist of AgNO_3/HF) followed by solution II (contain $\text{H}_2\text{O}_2/\text{HF}$).

The main factors that can influence the Si NWs formation are the AgNO_3 concentration, the HF concentration, and the etching time [137]. After several experiments, using different conditions, here the most reproducible results are introduced, which can produce Si NWs with the same structural characteristics. Figure 39a shows the cross-sectional SEM images of the Si NWs after etching and before removing of the Ag particles by immersion in concentrated HNO_3 . It clearly shows the presence of Ag nanoparticles with 90-130 nm of average diameters and also some Ag nanoclusters can be observed.

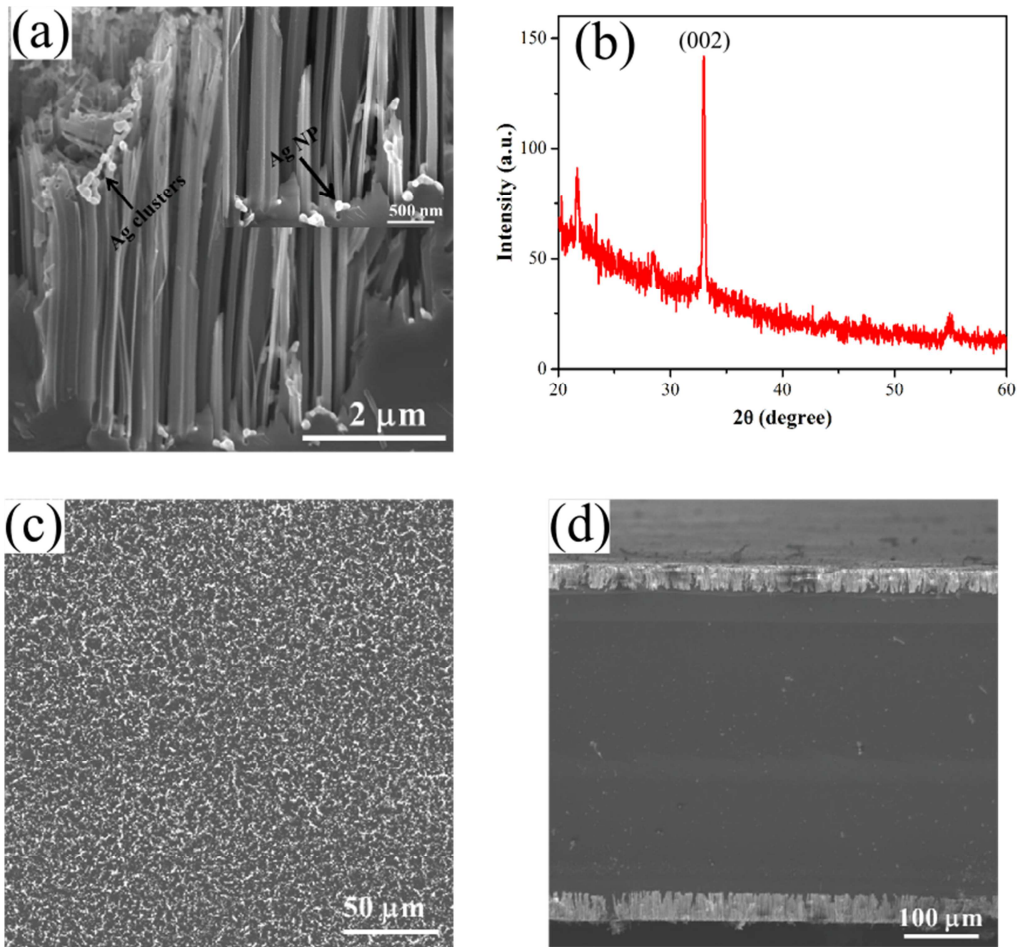


Figure 39: (a) Cross-sectional SEM image of etched Si NWs with Ag nanoparticles and nanoclusters, (b) XRD pattern of Si NWs etched for 1 h, (c) their top view SEM image. (d) the effect of etching on both sides of Si wafer.

The etched Si NW array architecture strongly depends on the orientation of the used silicon wafer, which is p-Si (100) in case. XRD patterns of the wet etched Si NWs (figure 39b) shows a preferential orientation along [100] direction with a good crystalline quality. The top- and cross-sectional SEM images, shown in figure 39 (a, c), of the Si NWs formed by etching the silicon wafer for 1 h with a silver layer deposited for 1 minute show that the Si NWs are uniform and vertically oriented to the substrate. They have a uniform length of about 25 μm with a diameter ranges from 120 to 270 nm. As can be noticed on figure 39d, the backside of the Si wafer was also etched and Si NWs were formed, which may or may not be detrimental depending on their desired applications. Since the nature and the quality of the Si backside can influence the nanodevice performance and hence their functional properties, it is crucial to protect the backside

of Si wafer before etching. This effect of double side etching, if controlled, can be taken as an advantage to fabricate so called hybrid devices which use the double sides of Si wafer to reach a maximum efficiency per unit device.

The length of Si NWs on a Si (100) wafer shows almost a linear relationship with the etching time as can be seen from the cross-sectional SEM images of Si NWs which were etched at different periods (see figure 40).

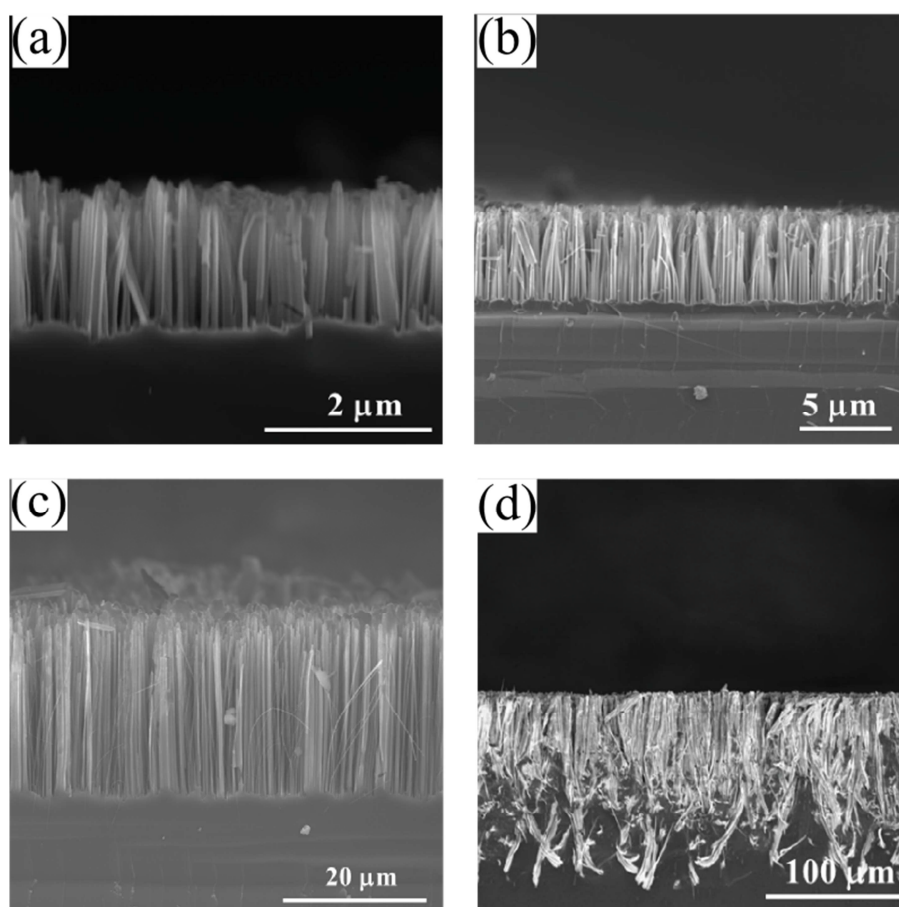


Figure 40: Cross sectional SEM view of Si NWs etched for (a) 3 min with length of 1.2 μm , (b) 10 min with length of 4.8 μm , (c) 1 h with length of 25.9 μm , and (d) 3h with length of 60 μm .

4.3 Fabrication of p-n heterojunctions and their heterostructures

Heterostructures with a suitable band energy alignment and high-quality interfaces are good candidates to build nanosystems with multifunctional properties. Heterojunction is formed at the interface of two doped semiconductor materials (doped with either p- or n-extrinsic dopant atoms or intrinsic defects) to produce p-n junction. These junctions promote the charge separation and

collection at their interfaces [163]. The heterojunction can occur along the diameter (i.e. radial junction) or length (axial junction) of the nanowire or at the substrate interface (planar junction). The junction can induce a chemical potential difference that causes electrons and holes to move in opposite directions to allow for carrier collection [163].

In this work, p-n heterojunctions composed of n-ZnO and other p-doped materials (such as p-Si substrate, p-Si nanowires, p-NiO) were fabricated, as alternatives to overcome the difficulty in the reproducible growth of high quality, stable, and controllable p-type ZnO [164].

4.3.1 Planar Heterojunctions

4.3.1.1 Planar n-ZnO film/p-Si (substrate) heterojunction

Planar n-ZnO/p-Si heterojunctions were fabricated by deposition of n-ZnO thin films by a variety of deposition techniques like ALD and DC-sputter annealing, on a p-doped Si wafer. The details and the optimization of deposition process were discussed above in section 4.1.1.

4.3.1.2 Planar p-NiO film/n-Si (substrate) heterojunction

NiO is a promising semiconductor material for optoelectronic applications such as light emitting diodes, photodetectors, and solar light activated gas sensors. The p-NiO/n-Si heterojunction diode was fabricated by DC-sputtering of a Ni metal film on n-doped Si wafer followed by a post annealing in air.

XRD patterns of deposited films post-annealed at 500 °C reveal the formation of p-NiO, as shown in figure 41c. The post-annealing temperature used was held at 500 °C as requirement for device fabrication as well explained later. Oxygen plasma treatment of the as-deposited NiO films does not show better crystallinity which can be caused due to the physical ablation effect of the oxygen plasma on the surface of the NiO films. The cross sectional-SEM image of p-NiO film confirms the deposition of p-NiO films with thickness of 160 nm (see figure 41b).

The electrical as well as the functional properties of the planar p-NiO film/n-Si (substrate) heterojunction will be discussed in detail in chapter 5.

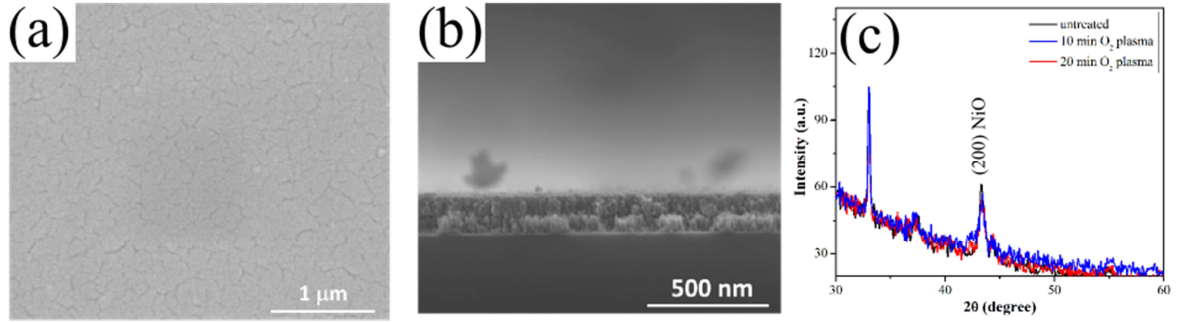


Figure 41: Top- and cross sectional- SEM view of p-NiO/n-Si heterojunction (a, b) and its corresponding XRD pattern (c).

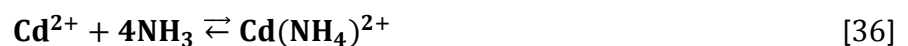
4.3.1.3 Planar ZnO nanowires/p-Si (substrate) heterojunction

The ZnO nanowires were grown on p-Si wafer with a ZnO seed layer. The structural properties and synthesis details were described before in section 3.1.1 and their electrical and optical properties as well functional characterization will be given in the next chapter.

Surface modification of ZnO nanowires/p-Si (substrate) heterojunction

CdS is used as sensitizer to decorate the as-grown ZnO nanowires, because its relatively narrow bandgap (2.42 eV) enables light harvesting in the visible light region [165]. This modification is necessary since the absorption of bare ZnO, which is a typical wide band gap semiconductor (3.37 eV), occurs in the UV region (i.e. $\lambda < 400$ nm) [166].

CdS nanoparticles (NPs) were deposited on ZnO nanowires via chemical bath deposition (CBD) by using an aqueous solution of cadmium salt (CdSO_4), aqueous ammonia (as a complexing agent), and thiourea ($(\text{NH}_2)_2\text{CS}$, as a sulfur source). The decoration density of CdS NPs was controlled by the time of CBD process. The general reaction pathway for the CdS formation can be described as follows [138]:





By dissolving ammonia in water two equilibrium reactions can take place (equations 35 or 36) where OH^- ions are produced as well as cadmium tetraamine complex is formed. Meanwhile, thiourea decomposes and generates free sulfide ions (equations 37 and 38). CdS can be formed either by an ion-by-ion mechanism (equation 39) or a hydroxide cluster mechanism (equations 40 and 41), or by both mechanisms [138].

The SEM images in figure 42 show the deposition of CdS NPs by heterogeneous nucleation on ZnO nanowires by CBD method for 10, 20 and 60 min deposition times. As can be observed from SEM images, after 10 min deposition time, only few nanoparticles were deposited on the surface of one ZnO nanowire and size and density of the CdS NPs are increasing for 20 min deposition. After 60 min deposition of CdS a core-shell structure is obtained where the core of n-ZnO nanowire is fully covered with a shell of CdS NPs. Similar behavior were observed by Li *et al.* for CdS deposition on TiO_2 surface [167]. The EDX analysis shown in figure 42d for 10 and 60 min deposition time reveal the characteristic peaks corresponding to elements of Zn, O, S, and Cd. The atomic ratio of Cd/S was almost 1 which confirms the formation of CdS nanoparticles.

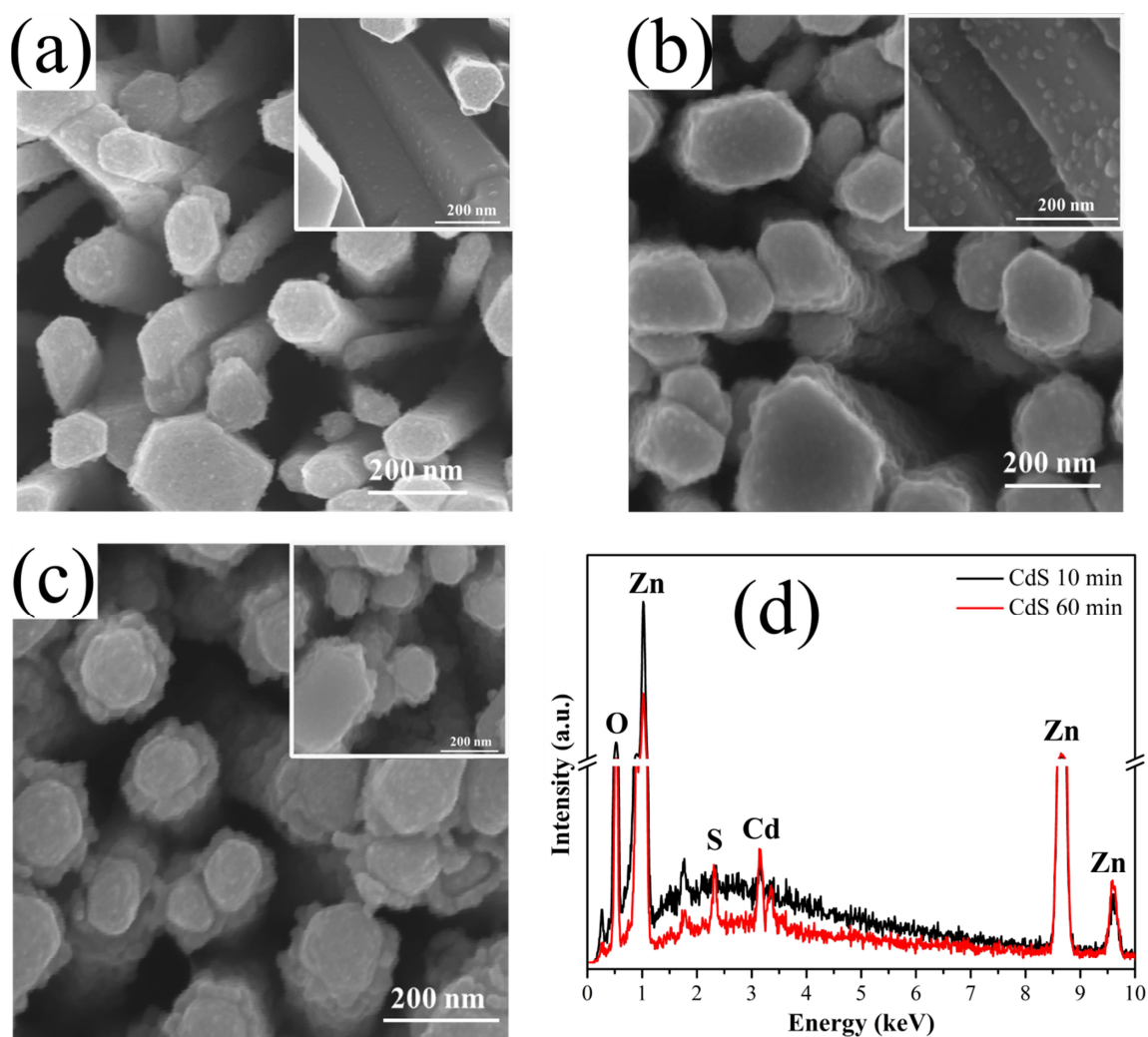


Figure 42 SEM micrographs of CdS NP/ZnO nanowires heterostructure arrays deposited at 60 °C for different times of (a) 10 min, (b) 20 min, and (c) 60 min, respectively. (d) EDX spectra of samples deposited at 10 and 60 min.

4.3.2 Radial Heterojunctions

Radial heterojunctions have superior properties including optical properties (such as optimal light absorption, low reflection of the sun illumination spectrum), and electrical properties (e.g. efficient free carrier collection) as compared to their conventional planar p-n junctions [168]. This can be attributed to their high surface/volume ratio and geometry characteristics as will be discussed later [168].

4.3.2.1 ZnO/p-Si NWs radial heterojunction and their modifications

The radial p-n heterojunction based on Si NWs and ZnO are expected to show better performance in solar cell applications, when compared the n-ZnO/ p-Si planar heterojunction. As their geometry enable a decoupling of the requirements for light absorption and carrier extraction into orthogonal spatial directions. Each individual radial junction could be long in the direction of incident light, allowing for optimal light absorption, but thin in another dimension and thus allowing an effective carrier collection [163,168].

Radial n-ZnO/p-Si heterojunction

ZnO films were deposited on the Si NWs by using ALD and DC-sputtering and annealing techniques. The SEM images (see figure 43) of ZnO/p-Si NWs heterojunctions show the conformal coating of ZnO on the Si NWs of the ALD deposited film over the DC-sputtered film.

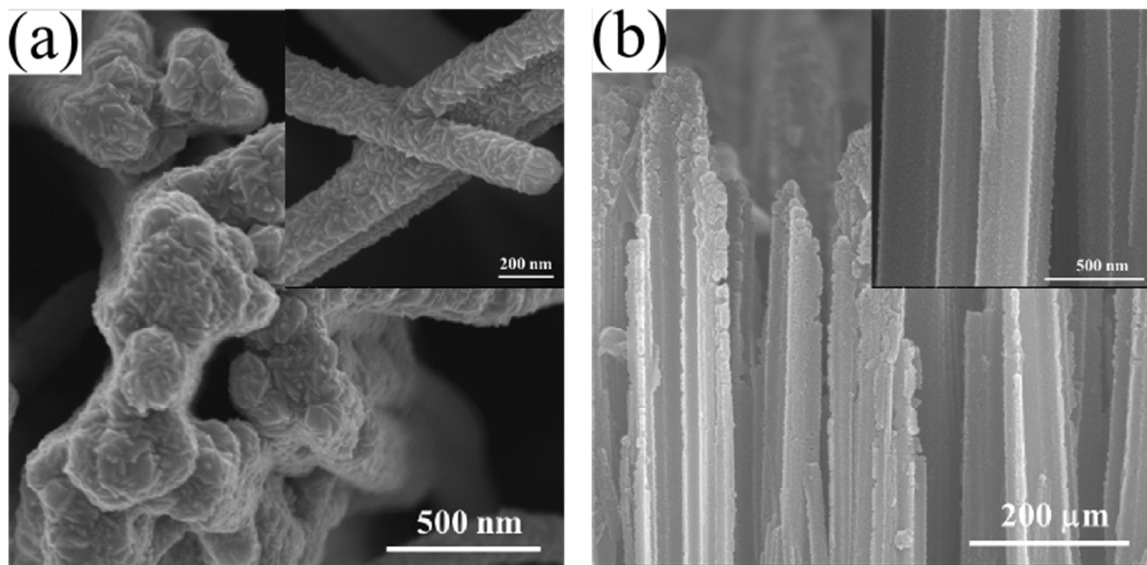


Figure 43 SEM image of n-ZnO film deposited by (a) ALD and (b) DC-sputtered/annealed techniques on p-Si NWs to form radial p-n heterojunction.

XRD pattern of n-ZnO deposited by ALD technique on p-Si NWs (figure 44a) shows the predominant growth of Si NWs along the (100) direction flanked by distinctive minor peaks in the 30°-40° range ascribable to the wurzite phase of polycrystalline ZnO film. The intensity of ZnO peaks indicated good crystallinity of the film, which was enhanced by a post-annealing

treatment at 500 °C in air. The TEM image of the ALD deposited ZnO film on Si NWs is shown in figure 44b, it can be seen that ZnO film is crystalline and anchored to the surface of the core Si NW with a thickness of ~ 60 nm.

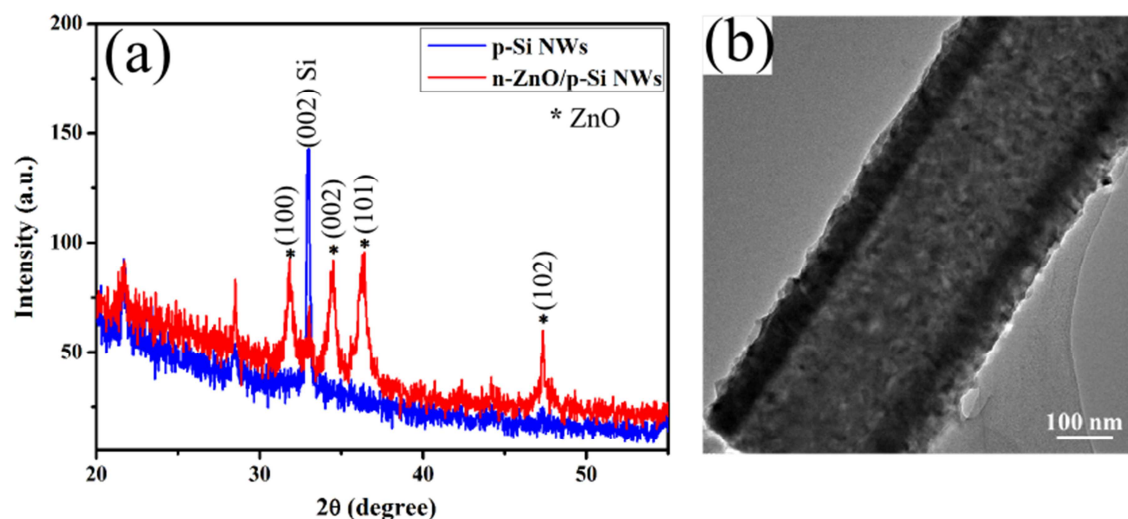


Figure 44 (a) XRD pattern of n-ZnO film deposited by ALD technique on p-Si NWs and the etched p-Si NWs. (b) TEM image of n-ZnO film deposited by ALD technique on p-Si NWs.

Controlled shell thickness of the radial heterostructures allows the control over their optical and electrical properties. This can be achieved by controlling the number of the ALD deposition cycles. In addition to the fact that the elementary components existing in the EDX spectrum are only Zn, O, and Si; it can be noticed that the intensity of the Si peak is decreasing with increasing the number of ALD deposition cycles, which is an indication for the increment in the shell thickness. The EDX spectroscopic mapping of the ZnO shell with thickness of about 20 nm (100 ALD deposition cycles) on the p-Si NW core is shown in figure 45 (d-f); these figures correspond to the SEM image shown in figure 45c. The characteristics peaks of zinc [Zn (L)], oxygen [O (K)] and silicon [Si (K)] appear and it is clear that Zn, O and Si atoms are concentrated in the whole area of nanowire. These analyses confirmed that the coaxial nanowires have a closed ZnO shell and a Si core, respectively and they also reveal the good coverage of ZnO shell on the Si NWs surface.

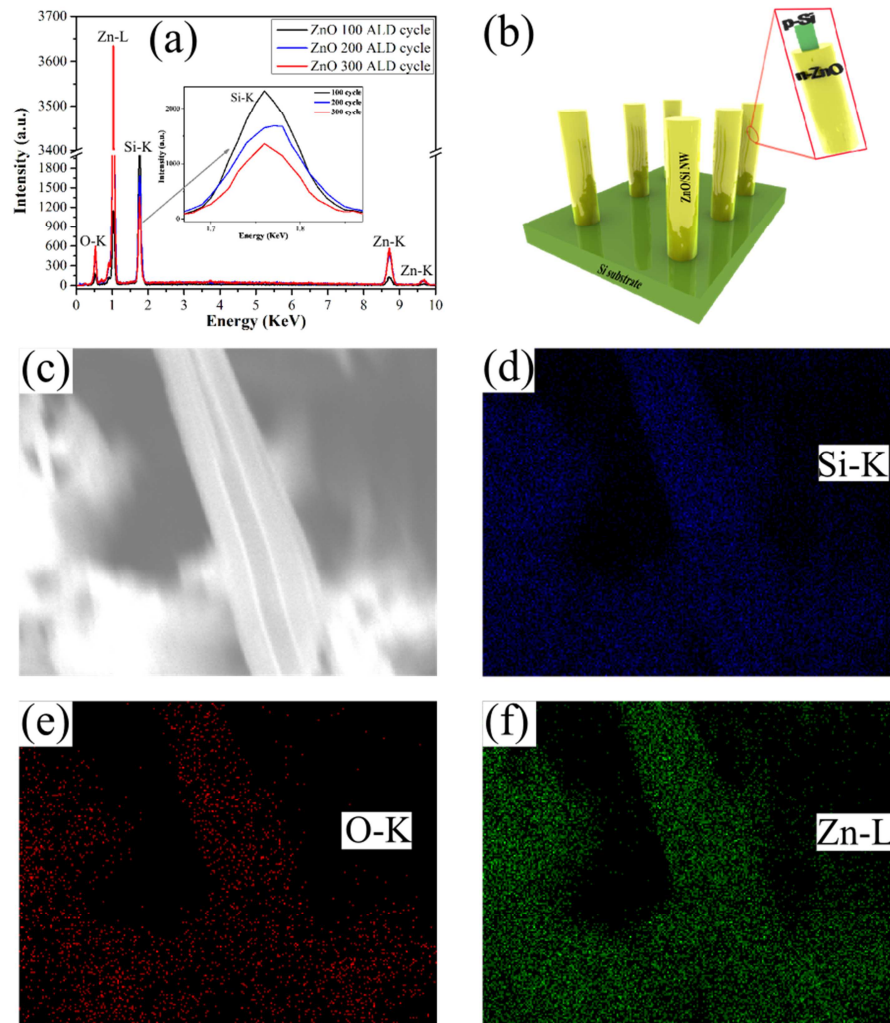


Figure 45 (a) EDX analysis of n-ZnO shells with different thicknesses on p-Si nanowires. (b) a schematic illustration of radial n-ZnO/p-Si NWs heterojunction. (c-f) EDX spectroscopic mapping of ZnO (shell) deposited with 100 cycles of ALD on p-Si NWs (core).

Surface modification of n-ZnO/p-Si NWs heterojunctions

The modification and integration of nanowires in desirable fashion is still a challenging avenue. Surface modifications and compositional tuning of produced heterostructures was used to achieve the desired properties required for energy harvesting applications. The solar light harvesting efficiencies can be improved by extending the light absorption of ZnO/p-Si NWs into the visible light region of the sun spectrum.

- **CdS@n-ZnO/p-Si NWs**

The n-ZnO/p-Si NWs were modified by deposition of CdS NPs on their surface to enable visible light harvesting, which is required for solar light activated gas sensors as well as for other optoelectronic applications.

The SEM images show that uniform decorations of CdS NPs on the n-ZnO surface were achieved with control over the coverage densities of the nanoparticles on the surface (see figure 46 (a, b)). It can be seen that for longer deposition times of CBD (120 minutes, figure 46c), the ZnO layer is totally etched during the CBD process and big agglomerated of CdS NPs are formed on Si NWs. The etching of ZnO during the CBD was reported before and it can be attributed to its amphoteric nature, as it can react with both acidic and basic solutions and dissolve. Since the CdS deposition solution is highly basic, therefore, the *in situ* etching of the ZnO can take place during the deposition reaction [138].

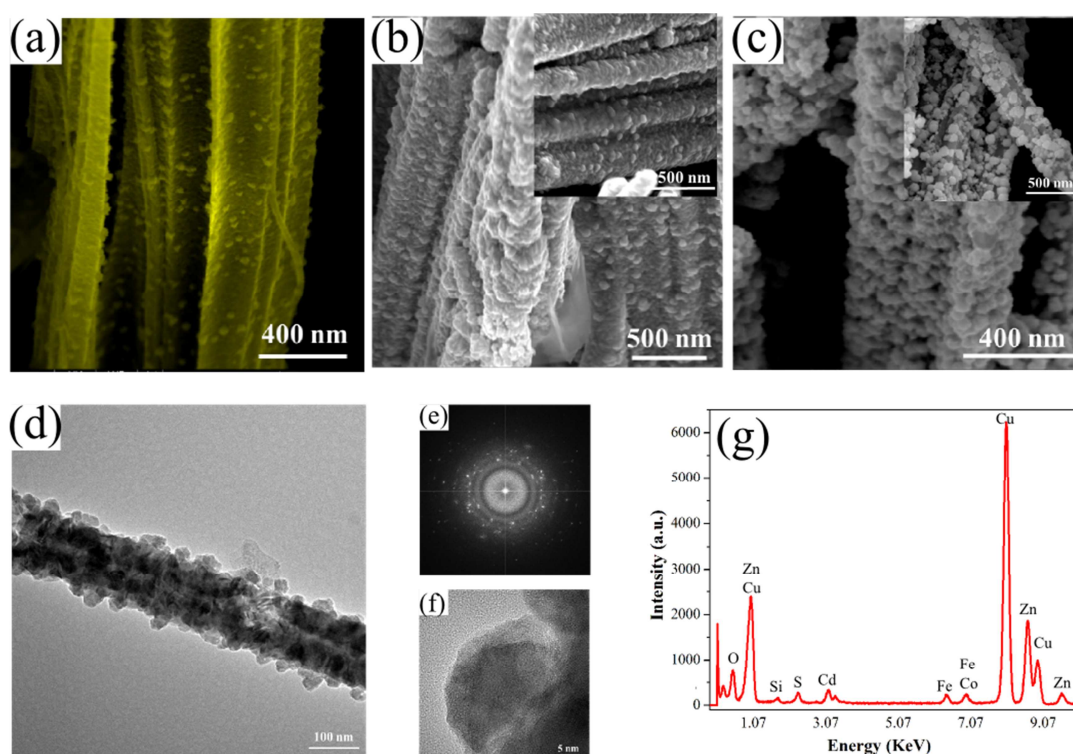


Figure 46 Cross-sectional SEM images of CdS deposited by CBD on ZnO/p-Si heterojunction at 60 °C for (a) 10, (b) 25, and (c) 120 min respectively. (d) TEM, (e) FFT, (f) HRTEM images, and (g) TEM-EDX spectrum of CdS deposited for 25 min on ZnO/p-Si heterojunction.

- **ZnS@ZnO/pSi NWs**

Complex heterostructures extend the solar light absorption range for optoelectronic applications. A proper engineering of the interfaces of complex heterostructures can promote efficient photo-induced charge carrier excitation and enable their transfer through energetically aligned interfaces [169].

ZnS is a wide band semiconductor with a bandgap of 3.66 eV at room temperature [170]. ZnS is used as a buffer layer between light absorber (like CdS) and ZnO to reduce recombination of electrons in the ZnO with holes in the absorber by introducing a potential barrier [171]. In this work, ZnS/ZnO heterostructures were synthesized by a simple sulfidation conversion of ZnO. In the reaction system, thioacetamide (TAA) as S source hydrolyzes and releases H₂S under 90 °C, and then H₂S reacts with ZnO surface to form ZnS [139]. The SEM image in figure 30 a shows the ZnO shell with smooth surface and sharp edges. Figure 47b shows that after conversion of ZnO to ZnS the nanowire surface became rougher, indicating the formation of a ZnS shell on the ZnO. The TEM image further confirmed the formation of a thin layer of ZnS on the surface of ZnO.

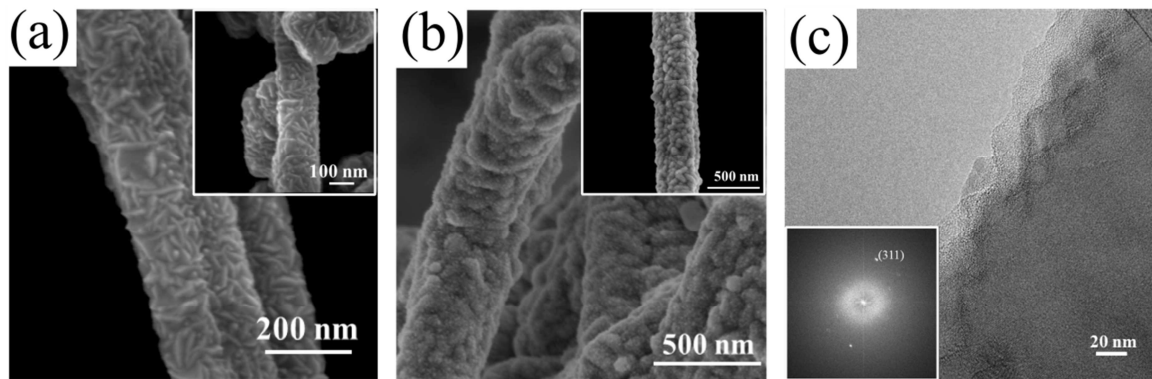


Figure 47 (a) SEM image of the n-ZnO/p-Si NWs heterojunction. (b) SEM and (c) TEM (inset image is the FFT pattern) of ZnS@ZnO/p-Si NWs heterojunction.

- **CdS/ZnS@n-ZnO/p-Si NWs**

Besides the expected charge separation improvement at the interface of CdS and ZnO by using a thin interlayer of ZnS film, it can clearly be seen from the SEM observations (see figure 48) that the solution pretreatment of the ZnO nanowires with a sulfide solution to form a thin ZnS

shell on ZnO surface is found to improve coverage and uniformity of the CdS NPs deposited by CBD method. The increase of the density of CdS NPs on the surfaces of ZnO nanowires will result in an increase in the visible-light absorption and therefore the efficiency of their devices.

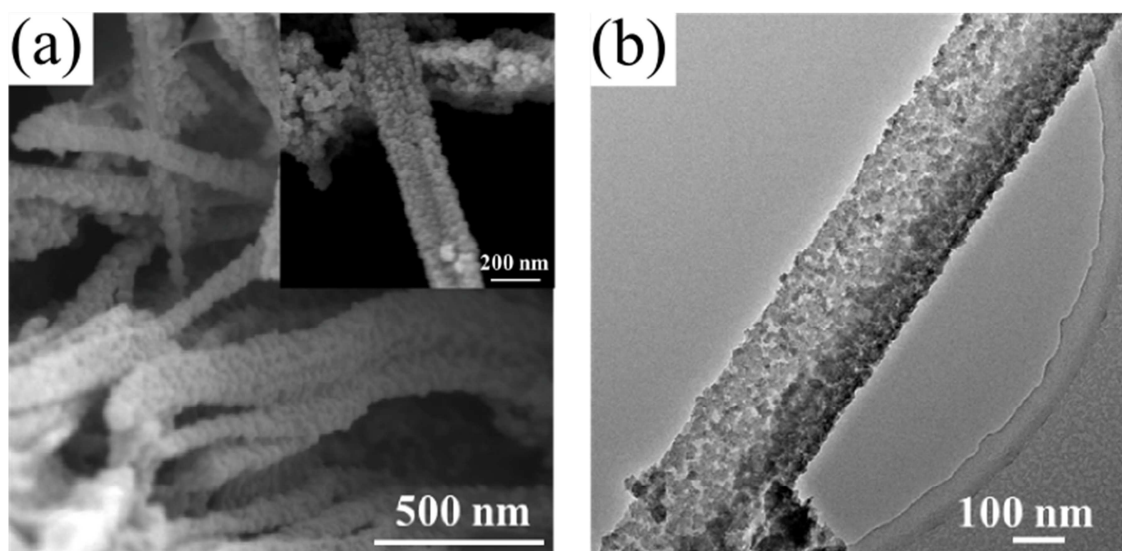


Figure 48: SEM (a) and TEM (b) images of CdS NPs deposited by CBD at 60 °C for 25 min on ZnS@ZnO/p-Si NWs heterojunction.

4.3.2.2 Three dimensional (3D) radial CdS@n-ZnO/p-Si NWs heterostructures

As previously mentioned, well-defined 1D nanostructures and their hetero-architectures are at the heart of building blocks for future nanodevices with multifunctional characteristics. The integration of these simpler 1D nanoscale building blocks, e.g. nanowires, into hierarchical 3D nanostructures, through a secondary engineered growth, can significantly enhance their electrical and optical, and functional properties. Such complex 3D architectures may benefit applications that require higher specific surface and porosity [172]. The rational synthesis of 3D nanostructures with controlled structural complexity will enable the design of smaller devices with enhanced functionalities.

Fabrication of 3D heterostructures and their modification

In this work [151], 3D heterostructures of ZnO NWs/p-Si NWs were fabricated through a two-step process. Firstly, a ZnO seed layer were deposited, either ALD or DC-sputtering techniques, on the wet-etched p-Si NW backbone, followed by a hydrothermal synthesis of ZnO NWs branches on the seeded Si NWs. The cross sectional SEM images indicate the growth of branched ZnO NWs on ALD deposited seed layer perpendicular to their Si NWs backbone. The length of the n-ZnO NW branches is adjustable by controlling the growth time of the hydrothermal process as can be seen in figure 49 (a-d), while the diameter is around 35-70 nm.

Furthermore CdS NPs were deposited on the 3D heterostructures of ZnO NWs/p-Si NWs by chemical bath deposition to enable their solar light absorption capabilities. SEM images in figure 49 (e, f) confirm that CdS NPs were deposited uniformly on the surface of ZnO branches.

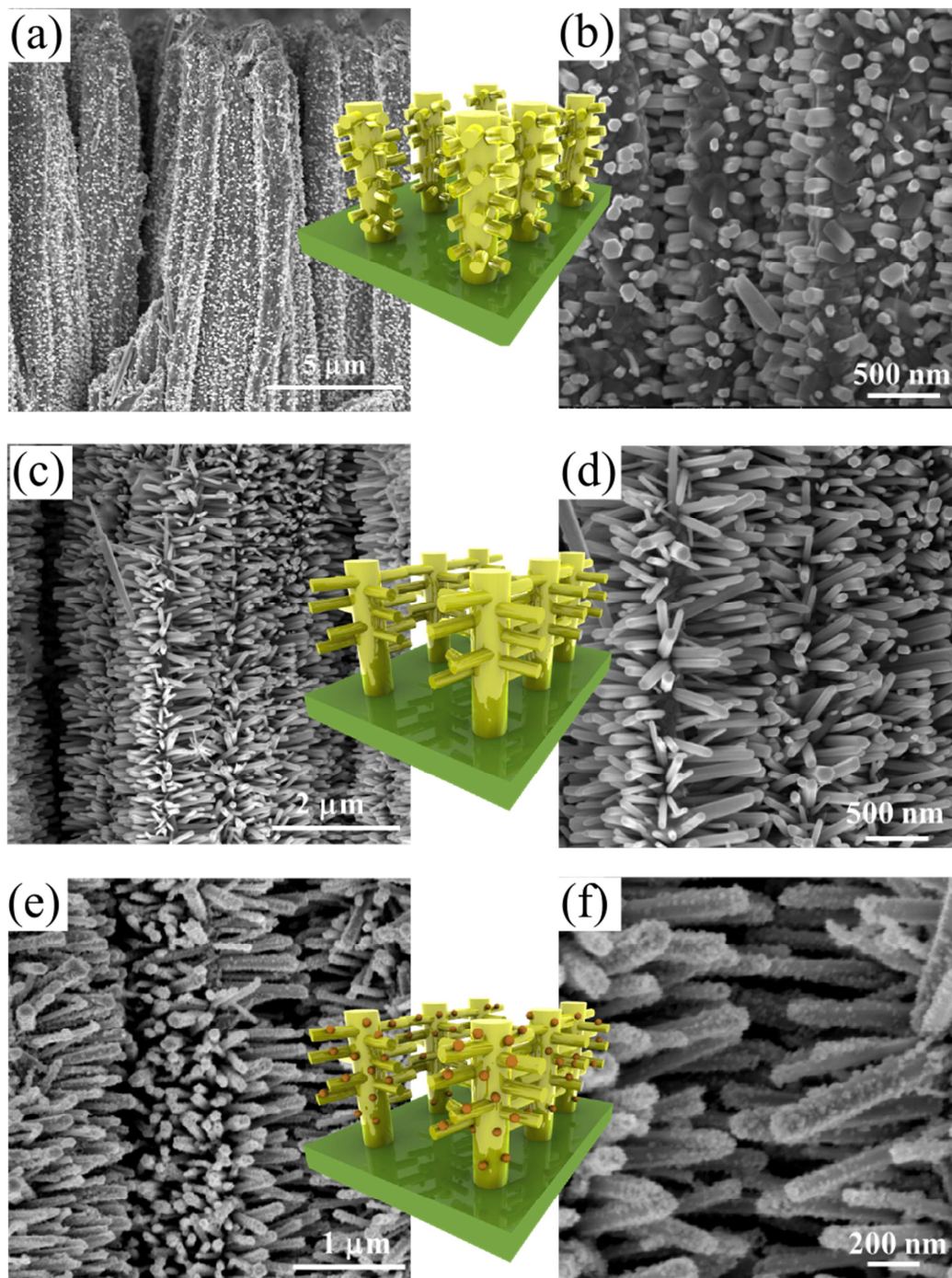


Figure 49 Cross-sectional SEM images of 3D ZnO NWs branches grown by hydrothermal growth for (a, b) 4h, (c, d) 20h, and (e, f) CdS NPs decorated 3D ZnO NWs branches grown by hydrothermal synthesis for 20h.

The electrical characterization of 3D radial heterojunctions based on n-ZnO NWs/p-Si NWs

Recently there is a growing interest in the fabrication of 3D hierarchical nanomaterials, as they possess unique optical and electronic properties due to their substantially enhanced surface areas [172–174]. However, studying the electrical properties of such systems in correlation to the 3D structural complexity of their geometries is still lacking. The investigation of their electrical properties is a key point in the rational design of such complex nanostructured and their integration in functional devices.

A prototype device was designed to test the intrinsic electrical properties of the 3D heterojunctions by using conductive glass (F:SnO₂, FTO) as a transparent top contact on the n-ZnO NW shell whereas the p-Si backside was contacted with silver paste.

From the capacitance-voltage measurements, by plotting the inverse squared of the junction capacitance against the applied reverse voltage, the donor density (N_D) of the n-doped material (i.e. ZnO) can be extracted. For ideal p-n diode, the capacitance (C) per unit area can be expressed as [175]:

$$\frac{1}{C^2} = \frac{2(N_A \epsilon_1 + N_D \epsilon_2)}{q N_D N_A \epsilon_1 \epsilon_2} (V_{bi} - V) \quad [42]$$

where N_D is the donor density of the n-doped material (ZnO), N_A is the acceptor density in p-Si NWs, ϵ_1 and ϵ_2 are the dielectric constants of n-ZnO and p-Si, respectively, q is the charge on the carriers, V_{bi} is the built-in potential of the p-n diode and V is the applied bias voltage.

The slope of $1/C^2$ - V plots can be used to calculate the donor density of ZnO (N_D) according to equation 42. Figure 50 shows the capacitance-voltage (C-V) measurements of 3D ZnO NWs/p-Si NWs heterojunctions (Mott-Shottky plot) with different n-ZnO NWs branches lengths. $1/C^2$ vs. voltage plot displayed a linear behavior which confirms the formation of a p-n heterojunction diode at the n-ZnO NW/p-Si NW interface. The value of donor densities (N_D) for smaller branches of about 100 nm length was determined as $1.15 \times 10^{19} \text{ m}^{-3}$ and by increasing the branches length the donor density decreases to $1.02 \times 10^{19} \text{ m}^{-3}$ and with further increase of the branches length, the value continues to decrease to $N_D = 1.01 \times 10^{18} \text{ m}^{-3}$. Donor density values in order of 10^{17} -

10^{19} m^{-3} were typically observed in ZnO nanowires [176,177]. From these findings it is evident, that the donor density of n-ZnO (which is related to the oxygen vacancies) can be tuned by varying the length of 3D ZnO branches and is found to decrease with increasing growth time, which might be attributed to the decrease in the defects and the increase in crystallinity.

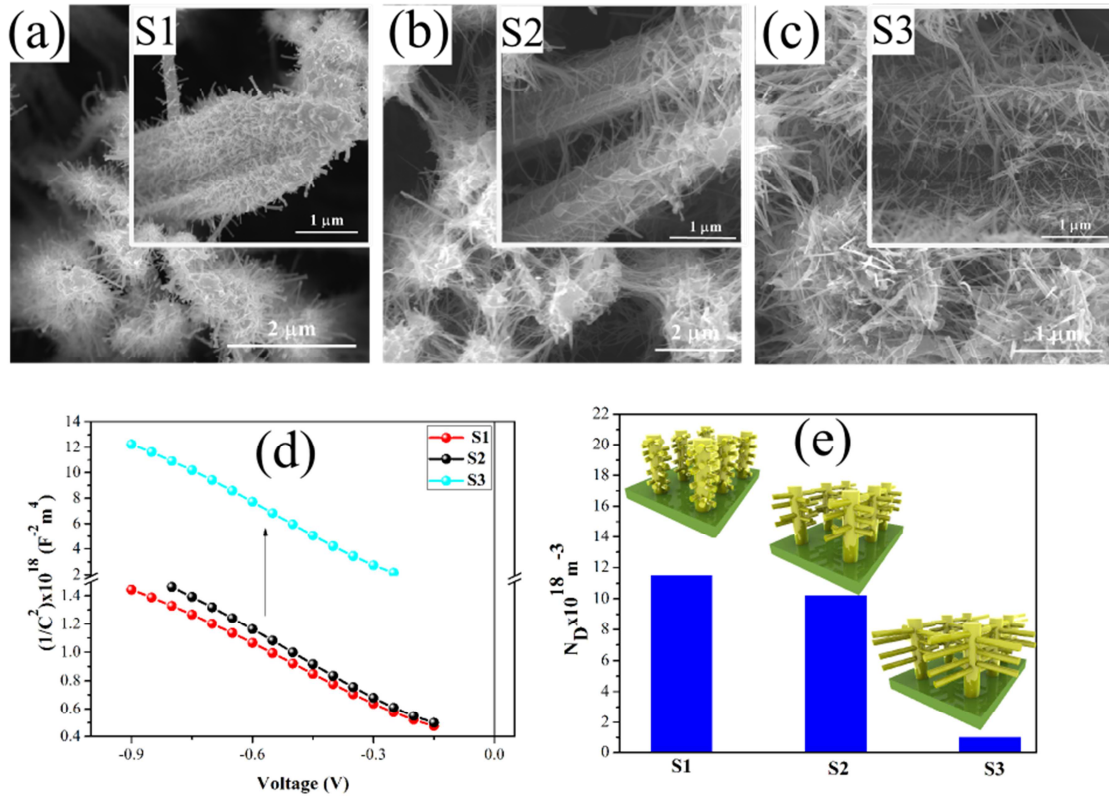


Figure 50: SEM images of 3D ZnO NWs branches grown by hydrothermal method for (a) 4h (S1) (b) 20h (S2) and (c) 40h (S3). (d) Capacitance-voltage measurement. Mott Schottky plots ($1/C^2$ vs. V) of n-ZnO/p-Si nanowires acquired at 1 MHz in the reverse bias region for samples S1 and S2, and S3 and (e) their calculated donor densities (N_D).

4.3.2.3 p-NiO/n-ZnO NWs radial heterojunction

ZnO is an n-type semiconductor that is usually deposited on a variety of p-type materials, such as GaN, Si to form p-n heterojunctions. NiO is p-type wide band gap semiconductor that has a low lattice mismatch with ZnO which is fabrication key requirement for the formation of material interfaces with low lattice stress and thus, a lower defect density or dislocations in this area of the p-n heterojunction. ZnO NWs were directly synthesized on conductive glass (F:SnO₂,

FTO) as a transparent substrate by the hydrothermal route followed by a deposition of p-NiO thin film by DC-sputtering of Ni followed by thermal annealing.

The SEM images shown in figure 51a reveal the growth of highly uniform and well oriented ZnO nanowires with a diameter of 140-160 nm.

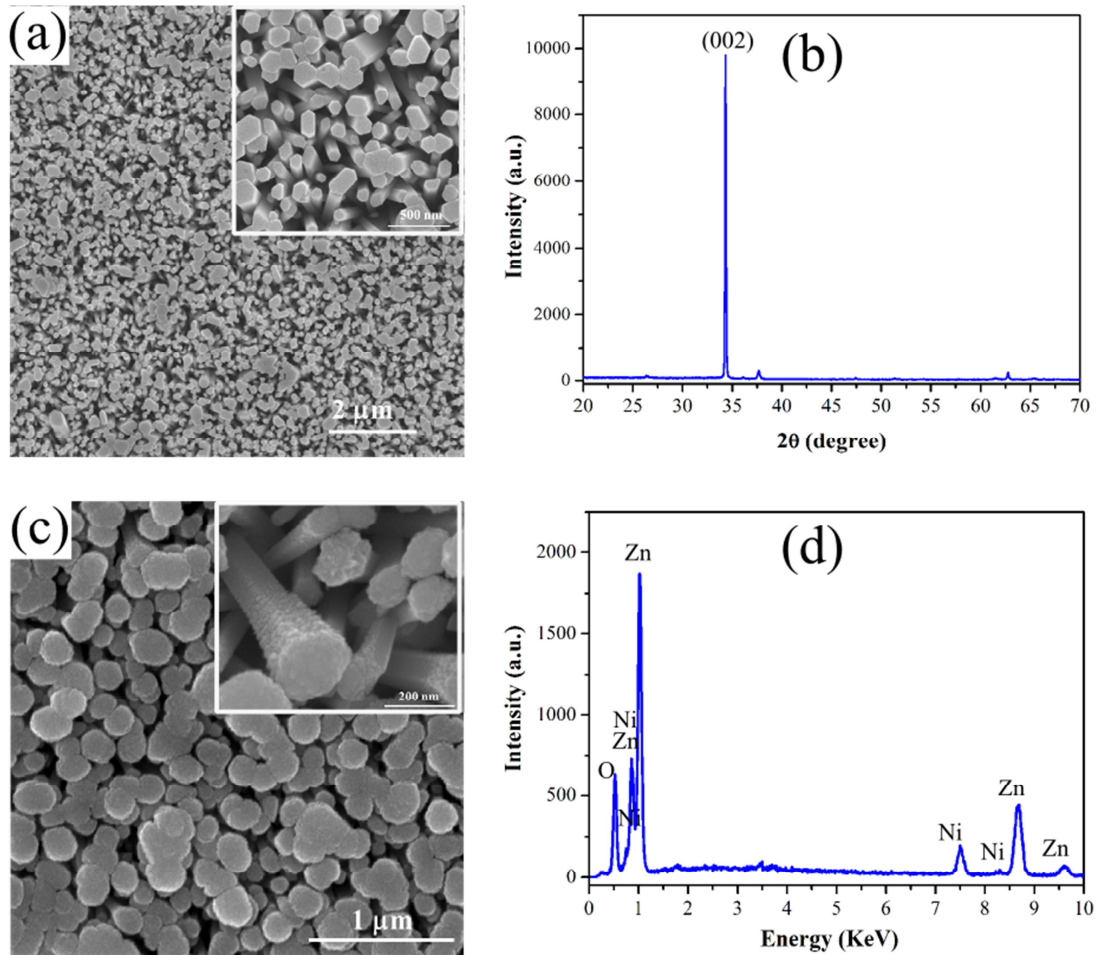


Figure 51 (a) SEM image and (b) XRD pattern of ZnO nanowires on FTO substrate. (c) SEM image and (d) EDX spectra of p-NiO/n-ZnO nanowires [151].

The XRD pattern (figure 51b) indicates the presence of hexagonal wurtzite ZnO with a preferential (002) c-axis orientation perpendicular to the FTO substrate. The uniform coating with NiO film can be seen from SEM image in figure 51c. Additionally, the observed elementary components in the EDX spectrum are only Zn, O, and Ni (see figure 51d)

The current-voltage (I-V) curve of the p-NiO/n-ZnO NWs heterojunction measured in dark condition shows a typical rectifying diode behavior and very low leakage current of the formed p-

NiO/n-ZnO junction (see figure 52a). The threshold voltage of the p-n junction is about 1 V in forward bias. The capacitance-voltage (C-V) measurements were performed and shown in figure 52b. $1/C^2$ vs. voltage plot displayed a linear function of bias which indicating the successful formation of a p-n heterojunction at the p-NiO/n-ZnO NWs interface.

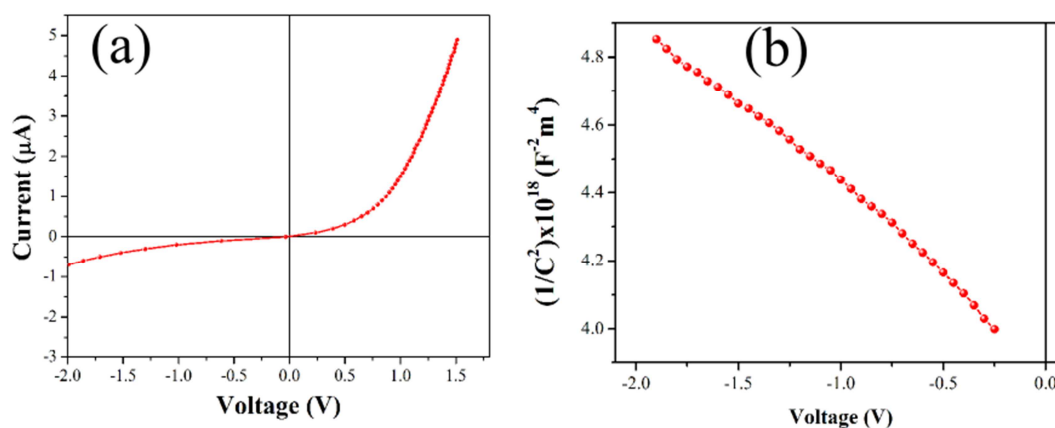


Figure 52 (a) I - V characteristics of p-NiO/n-ZnO NWs heterojunction under dark conditions and (b) the Capacitance-voltage measurement. Mott Schottky plots ($1/C^2$ vs. V) of n-ZnO/p-Si nanowires acquired at 1 MHz in the reverse bias region [151].

5. Self-Powered Solar Diode Sensors (SP-SDS)

Spiraling energy requirements place a demand on using the renewable energy resources more efficiently and developing new platforms of green technologies. Fabrication of intelligent devices based on functional nanomaterials that can harvest energy required to run the device through functionalities embedded in the system are currently required.

Low power consumption, low operating temperature and cost effective production are the most challenging issues in gas sensor technologies [178], the device architecture presented here has been designed to palliate such issues. The conductometric gas sensors made of semiconductor metal oxides are among the most commonly used gas sensors in market due to their low costs and high robustness [19]. The energy needed to operate such gas sensors are supplied either in form of thermal heating or light to activate the analyte gas/ metal oxide chemical interaction. In addition to the traditional activation of metal oxide surface by thermal heating, recently UV light is also used to activate the sensor response at room temperature conditions [36,179,180]. The requirement of a UV light source to generate excitons in the wide band gap of common metal oxides is a difficulty for commercializing such approach.

Recently much research efforts have been devoted to the development of self-powered nanodevices that are capable of harvesting renewable energies such as solar and mechanical energies and converting them into electricity. Nevertheless, the current concept of self-powered nanodevices is based on coupling an external energy harvesting unit, such as a solar cell or piezoelectric nanogenerator, with the functional nanodevices to meet the demand for the self-sustained operation [89,93,181,182]. In all these cases, the powering solution manifested the integration of different macroscopic functional units and the challenge associated with the assembly of complementary functionalities, such as powering and sensing units at the nanoscale, are inherent difficulties of this concept. An innovative approach, namely solar diode sensor (SDS), has been developed to realize a real self-powered gas sensor that is autonomously operated with no additional need of other powering devices [183,184]. The solar diode sensor (SDS) is based on the integration and correlation of complementary functionalities originating from multiple junctions in a singular nanostructure. In this work, the gas sensing and solar energy harvesting abilities of metal oxide semiconductors were utilized to deliver a self-sustained gas sensing signal without any external power sources.

5.1 Solar diode sensor (SDS) based on CdS@ZnO nanowires/p-Si heterojunction

One dimensional ZnO nanostructures such as nanorods or nanowires are highly sensitive gas sensor materials compared to their bulk counterparts due to their high surface to volume ratio [185]. The heterojunctions based on n-ZnO/ p-Si substrates are interesting for applications such as solar cells or photodiodes due to their good photon-to-electron conversion efficiency [186–188]. The deposition of a narrow band gap sensitizer such as CdS (2.4 eV) [189] on the surface of a wide band gap semiconductor such as ZnO (3.37 eV) [190], is found to extend the photo-response of the heterostructure into the visible-light region [32,80,191–193].

The potentials of the aforementioned systems was the base to fabricate a new combinatorial complex architecture of CdS@n-ZnO/p-Si which is based on the synergetic overlap between a photo-activated gas sensing unit (CdS@n-ZnO) with a p-n heterojunction (n-ZnO/p-Si) capable of harvesting the energy required to operate the sensor from the environment.

5.1.1 Structural analysis of the system and the prototype device fabrication

The detailed structural properties of CdS@ZnO/p-Si were discussed before (see section 4.3.1). In brief, a seed layer of about 20 nm of ZnO was deposited by the DC-sputtering/annealing technique, as it has the preferred growth orientation to grow well aligned ZnO nanowires, on a p-Si substrate. In a second step, ZnO nanowires were grown by a modified hydrothermal method, by adding aluminum-iso-propylate to provide a sustainable support for the preparation of long length and high aspect ratio nanowires, at 75°C for 20 h on the top of deposited ZnO seed layer. ZnO nanowires (ca. 150 nm) were vertically aligned with uniform size and areal density of $\sim 20/\mu\text{m}^2$ and this was more confirmed by the XRD which reveals that the as-prepared nanowire arrays had a wurtzite ZnO structure with vertical orientation along the c-axis.

The surface decoration of ZnO with CdS NPs as a narrow band gap semiconductor was achieved by chemical bath deposition (CBD), in which a direct growth of the CdS NPs on the electrode surface by chemical reaction of ionic species is taking place [194,195]. The advantage of using CBD is that it produces high surface coverage of CdS with good anchoring to the surface of ZnO, which is needed to enhance the charge separation at the CdS/ZnO interface and to also minimize the surface trapping and consequently losses due to charge recombination [196]. The aforementioned features of CBD are very crucial for gas sensing application. In this regard, CdS

NPs were deposited by CBD method for 15 min, SEM images, shown in figure 53 (a, b), demonstrate a particular and uniform assembly of CdS NPs on the surface of ZnO. The homogenous decoration of CdS NPs was further confirmed by TEM analysis shown in figure 53 d. CdS NPs with average diameters of 10 -20 nm were deposited on surface of ZnO nanowires. The coverage density of CdS was carefully chosen, by controlling the CBD deposition time as discussed previously in section 4.3.1, to ensure that the surface of ZnO is not fully covered by CdS. The low coverage density (ca. 11 %) of CdS on ZnO allows the existence of partial uncovered surface of ZnO that can be exposed and react with different gas molecules. The CdS/ZnO interface quality was demonstrated as shown in the inset of figure 53d, the HR-TEM image reveal a coherent ZnO-CdS interface. The marked spacings of the crystallographic planes correspond to the (100) and (200) of CdS. The EDX analysis showed the characteristic spectra of Cd and S and revealed a Cd/S ratio of 1:1 which additionally confirm the presence of CdS (see figure 42d). The EDX spectroscopic mapping reveal the homogenous coverage of CdS on ZnO, where the characteristic peaks of Cd [Cd (L)], S [S (K)], Zn [Zn (L)], and O [O (K)] appear (see figure 54) .

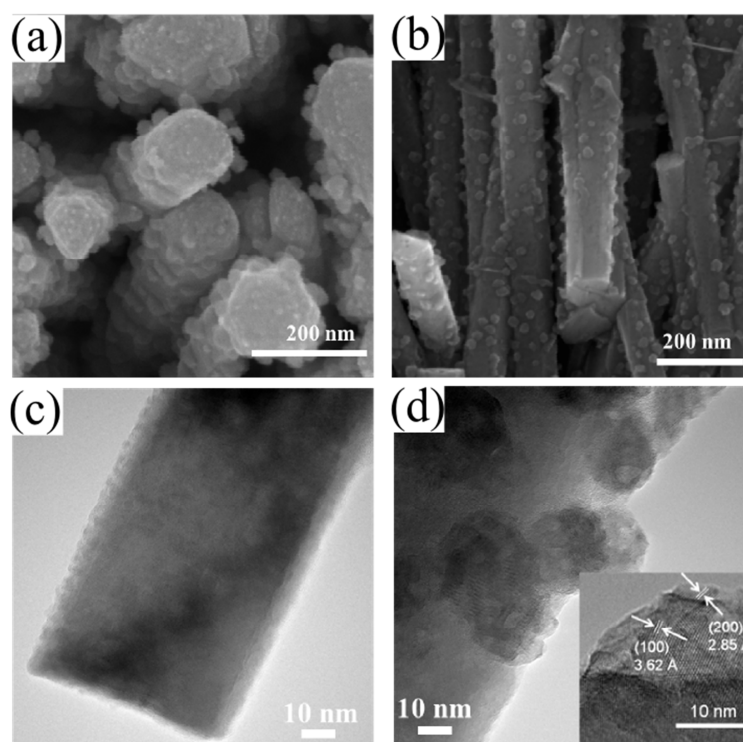


Figure 53 (a, b) In plane and tilt-view SEM images of CdS@ZnO NWS on p-Si substrate. (c) TEM images of ZnO and CdS@ZnO NWs, (d) the inset shows the lattice fringes of a CdS NP decorated on the ZnO surface.

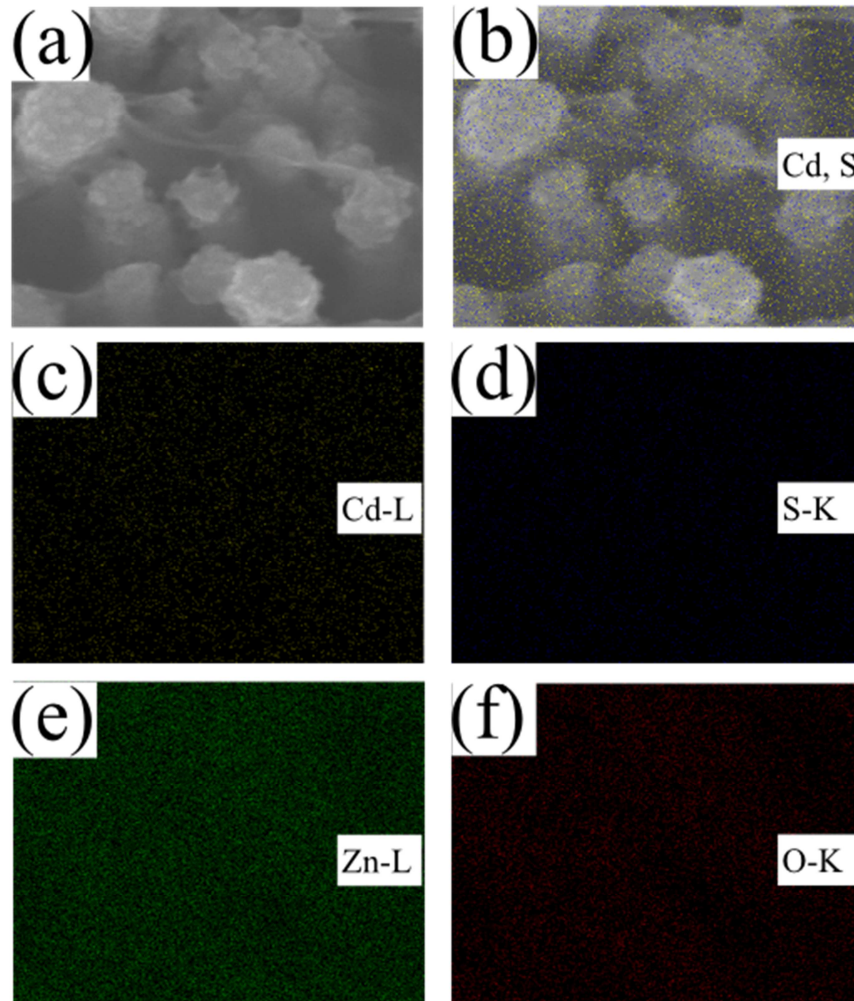


Figure 54 EDX spectroscopic mapping images of CdS NPs/ZnO nanowires.

The prototype device fabrication

Prototype devices were designed to test the corresponding functional properties of CdS@ZnO/p-Si system. As can be seen from the schematic representation in figure 55a, the SDS prototype device were fabricated by using a conductive glass (F:SnO₂, FTO) as a transparent top contact on the vertically aligned ZnO nanowires arrays whereas the p-Si substrate was contacted as the back electrode with silver paste [193]. The different components were contacted mechanically by using conventional metal clamps. The advantage of the current device design is that it does not require any complicated assembly process.

AFM topography measurements were performed in order to investigate the uniformity of the lengths of ZnO nanowires. 2D and 3D AFM plots of the topography of ZnO nanowires, in figure

55 (b,c), reveal that most of the ZnO nanowires exhibit very similar lengths, which was also confirmed by a line scan across the blue line indicated in Figure 55d. This uniformity of ZnO nanowires guarantees a suitable contact between the nanowires and the top electrode (the FTO substrate) that can be further enhanced by the applied mechanical force of the clamps. This is very important to ensure that the SDS device is producing the synergetic effects of its components.

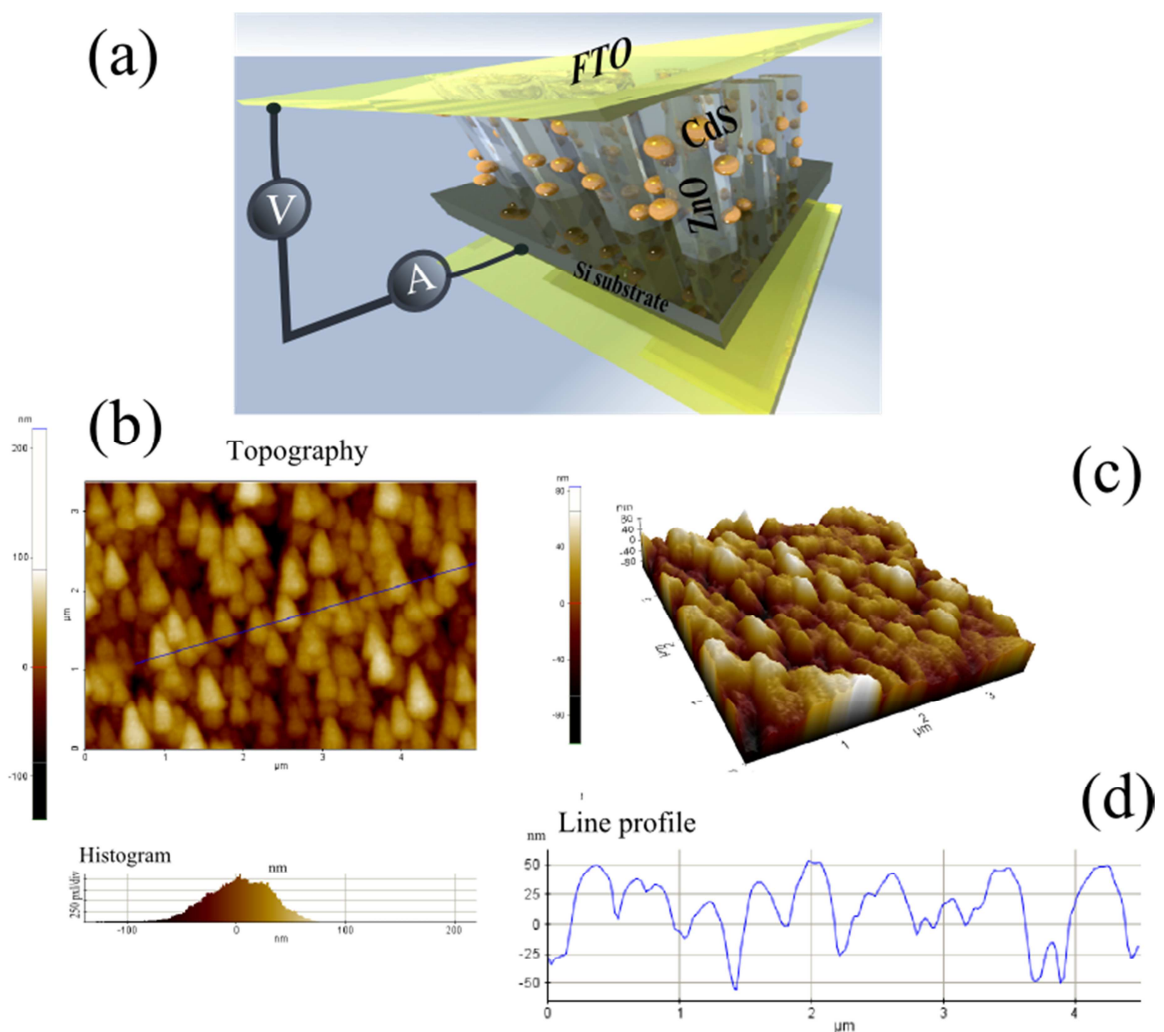


Figure 55 (a) Schematic representation of the SDS device. (b) 2D and (c) 3D plots of the topography of ZnO nanowires measured by AFM in non-contact mode; and (d) a line scan profile corresponding to the blue line in figure b [151].

5.1.2 The electrical and optical characterization of the SDS system

The modification of ZnO nanowires with CdS is expected to modify the optical as well as the electrical properties as CdS extends the absorption spectra of into visible light range. Figure 56a shows the UV–Vis absorption spectra of CdS/ZnO nanowires and naked ZnO nanowires, the optical absorption of CdS@n-ZnO/p-Si sample started from 520 nm whereas the spectrum of naked n-ZnO/p-Si sample is located at 400 nm deriving from the ZnO band gap. CdS and ZnO form a type II heterojunction as shown in figure 56b, where an efficient spatial charge separation of electrons and holes upon photo-generation is promoted. The electrons from the conduction band of CdS will be transferred quickly into the conduction band of ZnO nanowire [77,197].

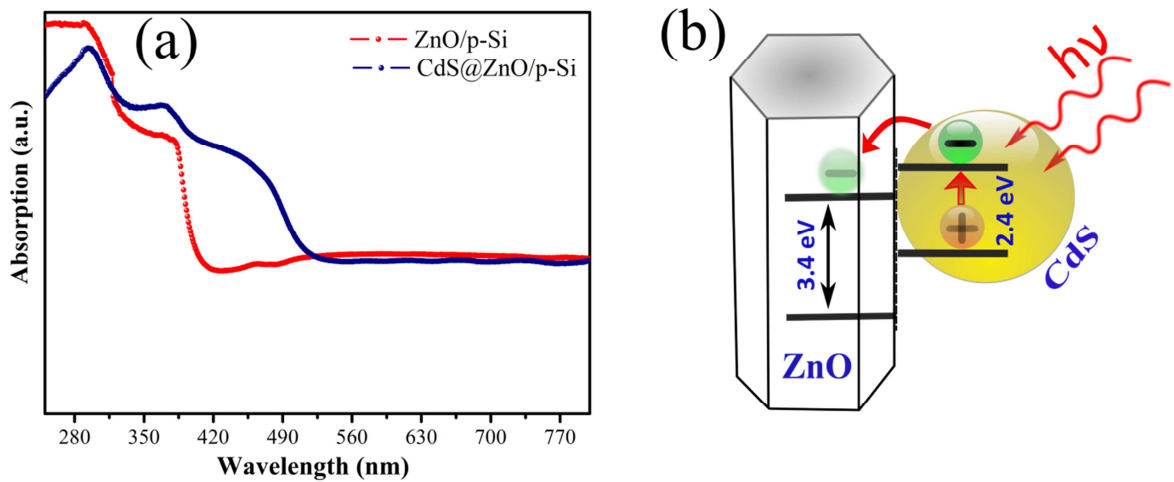


Figure 56 (a) UV-Vis optical absorption spectra of ZnO and CdS@ZnO grown on p-Si substrate (b) schematic diagram showing the energy band structure and electron–hole pair separation in the CdS NP/ZnO heterostructure.

The electrical properties of the prototype SDS device were investigated by testing the current–voltage (I–V) characteristics (see figure 57). The evolution of the I–V characteristics in dark confirmed that the typical non-linear and rectifying diode behaviour, which reveals that the prototype device was successfully fabricated and n-ZnO/p-Si heterogeneous junction is formed. The solar illumination of the device shifts the I–V characteristics to a photovoltaic effect. This indicates that the device is capable of directly transforming sunlight into electrical power. Possibly due to interface defects at the n-metal oxide/p-silicon junction, a shift to more linear behaviour is noticed in the I–V characteristics under illumination, indicating a lower resistance of

the diode under reverse biased conditions. These defects enable a conduction pathway parallel to the reverse biased direction and cause the partial loss of the diode characteristics.

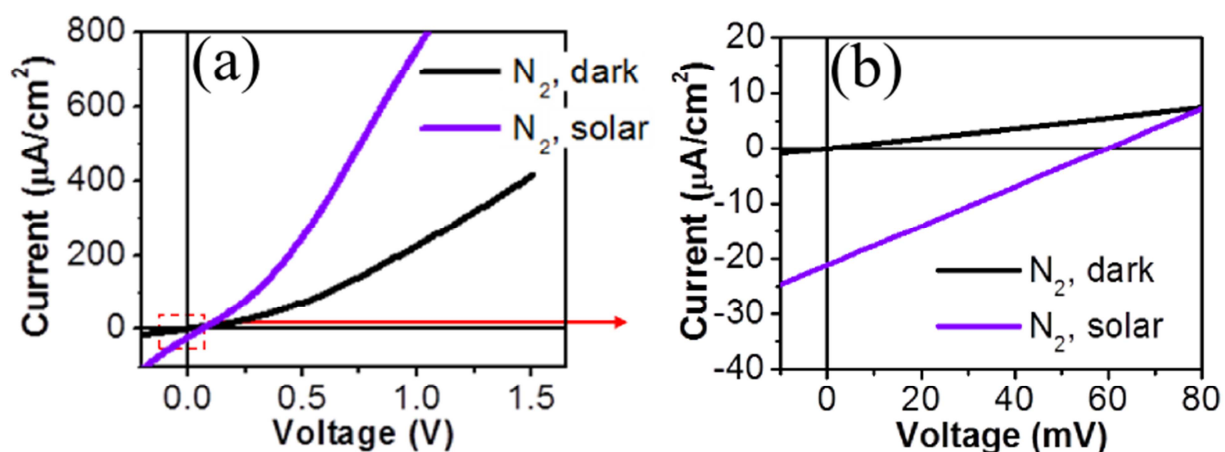


Figure 57 (a) Current-voltage characteristics of CdS@n-ZnO/p-Si in dark and under solar illumination in N₂ atmosphere, (b) a magnified part of the I-V curve.

5.1.3 Gas sensing properties of SDS

The key idea of the SDS is based on integration of multicomponent units with multiple and complementary functionalities in a singular device. Based on our experimental findings and with the help of state-of-the-art literature, a novel SDS sensing concept was developed, based on monitoring the change of open circuit voltage, (ΔV_{oc}), in comparison to the well-known conductometric sensors which are based on monitoring the change of resistance (ΔR). The fabricated SDS was capable of detecting oxidising and reducing gases with reproducible response at room temperature and without the need of any other energy sources except solar illumination to deliver a self-sustained gas sensor.

The SDS gas sensor devices were tested to demonstrate their self-sustainability to power and to deliver reliable gas sensing signals corresponding to different surrounding gases. The devices were operated under the following two different conditions

1. Applied current mode (APP-mode): where the device was monitored by applying regulated bias currents (+25 and +50 μA) and the corresponding voltages were measured under simulated solar light illumination (AM 1.5) at room temperature.

2. Self-powered mode (SP-mode): no external current applied under simulated solar light illumination (AM 1.5) at room temperature.

Gas sensing response of SDS under applied current mode (APP-mode)

The gas sensing properties of SDS device were tested first by the traditional sensing measurements by applying different currents to power the sensor (APP-mode). In the APP-mode the sensor is working as a visible light assisted gas sensor rather than a self-powered one. Figure 58 (a,b) presents the different gas sensing behaviours of CdS@n-ZnO/p-Si in dark and under illumination conditions.

- **In dark conditions**

CdS@n-ZnO/p-Si showed no response for different applied forward bias currents (+25 and +50 μA) in nitrogen and oxygen atmospheres (see figure 58a) probably due to insufficient activation energy for interaction of oxygen species on the surface of ZnO as there was no external activation (such as irradiation with light or thermal heating) [198].

- **Under solar illumination**

In contrast, under illumination conditions (simulated sun spectrum; AM1.5) the sensing behavior of CdS@n-ZnO/p-Si was totally different. The system showed an increase of the measured voltages at constant applied current upon exposure to oxygen atmosphere which is reflecting an increase in the resistance of the sensor under oxygen gas. The measured responses were fully reversible and reproducible in different bias currents (Figure 58b).

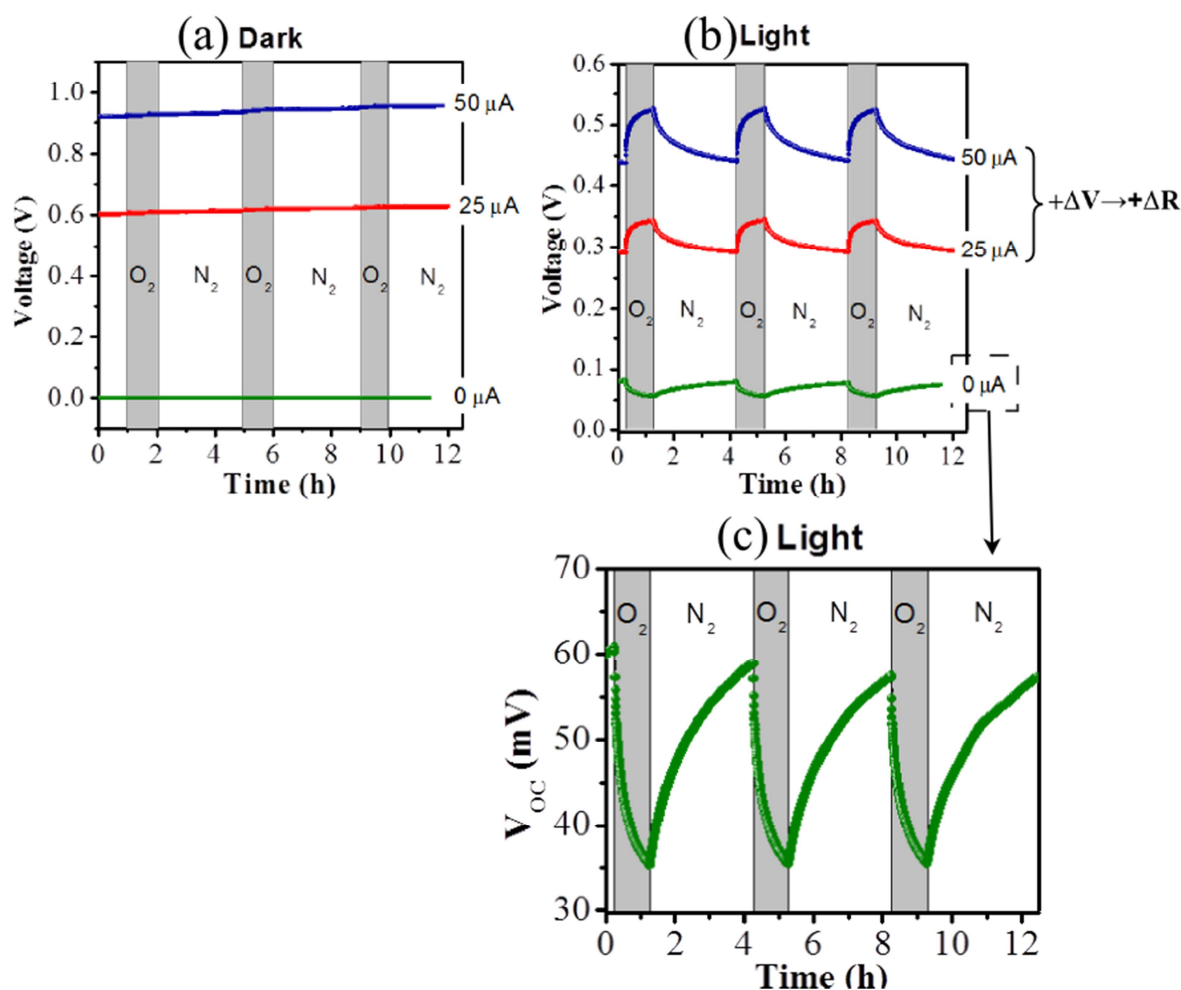


Figure 58 Gas sensing characteristics of CdS@n-ZnO/p-Si system. ON/OFF curves (oxygen / nitrogen) recorded at different constant currents in (a) dark and under (b) solar illumination showing different gas sensing behaviors. (c) ON/OFF (oxygen / nitrogen) curve recorded with open circuit voltage V_{oc} ($I = 0$ A) under solar illumination condition.

- **The sensing mechanism at different applied bias currents (*APP-mode*)**

When a constant current is applied to the SDS device (CdS@n-ZnO/p-Si), the sensing mechanism is the same as for simple conductometric (n-type) gas sensors, in which the resistance is increased when an oxidizing gas such as oxygen is introduced. This effect can be explained in terms of the increase of the surface depletion zone and can be monitored by the increase of voltage as shown in Figure 58b in cases of 25 and 50 μA applied current [199].

Gas sensing response of SDS under Self-powered mode (*SP-mode*)

The most interesting finding was that, the CdS@n-ZnO/p-Si showed significant gas sensing responses even at zero bias current, i.e. no external electric power applied (see figure 58c). The response at zero bias current was opposite to those of bias currents, indicating a different underlying sensing mechanism in comparison to the traditional conductometric sensing principle. Since there is no current flowing at zero bias conditions, the measured voltage signal displays the open circuit voltage (V_{oc}) of n-ZnO/p-Si heterojunction diode and not the simple resistive character of ZnO itself. In other words, the signal response cannot reflect the change of the conductometric properties of ZnO but has to be originated in a change of the n-ZnO/p-Si diode properties. A series of gas sensing measurements were performed in the self-powered mode (i.e. zero applied current and visible light illumination at room temperature) to investigate the observed self-powered gas sensing response of SDS.

Figure 58c shows the ON/OFF curve (oxygen / nitrogen) of CdS@ZnO/p-Si recorded at zero applied current and under illumination. From the evolution of the open circuit voltage V_{oc} (zero current) it is clear that the value of V_{oc} decreases in oxygen (about 41%) in comparison to nitrogen atmospheres (the reference gas). Evidently, V_{oc} is an auto-generated signal that correlates with the atmospheric composition.

In order to demonstrate that this proof-of-concept device (CdS@ZnO/p-Si) can be used to detect other common target gases, the device was exposed to ethanol gas (50-200 ppm) and operated in the SP-mode. Figures 59 (a,b) show the V_{oc} signals of CdS@n-ZnO/p-Si in dark and under solar illumination conditions upon exposure to a sequence of ethanol pulses diluted in synthetic dry air. Under dark conditions, no V_{oc} sensing signal was obtained and consequently no modulation of V_{oc} , was observed. Upon illumination, the CdS@n-ZnO/p-Si showed significant dependence of V_{oc} on the ethanol concentration (inset of Figure 59b) making the monitoring and correlations of V_{oc} suitable for quantitative sensing purpose. The response and recovery sequence repeated over a long time (~ 8 weeks) showed good stability and reproducibility of the monitoring system.

To further assess the sensing behaviour of SDS device under different reducing gases, the sensor was exposed to methane gas and operated in the self-powered mode. The response of CdS@n-ZnO/p-Si towards different concentrations of methane exhibited similar gas sensing properties (Figure 60a).

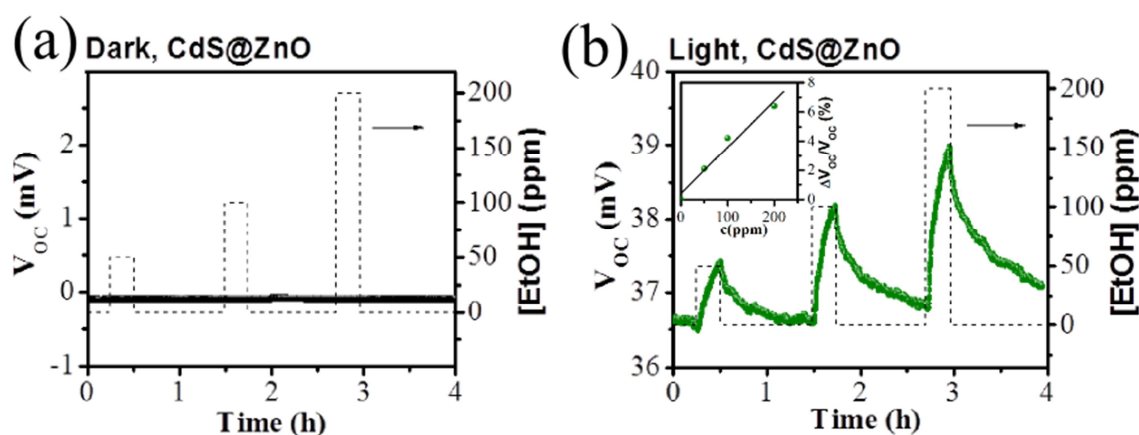


Figure 59 Gas sensing characteristics of CdS@n-ZnO/p-Si system. ON/OFF (ethanol / air) curves of CdS@n-ZnO/p-Si recorded in (a) dark and under (b) solar illumination (Inset shows the sensitivity of the device with different ethanol concentrations).

In contrast to the good sensing responses observed for CdS@n-ZnO/p-Si system, the bare p-n junction (n-ZnO/p-Si) without CdS decoration only showed low, unstable and non-scalable response to different methane concentrations (see figure 60b). This is demonstrating the key role of the CdS@n-ZnO gas sensing unit in the CdS@n-ZnO/p-Si system under solar light illumination.

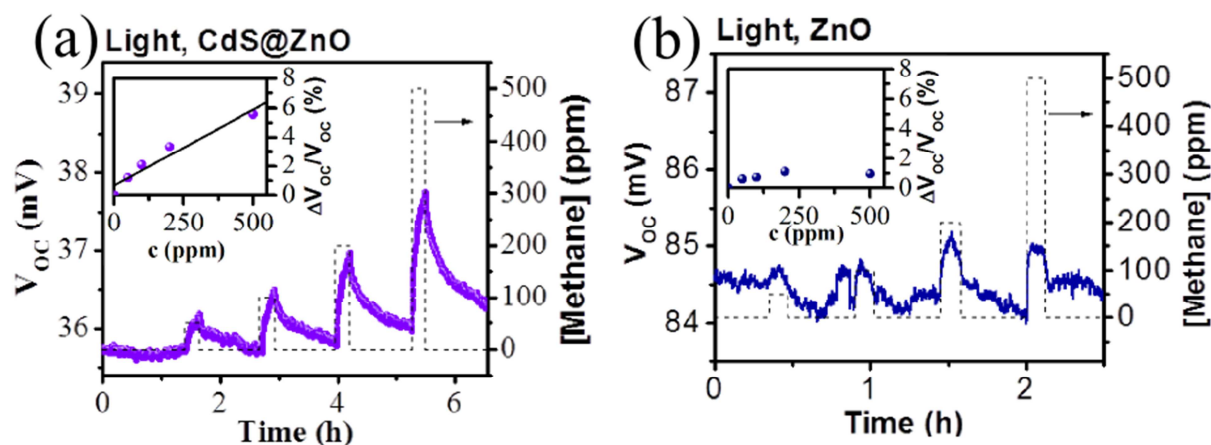


Figure 60 ON/OFF (methane / air) curves of (a) CdS@n-ZnO/p-Si and (b) n-ZnO/p-Si recorded under solar illumination. Insets show the sensitivity of the device with different methane concentrations.

The V_{oc} was found to be higher for ZnO/p-Si system compared to the CdS@n-ZnO/p-Si sample, because in case of bare n-ZnO/p-Si device no light is absorbed by CdS and consequently the incident light reaches the p-n junction of n-ZnO/p-Si with a higher intensity. This suggests that the response of SDS is mainly depends on the change of V_{oc} (ΔV_{oc}) under ambient gases and not on the absolute V_{oc} value of the system.

5.1.4 The proposed sensing mechanism of self-powered SDS (*SP-mode*)

As discussed before, the system fabricated here contains two main components: the CdS decorated ZnO nanorods as active sensing unit and n-ZnO/p-Si heterojunction as the self-powering unit. Therefore, in this concern, an operation correlation between these two components, active sensing unit and self-powering unit, have been established in order to better understand the sensing mechanism of the system. The device response in different gaseous species at different working conditions have been analyzed in details and a sensing mechanism has been proposed. The proposed mechanism will be explained in terms of modulated polarization of nanoparticles/nanorods interface, gas-material surface interactions and the subsequent changes in the doping level (N_D), which is manifested in the variation of V_{oc} in CdS@n-ZnO/p-Si. Here a step by step proposed mechanism is introduced:

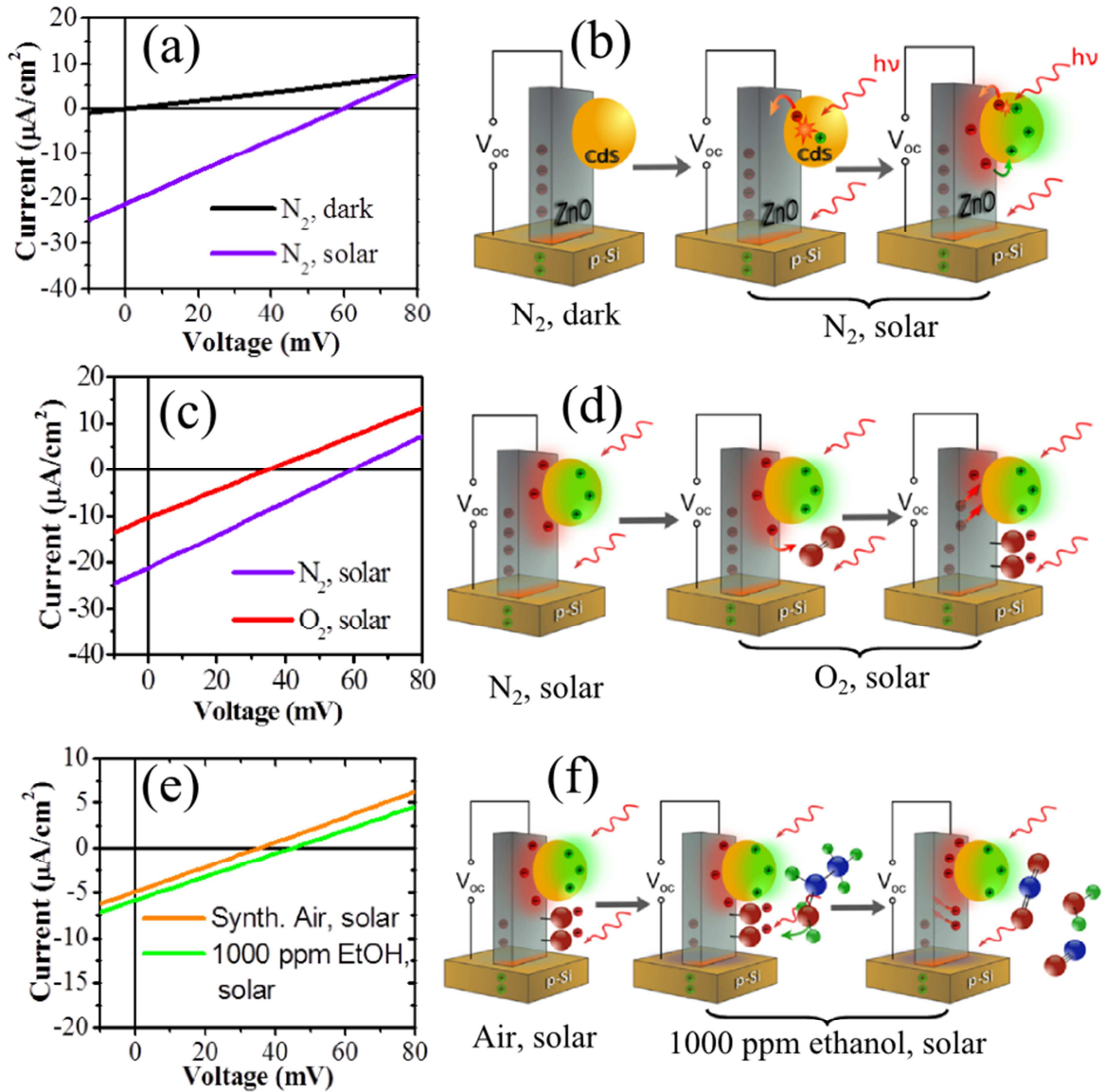


Figure 61 Step-by-step SDS proposed mechanism: (a) I-V curves recorded in dark and under solar illumination of CdS@n-ZnO/p-Si, (b) a sketch of their high energy electron patterning under solar illumination, (c) I-V curves recorded under solar illumination in N_2 and O_2 atmospheres of CdS@n-ZnO/p-Si, (d) their corresponding charge carrier distribution sketches, (e) I-V curves recorded under solar illumination in air and 1000 ppm ethanol atmospheres of CdS@n-ZnO/p-Si, and (f) the corresponding charge carrier distribution sketches.

I. The effects of the solar illumination

Figure 61 (a,b) shows the I-V characteristics of CdS@ZnO/p-Si in dark and under solar illumination under N_2 and the corresponding sketches of a non-equilibrium process that could explain the response of the system in the following manners:

(i) Once the photon is absorbed by CdS, a photo-generation of electron-hole pairs takes place in CdS NPs. (ii) As CdS and ZnO have proper band alignment of type II heterojunction [197], whereby the lower conduction band edge of ZnO favours an effective charge separation. The excited electrons (e^{*-}) are injected from the conduction band of CdS NPs into the conduction band of ZnO nanowire, whilst the mismatch in the valance band and absence of a hole extracting agent, such as electrolyte, forces holes to remain in CdS side (i.e. efficient carrier separation) [200]. (iii) The number of holes within CdS increases by the ongoing electrons injection which leads to a transient electrical polarization corresponding to dynamic accumulations of holes on CdS side and electrons on ZnO surface. This is a self-limiting process that continues until the formed electric field blocks any further injections of electrons into ZnO. The dynamic processes of electron injection ($\text{CdS} \rightarrow \text{ZnO}$) and recombination ($\text{ZnO} \rightarrow \text{CdS}$) end up in a steady state in which an overall increased electron density on the surface of ZnO is achieved [77,201]. These changes in the surface charge distribution i.e. the creation of local electric fields between ZnO (-) and CdS (+) causes a polarization of the ZnO surface, which is accountable for variations in the gas-surface interaction causing the activation of the sensing that drive the sensor response[28]. Some previous works demonstrated that similar effects, by using external electric fields, can activate the gas-metal oxide interaction [202,203].

II. Effects of oxidizing gases under illumination

Figure 61c shows the change of I-V characteristics of CdS@ZnO/p-Si under N_2 and O_2 atmospheres in order to study the influence of oxidizing gas molecules on the I-V characteristics. It is well known that ZnO, like most of the n-type semiconductor oxides, can react with oxygen to form oxygen species (O^{2-} , O_2^- , O^-) [21] on its surface. A schematic representation of distribution of charge carriers on CdS@ZnO/p-Si under oxidizing atmosphere is shown in figure.61d. Under exposure to oxygen atmosphere, the electrons accumulated at the ZnO-CdS interface can be trapped by oxygen molecules to form oxygen species in an exergonic process (i.e. no need for additional energy) as shown in equation 43 [204].



The trapped electrons are subsequently compensated by bulk ZnO electrons, causing a decrease of the apparent donor density within the metal oxide (N_D decreases). Therefore this electron accumulation at the ZnO surface by carrier injection from CdS upon photo-excitation

can explain the vital role of CdS in the system in the activation of the sensing response to gases via sunlight photons. Since better gas sensing responses were observed for CdS coated n-ZnO/p-Si when compared to naked n-ZnO/p-Si. The primary experiment has shown that CdS@n-ZnO/p-Si with full decoration rate of CdS did not show any sensing behaviours indicating that ZnO surface and interface of CdS and ZnO could play a key role in the gas sensing mechanism.

The above proposed explanation postulated a decrease in the concentration of electrons in ZnO in presence of oxygen, which can be regarded as a decrease in the effective concentration of donor impurities N_D in the n-type ZnO. The equations of the semiconductor quantum theory can be used to support the described SDS mechanism. The relation between the donor concentration (N_D) and the built-in potential V_{bi} in a p-n junction is expressed by equation 44 [205]:

$$V_{bi} = \frac{kT}{q} \text{Ln}\left(\frac{N_D^{ZnO} N_A^{Si}}{N_i^{ZnO} N_i^{Si}}\right) \quad [44]$$

where N_D , N_A and N_i are donor, acceptor and intrinsic doping level, which corresponds with the free carrier concentration in the impurities ionization regime, k , T and q are Boltzmann constant, absolute temperature and electron charge, respectively .

According to equation 44, the reduction of N_D leads to a decrease of the V_{bi} value in oxygen atmosphere. Since the open circuit voltage (V_{oc}), that appears across the terminals of a p-n junction under illumination is caused by the ability of this built-in potential (V_{bi}) to separate the electron and hole pairs generated within and close to the depleted region, there is a positive correlation between the photo-voltage values (and in particular the open-circuit voltage V_{oc}) and built-in potential (V_{bi}) [206,207]. It can be concluded, according to equation 49, that the reduction of N_D leads to a decrease of V_{bi} and consequently the V_{oc} value in oxidizing atmosphere. Figure 61c shows the I-V characteristics of CdS@ZnO/p-Si recorded in oxygen and nitrogen atmospheres. The V_{oc} values obtained ($I = 0 \mu\text{A}$) in figure 61c can support the tendency of N_D in different atmospheres. Following the proposed mechanism, a reduction of N_D in oxidizing atmospheres causes a lower V_{oc} of the device and thus shows the opposite response direction compared to conventional n-type conductometric gas sensors.

III. Effects of reducing gases under illumination

The sensing behaviors of the SDS device were studied in correlation with the I-V characteristics in air and ethanol atmospheres respectively, in order to understand the underlying sensing mechanism. Figure 61e showed the I-V characteristics of CdS@ZnO/p-Si in air and ethanol (1000 ppm diluted in air) atmospheres under solar illumination. The V_{oc} values of CdS@ZnO/p-Si sensor was 36 mV in air and 44 mV in ethanol respectively. This increase in the V_{oc} value in ethanol can also be explained on the basis of the previously proposed model, where in this case the oxidation of ethanol molecules released electrons trapped at surface oxygen back to ZnO (see figure 61f) once the following reaction takes place [208]:



The consequent increase of N_D within the n-doped ZnO causes an increase in the recorded V_{oc} value of the sensor as a signal for the presence of the reductive gas.

Taken together, these results show that the SDS device can work as quantitative and also qualitative self-powered gas sensor under solar illumination and it is capable of detecting and distinguishing between reductive and oxidative gas species. Finally it is worth to mention here that there are some limitations need to be considered to improve the introduced proof-of-concept devices such as the limited response and recovery times as well as sensitivity values of the system due to the fact that the gas diffusion through the nanostructures was slowed down, caused by the easy to build device setup. The possible attempts that were done in this respect as well as the promising ideas to improve the performance will be discussed in detail in the outlook section.

Validation of the sensing mechanism

To this end, the proof of concept of SDS was demonstrated in the previous discussions but if this debate is to be moved forward, a deeper understanding of SDS concept is needed to validate the proposed mechanisms.

I. Capacitance-voltage (C-V) characteristics

The capacitance-voltage (C-V) characteristics of the SDS system can be used as an indirect evidence of the SDS proposed sensing mechanism, through monitoring the dependence of N_D values of ZnO on different gas environments calculated from the capacitance-voltage (C-V) measurements. The capacitance per unit area of an ideal heterojunction diode can be expressed as (equation 46) [205]:

$$\frac{1}{C^2} = \frac{2(N_A \epsilon_1 + N_D \epsilon_2)}{q N_D N_A \epsilon_1 \epsilon_2} (V_{bi} - V) \quad [46]$$

where, in current case, N_D is the donor density in n-ZnO, N_A is the acceptor density in p-Si, ϵ_1 and ϵ_2 are the dielectric constants of n-ZnO and p-Si, respectively, q is the charge of the carriers, V_{bi} is the built-in potential of the p-n heterojunction and V is the external bias voltage. As the dielectric constants of both materials and the doping level of p-Si (N_A) are known, the slope of $1/C^2$ - V plots can be used to determine the donor density (N_D) of ZnO.

Capacitance data for all sample were plotted in Mott-Schottky style and fitted with a straight line for the negative bias, the slope of the line was used to determine the donor density (N_D) of ZnO. $1/C^2$ versus applied potential curves for the device in nitrogen, oxygen, air and ethanol (1000 ppm diluted in air) atmospheres were measured (see figure 62) at 1 MHz in order to confirm the environmental dependence of donor density N_D . $1/C^2$ vs. voltage curves displayed a linear behavior confirming the successful formation of a p-n heterojunction at the n-ZnO/p-Si interface.

The donor concentration of naked n-ZnO/p-Si ($2.5 \times 10^{19} \text{ m}^{-3}$) was insensitive to variation in the gas atmosphere or the illumination conditions (figure 62d) whereas the CdS@n-ZnO/p-Si system displayed significant variations (figure 62c).

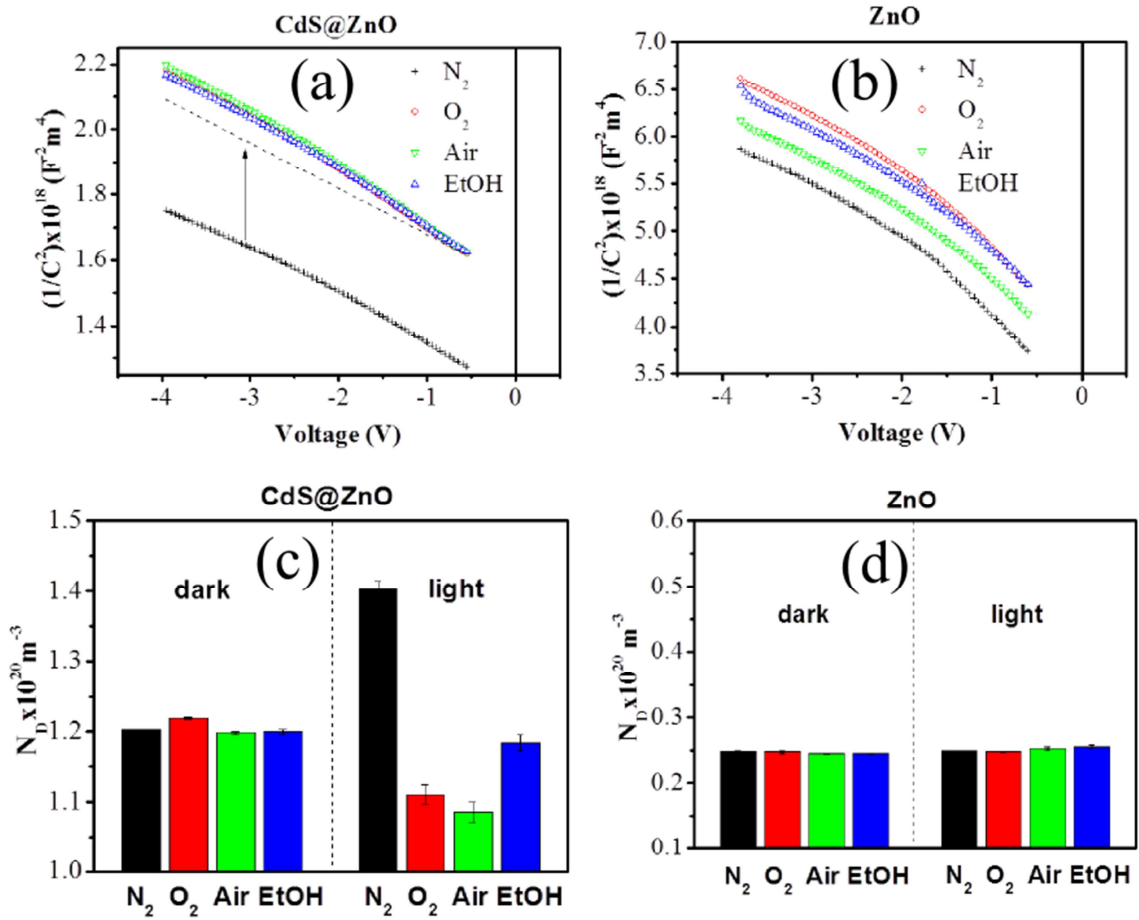


Figure 62 Capacitance-voltage measurements. Mott Schottky plots ($1/C^2$ vs. V) of (a) CdS@n-ZnO/p-Si, and (b) n-ZnO/p-Si acquired at 1 MHz in the reverse bias region. Environmental dependent N_D of (c) CdS@n-ZnO/p-Si and (d) n-ZnO/p-Si recorded in dark and under solar illumination.

The change of the donor density of CdS@ZnO/p-Si system under dark and illumination for all gases has been shown in figure 62c. It was observed that the donor density N_D remained constant in dark conditions (ca. $1.20 \times 10^{20} \text{ m}^{-3}$) but it was sensitive to the presence of different gases under illumination. Under illumination, the donor density was sharply increased under N_2 atmosphere (from 1.20×10^{20} to $1.40 \times 10^{20} \text{ m}^{-3}$, i.e. ca. 16 %) however an opposite effect was observed in oxygen and synthetic air atmosphere, where the density was decreased under illumination in case of oxygen and synthetic air atmospheres.

This observed behavior is fully consistent with the previously depicted sensing mechanism, where the optical sensitization of the CdS-ZnO interface is essential to achieve the sensing behavior. As it is clear from figure 62c, the change in N_D under O_2 and N_2 is more significant than that in air/ethanol. The quantitative evidence for N_D changes in different gases is comparable to the changes in open circuit voltage (ΔV_{oc}) which is 25 mV in oxygen/nitrogen condition (figure 61c) however, less change in N_D was observed in air/ethanol atmospheres in corresponding with the less change in open circuit voltage observed before (ΔV_{oc} , 8 mV) shown in Figure 61e. These results indicate that the change of the effective N_D within n-ZnO is the major factor influencing the V_{oc} value, which is the self-powered sensor signal in different gases.

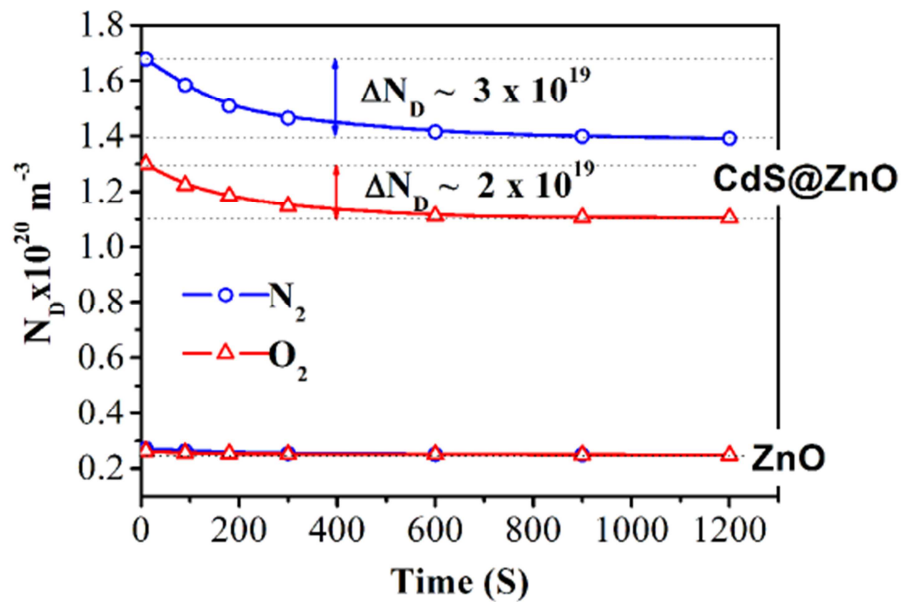


Figure 63 Evolution of N_D of CdS@n-ZnO/p-Si and n-ZnO/p-Si devices after switching off the solar simulator.

The dynamic evolution of N_D after switching off the illumination, $1/C^2$ versus applied voltage curves were measured at different time scales once the visible lamp was switched off ($t = 0$ s), clearly shows that the effective concentration of donor sites remains quenched depending on the surrounding atmosphere (see figure 63), can be explained by the so called persistent photoconductivity (PPC) [198], that is only observed after exposing ZnO to UV photons with energies above the bandgap of the material and needs the concurrence of surface distribution of charges

interacting with gaseous molecules. Remarkably, this effect seems to take place in ZnO/p-Si system with simulated sunlight only after coating them with a visible sensitizer (CdS), providing further evidences about the successful modification of the surface charge distribution in the ZnO nanorods.

II. The effect of incident light intensity on SDS response and the role of CdS NPs

To clarify the SDS sensing mechanism, the relation between incident light intensity and open circuit voltage (V_{oc}) in N_2 and O_2 atmosphere and their relative open circuit voltage change (ΔV_{oc}) have been studied. As shown in figure 64, the V_{oc} value in N_2 increases linearly with increasing the incident light intensity whereas the V_{oc} value in O_2 atmosphere drops nonlinearly with the increases of light intensity.

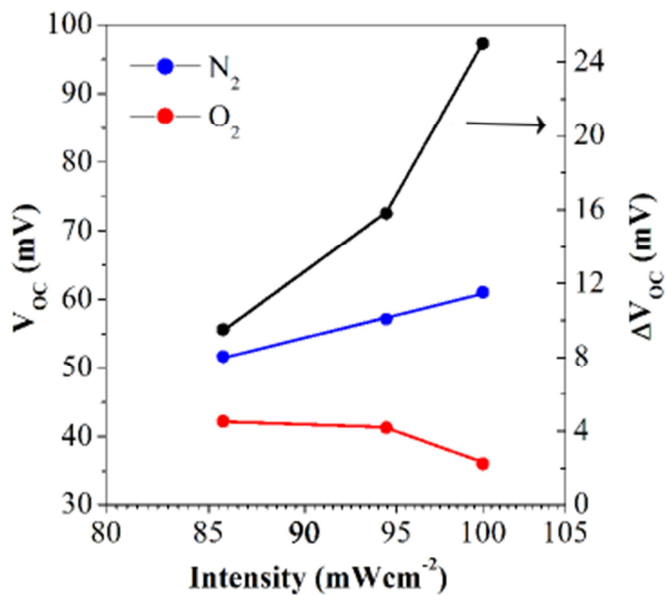


Figure 64 Light intensity dependence of the open circuit voltage (V_{oc}) of CdS@n-ZnO/p-Si system in N_2 and O_2 atmosphere and their relative change (ΔV_{oc}).

The first candidate explanation for these remarkable behaviours might be the change in the donor density of ZnO (N_D) and its correlation with injected photoelectrons. In the case of nitrogen, the donor density N_D of ZnO does not change as there is no interaction between ZnO and N_2 and thus the increase of V_{oc} is solely depends on the increase of photoelectrons injection from CdS into ZnO and the consequent increase in the photocurrent. This is very similar to previous

reports on CdS/ZnO solar cells, where there is usually a proportional increase of the open circuit voltages with the increase of light intensity and/or the CdS decoration density [59,80].

While in the case of oxygen atmosphere there is correlation between two major factors influencing the value of V_{oc} , namely the light intensity and the net donor density N_D . The injection rate of photoelectrons from CdS to ZnO is assumed to increase with increasing of the intensity of incident light, thus more electrons will react with the oxygen to form the adsorbed oxygen species which will result in a reduction of the net donor density of ZnO (N_D) (i.e. decrease of V_{oc}). According the previous assumption the reduction of donor density of ZnO is supposed to increase with increasing of the incident light intensity and thus the change of donor density (ΔN_D) is expected to increase (i.e. ΔV_{oc} increase) also with increasing the light intensity. The measured change of open circuit, ΔV_{oc} , values at different light intensities is constituent with the proposed assumption and ΔV_{oc} (i.e. ΔN_D) is found to increase with higher light intensities.

These results indicate that the variation of V_{oc} in different ambient is more meaningful than the absolute value of V_{oc} . The change of V_{oc} depends strongly on N_D , the donor density of ZnO which can be tuned by photo-sensitization of CdS nanoparticles decorated on ZnO surface. The role of CdS is indispensable for the SDS system not only to harvest the solar light but also to activate the analyte gas/ZnO interaction and to enhance the gas sensing response of the system. It is interesting to mention that in a recent report used CdS NP/ZnO microcrystal heterostructures to develop visible induced gas sensors (where a constant voltage were applied to measure the photocurrent and not a self-powered sensor) they used the similar concept of charge separation and confirmed also that the photo-generated electrons of CdS NPs can be transferred to ZnO under visible light irradiation [32].

To sum up, the results of this work demonstrated that the inclusion of a solar cell (n-ZnO/p-Si) and an active gas sensing material (CdS@ZnO) enabled the operation of the gas sensor device without any external electrical power sources, where by only solar illumination the open circuit voltage V_{oc} , produced by the n-ZnO/p-Si solar cell, acted as a self-generated sensing signal.

5.2 Solar diode sensor based on radial CdS@n-ZnO/ p-Si nanowires heterojunction

The proof of the SDS concept was demonstrated in the previous section, based on the CdS@ZnO nanowires/p-Si substrate system; however more research on the SDS concept needs to be undertaken to demonstrate the generality of the concept by extending the new sensing

approach to other nanomaterial geometries. Furthermore, the first SDS device suffers from a slow response and recovery characteristic, that is possibly caused by the slow diffusion of gas molecules through the compact ZnO NWs structure. In this respect, a new system based on the radial heterojunction of CdS@ZnO/p-Si nanowires has been investigated to prove the validity of SDS sensing concept. The radial one dimensional p-n heterojunction were chosen due to their superior and additional properties such as high surface/volume ratio, superior optical properties (such as optimal light absorption, low reflection of the sun illumination spectrum), and efficient free carrier collection, as compared to their conventional planar p-n junction counterparts [168].

5.2.1 Structural analysis of the system and the prototype device fabrication

CdS@n-ZnO/ p-Si nanowires heterojunction was fabricated through a combination of wet-chemical etching of Si wafer to produce p-Si nanowires, followed by atomic layer deposition of ZnO shell on the core Si nanowires for 300 ALD deposition cycles and finally the CdS NPs were deposited on the surface of ZnO shell by chemical bath deposition method (CBD) for 15 min. The details of the synthesis were discussed before in section 4.3.2. The CdS@ZnO/p-Si NWs system is composed of core of vertically aligned p-Si NWs arrays with a length of 24 μm and a shell of 60 nm thick ZnO film and a uniform decoration with CdS NPs with size of about 20 nm on the ZnO surface.

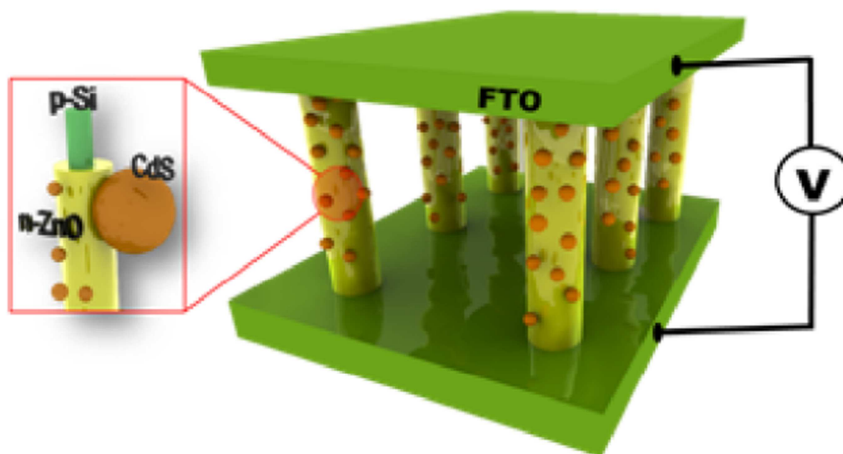


Figure 65 Schematic representation of the SDS device based on radial CdS@ZnO/p-Si NWs.

Figure 65 shows a representative sketch of the SDS radial device, where the same device design were used as described before (see section 5.1.1), where the only difference is that the p-n junction is formed here a long the radial surface of Si NWs and the surrounding ZnO shell. The current geometry is offering a higher surface to volume ratio and a less compact structure for enhanced gas diffusion. The conductive glass (F:SnO₂, FTO) was used as a transparent top contact on the top of the ZnO shell whereas the p-Si substrate underneath the Si NWs was contacted as the back electrode.

5.2.2 The electrical characterization of the radial SDS system

The current–voltage (I–V) characteristic of the CdS @ZnO/p-Si NWs heterojunction in dark conditions and at room temperature is shown in figure 66, the curve clearly shows a typical rectifying behaviour of a p-n heterojunction. Under solar illumination the I-V characteristics of the CdS @ZnO/p-Si NWs show a photovoltaic effect of the device with an open circuit voltage (V_{oc}) of 90 mV under solar illumination. It is worth to mention that this value of V_{oc} is higher than that obtained for the analogue system based on planar Si substrate (where V_{oc} was about 60 mV), which indicate the advantage of the radial heterostructures.

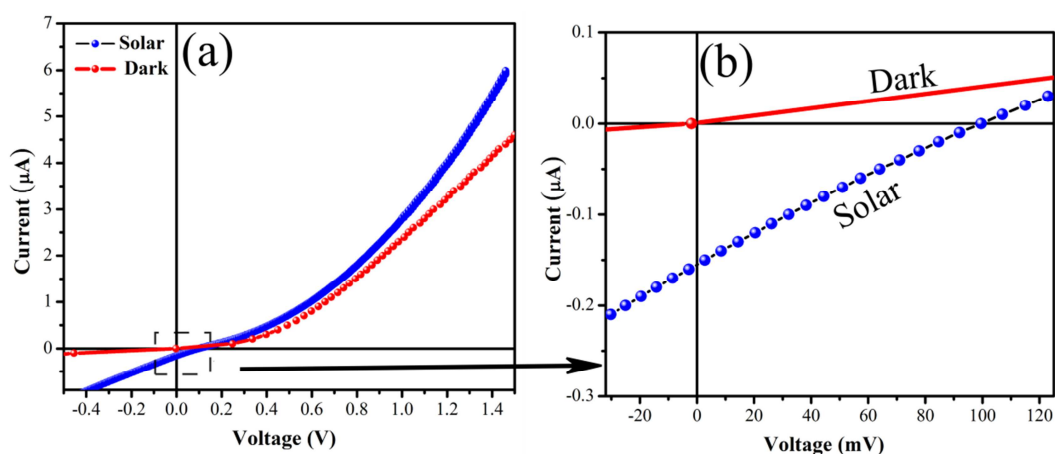


Figure 66 (a) I-V characteristics of CdS@n-ZnO/p-Si NWs heterojunction in dark and under solar illumination. (b) a magnified part of the I-V curve to show the open circuit voltage.

The capacitance-voltage (C-V) measurements of the CdS@n-ZnO/p-Si NWs heterojunction device are shown in figure.67. $1/C^2$ vs. voltage plot displayed a linear behavior confirming the formation of a heterojunction diode at the n-ZnO/p-SiNWs interface. The donor density of ZnO

was calculated from the slope of $1/C^2$ vs. voltage curve and is found to be $1.5 \times 10^{18} \text{ m}^{-3}$. It is important to point out that the value of donor density (N_D) of n-ZnO on the Si NWs deposited by ALD is slightly higher to the N_D value measured before for ALD films of ZnO deposited on flat substrates ($1.08 \times 10^{18} \text{ m}^{-3}$) which was reported in the previous section 4.1.1. The higher N_D value for the CdS@ZnO/p-Si NWs might be attributed to the defects introduced by the etching effect of CdS to the surface of ZnO which can result in more defects in ZnO surface. These etching effects are attributed to the amphoteric nature of ZnO as previously discussed [138].

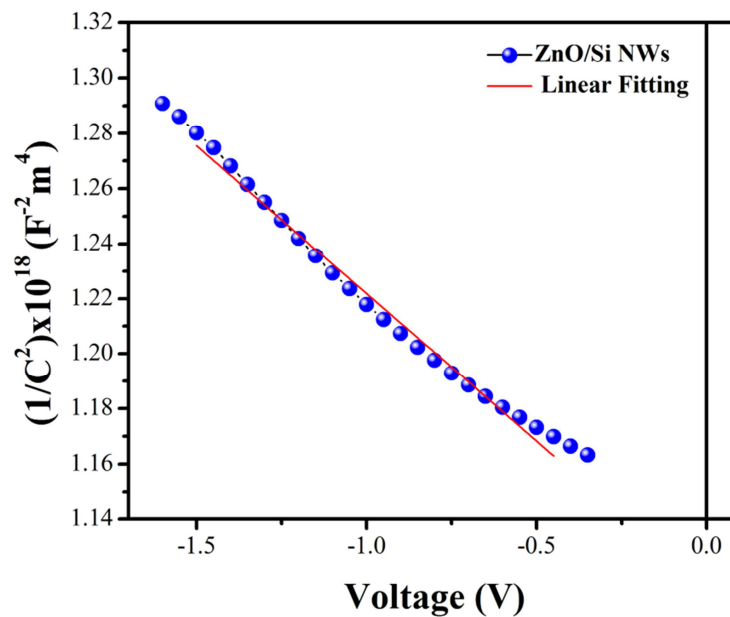


Figure 67 C-V measurement. Mott Schottky plots ($1/C^2$ vs. V) of CdS@n-ZnO/p-Si NWs acquired at 1 MHz in the reverse bias region.

5.2.3 The gas sensing properties and the proposed mechanism of the radial SDS device

Gas sensing measurements were performed under solar light illumination at room temperature under self-powered mode (i.e. zero bias current and solar illumination) and the change of the open circuit voltage (V_{oc}) was monitored under oxygen and nitrogen atmospheres.

As can be seen from the sensing behavior in figure 68, under illumination condition the V_{oc} sensing signal is depending on atmospheric composition and it decreases in oxygen and increases in nitrogen atmospheres. The change of open circuit voltage was lower than that observed for the CdS@ZnO nanowire/p-Si substrate.

The CdS@ZnO/p-Si NWs system showed the expected sensing behavior of the self-powered SDS systems, which confirm that the SDS concept is general and can be applied to different material combinations. The sensing response can be explained based on the same SDS sensing concept where the surface reaction of the n-ZnO surface with oxygen will form charged oxygen species (such as O^-) which will result in a decrease in the donor density (N_D) of ZnO. This reduction of donor density causes the decrease of the open circuit voltage (V_{oc}) observed under oxygen atmosphere.

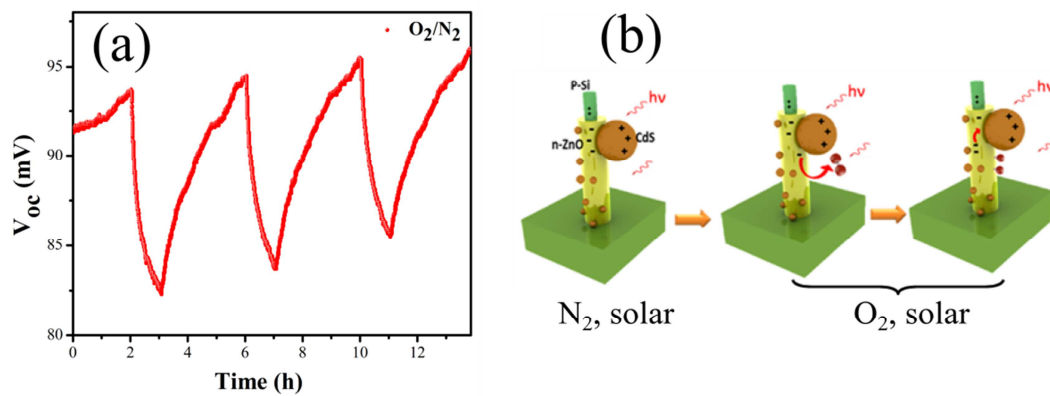


Figure 68 (a) ON/OFF (oxygen/ nitrogen) curves of CdS@n-ZnO/p-SiNWs sensor recorded under solar illumination with no applied current ($I = 0$ A) and at room temperature. (b) Charge carrier distribution of CdS@n-ZnO/p-SiNWs in N_2 and O_2 atmospheres under solar illumination.

Beside the confirmation of validity of the SDS concept, there are many open questions that need more investigation in the future about the relation between the value of the donor density of ZnO as the active sensing material in our system and the gas sensitivity. There are many interfering factors that can influence the device performance as well as the sensing response such as the nature of contact electrodes and the device configuration. If it is assumed that all other interfering parameters are constant for all samples, two major factors can influence the sensing response in SDS system; the value of the electron density in ZnO (where higher N_D might result in higher gas sensitivity) [209] and the surface modulation of donor density in ZnO by CdS interfaces. In self-powered operation, the second factor seems to be more dominating as can be concluded from the N_D values and the gas sensing responses of CdS@ZnO/p-Si nanowires ($N_D = 1.5 \times 10^{18} \text{ m}^{-3}$) and that of ZnO/p-Si substrate ($N_D = 2.5 \times 10^{19} \text{ m}^{-3}$), where the former system showed more stable, reproducible and better sensing response despite the lower N_D value. While, when comparing the

CdS@ZnO/p-Si NWs system with its analogue system of CdS@ZnO/p-Si substrate, where the later system have both higher donor density ($1.2 \times 10^{20} \text{ m}^{-3}$) besides the surface modulation, it showed a better sensing response compared to the former system.

As conclusion, through optimization and control over donor density of ZnO in correlation with surface modulation by introducing different hetero-interfaces, better gas sensing responses can be obtained.

5.3 Solar diode sensor based on thin-film planar heterojunctions

Thin film solar diode sensors were studied to prove the generality of SDS concept. The thin-film sensors operated under self-powered mode showed the SDS sensing behavior under different atmospheres, which is proving the generality as well as the validity of the new concept. The responses of SDS thin-film devices were poor compared to their nanowire/planar or radial p-n heterojunction counterparts due to their lower surface to volume ratio as compared to nanowires. Another factor affecting the response of thin film based SDS devices is the uncontrolled surface coverage of CdS on the planar films which results on deposition of CdS agglomerates that hinder the analyte gas interaction with the ZnO surface (which is the active sensing element in the SDS device).

5.3.1 n-ZnO/p-Si film junction

The n-ZnO/p-Si junction is one of the two components in the SDS system which is responsible for producing the output self-powered signal under illumination. Despite the fact that thin-film photodiodes are not expected to show either higher electrical responses or better sensing properties in comparison to their one-dimensional counterparts [210], basic investigation is needed to enhance their electrical properties which will be reflected in enhancement of whole SDS system performance.

Recent reports showed that the use of thin layer of insulating oxides (*i*-layer) between the n- and p-materials can enhance the photo response and reduce in the leakage currents of p-n photodiodes [211,212]. The commonly used insulating oxide, SiO₂, is usually deposited by plasma enhanced chemical vapor deposition (PECVD). It is not trivial to control the deposition of very thin films by PECVD technique (in the order of a few nm). Al₂O₃ is one of the technologically important oxides due to its high dielectric constant and being reasonably a good glass former besides SiO₂ [213]. Al₂O₃ can be easily deposited by ALD techniques with a precious control

over thickness down to few nanometers. In this regard, two different photodiodes have been fabricated; namely n-ZnO/p-Si (p-n junction) and n-ZnO/*i*-Al₂O₃/p-Si (p-*i*-n junction) to study the effect of using a thin insulating layer on the electrical properties of the photodiode.

The n-ZnO film was deposited on a p-Si substrate by 400 cycles of ALD depositions, the deposited film characteristics were discussed in section 4.1.1 in detail. Here, the electrical properties as well as the sensing properties of fabricated (n-p) and (n-*i*-p) heterojunctions were tested to demonstrate their device potential.

The n-ZnO/p-Si heterojunction showed a low open circuit voltage of about 14 mV under solar illumination. Interestingly when a thin layer of Al₂O₃ was deposited by ALD technique to form n-ZnO/*i*-Al₂O₃/p-Si heterojunction, the electrical properties improved compared to the n-ZnO/p-Si heterojunction. Figure 69 (a,b) shows the I-V characteristics of n-ZnO/*i*-Al₂O₃/p-Si heterojunction where an open circuit voltage of about 20 mV was produced. By comparing the I-V characteristics in the reverse bias region of I-V curves for both p-n and p-*i*-n heterojunctions shown in figure 69 c, it is clear that the leakage current of the p-*i*-n heterojunction was lower than that of the p-n junction which results in enhancement of the photocurrent.

The gas sensing response of the solar diode in the self-powered mode was very poor compared to other systems discussed before, where almost no response was observed for the n-ZnO/p-Si junction. The p-*i*-n junction of n-ZnO/*i*-Al₂O₃/p-Si, in figure 69d, showed a very low response of about 1 mV decrease in the open circuit voltage under oxygen atmosphere but the response was stable and reproducible compared to the almost no response and high noise observed in case of n-ZnO/p-Si junction. Interestingly, the observed sensing behaviour is similar to that observed in all previous systems, where the open circuit voltage decreased upon exposure to oxygen gas. The V_{oc} decrease can be explained on basis of previously discussed SDS sensing mechanism where the poor response towards oxygen gases is reasonable, due to the absence of CdS activation and also because ZnO can only absorb the UV light (4 %) of the whole solar spectrum, which is not sufficient to essentially activate the surface reaction with the ambient.

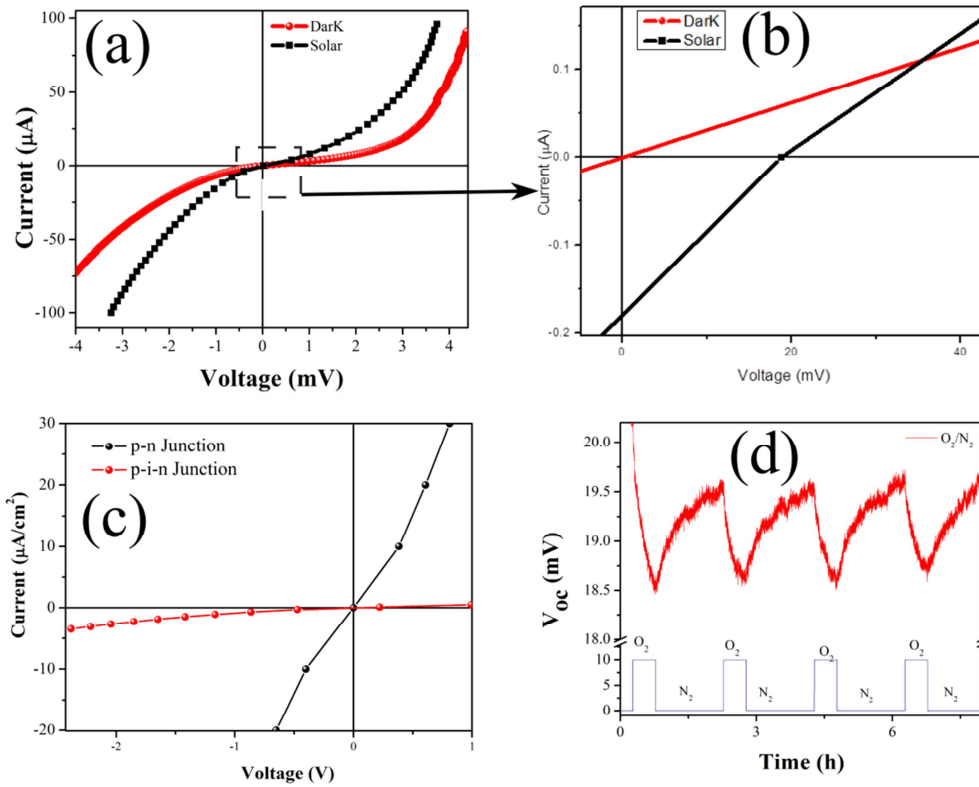


Figure 69 I-V characteristics of n-ZnO/i-AL₂O₃/p-Si heterojunction in dark and under solar illumination. (b) A magnified part of the I-V curve to show the open circuit voltage. (c) The reverse bias I-V characteristics of n-ZnO/p-Si (p-n junction) and n-ZnO/i-AL₂O₃/p-Si (n-i-p junction). (d) ON/OFF (oxygen/ nitrogen) curves of n-ZnO/i-AL₂O₃/p-Si sensor recorded under solar illumination with no applied current ($I = 0$ A) and at room temperature [151].

5.3.2 p-NiO/n-Si substrate

The former SDS systems based on heterojunctions with n-ZnO acting as the active sensing material, it is interesting to continue exploring the new sensing phenomena on planar based heterojunctions by using p-doped material as the active sensing material. Nickel oxide (NiO), a p-type semiconductor with a bandgap of 4.3 eV [214], is a promising material, due to its chemical stability as well as its optical and electrical properties [215] for optoelectronic applications such as gas sensors, organic light emitting diodes (OLED), and display devices [216–218]. In this work, the p-NiO/n-Si heterojunction was fabricated by DC-sputtering and post-annealing technique on n-doped Si substrate. Prior to the deposition of NiO a thin isolation layer of SiO₂ was deposited on a small area of the Si substrate by plasma enhanced chemical vapor deposition

technique (PECVD). Figure 70b shows the XRD patterns of deposited NiO films. The post-annealing temperature used was held at 500 °C in order to avoid destruction of the SiO₂ isolation thin film at higher temperatures. After heat treatment some cracks are visible on the film surface that can be caused by the fast heating rate during the annealing process of 100 °C/min. The in plane and cross sectional-SEM images shown in figure 70 (c,d) of p-NiO sample confirms the deposition of NiO films with a film of about 160 nm thickness.

The p–n diode device was fabricated as schematically represented in figure 70a, by depositing two gold electrodes on the top of NiO with the SiO₂ underneath (p-contact) and on the back side of the n-Si substrate (n-conatct). The SiO₂ layer was used to assure the formation of a p-n diode and not a Schottky diode.

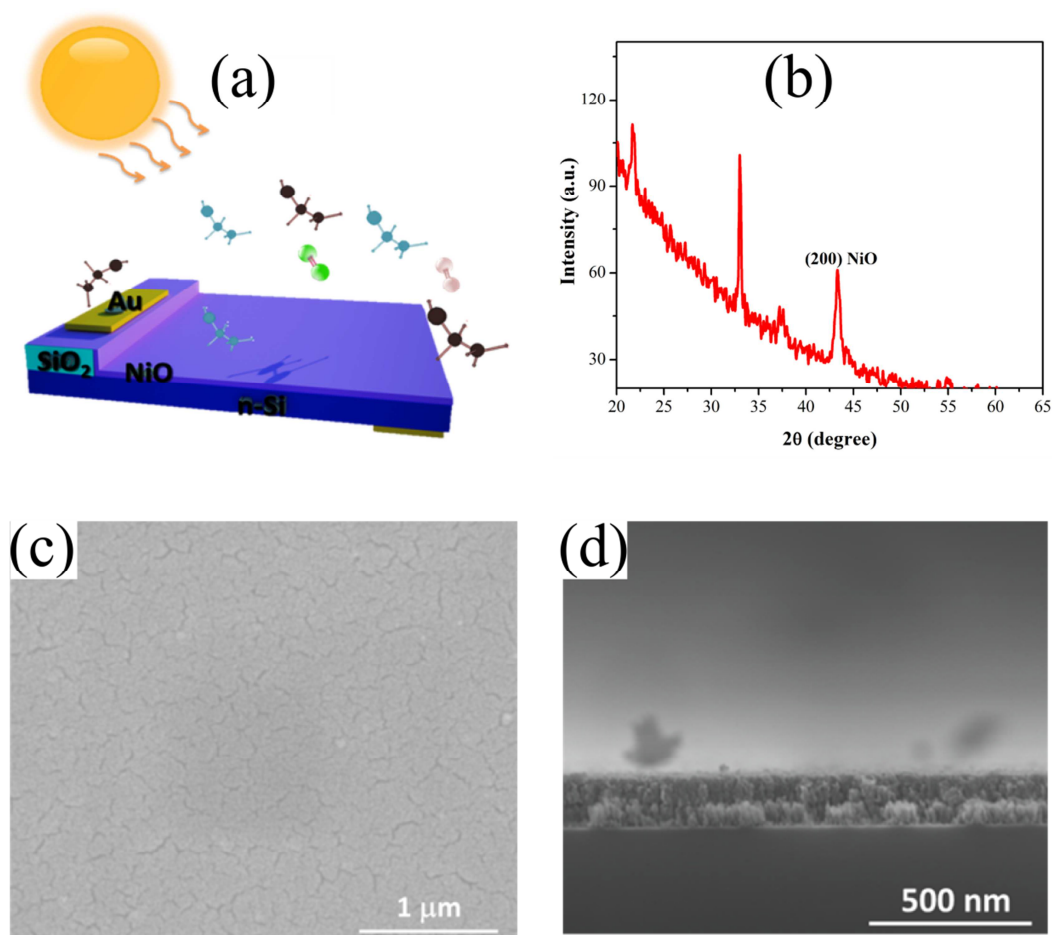


Figure 70 (a) Schematic representation of p-NiO thin film/n-Si heterojunction gas sensor device. (b) XRD pattern of the post-annealed NiO thin film. (c, d) in plane and cross-sectional SEM images of NiO thin film/n-Si heterojunction.

The (I–V) curve of the p-NiO/n-Si device in dark conditions and at room temperature in figure 71a clearly shows a typical rectifying behavior of the device. Under solar illumination the I-V characteristics show a photovoltaic effect of the device with an open circuit voltage (V_{oc}) of 140 mV, as shown in figure 71b.

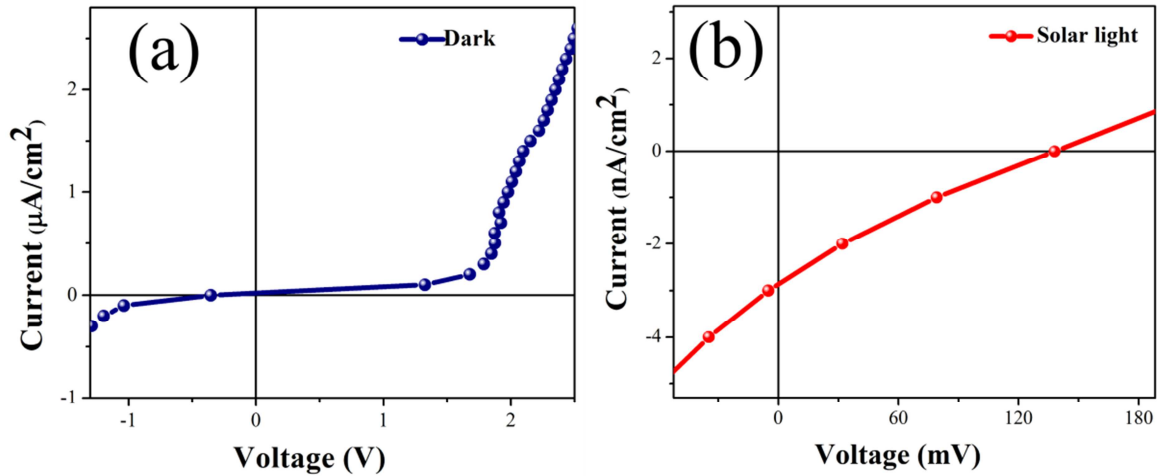


Figure 71 I-V characteristics of p-NiO/n-Si diode heterojunction (a) in dark and (b) under solar illumination.

The gas sensing properties of the p-NiO/n-Si diode were measured under solar illumination in the self-powered mode (see figure 72), where no current was applied. Interestingly the behavior of change in open circuit voltage (ΔV_{oc}) was opposite to that observed in the n-ZnO/p-Si devices, where the active sensing material was an n-type metal oxide. The V_{oc} is increasing in presence of oxidative gases (such as oxygen and NO_2) and decreasing in reducing gases (such as ethanol). It notable that the sensor is more sensitive towards oxidative gases and it shows a poor sensitivity towards reducing gases. The change in open circuit voltage ($\Delta V_{oc} \approx 10$ mV for Oxygen (100%), and 8 mV for NO_2 (20 ppm), and 4 mV for ethanol (1000 ppm diluted in air).

The proposed sensing mechanism can be explained in terms of the surface reaction between p-NiO with oxidizing gases such as oxygen and NO_2 . Under oxygen atmosphere, the electrons at the NiO surface can be trapped by oxygen molecules to form oxygen species. The trapped electrons are subsequently compensated by bulk NiO electrons, causing a decrease of the minor carrier donor density within NiO and result in increase in the open circuit voltage at the p-n interface. In reducing gas atmosphere, the oxidation of EtOH molecules release electrons trapped

at surface oxygen back to NiO. The consequent increase of the minor carrier density within the p-doped material causes the lower V_{oc} value as a signal for the presence of the reductive gas. The low sensing response toward ethanol can be explained in terms of the high activation energy needed for oxidation of ethanol and to activate the interaction with the NiO surface. In future modification of the NiO surface with visible light harvesting nanomaterials can be used to modify NiO surface to increase the solar light absorption and thus to further activate the gas/sensor interaction and hence increase the sensor response.

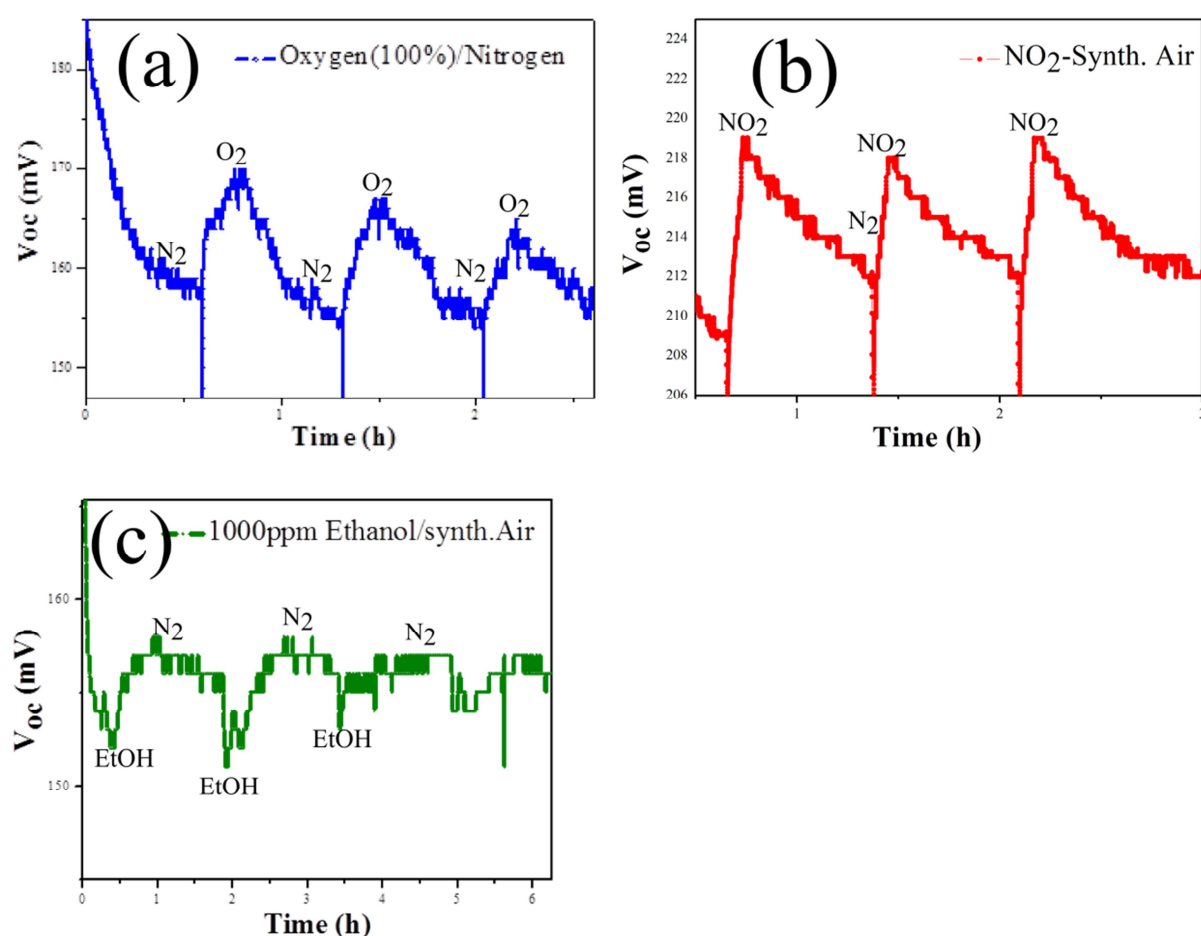


Figure 72 (a) ON/OFF (oxygen/ nitrogen), (b) ON/OFF (NO₂/ synthetic air), c) ON/OFF (1000 ppm ethanol/synthetic air) curves of p-NiO/n-Si sensor recorded under solar illumination with no applied current ($I = 0$ A) and at room temperature.

5.4 Current challenges and future prospects of SP-SDS concept

A new complex nano-system has been developed together with a new sensing concept. Obviously, having a deeper insight on the intimate details of the effects that occur in such a system is instrumental to continue with its further development as well as to extend its applicability to other fields. Here in the major challenges that need to be addressed together with primary results will be discussed with the intention to stimulate the development and movement of SDS concept beyond the current approaches for future development of real self-powered devices.

5.4.1 Charge separation at CdS/ZnO interface

Although time-dependent C-V measurements were performed to elucidate the possible sensing mechanism, however the local optoelectronic properties of CdS/ZnO are still unclear.

Kelvin probe force microscopy (KPFM), as one of scanning probe microscopy, have attracted recent attention as a very powerful tool for real space exploration of the correlation between structural and electrical/electronic properties of hybrid interfaces [83,84,219–221]. KPFM measurements have the ability to map the potential of different nanostructures with a spatial and voltage resolution of a few nanometers and millivolts [84]. KPFM will be used for the SDS system to visualize the photo-generation and charge separation at CdS/ZnO interfaces. The knowledge of CdS-ZnO interplay at nanoscale can provide a direct insight for deeper understanding of the SDS novel sensing mechanism.

The preliminary results are shown in figure 73, where a uniform charge distribution along the ZnO nanowire under UV light illumination can be observed. The generated charge carriers are directed by an alignment of the NW axis which might attributed to the exciton diffusion along the NW axis [83]. When the UV light turned off ZnO nanowire was returned again to a uniform charge distribution.

The ongoing and future experiments will fulfill the KPFM requirements (such as preparation of single nanowire sample with at least 5 μm lengths, choose the right substrate with suitable conductivity, and the single nanowire fixation on host substrates) to improve the resolution and to obtain more precious results. In addition measuring the surface potential under visible light will be performed to demonstrate the effect of CdS on the SDS system.

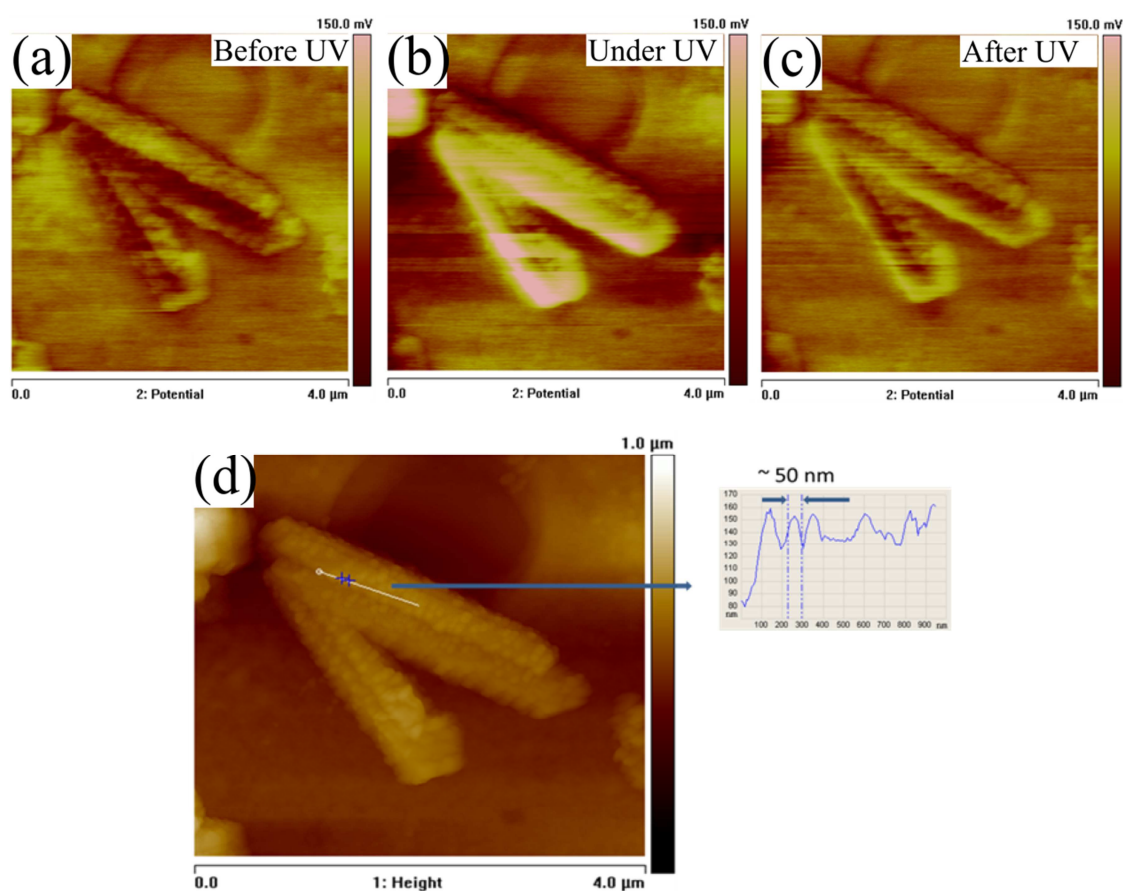


Figure 73 KPFM Image of a CdS decorated ZnO nanowire (a) before UV exposure, (b) under UV exposure, (c) after UV exposure, (d) the corresponding AFM topographic image [151].

5.4.2 Modification and miniaturization of SDS device architecture

5.4.2.1 Improving the top-contact of the current SDS device

The top contact of vertical nanowires is one of the challenging issues which hinder their applications as their device performance can be affected due to poor top-contact. In the SDS proof of concept the mechanical top contact was used for device fabrication, but such design is affecting the sensor response such as slow response and slow recovery times observed as it hinders the gas diffusion into the active sensing material. The direct sputtering of a transparent conductive oxide (TCO) on the top of the nanowires is one of the promising approaches to overcome this problem (see figure 74b) [222,223]. As the nanowires will be more exposed to the surrounding gases and also the resistances in series, arising from the mechanical contact, will be avoided. In the first trails, an Indium doped tin oxide (ITO) layer was deposited directly on the top of the

nanowires, but the film formed was not continuous due to voids between the nanowires (see figure 74a).

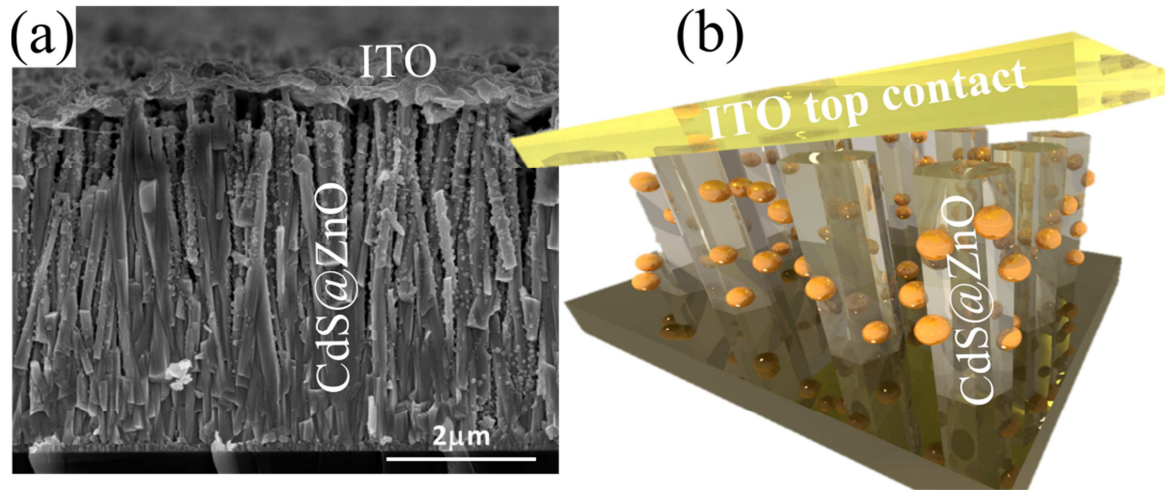


Figure 74 (a) SEM images of ITO layer on the top of CdS@ZnO/p-Si substrate. (b) A schematic representation of the final device with ITO top contact [151].

A different deposition protocol was tried by using a photoresist to fill the voids between the nanowires according to the following procedures as shown in figure 75.

1. Spin casting the photoresist on the sample (Before spinning, the photoresist covered sample was allowed to sit for 10 min to ensure that the photoresist filled the gaps between nanowires)
2. Oxygen Plasma reactive ion etch for 5 min to remove the photoresist from the tip of the nanowires.
3. Reactive ion etching can be repeated to have more exposed surface of nanowires.
4. Deposition of the transparent conducting oxide on the top of nanowires.
5. Removal of the photoresist by acetone.

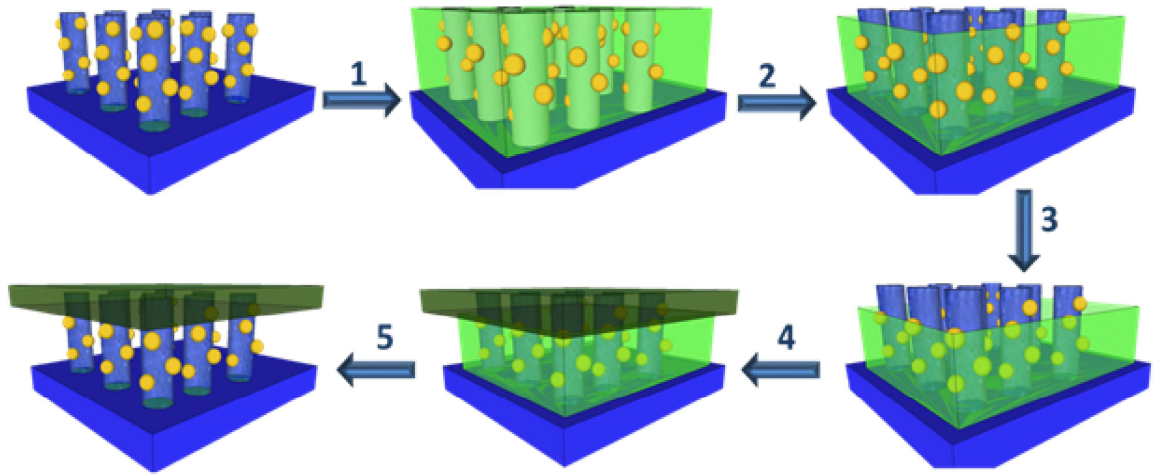


Figure 75 Schematic illustration of the ITO deposition on the top of nanowires. (1) Spin casting the photoresist, (2, 3) Oxygen Plasma reactive ion etch, (4) ITO deposition, (5) Removal of the photoresist.

The process needs more optimization in terms of the resistivity of the produced ITO layers as well as their transparency which is critical for the SDS light activation. After the required optimization steps the electrical as well as the gas sensing properties will be tested to demonstrate the device potential of such systems.

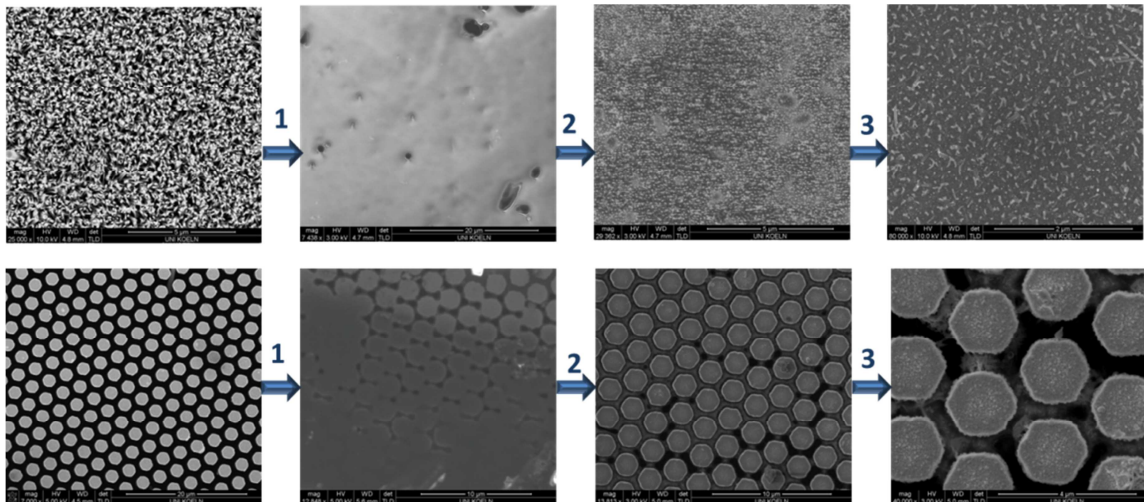


Figure 76 SEM images of ITO deposition steps on the top of nanowire arrays (top set of images) and top of nanopillars (down set images): (1) Spin casting the photoresist, (2, 3) Oxygen plasma reactive ion etch.

5.4.2.2 Development and miniaturization of the SDS device design

A new device design will be used to overcome the problem of slow response and recovery times as an alternative to the aforementioned ITO top contact, where photolithography were employed to produce Si micro-pillars in which ZnO film were deposited followed by a hydro-thermal growth of ZnO nanowires (as shown in figure77). The p-contact and the n-contact of the SDS device will be made directly on Si part and ZnO by masking techniques. The device design is expected to increase the gas/material interaction and enhance the gas diffusion between the pillars which is better than the compact nanowire arrays used in the first generation SDS devices. The electrical characterization as well as the sensing properties will be tested to demonstrate the device performance and the expected response improvement.

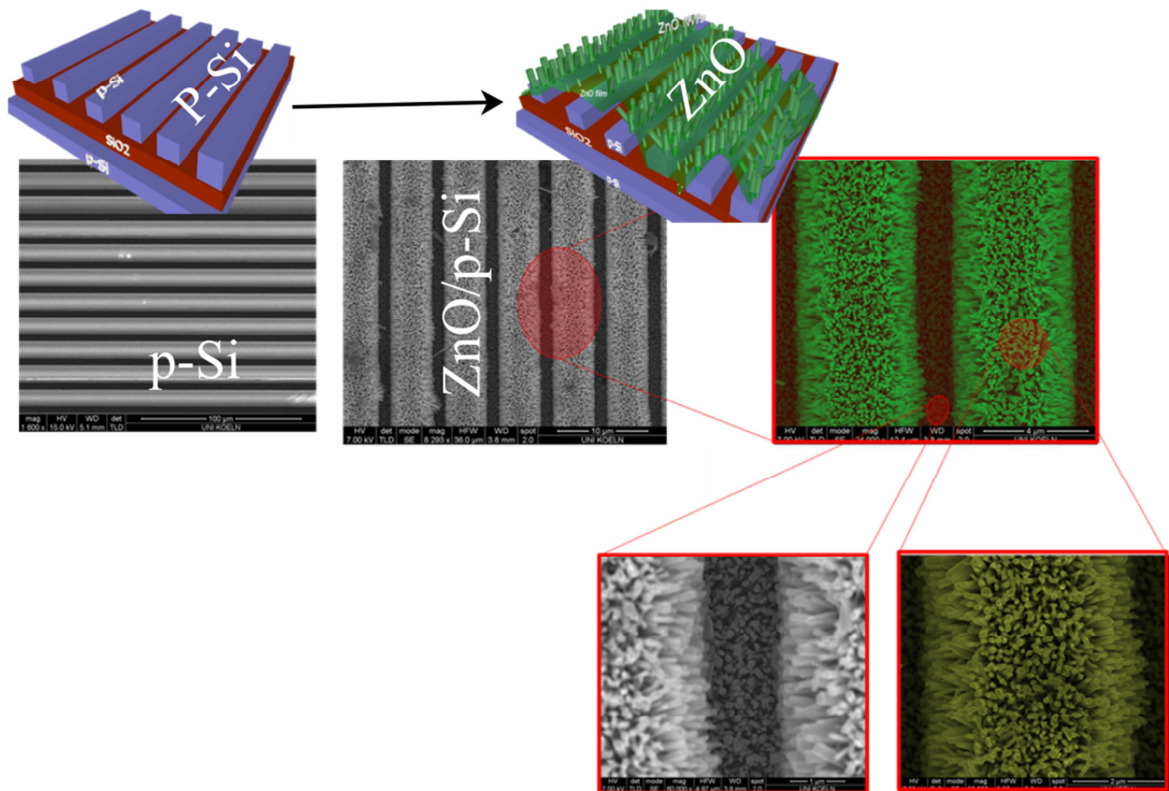


Figure 77 Tilted SEM images of n-ZnO NWs/p-Si/SiO₂/Si miniaturized sensor device.

6. Single Nanowire-Based Heterostructures for Energy and Sensing Applications

One dimensional metal oxide and their different modified heterostructures are a broad class of materials which are gaining a growing interest due to their potential in optoelectronics, gas sensing, and energy applications [210,224–226]. Although preliminary studies revealed promising outcomes of such systems but still further research is needed in order to reach complete control on their properties. The previous discussions have shown the promises of photodiode devices of a variety of complex heterostructures based on 1D nanomaterials. The functional properties of such systems are greatly influenced by their electrical properties, therefore studying such properties is crucial in order to fully understand and maximize their functional abilities for various applications. Working into this direction, the fabrication and demonstration of stand-alone single nanowire prototype devices analog to their multi-nanowires arrays is one of promising ways to advance our current approaches for future applications of nanodevices. Such stand-alone single nanowire devices are not a laboratory curiosity but rather a very efficient tool to achieve a good comprehension of the intrinsic phenomena of single complex heterostructures. Since the statistical dispersion typical of bulk-type systems is eliminated and contact effects are minimized [227].

The integration of active characteristics in a single nanostructure by combinatorial material architectures is a promising approach to develop diodes, transistors or any other active element equivalent to those employed in standard microelectronics [228]. New approaches can be developed and easily explained in single nanowire scale and then the know-how can be used to advance their analog bulk-type devices. In this work, prototype devices based on single nanowire heterostructures will be investigated in terms of their fabrication, electrical characterization as well as their potential applications as stand-alone devices for gas sensing applications.

6.1 Coaxial n-Zno/p-Si single nanowire heterostructures for energy and sensing applications

ZnO is considered an excellent candidate among all n-type metal oxide nanomaterials to obtain functional devices [229–231]. The development of ZnO nanosystems so far has been mainly focused on the use of bare nanowires as, for instance, mere passive resistors, nanogenerators, gas sensors or building-blocks of battery electrodes [227,229], despite some interesting attempts to integrate them as active elements in new technologies and systems [232,233]. In this

context, ZnO-based heterojunctions have recently attracted much focus for highly sophisticated electronic devices [164,234,235], such as n-ZnO/p-Si nanowire heterojunctions that are seen as an interesting alternative to overcome the pending issue of growing high quality and stable p-type ZnO [164].

Radial n-ZnO/p-Si nanowires are expected to exhibit superior performances compared to their conventional planar p-n junction counterparts due to their favorable geometry that maximizes the junction interface area and the built-in field established across it [236–238]. This is particularly interesting for any application involving massive charge carrier separation processes, as for instance, photovoltaics [239,240]. Nevertheless, the electrical access to the inner core of these nanostructures without shorting the final device remains as a challenging avenue from a fabrication point of view.

The previous devices based on n-p junctions were formed at the interface of a nanowire or nanowall with the underlying substrate [241,242], or at the cross interface of two nanowires [243]. The fabrication and the prototyping of single coaxial n-ZnO/p-Si nanowire heterojunction devices was studied to demonstrate their electrical properties at single nanowire scale beside the preliminary assessment of their photovoltaic and gas sensing properties, which has been published only recently based on this work.[227] These stand-alone n-ZnO/p-Si nanowire prototypes are paving the way to further and necessary developments in this incipient research area, and showing the potential to integrate heterostructures with modulated interfaces, and complementary functionalities in a single nanoarchitected device.

6.1.1 Structural characterization and prototype device fabrication

The coaxial heterostructure single nanowire is composed of a core of wet etched Si nanowire with about 24 μm length and a diameter of 300 nm, according to 1h etching time, and a 80 nm polycrystalline ZnO shell ZnO deposited by DC-sputtering/annealing technique at 500 °C (see section4.3.2.1).

The device processing of ZnO/p-Si nanowire (shown schematically in figure 78) includes a mechanical scratching of the as-grown n-ZnO/p-Si nanowires nanowire from its original substrate and dropped on a chip with pre-patterned gold microelectrodes. Then the individual n-ZnO/p-Si nanowires were subjected to a pre-milling step of the n-ZnO part, in order to gain access to the p-

Si core. Finally, platinum (Pt) electrical contacts were fabricated with FIB, where this fabrication process is known to form Ohmic and reliable contacts between platinum and typical semiconductor materials.

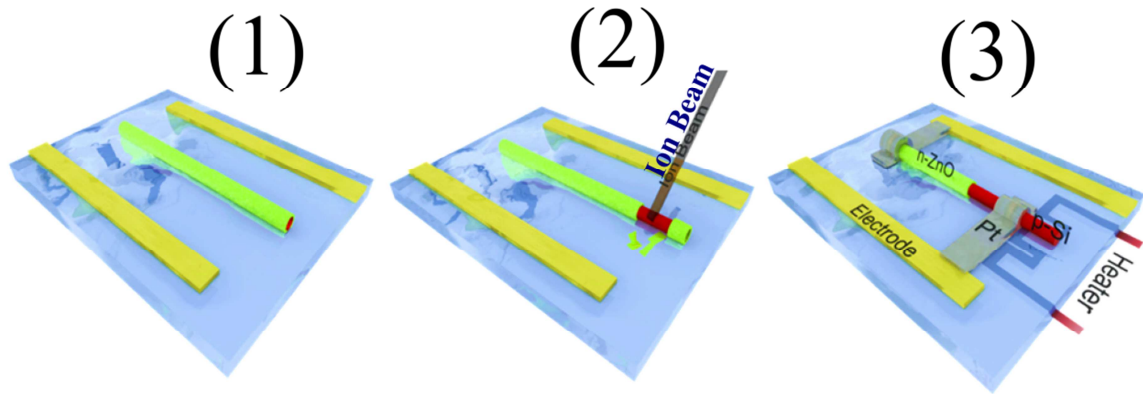


Figure 78 Scheme of an n-ZnO/p-Si nanowire device fabrication process: (1) the nanowire is positioned between two pre-patterned microelectrodes. (2) The n-ZnO shell at one end of the nanowire is removed by FIB milling, granting access to the p-Si core. (3) The nanowire is contacted with FIB nanolithography to the pre-patterned microelectrodes. Both the n-ZnO and p-Si parts are electrically accessible in the final device configuration.

SEM images (see figure 79) show the final device after fabrication, where the complete removal of the ZnO shell from one side of the nanowire to access the Si core is visible, which is the critical step to achieve the desired photodiode device. It's worth to mention here that the device processing steps, including the mechanical scratching as well as the following focused-ion-beam (FIB) processing steps (pre-milling, and electrodes deposition), is creating surface defects as well as surface non-uniformity at some parts of the nanowire as can be seen in the SEM pictures. Besides the aforementioned effects, non-conformal coatings characteristic of the DC-sputter technique used here for the deposition of ZnO shell contributes also to the surface non-uniformity. In this regard, atomic layer deposition technique (ALD) can be a better alternative to be used for deposition of conformal and uniform ZnO films.

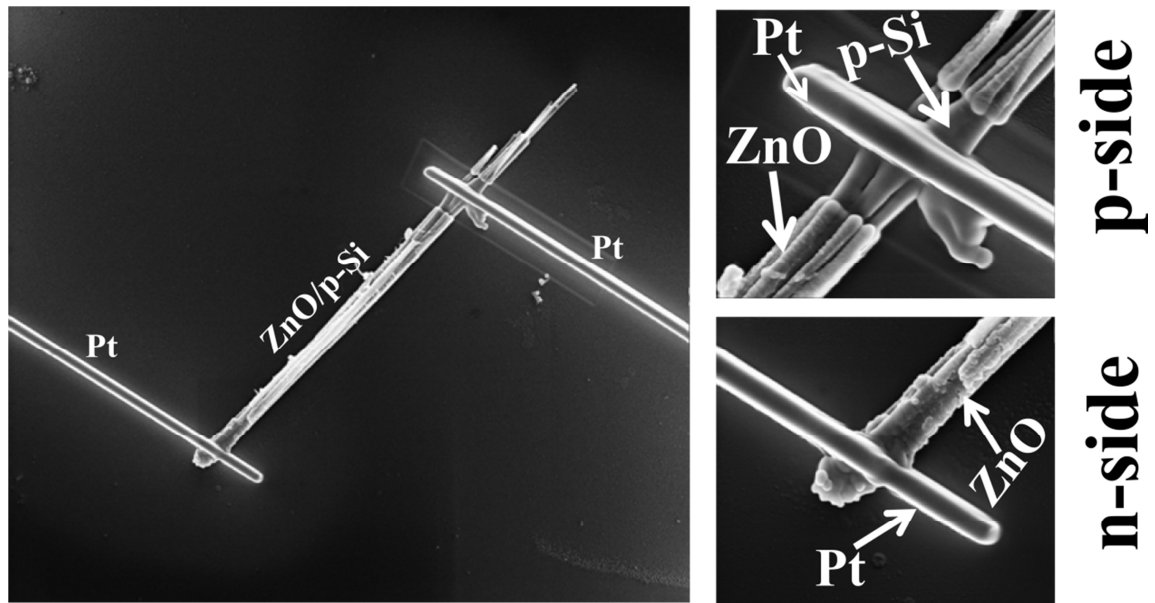


Figure 79 General view of an n-ZnO/p-Si coaxial nanowire device after the FIB fabrication process and the corresponding high magnification image of the p-Si contact area (The removal of the ZnO outer layer is clearly visible) and high magnification image of the n-ZnO contact area.

EDX line scans of the region beside the Pt contacts were performed to identify eventual residuals of the n-ZnO layer in the pre-milled area around the p-Si core contact. Experimental results showed well-detectable amounts of Zn around the n-contact, whereas no evidence of Zn was found within the p-contact area as can be seen from figure 80.

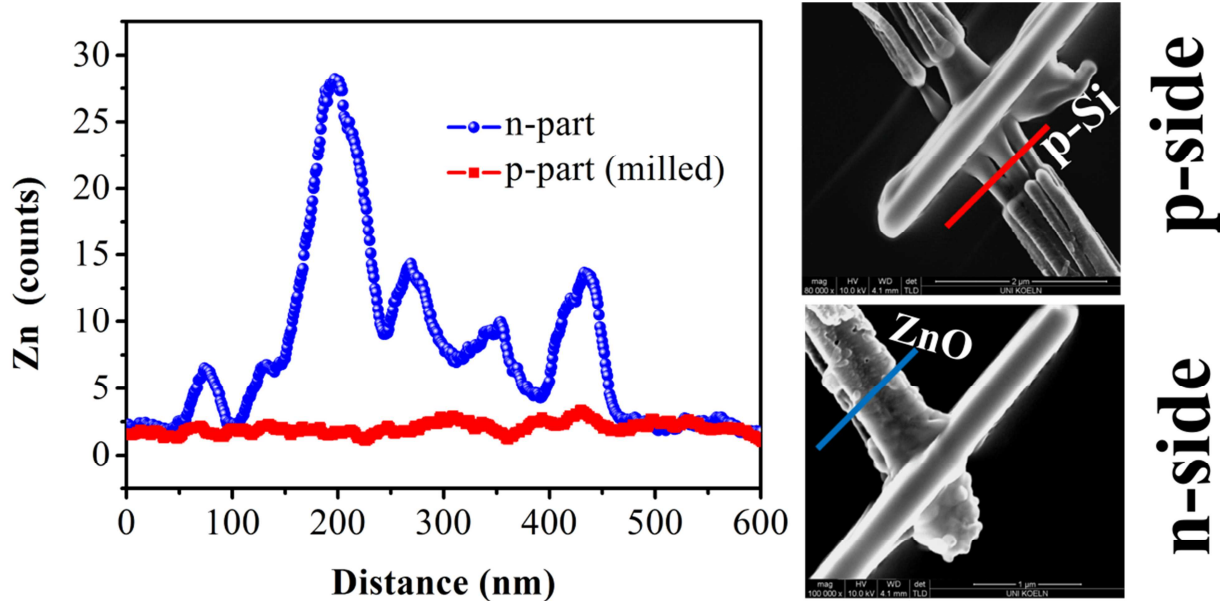


Figure 80 EDX line scans of the two contact areas (as-grown and milled) of the device shown in Fig.2. Zinc counts are only found in the as-grown area, indicating that the outer n-ZnO layer was completely removed after FIB milling.

6.1.2 Electrical properties

The electrical properties of n-ZnO/p-Si were evaluated through the measuring their current voltage curves. Current-voltage (I-V) characteristics of n-ZnO/p-Si nanowires under dark conditions at room temperature exhibited diode characteristics indicative of the formation of p-n junctions in a single nanowire (figure.81). Since no short-circuiting was observed between the two electrical contacts, current was expected to flow mainly through the space charge region inside the nanowires. However, a high reverse bias leakage current was always found, which might be attributed to large interfacial recombination at the p-n interface as a result of uncontrolled defects generated during the wet etching process of Si nanowires, and the later FIB milling step [227,237,244]. Other phenomena like Zn diffusion into the Si nanowires and change of their electrical behavior cannot be discarded. Consequently, the diode response of these devices strongly deviated from the ideal behavior and the electrical signal dramatically degraded in reverse conditions.

To evaluate the characteristics parameters of these devices further, an equivalent circuit formed from an ideal diode in parallel with a standard resistor was used to model their responses

as shown in figure 81. This later element was added to correctly reflect the above mentioned leakage current. The rest of contributions arising from cables and the metal-nanowire contacts were deliberately neglected to simplify the equivalent circuit. Thus, current (I) through the devices was given by the following (equation 47),

$$I(V) = \left[I_0 \left(e^{\frac{qV}{\eta k_B T}} - 1 \right) \right] + \frac{V}{R_L} \quad [47]$$

where I_0 is the reverse bias current, q is the elemental charge, V is the applied voltage, k_B is the Boltzmann constant, T is the working temperature, η is the diode ideality factor and R_L is the resistor used to take into account the deviation from the ideal situation introduced by the leakage current. As shown in figure 81, experimental data fitted well to Equation 52 ($r = 0.998$), being $I_0 = (6.2 \pm 0.9)$ nA, $\eta = (12.1 \pm 0.4)$ and $R_L = (1.5 \pm 0.7)$ M Ω . These values show that R_L is not large enough to avoid the reverse conduction through the p-n junction in normal working conditions.

The I-V curves of the n-ZnO/p-Si nanowire devices recorded under solar illumination showed photovoltaic (PV) properties, yielding a $V_{OC} = 1$ mV and $I_{ph} = 1.0$ nA as mean values for all the tested devices. To take into account the PV contribution, a current source was added to the equivalent circuit (figure 81). Again, experimental data fitted well ($r = 0.9998$) to the modified model given by equation 48 (see figure 81),

$$I(V) = \left[I_0 \left(e^{\frac{qV}{\eta k_B T}} - 1 \right) - I_{ph} \right] + \frac{V}{R_L} \quad [48]$$

where I_{ph} is the photocurrent contribution. It is important to mention that V_{OC} and I_{ph} values were still low compared to previous results reported in the past [243,245]. However, the comparison of the efficiency of the current devices with the other reported ZnO single nanowire devices, either positioned on different p-substrates or p-n homojunctions, is not straightforward. Since there are many other influences that affect the device performance such as the nanowire diameter, the crystallinity, the quality of the p-n interface, the intensity of light illumination and so on. The low efficiency of our devices is explained by the large surface recombination in our heterojunction-based nanowires, which might be aggravated by the surface roughness and the polycrystalline structure of the ZnO shell. Moreover, defects created during the synthesis and the later FIB

processing are expected to play a key role against [244]. For this reason, better design and fabrication strategies are required to minimize these contributions.

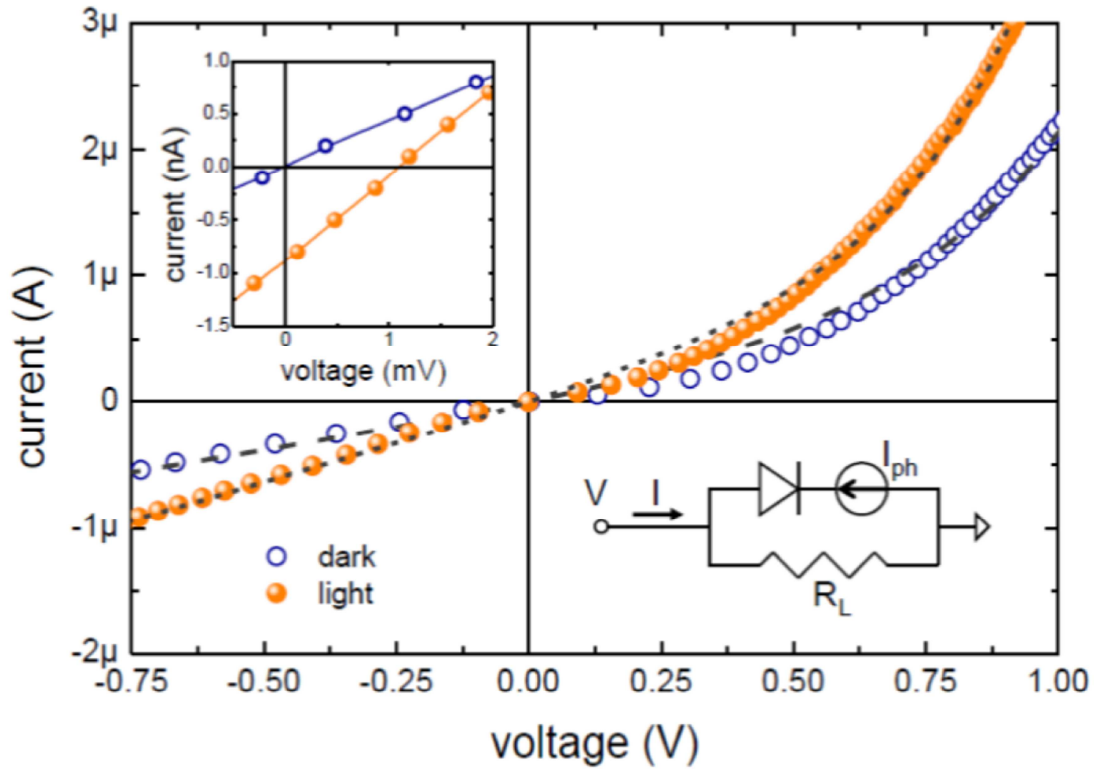


Figure 81 I-V curves from an n-ZnO/p-Si nanowire measured in dark and light conditions and at room temperature. The rectifying responses were fitted to the equivalent model shown in the inset (dashed line). A photogenerated current I_{ph} , and open voltage V_{oc} of 1,0 nA and 1mV respectively were observed under illumination (inset).

6.1.3 Gas sensing properties

Gas sensors based on p-n photodiodes are promising alternatives to replace the well-known resistive metal oxides that are widely used in sensor technology, as their sensing properties are greatly dependent on their electrical properties [183,184]. In the previous chapters the light interaction with photodiodes could produce novel sensing devices that can operate without any external power except the solar light. Here in the modulation of gas sensing response could be achieved through the control of the applied currents in correspondence to the diode characteristics to obtain maximum efficiency under same working temperatures. This is quite promising ap-

proach to reduce the needed power required to drive a highly sensitive gas sensors for real world applications.

The gas sensing characteristics of n-ZnO/p-Si heterojunction showed that the p-n devices can be operated under specific experimental conditions to maximize the response to gases, where their non-linear I-V characteristics could be used to define a differential resistance at a given point of the I-V curve which is calculated by,

$$r^{diff} \equiv \left. \frac{dV}{dI} \right|_{I_{bias}} \quad [49]$$

Therefore and similar to the standard response in conventional resistive metal oxide sensors [21,246], here the differential response S could be defined as,

$$S \equiv \frac{r_{O_2}^{diff} - r_{N_2}^{diff}}{r_{N_2}^{diff}} \times 100 \quad [50]$$

where $r_{O_2}^{diff}$ and $r_{N_2}^{diff}$ are the differential resistance in oxygen and nitrogen respectively.

To validate the key role of the bias current I_{bias} in the gas response, the nanowires were exposed to different oxygen concentrations and bias regimes of the p-n junction: (i) reverse mode, (ii) slightly reverse mode, (iii) slight forward mode and (iv) forward mode as shown in figure 82. The working temperature was kept above 100 °C to support oxygen desorption. Stable and reproducible responses were always found, showing a direct modulation of electrical density, as function of oxygen content in the air, without any evidence of saturation (figure 82). The oxygen sensing mechanism in ZnO is well-known, and it is mainly related to the role of oxygen vacancies and their compensation upon oxygen adsorption [244,246]. When S was plotted against I_{bias} , it was clearly observed that the optimum working condition (highest sensitivity) is found at slightly reverse mode (ii) as can be seen if figure 83, since total probing current through the devices is minimized. As a consequence, in these conditions surface effect contributions and the associated carrier exchange due to chemical reactions is maximized, compared to the total carriers flowing through the device.

On the contrary, if the devices were operated in the modes (i), (iii) and (iv) the response was progressively diminished due to the large number of carriers in the nanowire and their

associated screening effect. From figure 82, it is clear that this description is particularly true in direct mode (iii & iv), but it is also found in reverse mode if leakage current contribution becomes important (i).

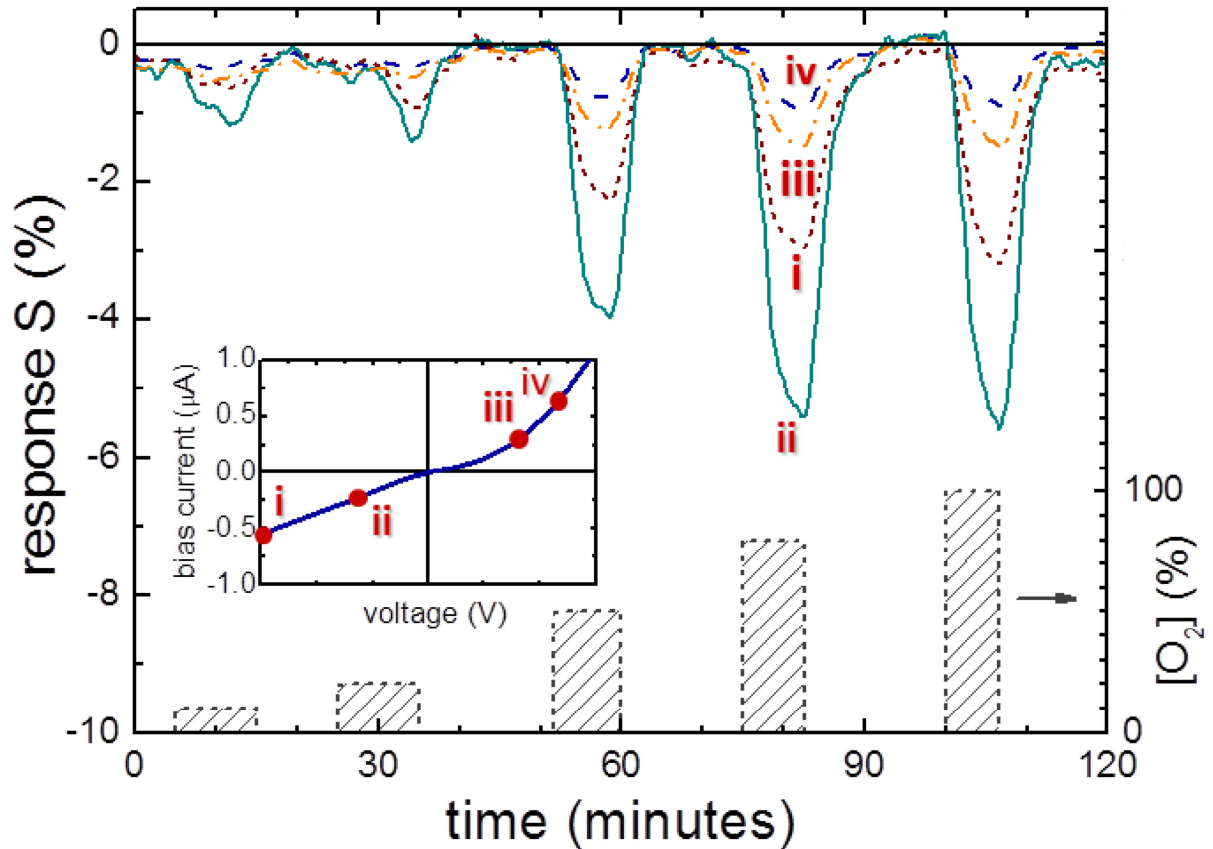


Figure 82 Dynamic response an n-ZnO/p-Si nanowire to different oxygen pulse concentrations as function of the selected bias regime (inset)

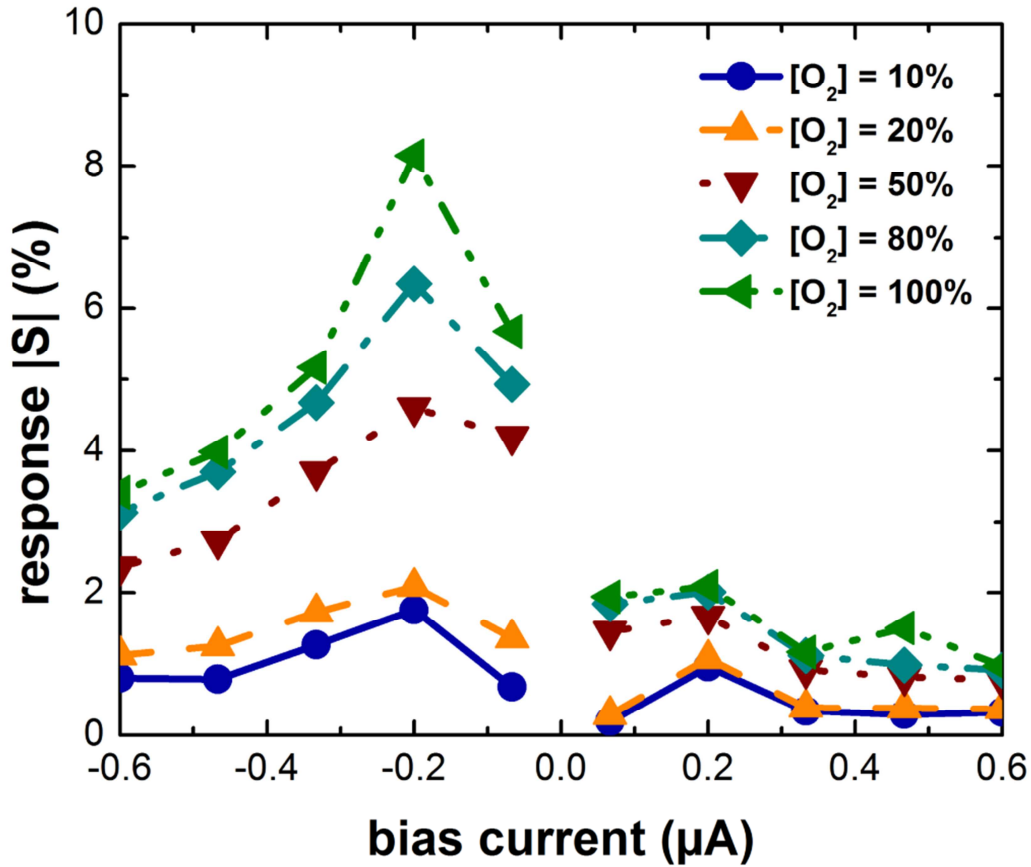


Figure 83 Response of an n-ZnO/p-Si nanowire prototype sensor device to different oxygen concentrations as function of the bias current through the device.

6.2 Current challenges and future prospects of single nanowire devices

The single nanowire sensor devices fabricated and discussed above could demonstrate the potential of using single nanowire diodes for gas sensor applications; however a number of important limitations were observed and need to be considered in future. The electrical characterization of single nanowire devices reveal a low interface quality between ZnO shell and Si nanowire core which was reflected in the high leakage currents observed in the I-V characteristics. For this reason new experiments were designed to deposit ZnO shell on the Si nanowire core by ALD technique to assure conformal coatings as well as better interface quality. The fabrication of the prototype devices of p-n heterojunction diodes could not be achieved due to some technical problems with FIB milling tool, this is the reason that two Ohmic contacts were made on the top of the ZnO shell to fabricate a traditional resistor sensor. The preliminary data are

shown here. SEM images in figure 84 (a,b) show the final device connected with two platinum electrodes. The preliminary sensing responses toward different gases are shown in figure 84c. It is worth to mention here that the lowest temperatures needed to activate the sensor was higher than that needed to activate the diode based sensors. More optimization is needed to develop more efficient single nanowire sensors near future.

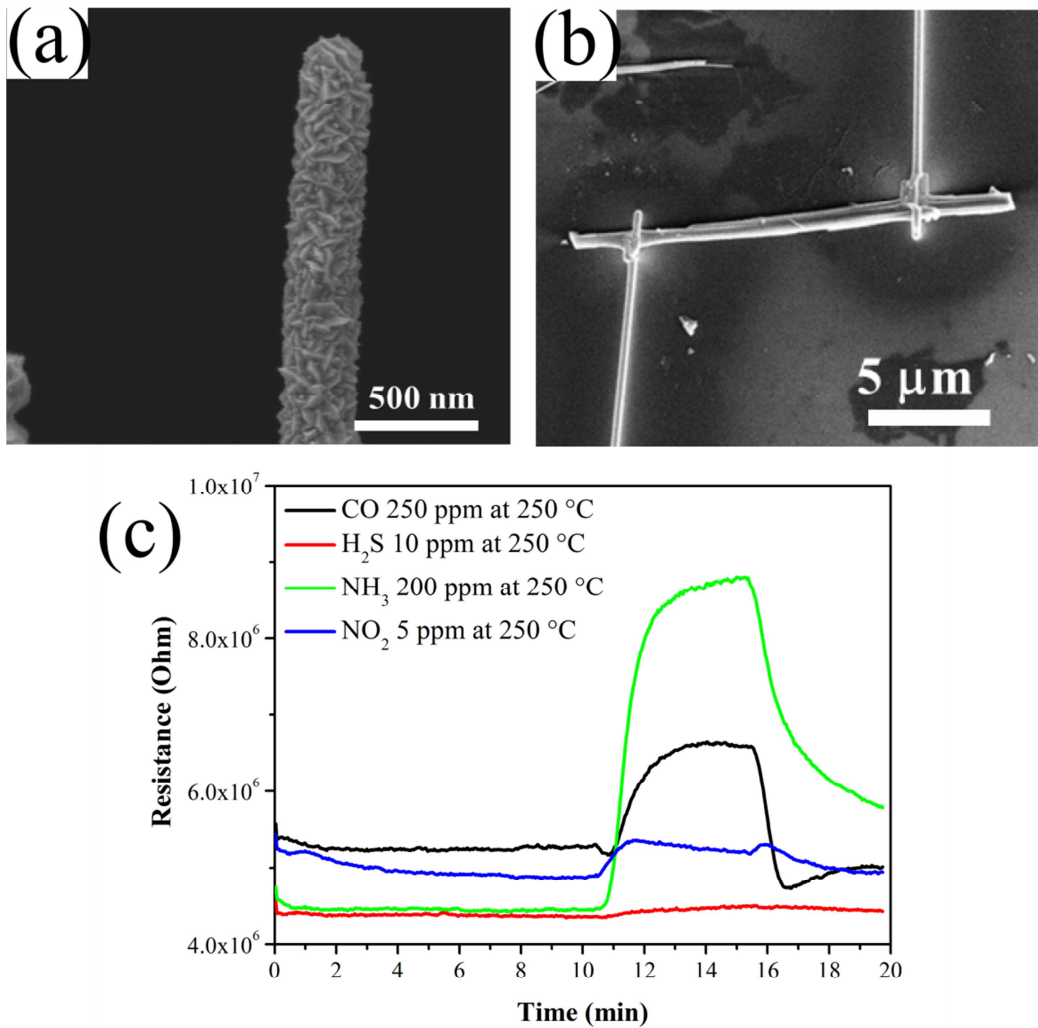


Figure 84 (a) SEM images of ZnO shell deposited by ALD technique a p-Si nanowire core, (b) the n-ZnO/p-Si nanowire single devices connected by two Pt electrodes, (c) the gas sensing responses toward different gases (5 ppm NO₂, 200 ppm NH₃, 10 ppm H₂S, 250 ppm CO) at 250 °C.

7. Summary

In this thesis, a systematic study has been conducted on the controlled synthesis of functional heterostructures and their applications as low- and self-powered gas sensors. The following goals have been achieved

1. Controlled synthesis of well aligned ZnO nanowires directly on the device substrates. This was achieved through the use of proper seed layer films of ZnO and optimization of the subsequent nanowire hydrothermal growth conditions. In this regard, the ZnO seed layers deposited by DC-sputtering/annealing technique were the most aligned films, which have reproducible depositions and controlled thickness. Afterwards, different hydrothermal growth conditions were varied, where the supersaturated growth solutions made by adding aluminum-iso-propylate, produced the best aligned nanowires in this work.

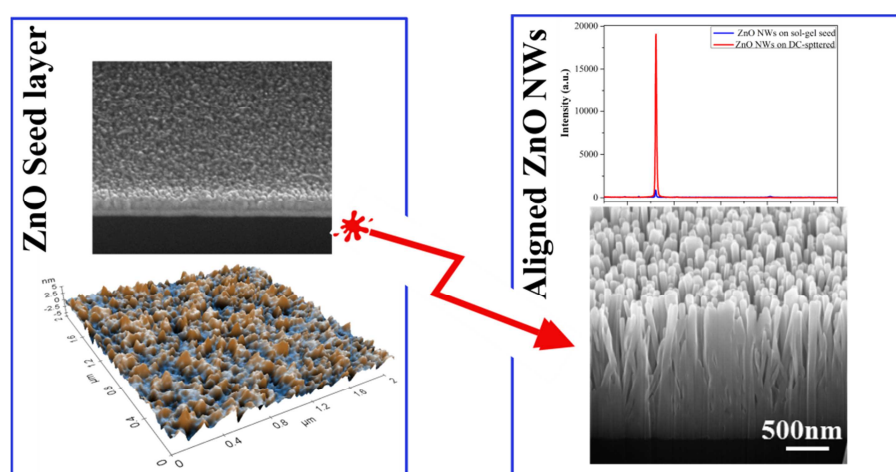


Figure 85 Controlled growth of well-aligned ZnO nanowires.

2. Fabrication of p-n heterojunctions and their complex heterostructures

Heterostructures with a suitable band energy alignment and high-quality interfaces are needed to build multifunctional nanosystems. In this work different heterostructures based on ZnO were successively fabricated such as p-n heterojunctions (in combination with different p-materials such as planar p-Si substrates and p-Si nanowires and different p-metal oxides), and complex 3D heterostructures. The produced heterostructures were further modified by CdS NPs decoration on their

surfaces to enable visible light harvesting, which was required for their application in solar light activated gas sensors.

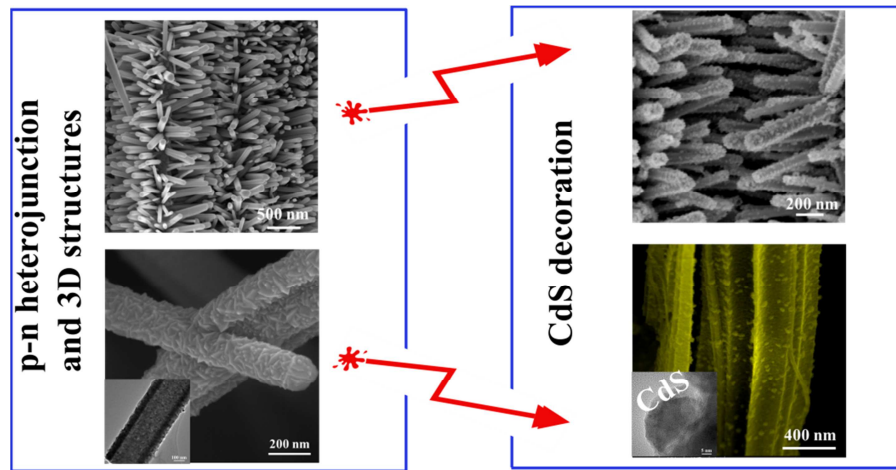


Figure 86 Fabrication of p-n heterojunctions based on ZnO and their complex heterostructures as well as CdS decoration.

3. Development of an innovative approach of autonomously operated gas sensors, named solar diode sensor (SDS). It is based on a CdS@n-ZnO/p-Si nanosystem which unifies gas sensing (CdS@n-ZnO) and solar energy harvesting (n-ZnO/p-Si) functionalities in one single device. A novel sensing mechanism (change of open circuit voltage, ΔV_{oc}), in comparison to the well-known conductometric sensors (ΔR), was demonstrated. It was explained in terms of modulated polarization of the nanoparticles/nanowire interface, gas-material surface interactions and the subsequent changes in the doping level (N_D), which is manifested in the variation of V_{oc} in CdS@n-ZnO/p-Si. The fabricated sensors were capable of detecting oxidizing and reducing gases with reproducible response at room temperature and with no need of any other energy source except solar light illumination to deliver a self-sustained gas sensor signal. The generality of the new concept was demonstrated by extending the approach to other nanomaterial geometries including radial heterojunctions of CdS@ZnO/p-Si nanowires and thin-film planar heterojunction.

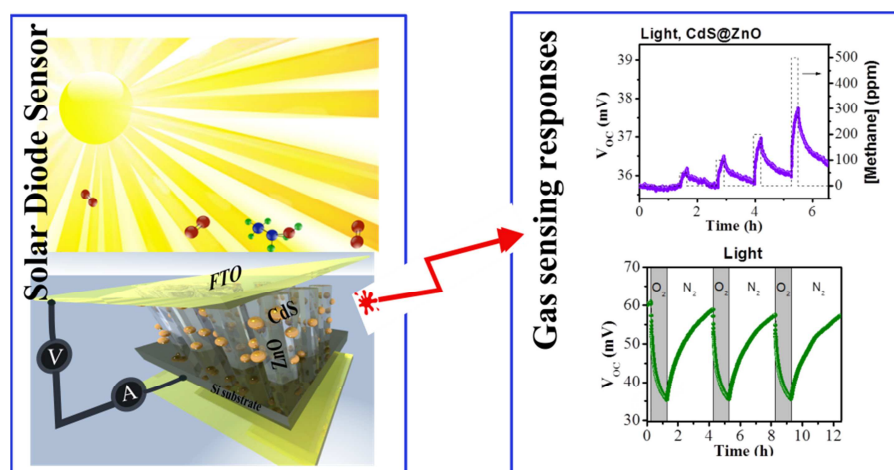


Figure 87 Autonomously operated solar diode sensors (SDS).

4. The fabrication of stand-alone single nanowire devices was employed to study the inherent intrinsic electrical and functional properties of single coaxial heterostructures. In this work, the electrical characterization, the photovoltaic and gas sensing performances of a hetero-junction device based on a single coaxial n-ZnO/p-Si nanowire were preliminary assessed. The gas sensing response of the p-n heterojunction could be usefully modulated by controlling the bias currents through the device.

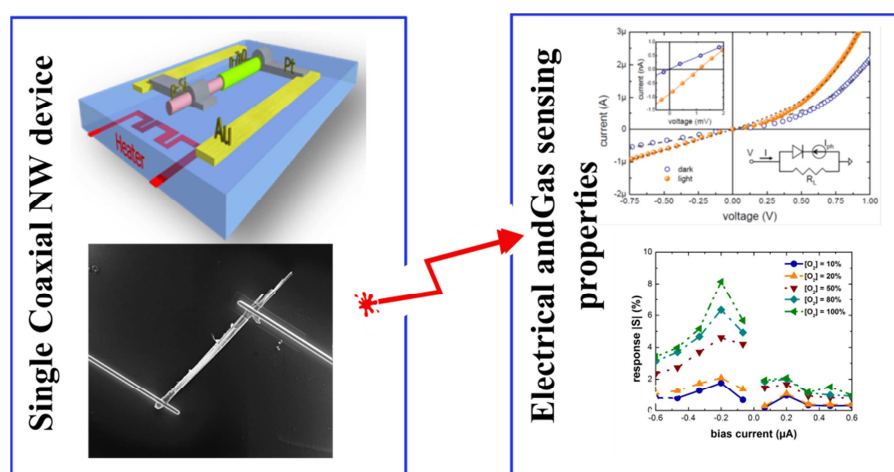


Figure 88 Heterojunction device based on a single coaxial n-ZnO/p-Si nanowire

8. References

- [1] H. W. Kroto, J. R. Heath, S. C. O'Brien, R. F. Curl, R. E. Smalley, *Nature* **1985**, *318*, 162–163.
- [2] M. Monthieux, V. L. Kuznetsov, *Carbon* **2006**, *44*, 1621–1623.
- [3] Lawrence M. Krauss, *Quantum Man: Richard Feynman's Life in Science (Great Discoveries)*, W. Norton & Company, 2011, **2011**.
- [4] N. Taniguchi, *Proceedings of the International Conference on Production Engineering, Tokyo, 1974, Part II (Japan Society of Precision Engineering)*. **1974**.
- [5] S. M. T. Fischer, A. P. Singh, T. Singh, F. Hernández Ramírez, D. Prades, *Multi-component Metal Oxide Nano-architectures for Chemical Sensors*, Springer Science, **2012**.
- [6] Ü. Morkoç, H. and Özgür, *Zinc Oxide: Fundamentals, Materials and Device Technology*, Wiley-VCH Verlag GmbH & Co. KGaA, Weinheim, Germany., **2009**.
- [7] H. S. S. Mathur, A. P. Singh, R. Müller, T. Leuning, T. Lehnen, *Metal–Organic Chemical Vapor Deposition of Metal Oxide Films and Nanostructures*, Wiley-VCH Verlag GmbH & Co. KGaA, Weinheim, Germany., **2011**.
- [8] S. Mathur, S. Barth, H. Shen, J.-C. Pyun, U. Werner, *Small (Weinheim an der Bergstrasse, Germany)* **2005**, *1*, 713–7.
- [9] C. Cao, R. P. Appelbaum, R. Parker, *Technology in Society* **2013**, *35*, 55–64.
- [10] P. Jayakumar, *Asian and Pacific Centre for Transfer of Technology Of the United Nations – Economic and Social Commission for Asia and the Pacific (ESCAP)* **2009**, 1–117.
- [11] “Solar Spectrum,” can be found under http://en.wikipedia.org/wiki/File:Solar_Spectrum.png, **n.d.**
- [12] Z. Wang, *Georgia Institute of Technology, SMARTech digital repository* (<http://hdl.handle.net/1853/39262>) **2011**, 1–131.
- [13] O. Arslan, A. P. Singh, L. Belkoura, S. Mathur, *Journal of Materials Research* **2013**, *28*, 1947–1954.
- [14] S. Xu, Z. L. Wang, *Nano Research* **2011**, *4*, 1013–1098.
- [15] J. Cui, *Materials Characterization* **2012**, *64*, 43–52.
- [16] T. Seiyama, A. Kato, K. Fujiishi, M. Nagatani, *Analytical Chemistry* **1962**, *34*, 1502–1503.
- [17] Taguchi N., *Japan Patent 45-38200*, **1962**.
- [18] J. Pan, H. Shen, S. Mathur, *Journal of Nanotechnology* **2012**, *2012*, 1–12.
- [19] G. Di Francia, B. Alfano, V. La Ferrara, *Journal of Sensors* **2009**, *2009*, 1–18.

References

- [20] F. Shao, M. W. G. Hoffmann, J. D. Prades, R. Zamani, J. Arbiol, J. R. Morante, E. Varechkina, M. Rumyantseva, A. Gaskov, I. Giebelhaus, T. Fischer, S. Mathur, F. Hernández-Ramírez, *Sensors and Actuators B: Chemical* **2013**, *181*, 130–135.
- [21] N. S. Ramgir, Y. Yang, M. Zacharias, *Small (Weinheim an der Bergstrasse, Germany)* **2010**, *6*, 1705–22.
- [22] J. Han, F. Fan, C. Xu, S. Lin, M. Wei, X. Duan, Z. L. Wang, *Nanotechnology* **2010**, *21*, 405203.
- [23] N. Yamazoe, *Sensors and Actuators B: Chemical* **1991**, *5*, 7–19.
- [24] E. Comini, C. Baratto, G. Faglia, M. Ferroni, a. Vomiero, G. Sberveglieri, *Progress in Materials Science* **2009**, *54*, 1–67.
- [25] X. Chen, C. K. Y. Wong, C. a. Yuan, G. Zhang, *Sensors and Actuators B: Chemical* **2013**, *177*, 178–195.
- [26] A. Menzel, K. Subannajui, F. Güder, D. Moser, O. Paul, M. Zacharias, *Advanced Functional Materials* **2011**, *21*, 4342–4348.
- [27] M. BATZILL, U. DIEBOLD, *Progress in Surface Science* **2005**, *79*, 47–154.
- [28] E. Comini, *Analytica chimica acta* **2006**, *568*, 28–40.
- [29] N. B rsan, U. Weimar, *Journal of Physics: Condensed Matter* **2003**, *15*, R813–R839.
- [30] S. . Hahn, N. Bârsan, U. Weimar, S. . Ejakov, J. . Visser, R. . Soltis, *Thin Solid Films* **2003**, *436*, 17–24.
- [31] L. Deng, X. Ding, D. Zeng, S. Tian, H. Li, C. Xie, *Sensors and Actuators B: Chemical* **2012**, *163*, 260–266.
- [32] J. Zhai, D. Wang, L. Peng, Y. Lin, X. Li, T. Xie, *Sensors and Actuators B: Chemical* **2010**, *147*, 234–240.
- [33] K. J. Choi, H. W. Jang, *Sensors (Basel, Switzerland)* **2010**, *10*, 4083–99.
- [34] B. P. J. de Lacy Costello, R. J. Ewen, N. M. Ratcliffe, M. Richards, *Sensors and Actuators B: Chemical* **2008**, *134*, 945–952.
- [35] L. Peng, Q. Zhao, D. Wang, J. Zhai, P. Wang, S. Pang, T. Xie, *Sensors and Actuators B: Chemical* **2009**, *136*, 80–85.
- [36] J. D. Prades, R. Jimenez-Diaz, F. Hernandez-Ramirez, S. Barth, a. Cirera, a. Romano-Rodriguez, S. Mathur, J. R. Morante, *Sensors and Actuators B: Chemical* **2009**, *140*, 337–341.
- [37] H. Chen, Y. Liu, C. Xie, J. Wu, D. Zeng, Y. Liao, *Ceramics International* **2012**, *38*, 503–509.
- [38] Y. Li, J. Gong, G. He, Y. Deng, *Materials Chemistry and Physics* **2012**, *134*, 1172–1178.

- [39] J. Sun, J. Xu, Y. Yu, P. Sun, F. Liu, G. Lu, *Sensors and Actuators B: Chemical* **2012**, *169*, 291–296.
- [40] S.-W. Fan, A. K. Srivastava, V. P. Dravid, *Applied Physics Letters* **2009**, *95*, 142106.
- [41] L. Han, D. Wang, Y. Lu, T. Jiang, B. Liu, Y. Lin, *The Journal of Physical Chemistry C* **2011**, *115*, 22939–22944.
- [42] L. Han, D. Wang, J. Cui, L. Chen, T. Jiang, Y. Lin, *Journal of Materials Chemistry* **2012**, *22*, 12915.
- [43] J. Zhai, L. Wang, D. Wang, H. Li, Y. Zhang, D. Q. He, T. Xie, *ACS applied materials & interfaces* **2011**, *3*, 2253–8.
- [44] M. Li, G. Meng, Q. Huang, Z. Yin, M. Wu, Z. Zhang, M. Kong, *Langmuir : the ACS journal of surfaces and colloids* **2010**, *26*, 13703–6.
- [45] L. Peng, Q. Zeng, H. Song, P. Qin, M. Lei, B. Tie, T. Wang, *Applied Physics A* **2011**, *105*, 387–392.
- [46] R. Chauhan, A. Kumar, R. P. Chaudhary, *Research on Chemical Intermediates* **2012**, *38*, 1483–1493.
- [47] T. Morikawa, T. Ohwaki, K. Suzuki, S. Moribe, S. Tero-Kubota, *Applied Catalysis B: Environmental* **2008**, *83*, 56–62.
- [48] N. V. Kaneva, D. T. Dimitrov, C. D. Dushkin, *Applied Surface Science* **2011**, *257*, 8113–8120.
- [49] Q. Xiao, L. Ouyang, *Journal of Alloys and Compounds* **2009**, *479*, L4–L7.
- [50] Y. Liu, J. Shi, Q. Peng, Y. Li, *Chemistry (Weinheim an der Bergstrasse, Germany)* **2013**, *19*, 4319–26.
- [51] B. Palanisamy, C. M. Babu, B. Sundaravel, S. Anandan, V. Murugesan, *Journal of hazardous materials* **2013**, *252-253*, 233–42.
- [52] X. Wang, G. Liu, Z.-G. Chen, F. Li, L. Wang, G. Q. Lu, H.-M. Cheng, *Chemical communications (Cambridge, England)* **2009**, 3452–4.
- [53] Y. Myung, D. M. Jang, T. K. Sung, Y. J. Sohn, G. B. Jung, Y. J. Cho, H. S. Kim, J. Park, *ACS nano* **2010**, *4*, 3789–800.
- [54] C.-H. Hsu, C.-H. Chen, D.-H. Chen, *Journal of Alloys and Compounds* **2013**, *554*, 45–50.
- [55] P. Chen, L. Gu, X. Cao, *CrystEngComm* **2010**, *12*, 3950.
- [56] A. Zaban, O. I. Mičić, B. A. Gregg, A. J. Nozik, *Langmuir* **1998**, *14*, 3153–3156.
- [57] J. Jiang, X. Zhang, P. Sun, L. Zhang, **2011**, 20555–20564.

References

- [58] D. K. Kanan, E. A. Carter, *The Journal of Physical Chemistry C* **2012**, *116*, 9876–9887.
- [59] Y. Tak, S. J. Hong, J. S. Lee, K. Yong, *Journal of Materials Chemistry* **2009**, *19*, 5945.
- [60] M. Seol, H. Kim, W. Kim, K. Yong, *Electrochemistry Communications* **2010**, *12*, 1416–1418.
- [61] E. Strelcov, S. Dmitriev, B. Button, J. Cothren, V. Sysoev, A. Kolmakov, *Nanotechnology* **2008**, *19*, 355502.
- [62] J. D. Prades, R. Jimenez-Diaz, F. Hernandez-Ramirez, S. Barth, A. Cirera, A. Romano-Rodriguez, S. Mathur, J. R. Morante, *Applied Physics Letters* **2008**, *93*, 123110.
- [63] L. F. Zhu, J. C. She, J. Y. Luo, S. Z. Deng, J. Chen, X. W. Ji, N. S. Xu, *Sensors and Actuators B: Chemical* **2011**, *153*, 354–360.
- [64] P. Hiralal, H. E. Unalan, G. A. J. Amaratunga, **2012**, *194002*, DOI 10.1088/0957-4484/23/19/194002.
- [65] P. V Kamat, *The Journal of Physical Chemistry Letters* **2013**, *4*, 908–918.
- [66] R. S. Selinsky, Q. Ding, M. S. Faber, J. C. Wright, S. Jin, *Chemical Society reviews* **2013**, *42*, 2963–85.
- [67] R. S. Selinsky, Q. Ding, M. S. Faber, J. C. Wright, S. Jin, *Chemical Society reviews* **2013**, *42*, 2963–85.
- [68] P. V Kamat, *Accounts of chemical research* **2012**, *45*, 1906–15.
- [69] L. Carbone, P. D. Cozzoli, *Nano Today* **2010**, *5*, 449–493.
- [70] K. Tvrdy, P. a Frantsuzov, P. V Kamat, *Proceedings of the National Academy of Sciences of the United States of America* **2011**, *108*, 29–34.
- [71] B. Hyun, Y. Zhong, A. C. Bartnik, L. Sun, H. D. Abrun, F. W. Wise, J. D. Goodreau, J. R. Matthews, T. M. Leslie, N. F. Borrelli, **n.d.**, *2*.
- [72] H. C. Leventis, F. O'Mahony, J. Akhtar, M. Afzaal, P. O'Brien, S. a Haque, *Journal of the American Chemical Society* **2010**, *132*, 2743–50.
- [73] D. F. Watson, *The Journal of Physical Chemistry Letters* **2010**, *1*, 2299–2309.
- [74] K. P. Acharya, N. N. Hewa-kasakarage, T. R. Alabi, I. Nemitz, E. Khon, B. Ullrich, P. Anzenbacher, M. Zamkov, **2010**, 12496–12504.
- [75] K. P. Acharya, T. R. Alabi, N. Schmall, N. N. Hewa-kasakarage, M. Kirsanova, A. Nemchinov, E. Khon, M. Zamkov, **2009**, 19531–19535.
- [76] T. Lana-villarreal, Q. Shen, T. Toyoda, R. Go, **2010**, 21928–21937.

-
- [77] Y. Tachibana, K. Umekita, Y. Otsuka, S. Kuwabata, *The Journal of Physical Chemistry C* **2009**, *113*, 6852–6858.
- [78] S. W. Verbruggen, J. J. J. Dirckx, J. a. Martens, S. Lenaerts, *Catalysis Today* **2013**, *209*, 215–220.
- [79] O. Ekiz, K. Mizrak, A. Dâna, *ACS nano* **2010**, *4*, 1851–1860.
- [80] Y. Zhang, T. Xie, T. Jiang, X. Wei, S. Pang, X. Wang, D. Wang, *Nanotechnology* **2009**, *20*, 155707.
- [81] Q. Zhang, S. Cao, M. Xia, X. Wang, Q. Wan, A. Pan, *Acta Chimica Sinica* **2013**, *71*, 634.
- [82] S. Gupta, Y. Batra, B. R. Mehta, V. R. Satsangi, *Nanotechnology* **2013**, *24*, 255703.
- [83] S. Schäfer, Z. Wang, R. Zierold, T. Kipp, A. Mews, *Nano letters* **2011**, *11*, 2672–7.
- [84] A. Liscio, V. Palermo, P. Samorì, *Accounts of chemical research* **2010**, *43*, 541–50.
- [85] W. Melitz, J. Shen, A. C. Kummel, S. Lee, *Surface Science Reports* **2011**, *66*, 1–27.
- [86] S.-S. Bae, N. Prokopuk, N. J. Quitoriano, S. M. Adams, R. Ragan, *Nanotechnology* **2012**, *23*, 405706.
- [87] C. Van Ben, D. Cho, W. Kang, W. Yang, **2011**, DOI 10.1002/sia.3867.
- [88] S. B. Block, L. a. Yurs, A. V. Pakoulev, R. S. Selinsky, S. Jin, J. C. Wright, *The Journal of Physical Chemistry Letters* **2012**, *3*, 2707–2712.
- [89] Z. L. Wang, J. Song, *Science (New York, N.Y.)* **2006**, *312*, 242–6.
- [90] X. Chen, S. Xu, N. Yao, Y. Shi, *Nano letters* **2010**, *10*, 2133–7.
- [91] K.-I. Park, S. Xu, Y. Liu, G.-T. Hwang, S.-J. L. Kang, Z. L. Wang, K. J. Lee, *Nano letters* **2010**, *2*, 0–4.
- [92] Z. L. Wang, *Advanced Functional Materials* **2008**, *18*, 3553–3567.
- [93] S. Xu, Y. Qin, C. Xu, Y. Wei, R. Yang, Z. L. Wang, *Nature nanotechnology* **2010**, *5*, 366–73.
- [94] Z. L. Wang, *Advanced Materials* **2012**, *24*, 280–285.
- [95] X. Yang, G. Zhu, S. Wang, R. Zhang, L. Lin, W. Wu, Z. L. Wang, *Energy & Environmental Science* **2012**, *5*, 9462.
- [96] T. Song, J. W. Choung, J.-G. Park, W. Il Park, J. a. Rogers, U. Paik, *Advanced Materials* **2008**, *20*, 4464–4469.
- [97] J. L. brahams, S.C.;Bernstein, *Acta Crystallographica B (24,1968-38,1982)* **1969**, *25*, 1233–1236.

References

- [98] G. M. Karzel, H., Potzel, U., Potzel, W., Moser, J., Schaefer, C., Steiner, M., Peter, M., Kratzer, A., Kalvius, *Materials Science Forum* **1991**, 79, 419–426.
- [99] M. K. Rabadanov, *Kristallografiya* **1995**, 40, 21–27.
- [100] C. Klingshirn, *Chemphyschem : a European journal of chemical physics and physical chemistry* **2007**, 8, 782–803.
- [101] A. Janotti, C. G. Van de Walle, *Reports on Progress in Physics* **2009**, 72, 126501.
- [102] J. Y. Lao, J. G. Wen, Z. F. Ren, **2002**, 02467.
- [103] A. Menzel, K. Subannajui, F. Güder, D. Moser, O. Paul, M. Zacharias, *Advanced Functional Materials* **2011**, 21, 4342–4348.
- [104] a B. Djuricic, X. Y. Chen, Y. H. Leung, *Recent patents on nanotechnology* **2012**, 6, 124–34.
- [105] B. Nikoobakht, X. Wang, A. Herzing, J. Shi, *Chemical Society reviews* **2013**, 42, 342–65.
- [106] J. Altmayer, S. Barth, S. Mathur, *RSC Advances* **2013**, 3, 11234.
- [107] G. Shen, *Recent patents on nanotechnology* **2008**, 2, 160–8.
- [108] J. Chun, J. Lee, *European Journal of Inorganic Chemistry* **2010**, 2010, 4251–4263.
- [109] B. Weintraub, Z. Zhou, Y. Li, Y. Deng, *Nanoscale* **2010**, 2, 1573–87.
- [110] S. Yamabi, H. Imai, *Journal of Materials Chemistry* **2002**, 12, 3773–3778.
- [111] L. E. Greene, B. D. Yuhas, M. Law, D. Zitoun, P. Yang, *Inorganic chemistry* **2006**, 45, 7535–43.
- [112] H. Hu, X. Huang, C. Deng, X. Chen, Y. Qian, *Materials Chemistry and Physics* **2007**, 106, 58–62.
- [113] Q. Zhou, W. Chen, L. Xu, S. Peng, *Sensors (Basel, Switzerland)* **2013**, 13, 6171–82.
- [114] B. Liu, H. C. Zeng, *Journal of the American Chemical Society* **2003**, 125, 4430–1.
- [115] X. Sun, X. Chen, Z. Deng, Y. Li, *Materials Chemistry and Physics* **2003**, 78, 99–104.
- [116] X. . Zhang, J. . Dai, H. . Ong, N. Wang, H. L. . Chan, C. . Choy, *Chemical Physics Letters* **2004**, 393, 17–21.
- [117] Z. Zhang, Y. Zhang, J. Bian, J. Sun, F. Qin, Y. Wang, M. Li, D. Zhang, Y. Luo, *Applied Physics A* **2012**, 111, 1071–1076.
- [118] Y. Tak, K. Yong, *The journal of physical chemistry. B* **2005**, 109, 19263–9.
- [119] K. Govender, D. S. Boyle, P. B. Kenway, P. O. Brien, **2004**, 2575–2591.

- [120] C. a. Grimes, *Journal of Materials Chemistry* **2007**, *17*, 1451.
- [121] S. J. Kim, J. Lee, J. Choi, *Electrochimica Acta* **2008**, *53*, 7941–7945.
- [122] P. K. Basu, P. Bhattacharyya, N. Saha, H. Saha, S. Basu, *Sensors and Actuators B: Chemical* **2008**, *133*, 357–363.
- [123] M. A. Farrukh, C.-K. Thong, R. Adnan, M. A. Kamarulzaman, *Russian Journal of Physical Chemistry A* **2012**, *86*, 2041–2048.
- [124] S. He, M. Zheng, L. Yao, X. Yuan, M. Li, L. Ma, W. Shen, *Applied Surface Science* **2010**, *256*, 2557–2562.
- [125] S. Sreekantan, L. R. Gee, Z. Lockman, *Journal of Alloys and Compounds* **2009**, *476*, 513–518.
- [126] S. J. Kim, J. Choi, *Electrochemistry Communications* **2008**, *10*, 175–179.
- [127] Z. Hu, Q. Chen, Z. Li, Y. Yu, L.-M. Peng, *The Journal of Physical Chemistry C* **2010**, *114*, 881–889.
- [128] J. Liu, G. Cao, Z. Yang, D. Wang, D. Dubois, X. Zhou, G. L. Graff, L. R. Pederson, J.-G. Zhang, *ChemSusChem* **2008**, *1*, 676–97.
- [129] L. Shen, N. Bao, K. Yanagisawa, Y. Zheng, K. Domen, A. Gupta, C. a. Grimes, *Journal of Solid State Chemistry* **2007**, *180*, 213–220.
- [130] J.-Y. Lee, D. Yin, S. Horiuchi, *Chemistry of Materials* **2005**, *17*, 5498–5503.
- [131] C. X. Xu, a Wei, X. W. Sun, Z. L. Dong, *Journal of Physics D: Applied Physics* **2006**, *39*, 1690–1693.
- [132] I. Mora-Seró, S. Giménez, F. Fabregat-Santiago, R. Gómez, Q. Shen, T. Toyoda, J. Bisquert, *Accounts of chemical research* **2009**, *42*, 1848–57.
- [133] M. Xiao, M. Kuwabara, *Journal of Materials Science & Technology* **2005**, *21*, 887–890.
- [134] M. Liu, X. Li, K. Karuturi, I. Yoong, H. Jin, **2012**, DOI 10.1039/c2nr11875k.
- [135] J. Malm, E. Sahrmo, J. Perälä, T. Sajavaara, M. Karppinen, *Thin Solid Films* **2011**, *519*, 5319–5322.
- [136] G. Hua, Y. Tian, L. Yin, L. Zhang, *Crystal Growth & Design* **2009**, *9*, 4653–4659.
- [137] V. a. Sivakov, G. Brönstrup, B. Pecz, A. Berger, G. Z. Radnoczi, M. Krause, S. H. Christiansen, *The Journal of Physical Chemistry C* **2010**, *114*, 3798–3803.
- [138] Y. Tak, S. J. Hong, J. S. Lee, K. Yong, *Crystal Growth & Design* **2009**, *9*, 2627–2632.
- [139] X. M. Shuai, W. Z. Shen, *The Journal of Physical Chemistry C* **2011**, *115*, 6415–6422.

References

- [140] H.-M. Cheng, W.-H. Chiu, C.-H. Lee, S.-Y. Tsai, W.-F. Hsieh, *Journal of Physical Chemistry C* **2008**, *112*, 16359–16364.
- [141] K. Kalantar-zadeh, B. Fry, *Nanotechnology-Enabled Sensors*, Springer US, Boston, MA, **2008**.
- [142] Y. Kim, A. Danner, *Selected Topics in ...* **2005**, *11*, 1292–1298.
- [143] J. Han, W. Gao, *Journal of Electronic Materials* **2008**, *38*, 601–608.
- [144] Z. B. Fang, Z. J. Yan, Y. S. Tan, X. Q. Liu, Y. Y. Wang, *Applied Surface Science* **2005**, *241*, 303–308.
- [145] C. Dwivedi, V. Dutta, *Advances in Natural Sciences: Nanoscience and Nanotechnology* **2012**, *3*, 015011.
- [146] J. B. Baxter, a M. Walker, K. Van Ommering, E. S. Aydil, *Nanotechnology* **2006**, *17*, S304–S312.
- [147] A. TOMASZ, G. ŁUKA, *Optica Applicata* **2009**, 865–874.
- [148] J. Lü, K. Huang, X. Chen, J. Zhu, F. Meng, X. Song, Z. Sun, *Applied Surface Science* **2010**, *256*, 4720–4723.
- [149] K. Govender, D. S. Boyle, P. B. Kenway, P. O. Brien, **2004**, 2575–2591.
- [150] Q. Peng, Y. Qin, **2009**.
- [151] A. E. Gad, S. Mathur, *Manuscript in progress for publication.*.
- [152] H. Chen, X. Wu, L. Gong, C. Ye, **2010**, 570–575.
- [153] G. Shen, Y. Bando, D. Golberg, *Applied Physics Letters* **2006**, *88*, 123107.
- [154] Z. Zhang, H. Yu, Y. Wang, M.-Y. Han, *Nanotechnology* **2006**, *17*, 2994–2997.
- [155] C. Chandrinou, N. Boukos, K. Giannakopoulos, A. Lusson, A. Travlos, *Superlattices and Microstructures* **2007**, *42*, 431–437.
- [156] N. Boukos, C. Chandrinou, K. Giannakopoulos, G. Pistolis, A. Travlos, *Applied Physics A* **2007**, *88*, 35–39.
- [157] J. Qiu, X. Li, W. Yu, X. Gao, W. He, S.-J. Park, Y.-H. Hwang, H.-K. Kim, *Thin Solid Films* **2008**, *517*, 626–630.
- [158] N. Ekthammathat, T. Thongtem, A. Phuruangrat, S. Thongtem, *Superlattices and Microstructures* **2013**, *53*, 195–203.
- [159] J.-Y. Jung, Z. Guo, S.-W. Jee, H.-D. Um, K.-T. Park, M. S. Hyun, J. M. Yang, J.-H. Lee, *Nanotechnology* **2010**, *21*, 445303.

- [160] R. Yu, Q. Lin, S.-F. Leung, Z. Fan, *Nano Energy* **2012**, *1*, 57–72.
- [161] Z. Huang, N. Geyer, P. Werner, J. de Boor, U. Gösele, *Advanced materials (Deerfield Beach, Fla.)* **2011**, *23*, 285–308.
- [162] X. Li, K. Liang, B. K. Tay, E. H. T. Teo, *Applied Surface Science* **2012**, *258*, 6169–6176.
- [163] E. C. Garnett, M. L. Brongersma, Y. Cui, M. D. McGehee, **2011**, DOI 10.1146/annurev-matsci-062910-100434.
- [164] J.-H. Choi, S. N. Das, K.-J. Moon, J. P. Kar, J.-M. Myoung, *Solid-State Electronics* **2010**, *54*, 1582–1585.
- [165] S.-H. Hsu, S.-F. Hung, S.-H. Chien, *Journal of Power Sources* **2013**, *233*, 236–243.
- [166] S. Majumdar, S. Chattopadhyay, P. Banerji, *Applied Surface Science* **2009**, *255*, 6141–6144.
- [167] J. Li, M. W. G. Hoffmann, H. Shen, C. Fabrega, J. D. Prades, T. Andreu, F. Hernandez-Ramirez, S. Mathur, *Journal of Materials Chemistry* **2012**, *22*, 20472.
- [168] B. M. Kayes, H. a. Atwater, N. S. Lewis, *Journal of Applied Physics* **2005**, *97*, 114302.
- [169] R. Agarwal, *Small (Weinheim an der Bergstrasse, Germany)* **2008**, *4*, 1872–93.
- [170] P. Verma, A. C. Pandey, R. N. Bhargava, *Physica B: Condensed Matter* **2009**, *404*, 3894–3897.
- [171] E. Edri, E. Rabinovich, O. Niiitsoo, H. Cohen, T. Bendikov, G. Hodes, **2010**, 13092–13097.
- [172] H. S. Song, W. J. Zhang, C. Cheng, Y. B. Tang, L. B. Luo, X. Chen, C. Y. Luan, X. M. Meng, J. a. Zapien, N. Wang, C. S. Lee, I. Bello, S. T. Lee, *Crystal Growth & Design* **2011**, *11*, 147–153.
- [173] M. Devika, N. K. Reddy, A. Pevzner, F. Patolsky, *Chemphyschem : a European journal of chemical physics and physical chemistry* **2010**, *11*, 809–14.
- [174] C. Cheng, B. Yan, S. M. Wong, X. Li, W. Zhou, T. Yu, Z. Shen, H. Yu, H. J. Fan, *ACS applied materials & interfaces* **2010**, *2*, 1824–8.
- [175] S. M. Sze, K. K. Ng, *Physics of Semiconductor Devices*, John Wiley & Sons, New Jersey, **2007**.
- [176] I. Mora-Seró, F. Fabregat-Santiago, B. Denier, J. Bisquert, R. Tena-Zaera, J. Elias, C. Lévy-Clément, *Applied Physics Letters* **2006**, *89*, 203117.
- [177] D. S. Kim, J.-P. Richters, R. Scholz, T. Voss, M. Zacharias, *Applied Physics Letters* **2010**, *96*, 123110.
- [178] J. D. Prades, R. Jimenez-Diaz, F. Hernandez-Ramirez, S. Barth, A. Cirera, A. Romano-Rodriguez, S. Mathur, J. R. Morante, *Applied Physics Letters* **2008**, *93*, 123110.

References

- [179] P. Camagni, G. Faglia, P. Galinetto, C. Perego, G. Samoggia, G. Sberveglieri, *Sensors and Actuators B: Chemical* **1996**, *31*, 99–103.
- [180] M. Law, H. Kind, B. Messer, F. Kim, P. Yang, *Angewandte Chemie (International ed. in English)* **2002**, *41*, 2405–8.
- [181] X. Wang, J. Song, J. Liu, Z. L. Wang, *Science (New York, N.Y.)* **2007**, *316*, 102–5.
- [182] R. Yang, Y. Qin, L. Dai, Z. L. Wang, *Nature nanotechnology* **2009**, *4*, 34–9.
- [183] S. M. Alaa Eldin Gad, Martin Hoffmann, Tessa Leuning, Joan Daniel Prades, Francisco H. Ramirez, Hao Shen, *conference proceedings of the 14th International Meeting on Chemical Sensors (IMCS 2012), 20-23 May 2012 Nürnberg, Germany* **2012**, 1312–1315.
- [184] M. W. G. Hoffmann, A. Eldin Gad, J. Daniel Prades, F. Hernandez-Ramirez, R. Fiz, H. Shen, S. Mathur, *Nano Energy* **2013**, 1–9.
- [185] F. Hernandez-Ramirez, J. D. Prades, R. Jimenez-Diaz, T. Fischer, A. Romano-Rodriguez, S. Mathur, J. R. Morante, *Physical chemistry chemical physics : PCCP* **2009**, *11*, 7105–10.
- [186] Y.-P. Hsieh, H.-Y. Chen, M.-Z. Lin, S.-C. Shiu, M. Hofmann, M.-Y. Chern, X. Jia, Y.-J. Yang, H.-J. Chang, H.-M. Huang, S.-C. Tseng, L.-C. Chen, K.-H. Chen, C.-F. Lin, C.-T. Liang, Y.-F. Chen, *Nano letters* **2009**, *9*, 1839–43.
- [187] Z. Z. Ye, J. G. Lu, Y. Z. Zhang, Y. J. Zeng, L. L. Chen, F. Zhuge, G. D. Yuan, H. P. He, L. P. Zhu, J. Y. Huang, B. H. Zhao, *Applied Physics Letters* **2007**, *91*, 113503.
- [188] N. Koteeswara Reddy, Q. Ahsanulhaq, J. H. Kim, Y. B. Hahn, *Applied Physics Letters* **2008**, *92*, 043127.
- [189] N. Bao, L. Shen, T. Takata, K. Domen, a. Gupta, K. Yanagisawa, C. a. Grimes, *Journal of Physical Chemistry C* **2007**, *111*, 17527–17534.
- [190] L. Li, C. X. Shan, B. H. Li, B. Yao, D. Z. Shen, B. Chu, Y. M. Lu, *Journal of Electronic Materials* **2010**, *39*, 2467–2470.
- [191] X. Wang, H. Zhu, Y. Xu, H. Wang, Y. Tao, S. Hark, X. Xiao, Q. Li, *ACS nano* **2010**, *4*, 3302–8.
- [192] N. Du, H. Zhang, B. Chen, J. Wu, D. Yang, *Nanotechnology* **2007**, *18*, 115619.
- [193] J.-Y. Zhang, Q.-F. Zhang, T.-S. Deng, J.-L. Wu, *Applied Physics Letters* **2009**, *95*, 211107.
- [194] L. J. Diguna, Q. Shen, J. Kobayashi, T. Toyoda, *Applied Physics Letters* **2007**, *91*, 023116.
- [195] O. Niitsoo, S. K. Sarkar, C. Pejoux, S. Rühle, D. Cahen, G. Hodes, *Journal of Photochemistry and Photobiology A: Chemistry* **2006**, *181*, 306–313.
- [196] A. Salant, M. Shalom, I. Hod, A. Faust, A. Zaban, U. Banin, *ACS nano* **2010**, *4*, 5962–8.

- [197] J. Nayak, S. Sahu, J. Kasuya, S. Nozaki, *Applied Surface Science* **2008**, *254*, 7215–7218.
- [198] J. D. Prades, F. Hernandez-Ramirez, R. Jimenez-Diaz, M. Manzanares, T. Andreu, A. Cirera, A. Romano-Rodriguez, J. R. Morante, *Nanotechnology* **2008**, *19*, 465501.
- [199] T. Gao, Q. Li, T. Wang, *Chemistry of Materials* **2005**, *17*, 887–892.
- [200] J. Piris, A. J. Ferguson, J. L. Blackburn, A. G. Norman, G. Rumbles, D. C. Selmarten, N. Kopidakis, *Journal of Physical Chemistry C* **2008**, *112*, 7742–7749.
- [201] X. Song, X.-L. Yu, Y. Xie, J. Sun, T. Ling, X.-W. Du, *Semiconductor Science and Technology* **2010**, *25*, 095014.
- [202] T. Sauerwald, D. Skiera, C.-D. Kohl, *Applied Physics A* **2007**, *87*, 525–529.
- [203] I. Kiselev, M. Sommer, *Thin Solid Films* **2010**, *518*, 4533–4536.
- [204] F. Hernandez-Ramirez, J. D. Prades, A. Tarancon, S. Barth, O. Casals, R. Jimenez-Diaz, E. Pellicer, J. Rodriguez, J. R. Morante, M. A. Juli, S. Mathur, A. Romano-Rodriguez, *Advanced Functional Materials* **2008**, *18*, 2990–2994.
- [205] S. Sze, K. Ng, *Physics of Semiconductor Devices*, (John Wiley & Sons, New Jersey, 2007), **2006**.
- [206] B. Kaplan, *Physica B: Condensed Matter* **2004**, *351*, 90–95.
- [207] C. Xiong, R.-H. Yao, K.-W. Geng, *Chinese Physics B* **2011**, *20*, 057302.
- [208] H. Idriss, *Journal of Molecular Catalysis A: Chemical* **2000**, *152*, 201–212.
- [209] M.-W. Ahn, K.-S. Park, J.-H. Heo, J.-G. Park, D.-W. Kim, K. J. Choi, J.-H. Lee, S.-H. Hong, *Applied Physics Letters* **2008**, *93*, 263103.
- [210] X. Chen, C. K. Y. Wong, C. a. Yuan, G. Zhang, *Sensors and Actuators B: Chemical* **2012**, DOI 10.1016/j.snb.2012.10.134.
- [211] C.-Y. Huang, Y.-J. Yang, J.-Y. Chen, C.-H. Wang, Y.-F. Chen, L.-S. Hong, C.-S. Liu, C.-Y. Wu, *Applied Physics Letters* **2010**, *97*, 013503.
- [212] K. Wang, Y. Vygranenko, A. Nathan, *Journal of Applied Physics* **2007**, *101*, 114508.
- [213] C. Sevik, C. Bulutay, *Journal of Materials Science* **2007**, *42*, 6555–6565.
- [214] I. de P. R. Moreira, F. Illas, R. Martin, *Physical Review B* **2002**, *65*, 155102.
- [215] J. Choi, S. Im, *Applied Surface Science* **2005**, *244*, 435–438.
- [216] P. . Patil, L. . Kadam, *Applied Surface Science* **2002**, *199*, 211–221.

References

- [217] C. Cantalini, M. Post, D. Buso, M. Guglielmi, A. Martucci, *Sensors and Actuators B: Chemical* **2005**, *108*, 184–192.
- [218] W.-L. Jang, Y.-M. Lu, W.-S. Hwang, W.-C. Chen, *Journal of the European Ceramic Society* **2010**, *30*, 503–508.
- [219] C. Liu, Y. J. Hwang, H. E. Jeong, P. Yang, **2011**, 3755–3758.
- [220] C. S. Nanowires, B. M. Wong, Q. Li, G. T. Wang, **2011**, 1–6.
- [221] S. H. Nanocrystals, K. P. Acharya, R. S. Khayzer, T. O. Connor, G. Diederich, M. Kirsanova, A. Klinkova, D. Roth, E. Kinder, M. Imboden, M. Zamkov, **2011**, 2919–2926.
- [222] K. Sun, Y. Jing, N. Park, C. Li, Y. Bando, D. Wang, *Nano* **2010**, 9–11.
- [223] W. Wang, Q. Zhao, K. Laurent, Y. Leprince-Wang, Z.-M. Liao, D. Yu, *Nanoscale* **2012**, *4*, 261–8.
- [224] B. D. Yuhas, P. Yang, *Journal of the American Chemical Society* **2009**, *131*, 3756–61.
- [225] C. Shang, S. Dong, S. Wang, D. Xiao, P. Han, X. Wang, L. Gu, G. Cui, *ACS nano* **2013**, DOI 10.1021/nm401402a.
- [226] J. M. Schnorr, D. van der Zwaag, J. J. Walish, Y. Weizmann, T. M. Swager, *Advanced Functional Materials* **2013**, n/a–n/a.
- [227] a. E. Gad, M. W. G. Hoffmann, F. Hernandez-Ramirez, J. D. Prades, H. Shen, S. Mathur, *Materials Chemistry and Physics* **2012**, *135*, 618–622.
- [228] J. Martinez-Duart, R. Martin-Palmer, F. Agulló-Rueda, *Nanotechnology for Microelectronics and Optoelectronics*, **2006**.
- [229] L. Zhang, Y. Yin, *Sensors and Actuators B: Chemical* **2013**, *183*, 110–116.
- [230] G. Yang, C. Miao, Z. Bu, Q. Wang, W. Guo, *Journal of Power Sources* **2013**, *233*, 74–78.
- [231] X. Sun, Q. Li, Y. Lü, Y. Mao, *Chemical communications (Cambridge, England)* **2013**, *49*, 4456–8.
- [232] Z. N. Arrays, C. Chen, J. Huang, J. Song, Y. Zhou, L. Lin, P. Huang, C. E. T. Al, **2011**.
- [233] M. Riaz, J. Song, O. Nur, Z. L. Wang, M. Willander, *Advanced Functional Materials* **2011**, *21*, 628–633.
- [234] C.-Y. Huang, Y.-J. Yang, J.-Y. Chen, C.-H. Wang, Y.-F. Chen, L.-S. Hong, C.-S. Liu, C.-Y. Wu, *Applied Physics Letters* **2010**, *97*, 013503.
- [235] Y. Tak, K. Yong, *Journal of Physical Chemistry C* **2008**, *112*, 74–79.
- [236] T. J. Kempa, B. Tian, D. R. Kim, J. Hu, X. Zheng, C. M. Lieber, *Nano letters* **2008**, *8*, 3456–60.

-
- [237] B. Tian, T. J. Kempa, C. M. Lieber, *Chemical Society reviews* **2009**, *38*, 16–24.
- [238] H. D. Cho, A. S. Zakirov, S. U. Yuldashev, C. W. Ahn, Y. K. Yeo, T. W. Kang, *Nanotechnology* **2012**, *23*, 115401.
- [239] B. Tian, X. Zheng, T. J. Kempa, Y. Fang, N. Yu, G. Yu, J. Huang, C. M. Lieber, *Nature* **2007**, *449*, 885–9.
- [240] J. M. Spurgeon, H. a. Atwater, N. S. Lewis, *Journal of Physical Chemistry C* **2008**, *112*, 6186–6193.
- [241] Y.-Q. Bie, Z.-M. Liao, P.-W. Wang, Y.-B. Zhou, X.-B. Han, Y. Ye, Q. Zhao, X.-S. Wu, L. Dai, J. Xu, L.-W. Sang, J.-J. Deng, K. Laurent, Y. Leprince-Wang, D.-P. Yu, *Advanced materials (Deerfield Beach, Fla.)* **2010**, *22*, 4284–7.
- [242] B. Nikoobakht, J. Bonevich, A. Herzing, *The Journal of Physical Chemistry C* **2011**, *115*, 9961–9969.
- [243] K. Kim, J. Kang, M. Lee, C. Yoon, K. Cho, S. Kim, *Japanese Journal of Applied Physics* **2010**, *49*, 06GG05.
- [244] X. Wang, K. L. Pey, C. H. Yip, E. a. Fitzgerald, D. a. Antoniadis, *Journal of Applied Physics* **2010**, *108*, 124303.
- [245] Y.-Q. Bie, Z.-M. Liao, P.-W. Wang, Y.-B. Zhou, X.-B. Han, Y. Ye, Q. Zhao, X.-S. Wu, L. Dai, J. Xu, L.-W. Sang, J.-J. Deng, K. Laurent, Y. Leprince-Wang, D.-P. Yu, *Advanced materials (Deerfield Beach, Fla.)* **2010**, *22*, 4284–7.
- [246] G. Korotcenkov, *Materials Science and Engineering: B* **2007**, *139*, 1–23.

9. List of Figures

Figure 1 The solar spectrum [11].....	2
Figure 2 Schematic representation of the research objectives of this thesis: 1) controlled synthesis of 1D ZnO nanostructures, 2) Fabrication of ZnO based heterostructures with tailored properties, 3) Integration and testing their device potential, and 4) Investigation of self-and low powered gas sensing applications.	8
Figure 3 (a) Lennard-Jones model for physisorption and chemisorption of a molecule. An energy barrier ΔE_A has to be overcome for a physisorbed molecule to reach the chemisorption well. Typical adsorption isobars are shown in (b). The solid lines are equilibrium physisorption and a chemisorption isobar, the dashed line represents irreversible chemisorption. A maximum coverage of chemisorbed molecules is obtainable at a temperature T_{max} . Below T_{max} the chemisorption is irreversible because the rate of desorption becomes negligible [27].	13
Figure 4 Schematic representation of the UV-activated gas sensing mechanism of metal oxides at room-temperature. The photoinduced oxygen ions are highly reactive and able to interact with H_2 at room temperature [40].	15
Figure 5 Schematic representation of visible-light assisted gas sensor based on CdS/ZnO heterostructures [32].....	17
Figure 6 Schematic representation of the visible-light activated gas sensing mechanism of metal oxides at room- temperature [31].	18
Figure 7 A schematic representation of the charge transfer processes that occur upon illumination in quantum dot sensitized solar cells (QDSCs). The electron transfer steps are described on the text [68].	20
Figure 8 Different types of heterostructure band alignments [67].....	21
Figure 9 Time resolved spectroscopic investigation of chemically linked CdSe QDs. (A) UV-visible and (B–E) transient absorption spectral traces of 4.2-nm-diameter CdSe quantum dots (A) in toluene and attached to (B) SiO_2 , (C) SnO_2 , (D) TiO_2 , and (E) ZnO. Transient spectra shown at pump-probe delay times of 0 (black), 1 (red), 10 (blue), 100 (cyan), and 1,000 ps (pink). Also, transient absorption kinetic traces (F) of 4.2-nm-diameter CdSe quantum dots attached to each MOx substrate at the $1S_{3/2}-1S_e$ transition [Taken from reference [70]].....	23
Figure 10 (a) Topography image and (b) KPFM image of a homojunction ZnO nanorods, where brightness contrast appears obviously near the middle region of the nanorod where the brighter region corresponds to the n-ZnO part, whereas the darker region corresponds to the p-doped ZnO part in the homojunction [taken from reference [87]].	24

Figure 11 Different forms of mechanical energy that can be harvested by a nanogenerators and the potential future applications of nanogenerators for powering variety of functional devices [92].25

Figure 12 The voltage drop across a humidity sensor as a function of the relative humidity (RH). The sensor was powered by a DSSC shown by the schematic circuit in the inset [Taken from reference [22]].
.....26

Figure 13 Stick-and-ball representation of ZnO crystal structures: (a) hexagonal wurtzite [97], (b) cubic rocksalt [98], (c) cubic zinc blende [99]. Green and red spheres denote Zn and O atoms, respectively.
.....28

Figure 14 Examples of different ZnO nanostructures synthesized under controlled conditions by solution based synthesis methods; a) nanorods, b) nanotubes, c) nanowires, d) needles, e) flower-like, and f) platelets.29

Figure 15 Phase stability diagrams for the ZnO (s)–H₂O system at 25 °C as a function of precursor concentration and pH value, where the dashed lines denote the thermodynamic equilibrium between the Zn²⁺ soluble species and the corresponding solid phases [Taken from reference [110]]. 32

Figure 16 Schematic illustrations of different binding strategies of NPs/MOx heterostructure and their corresponding deposition techniques.37

Figure 17 Schematic representation of the PC-automated gas sensing system used in this work.50

Figure 18 XRD pattern of ZnO seed layer prepared by spin-coating and DC-sputtering and annealing technique (a). SEM of ZnO seed layer prepared by spin-coating (b) and by DC-sputtering technique (c).
.....53

Figure 19 Cross-sectional SEM images of DC-sputtered/annealed seed layer deposited for (a) 4 minutes, (b) 20 minutes. (c) the change of film thickness with deposition time and (d) EDX spectrum of ZnO DC-sputtered/annealed seed layer.54

Figure 20 (a) XRD pattern of DC-sputtered ZnO film at different annealing temperatures. (b) the variation of FWHM of the (002) peak and the grain size of the ZnO film with the annealing temperature. (c) AFM image of DC sputtered film and annealed at 500 °C. (d) the contact angle measurement for surfaces of the DC-sputtered ZnO film at 500 °C.55

Figure 21 SEM micrographs (top and cross sectional view) of ZnO nanowires on seed layer prepared by (a,c) sol–gel/ spin-coating and (b,d) DC sputtering and annealing depositions.57

Figure 22 XRD patterns of ZnO nanowires on the top of seed layer prepared by DC-sputtering and annealing, and sol-gel spin-coated techniques. Inset shows a magnified part of these spectra....58

Figure 23 (a) XRD patterns of ALD ZnO films at different ALD deposition temperatures, and (b) for the film deposited at 200 °C with different post annealing temperatures.59

Figure 24 Cross-sectional SEM images of ALD deposited ZnO seed layer for (a) 400 cycles, (b) 600 cycles, and (c) 1000 cycles. (d) the relation between the number of deposition cycles and the film thickness.....	60
Figure 25 AFM images of ZnO films deposited by ALD after (a) 100 cycles, (b) 250 cycles, and (c) 300 cycles.	61
Figure 26 Contact angle measurements for surfaces under UV-light irradiation and in dark condition of the ZnO film deposited at different temperatures of (a, b) 125 °C, (c, d) 175 °C, and (e, f) 200 °C. .	62
Figure 27 (a) XRD pattern and (b) top-view SEM image of ZnO nanowires on ALD deposited ZnO seed layer.	63
Figure 28: cross-sectional SEM images of ZnO nanowires on sol-gel spin coated seed layer without (a) and with (b) aluminum-iso-propylate, and (c) on DC sputter seed layer with aluminum-iso-propylate.	65
Figure 29: cross-sectional SEM of ZnO nanowires produced after (a) 1 cycle and (b) 3 cycles of growth, where the duration of each cycle was of 8 hours.....	66
Figure 30: (a) XRD patterns of Zn foil anodized at 5 and 10 °C under the same anodization conditions followed by annealing treatment at 250 °C. (b, c) SEM and (d) TEM images of ZnO nanowires and nanotubes obtained from anodization at 10 °C under 10V applied voltage for 1 h.	67
Figure 31 SEM of Zn foil with (a) no pretreatment and (b) electropolishing pretreatment.	68
Figure 32 SEM images of ZnO nanowires at different growth times of (a) 1 min., (b) 5 min., (c) 10 min., and (d) 20 min.	69
Figure 33 SEM images of ZnO nanowires at different applied voltages of (a) 5 V, (b) 10 V, (c) 15 V, and (d) 20 V.....	70
Figure 34 SEM images of ZnO nanowires at different growth temperatures of (a) 10 °C, (b) room temperature, (c) 40 °C, and (d) 70 °C.....	71
Figure 35 (a) XRD patterns, (b) SEM image of ZnO nanorods grown on a zinc substrate immersed in an aqueous formamide solution for 24 h at 66 °C.	73
Figure 36 (a) SEM image and (b) EDX spectra of platelet-like ZnO grown on a zinc substrate immersed in 5% formamide aqueous solution containing 0.45 M NaCl salt for 24 h at 65 °C.....	74
Figure 37 (a) SEM image and (b) EDX spectra of ZnO nanorods with pyramid-like sharp tips grown on a zinc substrate. (c) the pattern left on the ZnO foil after ultrasonic treatment. (d) multi-segments nanorods formed on the pattern in shown in c.....	75
Figure 38: A schematic illustration of wet chemical etching process of silicon substrate by using two solutions; solution I (consist of AgNO ₃ /HF) followed by solution II (contain H ₂ O ₂ /HF).	77

Figure 39: (a) Cross-sectional SEM image of etched Si NWs with Ag nanoparticles and nanoclusters, (b) XRD pattern of Si NWs etched for 1 h, (c) their top view SEM image. (d) the effect of etching on both sides of Si wafer. 78

Figure 40: Cross sectional SEM view of Si NWs etched for (a) 3 min with length of 1.2 μm , (b) 10 min with length of 4.8 μm , (c) 1 h with length of 25.9 μm , and (d) 3h with length of 60 μm 79

Figure 41: Top- and cross sectional- SEM view of p-NiO/n-Si heterojunction (a, b) and its corresponding XRD pattern (c). 81

Figure 42 SEM micrographs of CdS NP/ZnO nanowires heterostructure arrays deposited at 60 °C for different times of (a) 10 min, (b) 20 min, and (c) 60 min, respectively. (d) EDX spectra of samples deposited at 10 and 60 min. 83

Figure 43 SEM image of n-ZnO film deposited by (a) ALD and (b) DC-sputtered/annealed techniques on p-Si NWs to form radial p-n heterojunction. 84

Figure 44 (a) XRD pattern of n-ZnO film deposited by ALD technique on p-Si NWs and the etched p-Si NWs. (b) TEM image of n-ZnO film deposited by ALD technique on p-Si NWs. 85

Figure 45 (a) EDX analysis of n-ZnO shells with different thicknesses on p-Si nanowires. (b) a schematic illustration of radial n-ZnO/p-Si NWs heterojunction. (c-f) EDX spectroscopic mapping of ZnO (shell) deposited with 100 cycles of ALD on p-Si NWs (core). 86

Figure 46 Cross-sectional SEM images of CdS deposited by CBD on ZnO/p-Si heterojunction at 60 °C for (a) 10, (b) 25, and (c) 120 min respectively. (d) TEM, (e) FFT, (f) HRTEM images, and (g) TEM-EDX spectrum of CdS deposited for 25 min on ZnO/p-Si heterojunction. 87

Figure 47 (a) SEM image of the n-ZnO/p-Si NWs heterojunction. (b) SEM and (c) TEM (inset image is the FFT pattern) of ZnS@ZnO/p-Si NWs heterojunction. 88

Figure 48: SEM (a) and TEM (b) images of CdS NPs deposited by CBD at 60 °C for 25 min on ZnS@ZnO/p-Si NWs heterojunction. 89

Figure 49 Cross-sectional SEM images of 3D ZnO NWs branches grown by hydrothermal growth for (a, b) 4h, (c, d) 20h, and (e, f) CdS NPs decorated 3D ZnO NWs branches grown by hydrothermal synthesis for 20h. 91

Figure 50: SEM images of 3D ZnO NWs branches grown by hydrothermal method for (a) 4h (S1) (b) 20h (S2) and (c) 40h (S3). (d) Capacitance-voltage measurement. Mott Schottky plots (I/C^2 vs. V) of n-ZnO/p-Si nanowires acquired at 1 MHz in the reverse bias region for samples S1 and S2, and S3 and (e) their calculated donor densities (N_D). 93

Figure 51 (a) SEM image and (b) XRD pattern of ZnO nanowires on FTO substrate. (c) SEM image and (d) EDX spectra of p-NiO/n-ZnO nanowires. 94

Figure 52 (a) <i>I-V</i> characteristics of p-NiO/n-ZnO NWs heterojunction under dark conditions and (b) the Capacitance-voltage measurement. Mott Schottky plots ($1/C^2$ vs. V) of n-ZnO/p-Si nanowires acquired at 1 MHz in the reverse bias region.....	95
Figure 53 (a, b) In plane and tilt-view SEM images of CdS@ZnO NWS on p-Si substrate. (c) TEM images of ZnO and CdS@ZnO NWs, (d) the inset shows the lattice fringes of a CdS NP decorated on the ZnO surface.....	99
Figure 54 EDX spectroscopic mapping images of CdS NPs/ZnO nanowires.....	100
Figure 55 (a) Schematic representation of the SDS device. (b) 2D and (c) 3D plots of the topography of ZnO nanowires measured by AFM in non-contact mode; and (d) a line scan profile corresponding to the blue line in figure b.....	101
Figure 56 (a) UV-Vis optical absorption spectra of ZnO and CdS@ZnO grown on p-Si substrate (b) schematic diagram showing the energy band structure and electron-hole pair separation in the CdS NP/ZnO heterostructure.....	102
Figure 57 (a) Current-voltage characteristics of CdS@n-ZnO/p-Si in dark and under solar illumination in N ₂ atmosphere, (b) a magnified part of the <i>I-V</i> curve.....	103
Figure 58 Gas sensing characteristics of CdS@n-ZnO/p-Si system. ON/OFF curves (oxygen / nitrogen) recorded at different constant currents in (a) dark and under (b) solar illumination showing different gas sensing behaviors. (c) ON/OFF (oxygen / nitrogen) curve recorded with open circuit voltage V_{oc} ($I = 0$ A) under solar illumination condition.....	105
Figure 59 Gas sensing characteristics of CdS@n-ZnO/p-Si system. ON/OFF (ethanol / air) curves of CdS@n-ZnO/p-Si recorded in (a) dark and under (b) solar illumination (Inset shows the sensitivity of the device with different ethanol concentrations).....	107
Figure 60 ON/OFF (methane / air) curves of (a) CdS@n-ZnO/p-Si and (b) n-ZnO/p-Si recorded under solar illumination. Insets show the sensitivity of the device with different methane concentrations.....	107
Figure 61 Step-by-step SDS proposed mechanism: (a) <i>I-V</i> curves recorded in dark and under solar illumination of CdS@n-ZnO/p-Si, (b) a sketch of their high energy electron patterning under solar illumination, (c) <i>I-V</i> curves recorded under solar illumination in N ₂ and O ₂ atmospheres of CdS@n-ZnO/p-Si, (d) their corresponding charge carrier distribution sketches, (e) <i>I-V</i> curves recorded under solar illumination in air and 1000 ppm ethanol atmospheres of CdS@n-ZnO/p-Si, and (f) the corresponding charge carrier distribution sketches.....	109
Figure 62 Capacitance-voltage measurements. Mott Schottky plots ($1/C^2$ vs. V) of (a) CdS@n-ZnO/p-Si, and (b) n-ZnO/p-Si acquired at 1 MHz in the reverse bias region. Environmental dependent N_D of (c) CdS@n-ZnO/p-Si and (d) n-ZnO/p-Si recorded in dark and under solar illumination.....	114

Figure 63 Evolution of N_D of CdS@n-ZnO/p-Si and n-ZnO/p-Si devices after switching off the solar simulator..... 115

Figure 64 Light intensity dependence of the open circuit voltage (V_{oc}) of CdS@n-ZnO/p-Si system in N_2 and O_2 atmosphere and their relative change (ΔV_{oc}). 116

Figure 65 Schematic representation of the SDS device based on radial CdS@ZnO/p-Si NWs. 118

Figure 66 (a) I-V characteristics of CdS@n-ZnO/p-Si NWs heterojunction in dark and under solar illumination. (b) a magnified part of the I-V curve to show the open circuit voltage..... 119

Figure 67 C-V measurement. Mott Schottky plots ($1/C^2$ vs. V) of CdS@n-ZnO/p-Si NWs acquired at 1 MHz in the reverse bias region..... 120

Figure 68 (a) ON/OFF (oxygen/ nitrogen) curves of CdS@n-ZnO/p-SiNWs sensor recorded under solar illumination with no applied current ($I = 0$ A) and at room temperature. (b) Charge carrier distribution of CdS@n-ZnO/p-SiNWs in N_2 and O_2 atmospheres under solar illumination. 121

Figure 69 I-V characteristics of n-ZnO/i- Al_2O_3 /p-Si heterojunction in dark and under solar illumination. (b) A magnified part of the I-V curve to show the open circuit voltage. (c) The reverse bias I-V characteristics of n-ZnO/p-Si (p-n junction) and n-ZnO/i- Al_2O_3 /p-Si (n-i-p junction). (d) ON/OFF (oxygen/ nitrogen) curves of n-ZnO/i- Al_2O_3 /p-Si sensor recorded under solar illumination with no applied current ($I = 0$ A) and at room temperature. 124

Figure 70 (a) Schematic representation of p-NiO thin film/n-Si heterojunction gas sensor device. (b) XRD pattern of the post-annealed NiO thin film. (c, d) in plane and cross-sectional SEM images of NiO thin film/n-Si heterojunction. 125

Figure 71 I-V characteristics of p-NiO/n-Si diode heterojunction (a) in dark and (b) under solar illumination. 126

Figure 72 (a) ON/OFF (oxygen/ nitrogen), (b) ON/OFF (NO_2 / synthetic air), c) ON/OFF (1000 ppm ethanol/synthetic air) curves of p-NiO/n-Si sensor recorded under solar illumination with no applied current ($I = 0$ A) and at room temperature. 127

Figure 73 KPFM Image of a CdS decorated ZnO nanowire (a) before UV exposure, (b) under UV exposure, (c) after UV exposure, (d) the corresponding AFM topographic image. 129

Figure 74 (a) SEM images of ITO layer on the top of CdS@ZnO/p-Si substrate. (b) A schematic representation of the final device with ITO top contact..... 130

Figure 75 Schematic illustration of the ITO deposition on the top of nanowires. (1) Spin casting the photoresist, (2, 3) Oxygen Plasma reactive ion etch, (4) ITO deposition, (5) Removal of the photoresist. 131

Figure 76 SEM images of ITO deposition steps on the top of nanowire arrays (top set of images) and top of nanopillars (down set images): (1) Spin casting the photoresist, (2, 3) oxygen plasma reactive ion etch.	131
Figure 77 Tilted SEM images of n-ZnO NWs/p-Si/SiO ₂ /Si miniaturized sensor device.....	132
Figure 78 Scheme of an n-ZnO/p-Si nanowire device fabrication process: (1) the nanowire is positioned between two pre-patterned microelectrodes. (2) The n-ZnO shell at one end of the nanowire is removed by FIB milling, granting access to the p-Si core. (3) The nanowire is contacted with FIB nanolithography to the pre-patterned microelectrodes. Both the n-ZnO and p-Si parts are electrically accessible in the final device configuration.	135
Figure 79 General view of an n-ZnO/p-Si coaxial nanowire device after the FIB fabrication process and the corresponding high magnification image of the p-Si contact area (The removal of the ZnO outer layer is clearly visible) and high magnification image of the n-ZnO contact area.....	136
Figure 80 EDX line scans of the two contact areas (as-grown and milled) of the device shown in Fig.2. Zinc counts are only found in the as-grown area, indicating that the outer n-ZnO layer was completely removed after FIB milling.....	137
Figure 81 I-V curves from an n-ZnO/p-Si nanowire measured in dark and light conditions and at room temperature. The rectifying responses were fitted to the equivalent model shown in the inset (dashed line). A photogenerated current I_{ph} , and open voltage V_{oc} of 1,0 nA and 1mV respectively were observed under illumination (inset).....	139
Figure 82 Dynamic response an n-ZnO/p-Si nanowire to different oxygen pulse concentrations as function of the selected bias regime (inset)	141
Figure 83 Response of an n-ZnO/p-Si nanowire prototype sensor device to different oxygen concentrations as function of the bias current through the device.....	142
Figure 84 (a) SEM images of ZnO shell deposited by ALD technique a p-Si nanowire core, (b) the n-ZnO/p-Si nanowire single devices connected by two Pt electrodes, (c) the gas sensing responses toward different gases (5 ppm NO ₂ , 200 ppm NH ₃ , 10 ppm H ₂ S, 250 ppm CO) at 250 °C.	143
Figure 85 Controlled growth of well-aligned ZnO nanowires.	145
Figure 86 Fabrication of p-n heterojunctions based on ZnO and their complex heterostructures as well as CdS decoration.	146
Figure 87 Autonomously operated solar diode sensors (SDS).....	147
Figure 88 Heterojunction device based on a single coaxial n-ZnO/p-Si nanowire.....	147

10. List of Tables

Table 1 Commercially purchased chemicals and substrates.	39
Table 2 ALD deposition parameters and post annealing conditions used to deposit different ZnO seed layers on substrates.	41
Table 3 Summary of the experimental conditions used in the hydrothermal synthesis of ZnO NWs.	42
Table 4 Summary of different anodization parameters used for ultra-long ZnO NWs synthesis.	42
Table 5 Summary of ZnO nanostructures synthesized on Zn foil by different methods.	76

11. Erklärung

Ich versichere, dass ich die von mir vorgelegte Dissertation selbständig angefertigt, die benutzten Quellen und Hilfsmittel vollständig angegeben und die Stellen der Arbeit – einschließlich Tabellen, Karten, Abbildungen –, die anderen Werken im Wortlaut oder dem Sinn nach entnommen sind, in jedem Einzelfall als Entlehnung kenntlich gemacht habe; dass diese Dissertation noch keiner anderen Fakultät oder Universität zur Prüfung vorgelegen hat; dass sie – abgesehen von unten angegebenen Teilpublikationen – noch nicht veröffentlicht worden ist sowie, dass ich eine solche Veröffentlichung vor Abschluss des Promotionsverfahrens nicht vornehmen werde.

Die Bestimmungen dieser Promotionsordnung sind mir bekannt. Die von mir vorgelegte Dissertation ist zwischen 04.2010-10.2013 unter der Betreuung von Herrn Prof. Dr. Sanjay Mathur entstanden.

Alaaeldin Abdeltawab Mohamed Gad

Köln 21. 05. 2013

12. Teilpublikationen

PATENTS

- M Hoffmann, J. D. Prades, **Alaa E. Gad**, F. H. Ramirez, H. Shen, and S. Mathur “Fluid detector and method for detecting fluids” European Patent number: EP 11179783.3

PUBLICATIONS

- **Alaa E. Gad**, M. Hoffmann, F. H. Ramirez, J. D. Prades, H. Shen, S. Mathur, *Materials Chemistry and Physics*, 135, 618, 2012. (DOI: 10.1016/j.matchemphys.2012.05.034)
- M. Hoffmann*, **Alaa E. Gad***, J. D. Prade*, F. H. Ramirez, R. Fiz, H. Shen, and S. Mathur, *Nano Energy*, 2, 514-522, 2013. (DOI: 10.1016/j.nanoen.2012.12.003) (*first authors)
- **Alaa E. Gad**, M. Hoffmann, T. Leuning, J. D. Prades, F. H. Ramirez, H. Shen, S. Mathur, conference proceedings of the 14th International Meeting on Chemical Sensors (IMCS 2012), 20-23 May 2012 Nürnberg, Germany, 1312-1315, 2012. (DOI: 10.5162/IMCS2012/p2.0.16)
- **Alaa E. Gad**, M. Hoffmann, F. H. Ramirez, J. D. Prades, H. Shen, S. Mathur, *Procedia Engineering*, 47, 1279–1280, 2012. (26th European Conference on Solid-State Transducers, EUROSENSOR 2012).
- **Alaa E. Gad**, S. Mathur, conference proceedings of the 37th International Conference & Exposition on Advanced Ceramics & Composites (ICACC), January 22-27, 2012, Daytona Beach, Florida, USA.

Curriculum Vitae

Alaaeldin Abdeltawab Mohamed Gad

PERSONAL INFORMATION

- First Name : Alaaeldin
- Last Name : Gad
- Date/Place of Birth: 01 November 1980 in Fayoum, Egypt
- Email: agadnrc@gmail.com, alaanrc@yahoo.com
- Nationality: Egyptian

EDUCATION

- **Ph.D.** in Natural Sciences (Dr. rer. nat.)
Inorganic and Material Chemistry, University of Cologne (Germany) (*DAAD scholarship, GERLS program*)
Dissertation: Solar Diodes: Novel Heterostructured Materials for Self-Powered Gas Sensors
Supervisor: Prof. Dr. Sanjay Mathur
2010-2013
- **M.Sc.** in inorganic chemistry, faculty of science, Cairo University, Cairo, Egypt, 2007
- **Preliminary M.Sc. Courses** in inorganic chemistry, Cairo University, Cairo, Egypt, 2004.
- **B.Sc.** in Chemistry, faculty of science, Cairo University (Fayoum Branch), Cairo, Egypt, 2002. Grade: Very good.

INTERNATIONAL CONFERENCES

- **Alaa. E. Gad**, M. Hoffmann, J. D. Prades, F. H. Ramirez, H. Shen, S. Mathur, E-MRS European Materials Research Society Spring meeting 2013, 27-31 May 2013, congress center-Strasbourg, France. (Oral presentation)

- **Alaa. E. Gad**, M. Hoffmann, J. D. Prades, F. H. Ramirez, H. Shen, S. Mathur, the 37th International Conference & Exposition on Advanced Ceramics & Composites (ICACC), January 27-February 1, 2013, Daytona Beach, Florida, USA. (Oral presentation)
- **Alaa. E. Gad**, M. Hoffmann, J. D. Prades, F. H. Ramirez, H. Shen, S. Mathur, MRS Fall Meeting & Exhibit 2012, 25 – 30 November 2012, Boston, MA, USA. (Oral presentation)
- **Alaa. E. Gad**, M. Hoffmann, J. D. Prades, F. H. Ramirez, H. Shen, S. Mathur, Materials Science and Engineering 2012, 25 - 27 September 2012, Darmstadt, Germany. (Poster presentation)
- **Alaa. E. Gad**, M. Hoffmann, J. D. Prades, F. H. Ramirez, H. Shen, S. Mathur, 14th International Meeting on Chemical Sensors (IMCS 2012), 20 - 23 May 2012 Nürnberg, Germany. (Poster presentation)
- **Alaa E. Gad**, M. Hoffmann, H. Shen, S. Mathur, the 36th International Conference & Exposition on Advanced Ceramics & Composites (ICACC), January 22-27, 2012, Daytona Beach, Florida, USA. (Poster Presentation)

AWARDS AND HONORS

- The First Prize Poster Award of the 36th International Conference & Exposition on Advanced Ceramics & Composites (ICACC), January 22-27, 2012, Daytona Beach, Florida, USA.